Simulation aux Grandes Echelles et chimie complexe pour la modélisation de la structure chimique des flammes turbulentes

Cédric Mehl

université PARIS-SACLAY

NNT : 2018SACLC052

CentraleSupélec

Large Eddy Simulation and complex chemistry for modeling the chemical structure of turbulent flames

Thèse de doctorat de l'Université Paris-Saclay
préparée à CentraleSupélec

École doctorale n°579 : Sciences mécaniques et énergétiques, matériaux et géosciences (SMEMAG)
Spécialité de doctorat : Energétique

Thèse présentée et soutenue à Gif-sur-Yvette, le 12/06/2018, par

Cédric Mehl

Composition du Jury :

Bénédicte Cuenot Chercheur sénior, CERFACS	Rapporteur
Pascale Domingo Directrice de recherche, Université de Rouen (CORIA – UMR 6614)	Rapporteur & Présidente
Olivier Colin Ingénieur de recherche, IFPEN	Examinateur
Jérôme Idier Directeur de recherche, CNRS (LS2N – UMR 6004)	Examinateur
Andreas Kempf Professeur, Universität Duisburg-Essen	Examinateur
Vincent Moureau Chargé de recherche, Université de Rouen (CORIA – UMR 6614)	Examinateur
Benoît Fiorina Professeur, CentraleSupelec (EM2C – UPR 288)	Directeur de thèse

Thèse de doctorat

Remerciements

Je souhaiterais tout d'abord remercier les membres du jury. Merci à Mme Domingo d'avoir endossé le double rôle de présidente du jury et rapporteuse et à Mme Cuenot d'avoir accepté d'être rapporteuse. Je suis très reconnaissant pour votre lecture attentive du manuscript de thèse, ainsi que vos questions et remarques très pertinentes pendant la soutenance qui ont permis d'alimenter ma réflexion. Je remercie également Vincent, Christian, Jérôme et Andreas d'avoir pris part à mon jury et d'avoir pris la peine de lire mon mémoire.

Je tiens bien évidemment à remercier mon directeur de thèse, Benoît Fiorina, qui a su me guider durant cette tortueuse aventure qu'est la thèse. Tes conseils ont su me faire progresser de manière continue pendant ces trois années.

Certaines personnes ont joué un rôle particulier dans le déroulement de mes travaux. C'est ici que je souhaiterais addresser ma profonde gratitude envers Jérôme Idier, qui en plus de prendre part au jury a été d'une aide infinie pour traiter l'épineuse thématique de la déconvolution. De la même manière, j'aimerais remercier Vincent et Renaud, qui ont toujours été très disponibles pour répondre aux questions sur YALES2 et sur la modélisation de la combustion, et m'ont impliqué dans le projet "flammes plissées filtrées". Cela a grandement influé sur mon travail et ma thèse n'aurait pas été la même sans l'apport de ces idées novatrices.

Cette aventure n'aurait pas été la même non plus sans l'environnement de travail extraordinaire de l'EM2C. Je souhaite addresser de chaleureux remerciements à toutes les personnes que j'ai pu cotôyer lors de mon passage au laboratoire, incluant doctorants, secrétaires, chercheurs permanents, techniciens et j'en oublie. Merci d'avoir fait de ce laboratoire un endroit si accueillant. Je souhaite en particulier adresser des remerciements à mes différents collègues de bureaux de Châtenay ainsi que de Saclay, mais également à toutes les personnes avec qui j'ai eu l'occasion de partager cafés, repas, soirées et autres. Merci à la "team Benoît" de la première heure (Mélody, Adrien, Giampaolo), travailler à vos côtés était un plaisir, et je souhaite plein de réussite aux nouveaux doctorants qui reprennent le flambeau. Enfin, un petit mot pour l'équipe UJ2CP, l'organisation des afterworks et autres événements fut une expérience très en-

richissante pour moi.

Une pensée également pour toutes les personnes du "2A", qui se reconnaitront. Les multiples soirées et week-ends partagés avec vous ont été une bouffée d'oxygène incroyable. Et ce n'est évidemment pas terminé ! Petite dédicasse à la coloc de Sceaux, Julien, Solen, Amaury et en particulier Arthur qui a ensuite eu la bonne idée de se mettre en coloc avec moi pendant l'intégralité de la thèse. C'est ici que j'aimerais aussi remercier mes amis Alsaciens qui, comme moi, sont venu se perdre en région parisienne. Merci à Léo et Antoine, jamais réticents à l'idée de prendre une bière (ou plus si affiinités...). Merci à Charles, pour les multiples soirées passées ensemble et pour ta présence lors de la soutenance.

Merci à ma famille, et en particulier à ma mère, mon père, Jérémy et Anaïs qui ont toujours été présents, que ce soit lors de mes retours dans mon Alsace natale ou lors de leurs visites à Paris.

Enfin, je remercie Lucia qui m'a soutenu pendant ce périple, et sans qui les choses auraient été beaucoup plus difficiles.

Abstract

Numerical tools are widely used in the design process of industrial burners such as gas turbines, internal combustion engines or glass furnaces. Simulations indeed offer a way to drastically reduce research and development costs by enabling engineers to make design choices before carrying out expensive test campaigns. A wide range of engineering problems can be studied with state-of-the-art Computational Fluid Dynamics (CFD) solvers. Good examples are flame ignition, lean blow-out and pollutants formation, which are of primary interest for gas turbine development.

In any of the aforementioned systems, the flow is turbulent and interacts strongly with the chemical reactions taking place in the burner. Simplified models for chemical kinetics are often sufficient to predict basic flame dynamics, but more complex physical effects require the use of higher details in the chemical processes description. Thanks to the rapid improvement of computational resources, simulations of burners with detailed chemistry are nowadays accessible. Nevertheless, the cost induced by the simulation of the entire turbulence spectrum and the whole set of chemical scales is prohibitive. Large Eddy Simulation (LES) is a widespread technique for addressing this issue. LES consists in solving only large flow structures and modeling the small scales. In particular, interactions between turbulent eddies and the flame front at the subgrid scale must be modeled using a turbulent combustion model.

State-of-the-art turbulent combustion models lead to good results in many situations when it comes to flame dynamics and temperature fields, but the prediction of pollutants formation remains a challenging task. Indeed, the prediction of the correct flame chemical structure at low computational costs is hardly reachable in practice. In this thesis, two models are explored to improve pollutants formation in turbulent premixed combustion: (i) a model based on deconvolution of filtered scalars and explicit flame front filtering; (ii) a model involving the optimization of chemistry to reproduce filtered turbulent flames. The objective of the work is to achieve high accuracy in pollutants formation prediction at low computational costs.

Keywords: Large Eddy Simulation, Turbulent combustion, Pollutants predic-

tion, Subgrid scale wrinkling, Flame chemical structure, Deconvolution.

Résumé

Les outils numériques contribuent très largement au développement de chambres de combustion industrielles comme les turbines à gaz, les moteurs à combustion interne ou les fours verriers. Les simulations numériques constituent en effet un moyen efficace de réduire de manière significative les coûts de recherche et développement. Elles assistent les ingénieurs dans les choix de design des brûleurs et diminuent ainsi le nombre d'essais à réaliser en conditions réelles. Une large gamme de problèmes peuvent être étudiés grâce aux récentes avancées en mécanique des fluides numérique. L'étude des phénomènes d'allumage, d'extinction et de formation de polluants, essentiels pour le développement de turbines à gaz, en sont de bon exemples.

Quelque soit le système pratique considéré, l'écoulement est turbulent et intéragit fortement avec les réactions chimiques qui ont lieu dans la chambre de combustion. Une description simplifiée des processus chimiques est souvent suffisante pour prédire la dynamique de flamme, alors qu'une description plus fine des réactions est nécessaire pour étudier des phénomènes plus complexes. Grâce à l'amélioration continue des moyens de calcul, des simulations de brûleurs avec chimie complexe sont réalisables. Le coût de calcul induit par la résolution du spectre de turbulence dans sa totalité ainsi que l'ensemble des échelles chimiques est néanmoins trop important. Afin de remédier à ce problème, La Simulation aux Grande Echelles (SGE) a été développée. Le principe de la SGE est de résoudre les grandes échelles de l'écoulement et de modéliser les plus petites échelles. En particuler, les interactions entre les structures turbulentes et le front de flamme nécessitent une modélisation à l'aide d'un modèle dit de combustion turbulente.

Les modèles de combustion turbulente les plus avancés amènent à de bon résultats pour la plupart des systèmes de combustion lorsqu'il s'agit de prédire la dynamique de flamme et le champ de température. La prédiction de polluants reste cependant une difficulté majeure. Les polluants sont en effet liés à la structure chimique de la flamme, qui est difficile à prédire à coût de calcul modéré. Dans cette thèse, deux modèles dont le but est d'améliorer la prédiction des polluants dans les flammes sont étudiés: (i) le premier modèle est basé sur la déconvolution de quantités thermo-chimiques filtrées; (ii) le second modèle

implique l'optimization de la chimie pour obtenir des flammes turbulentes filtrées. L'objectif des travaux est d'obtenir une prédiction précise des polluants à coût de calcul réduit.

Keywords: Simulation aux Grandes Echelles, Combustion turbulente, Prédiction des pollutants, Plissement de sous-maille, Structure chimique de flamme, Déconvolution.

Contents

Introduction

The energy sector in the 21^{st} century

The energy sector has experienced a deep change in the past decades, shaped by the growing awareness of global warming. Energy related activities are indeed the largest contributor to the emission of Green House Gases (GHG). In 2010, 68% of emitted GHG was attributed to the energy sector, including contributions from electricity/heat generation, transportation, as well as industrial and residential consumption. To assess the importance taken by environmental concerns in decision making, the Research, Development & Demonstration (RD&D) expenditures in the energy sector are selected as an indicator of the change. The evolution of public sector RD&D budgets of IEA[1] member countries since 1974 is illustrated in Fig. 1. The total budget is split into expenditures for several energy technologies. The change in public policies results in an important diversification of RD&D portfolios: before the 21^{st} century most of the research budgets were spent on nuclear energy while in 2015 the budgets are evenly split. Some technologies such as fuel cells have even emerged after 2000. Unsurprisingly, renewable energies and energy efficiency attract a large part of the current RD&D expenditures. The former constitute solutions to produce emission-less energy while the latter is a way to reduce costs and improve existing technologies. The energy transition will heavily depend on the development of renewable energies in their different forms (wind, solar, geothermal, hydraulic and tidal energies for example) and intensive research is under way.

In this context, it might seem paradoxical that the budget spent on fossil fuels has stabilized in the past few years, apart from a peak due to the American Recovery and Reinvestment Act of 2009 following the economic downturn. Fossil fuels are the main source of GHG emissions while they also constitute the major part of the energy production. In 2014, 82% of energy was produced from fossil fuels (oil, gas and coal). Improvements of existing systems would hence lead to major gains in terms of pollutants emissions, justifying the ongoing research effort. A crucial step in the production of energy from fossil fuels

[1] International Energy Agency

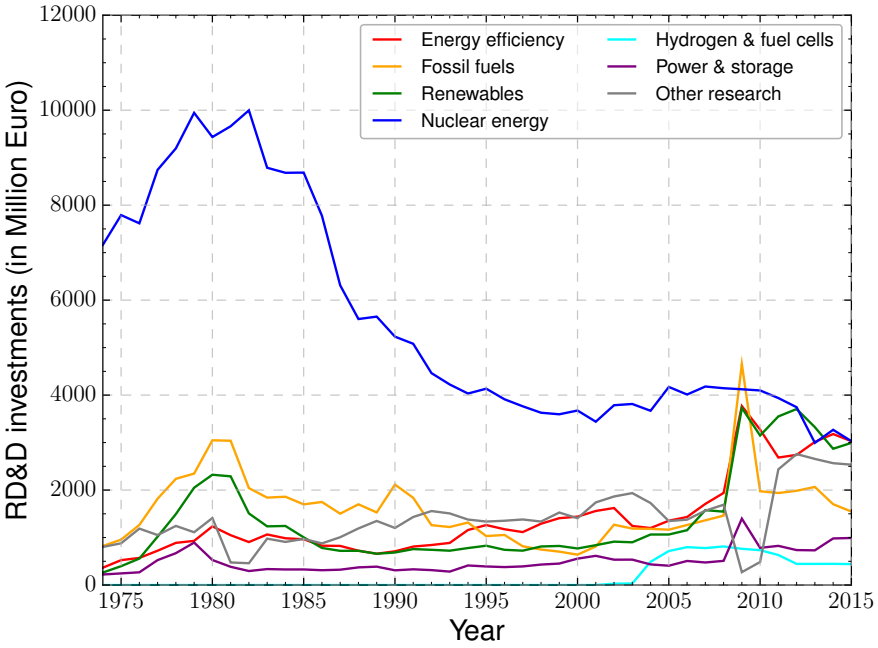

Figure 1: *Research, Development & Demonstration (RD&D) invesments made by IEA member countries since 1974 (data from* `http://www.iea.org`*).*

is combustion, during which fuel is transformed into heat and chemical products. In addition to a large amount of CO_2, pollutants such as nitrogen oxides (NO_x), carbon monoxide (CO) and soot particles are produced during combustion. The combustion process is responsible for a large part of the worldwide pollutants and CO_2 emissions, and has to be carefully optimized in order to meet the objectives set by governments in terms of environmental impact. As these objectives are getting more and more difficult to reach, engineers use numerical tools to design optimized systems. Numerical simulations offer indeed a cheaper alternative than real-scale experiments in order to improve the design of combustion systems, and also enable the access to data which cannot be measured experimentally. Numerical simulation applied to combustion has attracted the interest of many research teams, and transfer of techniques and knowledge towards the industry is now a common practice.

State of the art of numerical combustion

Simulation of complex phenomena with detailed chemistry

Modern computational facilities enable the simulation of complex burners and contribute to a significant decrease of research and development costs. Simulation tools are used for the modeling of systems as diverse as aeronautical

gas turbines, glass furnaces and internal combustion engines. The understanding of flame ignition processes, Lean Blow-Out (LBO) or pollutants formation are for instance essential in the gas turbine industry. These challenging engineering problems feature complex and coupled physical phenomena, nowadays predicted with state-of-the-art numerical tools (Philip et al. (2015); Jaravel (2016); Esclapez et al. (2017a)). Systems are mainly driven by the coupling between the turbulent flow, chemical species mixing, chemical reactions and heat transfers with the surrounding environment. Addressing these issues with numerical tools relies on a fine description of the underlying physics. In particular, the detailed description of chemical reactive pathways is necessary to compute complex phenomena. For hydrocarbons fuels, detailed mechanisms are described by up to hundreds of species and thousands of reactions, leading to expensive computations. However, simulations with more detailed chemistry are reachable thanks to the improvement and increasing availability of computational resources. An example of study performed to predict pollutants in a turbulent flame is shown in Fig. 2 for the sandia D flame (Jaravel et al. (2018)). The prediction of carbon monoxide (on the left in Fig. 2) and nitric oxide (on the right in Fig. 2) is made possible by using a 17 species methane/air mechanism.

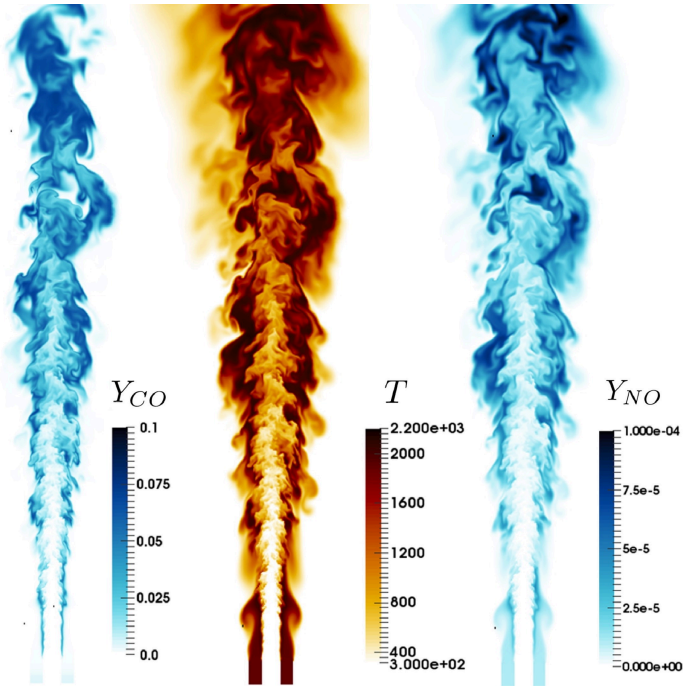

Figure 2: *Simulation of CO and NO formation in the Sandia D flame. Left: CO mass fraction field. Middle: temperature field. Right: NO mass fraction field (Jaravel et al. (2018)).*

Several simulations of turbulent flames with detailed chemistry have been re-

cently performed for a wide variety of fuels. Studies include investigations of flame extinction using a 57 species/383 reactions mechanism for ethanol (Giusti and Mastorakos (2017)), spray ignition of n-dodecane in IC engine conditions with a 106 species/420 reactions mechanism (Salehi et al. (2017)) and autoignition of n-heptane using a 37 species/70 reactions scheme (Mukhopadhyay and Abraham (2012)).

Large-Eddy Simulation and modeling of flame/turbulence interactions

Turbulent flows are characterized by a wide range of physical scales. Energy is transferred from large eddies, with sizes comparable to the system's dimensions, to smaller eddies which dissipate the energy. Additionally, chemical reactions have their own spatial and temporal scales, which are often very small due to the presence of highly reactive radical species. Computations of the entire spectrum of physical scales are called Direct Numerical Simulations (DNS), and are limited to very simple configurations due to their prohibitive computational costs (Mukhopadhyay and Abraham (2012); Xin et al. (2015); Hernández Pérez et al. (2018)). Affordable grid sizes for industrial applications usually range from $\Delta_x = 0.5$ to several millimeters, and are thus much larger than the smallest turbulent and chemical scales (Poinsot and Veynante (2005)).

Large Eddy Simulation (LES) is a mathematical framework enabling the computation of reacting flows on coarse grids. It consists in (i) resolving the large energy-containing structures of the flow on the numerical grid and (ii) modeling the small subgrid scales using dedicated models. Grid size requirements are hence less stringent and computations of realistic burners are possible. In the context of combustion, the flame front is typically much thinner than the LES mesh size. The reactive layer of an ambient methane/air flame has for instance a typical thickness of $\delta_r = 0.1$mm. Interactions between turbulent eddies and the flame thus mainly take place at subgrid scales and accurate models are essential. Major physical phenomena to model are subgrid mixing between chemical species, flame straining effects and flame subgrid scale (SGS) wrinkling.

Flame dynamics and flame stabilization are accurately retrieved in many situations using state-of-the-art LES turbulent combustion models. Engineering problems such as deflagrations (Vermorel et al. (2017)), swirling flame stabilization in gas turbines (Volpiani et al. (2017)) or annular combustor ignition (Philip et al. (2015)) are for example successfully tackled. Heat losses and differential diffusion effects, which have a significant influence on flame propagation and hence on heat release, have also been integrated in models (Donini et al. (2015); Mercier (2016)). Computation of pollutants in LES remains however a more challenging task. Good results are tightly linked to the correct

prediction of the flame chemical structure and require a fine coupling between detailed chemistry and LES. Accurate pollutants prediction have been obtained using models where thermo-chemical quantities are described in a statistical sense by probability density functions (Givi (2006); Raman and Pitsch (2007); Yaldizli et al. (2010)). The computation of the probability density functions is however expensive and prevents the simulation of complex burners. On the other hand, computationally cheaper models have been developed and led to accurate predictions of CO and NOx emitted at the exit of industrial burners (Jaravel et al. (2017)). These models lack however the ability to correctly predict the flame chemical structure and thus the pollutants in the flame front (Volpiani et al. (2017); Franzelli et al. (2012)). Therefore, no model is currently able to accurately predict pollutants in complex burners at an affordable cost.

Orientation of the thesis

The objective of this thesis is to investigate new modeling routes for the computation of complex burners at low computational costs and with an accurate prediction of pollutants formation. The emphasis is on the coupling between the chemical reactions and the turbulent flow field. An essential requirement is to preserve the correct flame chemical structure. The first step of the model development, treated in this thesis, addresses pollutants formation in premixed combustion. In this regime, where fuel and oxidizer are mixed before burning, pollutants emissions can be drastically reduced by an appropriate design of the combustion chamber and premixed combustion is hence used in several new combustion systems.

The following chapter provides a description of the chemistry modeling and explains in more details the issue of coupling combustion to fluid flow in turbulent conditions. An analysis of state-of-the-art turbulent combustion models compatible with turbulent premixed combustion using detailed chemistry is presented next. The selected modeling strategy explored in this thesis is finally explained.

Chapter 1

Turbulent combustion modeling with complex chemistry

Contents

The correct prediction of complex chemical effects in turbulent combustion requires an accurate description of chemical reactions rates, which are described by Arrhenius laws. This chapter first reviews the different methods used to describe chemical processes, in particular reduced and tabulated chemistry. A review of the methods used for coupling chemistry with turbulence in the LES formalism is then provided and conclusions about the shortcomings of current models are given along with perspectives for the development of new modeling strategies.

1.1 Modeling chemical source terms in combustion

ONE of the key ingredients to succeed in the computation of reacting flows is the correct description of chemical processes. Reactions rates control the production and consumption of chemical species and hence the heat release in combustion systems.

1.1.1 Description of chemical processes

A chemical mechanism is defined by a set of reactions involving several chemical species. A N_R-step mechanism involving N_S species can formally be written as:

$$\sum_{k=1}^{N_S} \nu'_{jk} \mathcal{M}_k \leftrightarrow \sum_{k=1}^{N_S} \nu''_{jk} \mathcal{M}_k \qquad (j = 1, ..., N_R) \tag{1.1}$$

where $\mathcal{M}_k$ is the kth species and ν'_{jk}, ν''_{jk} are the forward and backward molar stoechiometric coefficients. The rate of progress of the jth reaction is:

$$w_j = k_{f,j} \prod_{k=1}^{N_S} C_k^{\nu'_{jk}} - k_{b,j} \prod_{k=1}^{N_S} C_k^{\nu''_{jk}} \tag{1.2}$$

where C_k is the molar concentration of the kth species, and $k_{f,j}$, $k_{b,j}$ are respectively the forward and backward reaction constants. These constants are classically expressed as Arrhenius laws (Arrhenius (1967)) . The forward reaction constant can be written for instance:

$$k_{f,j} = A_j T^{\beta_j} exp\left(-\frac{E_{a,j}}{RT}\right) \tag{1.3}$$

where A_j is the pre-exponential factor of reaction j, $E_{a,j}$ the activation energy, R the perfect gas constant and β_j a temperature dependent coefficient. The forward and backward reaction constants for a given reaction j are linked

through the equilibrium constant $K_{e,j}$ of the reaction:

$$K_{e,j} = \frac{k_{f,j}}{k_{b,j}} \tag{1.4}$$

which is deduced from thermodynamics as:

$$K_{e,j} = \left(\frac{p_a}{RT}\right)^{\sum_{k=1}^{N_S} \nu_{jk}} exp\left[\frac{\Delta S_j^0}{R} - \frac{\Delta H_j^0}{RT}\right] \tag{1.5}$$

where $\nu_{jk} = \nu'_{jk} - \nu''_{jk}$, and ΔS_j^0 and ΔH_j^0 are the entropy and enthalpy changes during reaction j. p_a is the pressure of ambient air. By summing the contributions of each reaction, the reaction rate of a species k (in s^{-1}) reads:

$$\dot{\omega}_k = \frac{1}{\rho} W_k \sum_{j=1}^{N_R} \nu_{jk} w_j \tag{1.6}$$

A chemical mechanism must be selected to compute $\dot{\omega}_k$. Several levels of complexity exist for the definition of the chemical scheme, depending on the number of species and reactions considered. The most accurate type of chemical schemes, taking into account a whole set of elementary reactions, are called complete mechanisms[1]. They feature information about all the kinetic processes taking place in the flame, including all chemical time scales. These mechanisms typically involve thousands of species and hundreds of reactions and their domain of validity (in terms of pressure, temperature and equivalence ratio range) is typically very broad (Hilbert et al. (2004)).

Complete mechanisms are however not suited to practical turbulent combustion simulations as they induce a tremendous computation cost. Additionally, source terms are very stiff due to the presence of highly reactive radicals. Two different ways for computing the reaction rate $\dot{\omega}_k$ in a CFD simulation at lower cost are proposed in the literature:

- The first method, called reduced chemistry, consists in reducing the (N_S species ,N_R reactions) complete mechanism into a smaller (N_S^{red} species ,N_R^{red} reactions) mechanism (Hilbert et al. (2004)). Reduced mechanisms usually have a smaller domain of validity in terms of pressure, temperature and equivalence ratio, but are cheaper to use in 3-D simulations.

- The second method is named tabulated chemistry (Maas and Pope

[1]The terminology of Hilbert et al. (2004) is retained for classifying the mechanisms.

(1992); Gicquel et al. (2000)) and consists in storing the chemical information in tables which are subsequently read in CFD computations. The tables are built by computing simple flame configurations, most often 0-D and 1-D flames, which require low computation times (Gicquel et al. (2000); Fiorina et al. (2010)). Complete or reduced mechanisms can be used to built tables. Combustion is then described by a small set of variables used as coordinates of the tables. These variables are for example a progress variable c or a mixture fraction Z (Auzillon et al. (2012); Coussement et al. (2015)). The 3-D reaction rate is then computed as $\dot{\omega}_k = \dot{\omega}_k^{tab}(c, Z, ...)$, where the superscript tab denotes quantities read in a table.

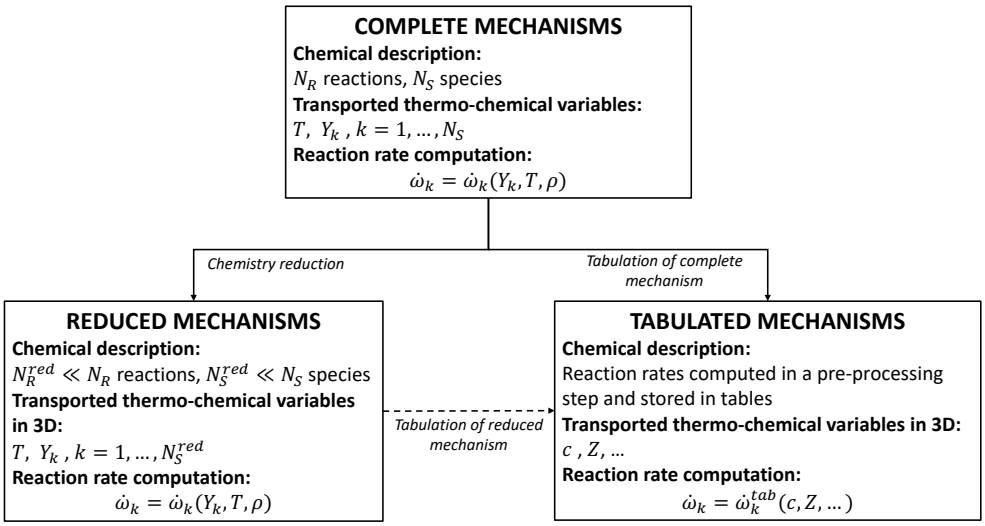

Figure 1.1: *Strategies for computing reaction rates at an affordable cost in 3D computations.*

In order to emphasize the distinction between tabulated and reduced mechanisms, the latter strategy is also referred to as *transported* chemistry. A summary of the chemical reduction approaches used in simulations is provided in Fig. 1.1. Tabulated and transported chemistry techniques are respectively detailed in Sec. 1.1.2 and Sec. 1.1.3, along with insights about their use in LES.

1.1.2 Tabulated chemistry

Methodology Tabulated chemistry consists in computing simple canonical flames with a complete or a reduced mechanism, and storing chemical information in look-up tables later read in the 3-D simulation. The strategy has been initiated in the work of Maas and Pope (1992), who argued that a reduced chemical-state space can be used to describe chemical reactions. In a tabulated chemistry context, combustion is described by a few controlling vari-

ables, and thermo-chemical variables are tabulated as a function of these variables in a pre-processing step. In the commonly used flamelet-based tabulation methods (Gicquel et al. (2000), Oijen and Goey (2000)), tables are built by computing sets of reference laminar flames. Only the controlling variables are transported in the simulation and thermo-chemical variables required for conservation equations closure and post-processing are extracted from the tables. The most common controlling variable is the progress variable c, defined as a monotonic function varying from 0 in fresh gases to 1 in burnt gases. Strong assumptions about the flame structure are made when building the table, and including additional physical processes requires additional controlling variables. A mixture fraction Z is for example used to describe mixing (Auzillon et al. (2012), Fiorina et al. (2005)), and a specific enthalpy h for modeling heat losses (Fiorina et al. (2005)).

Use in practical applications Due to affordable computational costs, tabulated chemistry has been widely used for the simulation of industrial burners (Esclapez et al. (2017b); See and Ihme (2015)), and good results are reported regarding flame dynamics (Auzillon et al. (2011)). As single flame archetypes are generally used to build chemical look-up table, tabulated chemistry is not adapted to multi-regime combustion mode. This is especially an issue for the pollutant such as CO whose production-consumption rate are very sensitive to the flame regime (Fiorina et al. (2005); Franzelli et al. (2013)).

1.1.3 Reduced chemistry

The second category of techniques used to make 3-D reacting flows computations affordable is chemistry reduction. Complete mechanisms are reduced using dedicated techniques and chemical reaction rates are computed in 3-D simulations from transported species mass fractions. Coupling a chemical mechanism to a flow solver requires however the solving of an additional transport equation for each species in a mechanism, which makes reduced chemistry usually more expensive than tabulated chemistry. The increasing interest in reduced chemistry is thus tightly linked to the evolution of supercomputing power. Several types of chemical schemes obtained from the reduction of complete mechanisms are defined (Hilbert et al. (2004), Fiorina et al. (2014) and Lu and Law (2009)) and the following classification is retained in this work: (1) Detailed/skeletal mechanisms; (2) systemically reduced mechanisms; (3) Global-step mechanisms. A brief description of these schemes is provided below.

1.1.3.1 Detailed/skeletal mechanisms

Methodology A first strategy used to reduce chemical mechanisms is to eliminate unimportant species and reactions from a complete mechanism. This

leads to the definition of detailed mechanisms. They typically include about 20 to 50 % of the species from the complete mechanism (Hilbert et al. (2004)). Different techniques have been designed in the literature to eliminate reactions (Whitehouse et al. (2004); Wang and Frenklach (1991); Lu et al. (2001); Massias et al. (1999); Elliott et al. (2005)) and species (Turanyi (1990); Pepiot-Desjardins and Pitsch (2008); Lu and Law (2005)). A more detailed list of such techniques with associated references is given by Lu and Law (2009). Detailed mechanisms including few species are also called skeletal mechanisms.

Use in practical applications Detailed and skeletal chemical mechanisms are often used in DNS of small size canonical configurations to conduct theoretical studies or LES model developments (Doan et al. (2018); Borghesi et al. (2013)). Detailed chemistry enables the prediction of complex chemistry effects and are for instance used to study ignition phenomena (Borghesi et al. (2013); Yoo et al. (2013); Dong et al. (2017)). Due to important computational costs, the use of detailed chemistry in LES is limited to a few academic configurations (Giusti and Mastorakos (2017); Irannejad et al. (2015)).

1.1.3.2 Systemically reduced mechanisms

Methodology Systematic reduction techniques aim at further reducing detailed mechanisms by analyzing chemical time scales. The Quasi Steady State Approximation (QSSA) and the Partial Equilibrium Assumption (PEA) are commonly used to build systematically reduced mechanisms (Lu and Law (2008); Jaravel et al. (2017)). QSSA and PEA give rise to algebraic relationships between some elementary reaction rates, thus reducing the number of species to transport in the simulation. An explanation of these techniques is provided by Goussis and Maas (2011).

Use in practical applications Systematically reduced mechanisms contain fewer species and reactions than detailed mechanisms and their numerical stiffness is also decreased (Lu and Law (2008)). Hence, coupled to the global increase of computational power, systematically reduced chemistry is well suited to LES. Examples include the Analytically Reduced Chemistry (ARC) developed by Pepiot-Desjardins and Pitsch (2008) and applied to academic configurations (Jaravel et al. (2018)) as well as semi-industrial burners (Jaravel et al. (2017); Felden et al. (2018)). Good results have been obtained for NOx and CO predictions (Jaravel et al. (2017); Jaravel et al. (2018)). Another recent methodology involving algebraic relationships between species concentrations is the automatic reduction technique developed by Jaouen et al. (2017) and applied to auto-thermal reforming of natural gas (Jaouen et al. (2017)).

In addition, systematically reduced mechanisms enable the study of complex chemical effects such as flame ignition (Lignell et al. (2011)).

1.1.3.3 Global-step mechanisms

Methodology Global step mechanisms have been initiated in the work of Westbrook and Dryer (1981) and consist in creating mechanisms with less than 5 reactions. This is accomplished by tuning the Arrhenius parameters of a few global reactions to reproduce physical characteristics such as flame speed, temperature, or species profiles. Many works have focused on the reduction of hydrocarbon chemistry in different flame configurations (Peters (1991); Bilger et al. (1990)). It was found that a dependance of these parameters with the equivalence ratio ϕ is necessary to ensure a correct flame propagation over a wide range of conditions (Fernandez-Tarrazo et al. (2006); Franzelli et al. (2010)). A further distinction can be made between schemes involving one or more intermediate species (typically CO) and one-step chemical schemes where only major reactants and products are involved.

Use in practical applications Global-step mechanisms are used to predict the flame dynamics in complex systems at small computational costs (Wang et al. (2011); Volpiani et al. (2017)). Complex chemistry effects such as ignition, extinction and pollutant formation are however out of reach with highly reduced schemes. Lu and Law (2009) showed for example the inability of a 4-step methane mechanism to capture auto-ignition delays as compared to systematically reduced and detailed mechanisms.

1.1.4 Summary of chemical description in LES

As the direct integration of complete mechanisms is not affordable in LES, tabulated chemistry and reduced chemistry (with a low number of species and reactions) are widely used to simulate academic and practical burners. Despite the low computational costs, LES with tabulated chemical mechanisms involve strong assumptions about the combustion mode. Flamelet-based tabulation techniques indeed rely on the use of libraries built using canonical flames, such as unstretched laminar flamelets (Fiorina et al. (2010)) for premixed combustion or counterflow diffusion flames (Coussement et al. (2015)) for non-premixed combustion. Simulation of complex systems, where multiple flame regimes coexist, is thus out of reach with tabulated chemistry.

The available computational power has increased in the past few years and an increasing number of studies with transported chemistry have been published. Tab.1.1 shows examples of recent LES with detailed or systematically reduced schemes on meshes with a large number of cells. The main advantage of transported chemistry is that the flame structure is solved directly on the

Table 1.1: *Examples of LES simulations with reduced mechanisms in the recent literature.*

Publication	Chemistry		Number of mesh cells
	Species	Reactions	
Jaravel et al. (2017)	22	n/a	120 millions
Irannejad et al. (2015)	44	185	20 millions
Zhang and Mastorakos (2016)	19	15	9 millions
Giusti and Mastorakos (2017)	57	383	5 millions

LES grid and the impact of the local flow field on the flame structure is thus recovered. Recent systematically reduced mechanisms reach a high accuracy on flame structure and pollutants prediction on complex burners (Jaravel et al. (2017)).

Hence, the remaining of this chapter focuses on the use of reduced mechanisms in LES of premixed combustion. The main challenge is the coupling between chemical reaction rates and turbulent flows (Poinsot and Veynante (2005)).

1.2 Coupling chemical source terms with turbulent premixed combustion

The flame front thickness and the flame wrinkling are not fully resolved in LES (Poinsot and Veynante (2005)). Two main challenges are thus met when dealing with LES of premixed flames: the flame front has to be resolved on the coarse LES mesh and the impact of sub-grid scale velocity fluctuations on the flame front must be modeled. A model for LES of premixed turbulent combustion is thus composed of (i) a methodology for numerically resolving the flame front; (ii) a strategy for modeling the effects of small scale structures on the flame front.

The two issues encountered in LES of premixed flames are further detailed in Sec. 1.2.1 and a review of the main models for LES of turbulent premixed flames is presented in Sec. 1.2.2 to 1.2.5.

1.2.1 The LES closure problem

1.2.1.1 Resolving premixed flame fronts

Premixed flames have a finite thickness, resulting from the balance between diffusive processes and source terms in the flame's inner reaction layer (Peters (1988)). In particular, laminar unstreched premixed flame fronts are character-

ized by a laminar flame thickness δ_l^0. A common definition for this thickness, which will be used throughout this work, is based on the maximal gradient of temperature in the flame (Poinsot and Veynante (2005)):

$$\delta_l^0 = \frac{\mid T_b - T_u \mid}{max\left(\mid \frac{\partial T}{\partial x} \mid\right)} \tag{1.7}$$

where T_b and T_u are respectively the burnt and fresh gas temperatures, and x represents the coordinate normal to the flame front. The propagation of the flame, in the direction normal to the reactive layer, is characterized by the laminar flame consumption speed S_l^0 defined as:

$$S_l^0 = \frac{1}{\rho_u(Y_{fuel}^b - Y_{fuel}^u)} \int_{-\infty}^{+\infty} \rho \dot{\omega}_{fuel}(x) dx \tag{1.8}$$

where Y_{fuel}^b and Y_{fuel}^u are respectively the mass fraction of fuel in the burnt and fresh gases, ρ_u the density in fresh gases and $\dot{\omega}_{fuel}$ the fuel reaction rate.

The reaction rate is a non-linear function of thermo-chemical variables and is sensitive to grid resolution. A sufficiently high grid resolution is hence essential to numerically predict correct flame speeds, as illustrated in the work of Kuenne et al. (2017). A major issue in LES is that grid sizes are usually equal or larger than laminar flame thicknesses. An ambient methane air flame in stoechiometric conditions has for instance a thermal thickness of about 0.5mm while typical LES grid sizes in real-scale applications are typically larger than this value (see for example recent simulations of semi-industrial burners by Jaravel et al. (2017) or Volpiani et al. (2017)).

LES models developed in the literature tackle the resolution issue with several strategies. Four main approaches are identified as:

- **No explicit flame front resolution method:** Some methods do not propose an explicit resolution of the flame front. In such cases, the flame front is thickened by numerical diffusion and errors made on source terms are not controlled.

- **Flame thickening:** A strategy for ensuring that enough points are used in the flame front is to artificially thicken the flame front (O'Rourke and Bracco (1979); Butler and O'Rourke (1977); Colin et al. (2000)). The flame front is broadened by a factor $\mathcal{F}$ and transport equations are adapted to correct flame propagation speed (see Sec. 1.2.4 for the description of equations in the thickened flame context). The thickening

factor is computed as (Kuenne et al. (2011)):

$$\mathcal{F} = \max\left(\frac{n_{res}\Delta_x}{\delta_l^0}, 1\right) \tag{1.9}$$

where n_{res} is a parameter representing the number of points in the flame thermal layer. It enables to explicitly control the number of points in the unstretched flame front thickness. A typical value used in LES is $n_{res} = 5$ (Jaravel (2016)), as it enables a correct prediction of the flame front propagation.

- **Flame filtering:** Another option used in recent models is to explicitly filter the flame front (Fiorina et al. (2010); Abou-Taouk et al. (2015); Nambully et al. (2014b)). The spatially filtered value of a physical quantity φ is written:

$$\overline{\varphi}(\mathbf{x}, t) = \int_{\mathbb{R}^3} G_\Delta(\mathbf{x} - \mathbf{u})\varphi(\mathbf{u})d\mathbf{u} \tag{1.10}$$

where G_Δ is the filter kernel, characterized by a filter size Δ. The kernel is isotropic and normalized ($\int_{\mathbb{R}^3} G_\Delta(\mathbf{u})d\mathbf{u} = 1$). The Gaussian kernel $G_\Delta(\mathbf{x}) = \sqrt{\frac{6}{\pi\Delta^2}}exp\left(\frac{-6\mathbf{x}^2}{\Delta^2}\right)$ will be considered throughout this thesis. The resolution of the flame front in the filtered formalism is controlled by the filter size Δ. In the case of a Gaussian filter, the number of points in the flame front can be estimated as $2\Delta/\Delta_x$ (Fiorina et al. (2014)).

- **High resolution in the flame front direction:** An alternative is to use a DNS-like resolution of the flame front in the direction of flame propagation. In this way, the grid resolution can be set using knowledge about the flame thickness and ensuring a sufficiently high accuracy on the propagation prediction in the case of unstretched laminar flames. This is used in the LES-ODT model detailed in Sec. 1.2.3.

1.2.1.2 Coupling turbulence and chemical source terms

Part of the interactions between the flame front and turbulence take place at small scales which are not resolved on the LES mesh, and are thus called sub-grid scale interactions. The effects of unresolved eddies on the flame front have thus to be modeled.

For the sake of clarity, the four formalisms described in Sec. 1.2.1.1 and aimed at resolving flames on a LES mesh are unified in a single notation. This leads to the definition of LES filtered thermo-chemical variables written $\overline{\varphi}$. In a variable

density flow, Favre density-weighted filtered variables read:

$$\widetilde{\varphi}(\mathbf{x},t) = \frac{\overline{\rho\varphi}(\mathbf{x},t)}{\overline{\rho}(\mathbf{x},t)} \tag{1.11}$$

Balance equations can be derived for LES variables by applying a filter operator to reactive flow governing equations. The LES species mass fraction conservation reads (Poinsot and Veynante (2005)):

$$\frac{\partial\overline{\rho}\widetilde{Y_k}}{\partial t} + \nabla\cdot\left(\overline{\rho}\widetilde{\boldsymbol{u}}\widetilde{Y_k}\right) = \overline{\nabla\cdot\boldsymbol{\mathcal{J}_k}} + \nabla\cdot\left(\overline{\rho}\widetilde{u}\widetilde{Y_k} - \overline{\rho}\widetilde{uY_k}\right) + \overline{\rho}\widetilde{\dot{\omega}}_k \tag{1.12}$$

The following three RHS terms of Eq. (1.12) are unclosed:

1. The molecular transport $\overline{\nabla\cdot\boldsymbol{\mathcal{J}_k}}$. A Fick law $\boldsymbol{\mathcal{J}_k} = \rho D\nabla Y_k$ is commonly used for modeling diffusion processes so that: $\overline{\nabla\cdot\boldsymbol{\mathcal{J}_k}} = \overline{\nabla\cdot\rho D\nabla Y_k}$. Its modeling is crucial to predict the correct flame propagation speed (Fiorina et al. (2010)).

2. The unresolved convective transport term $\nabla\cdot\left(\overline{\rho}\widetilde{u}\widetilde{Y_k} - \overline{\rho}\widetilde{uY_k}\right)$. A gradient assumption is used in many cases: $\widetilde{u}\widetilde{Y_k} - \widetilde{uY_k} = -\frac{\nu_t}{Sc_k}\nabla\widetilde{Y_k}$, where Sc_k is a subgrid scale Schmidt number and ν_t a turbulent subgrid-scale viscosity computed using a turbulence model. While the gradient assumption is accurate in many applications (Poinsot and Veynante (2005)), countergradient contributions to the unresolved turbulent fluxes have been reported in the literature (Veynante and Trouvé (1997)) and are modelled in LES using dedicated models (Lecocq et al. (2010)).

3. The filtered reaction rate $\overline{\rho}\widetilde{\dot{\omega}}_k$. Most of the combustion studies focus on this term, as it is considered the most challenging to model.

Turbulent combustion models differ in the way the three RHS terms are computed. A review of the main closure models for Eq. (1.12) compatible with transported chemistry is proposed in the next sections:

- Sec. 1.2.2 reviews statistical methods, which do not propose an explicit method for resolving the flame front.
- Sec. 1.2.3 analyzes the ODT model, which is based on a DNS-like resolution of the flame front.
- Sec. 1.2.4 presents the TFLES model, a strategy based on flame thickening.

- Sec. 1.2.5 reviews two recent methodologies relying on flame front filtering.

An evaluation is carried out for each model in the light of the following elements: (i) the ability of the model to capture the correct flame propagation of laminar and turbulent premixed flames; (ii) the accuracy of pollutant predictions; (iii) the computational costs, which strongly influence the applicability of the model to industrial burners.

1.2.2 Statistical methods

Statistical methods are widely used for closing the turbulent combustion equations. In this category of models, flame resolution issues are not treated explicitly.

1.2.2.1 Filtered Density Function methods (FDF)

Originally designed for RANS simulations, PDF methods were suggested in an LES context by Givi (1989) and subsequently renamed as Filtered Density Function (FDF) methods (Pope (1991a)). In PDF methods, physical quantities such as enthalpy or species mass fractions are considered as random variables whose fluctuations around mean values are modeled by probability density functions. The rate-controlling processes (molecular transport and chemical reactions) take place at very small scales and are not resolved in LES. The fluctuations around filtered values can hence be modeled in a statistical sense following a similar methodology than in RANS. A review about PDF/FDF methods in turbulent combustion can be found in Haworth (2010) and a review focused on FDF methods in Givi (2006).

FDF definition For an ideal gas, low Mach number and single phase flow the thermo-chemical state of the mixture can be described by composition variables $\mathbf{\Phi} = (Y_1, ..., Y_{N_S}, h)$ (formally written $\mathbf{\Phi} = (\phi_1, ..., \phi_{N_S+1})$) (Haworth (2010)). For reacting flows, FDF's can be defined in composition space (Jaberi et al. (1999); Colucci et al. (1998)) or velocity-composition space (Sheikhi et al. (2003); Sheikhi et al. (2007)). Velocity-composition methods differ from composition methods by treating the three components of the velocity field as random variables. Sheikhi et al. (2003) show that velocity-composition space methods improve the prediction of turbulent statistics compared to finite-difference based resolutions of the flow in LES. An increase of computational costs by a factor $\mathcal{O}(30)$ is however observed for velocity-composition space method compared to traditional LES (Sheikhi et al. (2003)). The method is here exposed in composition space only for clarity. The composition space FDF

is defined as (Haworth (2010)):

$$f_{\Delta,\mathbf{\Phi}}(\mathbf{\Psi};\mathbf{x},t) = \int_{\mathbb{R}^3} \delta(\mathbf{\Psi} - \mathbf{\Phi}(\mathbf{y},t)) G_\Delta(\mathbf{x}-\mathbf{y}) d\mathbf{y} \tag{1.13}$$

where δ is the multi-dimensional Dirac delta function. Physically, $f_{\Delta,\mathbf{\Phi}}$ is the G_Δ-weighted fraction of the fluid near $\mathbf{x}$ having a composition in the range $\mathbf{\Psi} \leq \mathbf{\Phi} \leq \mathbf{\Psi} + d\mathbf{\Psi}$. For variable density flows, a density-weighted FDF, also called Filtered Mass Density Function (FMDF), is introduced:

$$\mathcal{F}_{\Delta,\mathbf{\Phi}}(\mathbf{\Psi};\mathbf{x},t) = \int_{\mathbb{R}^3} \rho(\mathbf{y},t)\delta(\mathbf{\Psi} - \mathbf{\Phi}(\mathbf{y},t)) G_\Delta(\mathbf{x}-\mathbf{y}) d\mathbf{y} \tag{1.14}$$

Reynolds (respectively Favre) filtered variable $\overline{\varphi}$ (respectively $\widetilde{\varphi}$) depending on composition only can be computed using the FDF (respectively FMDF):

$$\overline{\varphi}(\mathbf{x},t) = \int_{\mathbf{\Psi}} \varphi(\mathbf{\Psi}) f_{\Delta,\mathbf{\Phi}}(\mathbf{\Psi};\mathbf{x},t) d\mathbf{\Psi} \tag{1.15}$$

$$\overline{\rho}\widetilde{\varphi}(\mathbf{x},t) = \int_{\mathbf{\Psi}} \varphi(\mathbf{\Psi}) \mathcal{F}_{\Delta,\mathbf{\Phi}}(\mathbf{\Psi};\mathbf{x},t) d\mathbf{\Psi} \tag{1.16}$$

The computation of the filtered reaction rate in Eq. (1.12) is straightforward when the FMDF is known:

$$\overline{\rho}\widetilde{\dot{\omega}}_k(\mathbf{x},t) = \int_{\mathbf{\Psi}} \dot{\omega}_k(\mathbf{\Psi}) \mathcal{F}_{\Delta,\mathbf{\Phi}}(\mathbf{\Psi};\mathbf{x},t) d\mathbf{\Psi} \tag{1.17}$$

where the dependence of $\dot{\omega}_k$ on $\mathbf{\Psi}$ is given by the Arrhenius laws used for modeling chemical processes.

Two methods have been proposed in the literature in order to compute the FMDF: (i) the presumed FDF method; (ii) the transported FDF method.

Presumed FDF The first way for evaluating the FDF is to presume the probability density function. Presumed FDF's are however limited to a few variables in both tabulated (Linse et al. (2014)) or transported chemistry contexts (Bray et al. (2010)). Multi-variables FDF are often built by assuming that thermo-chemical variables are statistically independent, so that the joint PDF can be written as a multiplication between several single variable FDF's (Fiorina et al. (2005)). The most widely used function is the beta PDF, for which the application to LES can be traced back to the work of Cook and

Riley (1994). Additional analysis has been carried out by Bray et al. (2006) who compared different presumed PDF's. Presuming a joint scalar FDF for a simulation with reduced chemistry and many transported species is difficult as the assumption of independent thermo-chemical variables is often not justified, except in simple configurations (Bray et al. (2010)). This approach is hence not well suited for transported chemistry.

Transported FDF The evaluation of the FDF in an Arrhenius chemistry context is done by solving a transport equation for $\mathcal{F}_{\Delta,\mathbf{\Phi}}$. Transported FDF methods were initiated in the work of Gao and O'Brien (1993) and an expression for the composition FMDF transport equation can be found in Haworth (2010):

$$\frac{\partial \mathcal{F}_{\Delta,\mathbf{\Phi}}}{\partial t} + \frac{\partial}{\partial x_i}\left(\widetilde{u}_i \mathcal{F}_{\Delta,\mathbf{\Phi}}\right) = \underbrace{-\sum_{\alpha=1}^{N_S+1} \frac{\partial}{\partial \psi_\alpha}\left(\dot{\omega}_\alpha(\mathbf{\Psi})\mathcal{F}_{\Delta,\mathbf{\Phi}}\right)}_{\text{Chemical reaction}} + \underbrace{\frac{\partial}{\partial x_i}\left[\left(\widetilde{u}_i - \overline{(u_i \mid \mathbf{\Psi})}\right)\mathcal{F}_{\Delta,\mathbf{\Phi}}\right]}_{\text{Unresolved convection}} + \underbrace{\sum_{\alpha=1}^{N_S+1}\left[\overline{\left(\rho^{-1}(\mathbf{\Psi})\frac{\partial \mathcal{J}_{\alpha,i}}{\partial x_i} \mid \mathbf{\Psi}\right)}\mathcal{F}_{\Delta,\mathbf{\Phi}}\right]}_{\text{Molecular diffusion}} \tag{1.18}$$

where the state vector is formally decomposed as $\mathbf{\Psi} = (\psi_1, ..., \psi_{N_S+1})$, and $\overline{(\varphi \mid \mathbf{\Psi})}$ is a conditional average of φ for a given state vector $\mathbf{\Psi}$. Newton summation convention is used for spatial directions. The terms in the LHS of Eq. (1.18) are written in a closed form while the terms in the RHS require modeling. In particular, the chemical source term is closed and the transported FDF method can be used for computing turbulent reacting flows with either detailed or reduced Arrhenius chemistry. The problem is however shifted towards the closure of the turbulent transport and molecular transport terms. Closure of the turbulent transport term in composition FDF method is usually based on a gradient assumption, which reads (Haworth (2010)):

$$\frac{\partial}{\partial x_i}\left[\left(\widetilde{u}_i - \overline{(u_i \mid \mathbf{\Psi})}\right)\mathcal{F}_{\Delta,\mathbf{\Phi}}\right] = \frac{\partial}{\partial x_i}\left[\frac{\Gamma_\Delta}{\overline{\rho}}\frac{\partial \mathcal{F}_{\Delta,\mathbf{\Phi}}}{\partial x_i}\right] \tag{1.19}$$

where $\Gamma_\Delta = \mu_\Delta / Sc_t$, with μ_Δ an apparent subfilter scale turbulent viscosity and Sc_t a turbulent Schmidt number (assumed to be equal for all scalars).

Molecular diffusivity is commonly computed using mixing models. A simple and widely used model is the Interaction with Exchange by the Mean model

(IEM) (Villermaux and Falk (1994)):

$$\overline{\left(\rho^{-1}(\mathbf{\Psi})\frac{\partial \mathcal{J}_{\alpha,i}}{\partial x_i} \mid \mathbf{\Psi}\right)} = -\frac{1}{\tau_\phi}(\psi_\alpha - \widetilde{\phi}_\alpha) \tag{1.20}$$

where τ_ϕ is a time scale of scalar ϕ computed from turbulence time scales, and $\widetilde{\mathbf{\Phi}} = (\widetilde{\phi}_1, ..., \widetilde{\phi}_{N_S+1})$ is the filtered scalar field. More details can be found in the comprehensive review of Haworth (2010), who also mentions alternatives to IEM.

Lagrangian stochastic methods for FDF transport Solving Eq. (1.18) using conventional techniques is however difficult due to the high number of independent variables involved in the equation (the three spatial coordinates, time and the $N_S + 1$ scalars). The cost for solving the system grows exponentially with the number of transported species. FDF transport models are thus rewritten and solved in a stochastic framework. Two types of methodologies are commonly used in this context: Lagrangian particle methods, where notional particles are used to described the composition FDF, and Eulerian stochastic fields methods were FDF's are described by Eulerian stochastic fields. In both strategies, costs vary linearly with the number of species.
The Lagrangian particle formalism was formally set by Pope (1985) and is based on a system of notional particles which yield the same FDF than the real fluid system. Hence, solving for the evolution of these particles is equivalent to solving Eq. (1.18). A set of N_p particles with masses $m^{(i)}$ ($i = 1, ..., N_p$ being the indexes of the particles) are characterized by their positions $x^{(i)}$ and compositions $\mathbf{\Phi}^{(i)}$. The methods is here presented for composition FDF. In velocity-composition method particles also carry a three-dimensional velocity vector and the modeling issues are slightly different. The evolution of particles for a time increment dt is described by a set of Stochastic Differential Equations (SDE):

$$\begin{cases} dx_i^\star = \widetilde{u}_i^\star dt + dx_{i,turb}^\star & \text{(1.21a)} \\ d\phi_\alpha^\star = \dot{\omega}_\alpha\left(\mathbf{\Phi}^\star\right) dt + \theta_{\alpha,mix}^\star dt & \text{(1.21b)} \end{cases}$$

where the star superscript denotes a particle, $\alpha = 1, ..., N_S + 1$ the scalar index. $dx_{i,turb}^\star$ represents the fluctuations around the filtered velocities and $\theta_{\alpha,mix}^\star$ is a term representing molecular diffusivity. For the system of notional particles to have a FDF whose evolution is the same than the FDF defined by Eq. (1.18), models for turbulent transport and molecular diffusivity coherent with the models given in Eqs. (1.19) and (1.20) have to be used. Particle

evolution equations are written under this requirement as (Haworth (2010)):

$$\begin{cases} dx_i^\star = \widetilde{u}_i^\star dt + \left(\overline{\rho}^{-1}\dfrac{\partial \Gamma_\Delta}{\partial x_i}\right)^\star dt + \left(\sqrt{2\overline{\rho}^{-1}\Gamma_\Delta}\right)^\star dW_i & \text{(1.22a)} \\ d\phi_\alpha^\star = \dot{\omega}_\alpha\left(\mathbf{\Phi}^\star\right)dt - \dfrac{1}{\tau_\phi}(\phi_\alpha^\star - \widetilde{\phi}_\alpha)dt & \text{(1.22b)} \end{cases}$$

where W_i's are Wiener processes which physically represent random walk in space due to turbulent fluctuations. They are consistent with the gradient assumption for turbulent transport (Haworth (2010)).

Several numerical strategies have been developed to solve the problem. The most popular is the hybrid Lagrangian/Eulerian mesh method (LPEM), in which the flow field is computed on a regular LES mesh using conventional techniques, while composition variables are computed using particles and solving Eqs. 1.22a. Other alternatives have been reported in the literature, such as the stand-alone Lagrangian particle methods, where flow field variables are also transported using notional particles, or Eulerian particle methods (Pope (1981)), where notional particles are bound to move only on the LES grid nodes.

Eulerian stochastic fields methods Describing FDF's by particles means that state-of-the-art Eulerian algorithms and existing CFD solvers aimed at solving gas phases cannot be used directly. To enhance the development of FDF methods in existing solvers, Eulerian stochastic fields methods have been suggested (Valino (1998)). In this strategy, notional particles are replaced by notional Eulerian fields. Similarly to notional particles, these fields are defined so that they yield the same FDF than the real fluid system, but vary on scales of the order of magnitude of the LES grid size. The effects of subgrid scale fluctuations, which cannot be resolved on the LES grid, are thus modeled through their effects on the stochastic fields. These fields are typically smoother than the real flow field and do not represent any of its physical realization. The FDF is described by N_F Eulerian stochastic fields and the evolution of the n^{th} field $\mathbf{\Phi}^{(n)}$ is dictated by:

$$d\phi_\alpha^{(n)} = \underbrace{-\widetilde{u}_i^{(n)}\frac{\partial \phi_\alpha^{(n)}}{\partial x_i}}_{\text{Advection by mean flow}} + \underbrace{\dot{\omega}_\alpha\left(\mathbf{\Phi}^{(n)}\right)dt}_{\text{Source term}} - \underbrace{\frac{1}{\tau_\phi}(\phi_\alpha^{(n)} - \widetilde{\phi}_\alpha)dt}_{\text{Mixing}} + \underbrace{\frac{1}{\overline{\rho}}\frac{\partial}{\partial x_i}\left[\Gamma_\Delta\frac{\partial \phi_\alpha^{(n)}}{\partial x_i}\right]dt + \sqrt{2\overline{\rho}^{-1}\Gamma_\Delta}\frac{\partial \phi_\alpha^{(n)}}{\partial x_i}dW_i^{(n)}}_{\text{Transport by velocity fluctuations}} \quad \text{(1.23)}$$

for $\alpha = 1, ..., N_S + 1$. Gradient transport and IEM model are assumed in Eq. (1.23). Filtered quantities can be computed as:

$$\widetilde{\phi}_\alpha(\mathbf{x}, t) = \frac{1}{N_F} \sum_{n=1}^{N_F} \phi_\alpha^{(n)}(\mathbf{x}, t) \tag{1.24}$$

as the stochastic fields yield, by construction, the same FDF than the real flow. A deterministic implementation of Eulerian stochastic fields has also been proposed (Tang et al. (2007)) but is not detailed here.

Analysis of transported FDF modeling Although PDF methods are most popular in a RANS context (Haworth (2010)), several works combining transported FDF methods with skeletal and reduced chemical mechanisms in LES have been published. Hybrid Lagrangian/Eulerian particle methods have been applied to non-premixed and partially premixed configurations (Raman and Pitsch (2007); Yaldizli et al. (2010)) as well as spray flames (Irannejad et al. (2015)) and more recently to a lean premixed burner (Ansari et al. (2015)). Many studies using Eulerian Stochastic fields have been made in the past decade, and the approach has been tested and validated in non-premixed (Jones and Prasad (2010); Mustata et al. (2006)), partially premixed (Jones and Prasad (2010); Brauner et al. (2016)) and premixed cases (Dodoulas and Navarro-Martinez (2013); Hodzic et al. (2017); Jones et al. (2012)). In all of the reported simulations, IEM modeling has been used for molecular diffusivity and gradient assumption for turbulent transport. These two models offer a satisfying compromise between accuracy and computational costs.

The inclusion of sub-grid scale wrinkling in transported FDF methods is not explicit. While sub-grid scale information is added via the FDF and the solving of either particle or stochastic field evolution equations, some studies have reported discrepancies in mixing layer position (Jones et al. (2012)) or flame position (Brauner et al. (2016)) in configurations where flame wrinkling is high. This suggests inaccuracies in the turbulent flame speed predictions in some situations.
A strong influence of the chemical mechanism is seen in reported results when it comes to CO predictions. This is for instance the case for the non-premixed Sandia D flame for which Jones and Prasad (2010) obtained accurate results with a 19-species mechanism while Mustata et al. (2006) over-predicted CO profiles by a factor two with a 6-species mechanisms. While some papers report good results in non-premixed (Raman and Pitsch (2007); Yaldizli et al. (2010); Jones and Prasad (2010)) and partially premixed (Raman and Pitsch (2007)) cases, others have put into evidence some limitations of FDF to accurately capture pollutants. Dodoulas and Navarro-Martinez (2013) reported for instance over-predictions of CO level for a turbulent premixed Bunsen flame simulated

with a 19-species mechanism. Difficulties for predicting CO are also observed in the works of Brauner et al. (2016) on a stratified swirled burner and James et al. (2006) on turbulent swirling flames.

In addition to momentum and mass conservation equations on the Eulerian LES grid, hybrid Lagrangian/Eulerian particle methods require the solving of the particles SDE's (position and composition), and stochastic Eulerian methods the solving of SDE's for each stochastic fields. To obtain statistically accurate results, it is argued in the literature that there should be around 10 to 40 particles per grid cells in LPEM, and 4 to 16 stochastic fields in ESFM. The number of particles in LPEM methods can be drastically decreased by using sparse Lagragian algorithms based on MMC mixing models. This strategy will be presented in section 1.2.2.4. Both LPEM and ESFM methods are equivalent in term of computational costs (Haworth (2010)) and are very expensive. Most of the reported studies use grids with 0.5 to 4 millions cells.

1.2.2.2 Monotonically Integrated LES (MILES)

Methodology An alternative method used for including finite rate chemistry effects in turbulent combustion is the MILES (Monotonically Integrated LES) or ILES (Implicit LES) model (Grinstein and Kailasanath (1995); Goldin (2005); Duwig and Fuchs (2008); Duwig et al. (2011)). The filtered reaction rate is modeled as:

$$\overline{\rho}\widetilde{\dot{\omega}}_k(\mathbf{x},t) = \overline{\rho}\dot{\omega}_k(\widetilde{T},\widetilde{Y}_1,...,\widetilde{Y}_{N_S}) \tag{1.25}$$

where reaction rates are computed using Arrhenius laws. It consists in a first order development of reaction rates and can be seen as a specific case of the FDF model where the FMDF is set to a density-weighted Dirac delta function:

$$\mathcal{F}_{\Delta,\mathbf{\Phi}} = \overline{\rho}\delta\left(Y_1 - \widetilde{Y}_1,...,Y_{N_S} - \widetilde{Y}_{N_S}, T - \widetilde{T}\right) \tag{1.26}$$

The model includes no specific treatment of the subgrid scales impact on the molecular processes and its validity domain is hence restricted to highly refined grids or situations where the turbulent mixing is strong enough to homogenize subgrid scale temperature and species mass fractions fields. According to Duwig et al. (2011), the MILES model is valid when the local Dahmkohler number defined as $Da_\Delta = \tau_\Delta/\tau_c$ is much smaller than one (where $\tau_\Delta = \Delta/u_\Delta$ is the large subgrid structures time scale and $\tau_c = \delta_L^0/S_L^0$ the chemical time scale).

Analysis of MILES modeling Premixed flames have been computed in Duwig et al. (2011) who simulated a pilot stabilized lean premixed flame us-

ing different chemical mechanisms (from 5 species/1 reaction to 20 species/82 reactions), and Fureby (2007) who studied a premixed propane/air bluff body stabilized flame. Non-premixed flames have also been tackled using MILES, with for example the work of Grinstein and Kailasanath (1995) on a reactive jet.

As pointed out by Duwig et al. (2011), MILES ensures a correct propagation if flames are not wrinkled at the subgrid level and the mesh is sufficiently fine. Fiorina et al. (2015) carried out a comparison between several models, including MILES, and highlighted the non-adequacy of MILES modeling for LES of turbulent flames on coarse grids.
Following these remarks, MILES model is also not adapted to CO predictions. Indeed, fluctuations of CO at the subgrid level have an impact on the predicted CO. Fureby (2007) show for instance a strong under-prediction of CO in a premixed case.

As MILES methods consist in the transport of species mass fractions on the LES grid with no subgrid-scale modeling, they are computationally cheap compared to FDF methods. Duwig et al. (2011) found that by using a 20-species mechanisms instead of a 5-species mechanisms, the cost of the MILES simulation is multiplied by a factor 2.35, which is an acceptable ratio. Accurate simulations require however very refined grids and become more expensive. This is not compatible with the realistic LES conditions targeted in this thesis.

1.2.2.3 Conditional Moment Closure (CMC)

A good compromise between cost-efficiency and accuracy is the Conditional Moment Closure (CMC) strategy. It is a statistical method which consists in solving only for statistical moments of scalars. The method was published independently by Klimenko (1990) and Bilger (1993), and later extended to LES by Navarro-Martinez et al. (2005). It has been initially proposed in a mixture-based context and hence particularly adapted to the modeling of non-premixed flames.

LES-CMC model The conditional filtered mean of a scalar φ, conditional on the mixture fraction Z is defined as (Navarro-Martinez et al. (2005)):

$$Q(Z^\star, \mathbf{x}, t) = \overline{(\varphi(\mathbf{x}, t) \mid Z(\mathbf{x}, t) = Z^\star)} = \frac{\int_{\mathbb{R}^3} \varphi(\mathbf{y}, t)\delta(Z(\mathbf{y}, t) - Z^\star)G_\Delta(\mathbf{x} - \mathbf{y})d\mathbf{y}}{f_{\Delta,Z^\star}(Z^\star, \mathbf{x}, t)} \tag{1.27}$$

where $f_{\Delta,Z^\star}$ is the FDF in Z-space. A Favre conditional mean can also be

computed as:

$$\widetilde{(\varphi \mid Z^\star)} = \frac{\overline{(\rho\varphi \mid Z^\star)}}{\overline{(\rho \mid Z^\star)}} \tag{1.28}$$

Filtered values can be recovered from conditional means by using the FDF $f_{\Delta,Z^\star}$ (or the FMDF $\mathcal{F}_{\Delta,Z^\star}$ for Favre-filtered variables):

$$\overline{\varphi} = \int_0^1 \overline{(\varphi(\mathbf{x},t) \mid Z(\mathbf{x},t) = Z^\star)} f_{\Delta,Z^\star}(Z^\star,\mathbf{x},t)dZ^\star \tag{1.29}$$

Equations can be derived for the conditional mass fractions $Q_k = \widetilde{(Y_k \mid Z^\star)}$ (Navarro-Martinez et al. (2005)):

$$\frac{\partial Q_k}{\partial t} + \widetilde{(\mathbf{u} \mid Z^\star)} Q_k = \widetilde{(\dot{\omega}_k \mid Z^\star)} + \frac{\widetilde{(\chi \mid Z^\star)}}{2} \frac{\partial^2 Q_k}{\partial (Z^\star)^2} + e_y \tag{1.30}$$

where e_y accounts for fluctuations around the conditional mean and χ is the scalar dissipation rate. CMC models rely on the assumption that reactive scalars are correlated to mixture fraction, and hence the conditional means of reaction rate show negligible fluctuations. The reactive terms are thus often modeled using first-order approximation:

$$\widetilde{(\dot{\omega}_k \mid Z^\star)} = \dot{\omega}_k \left(Q_k, \widetilde{(\rho \mid Z^\star)}, \widetilde{(T \mid Z^\star)} \right) \tag{1.31}$$

In situations where fluctuations of reactive scalars around their conditional means are high, first order modeling is however no longer valid. This happens for instance in premixed combustion, in cases where fuel and oxidyzer are fully or partially premixed before ignition in a non-premixed case or when local exctinction phenomena happen (Kronenburg and Mastorakos (2011)). In such cases, 2^{nd} order closure for the reaction rates (Kim and Huh (2004)) or conditioning on multiple variables (Kronenburg (2004)) have been proposed. These extensions are however expensive in a finite rate chemistry LES context.

The modeling of the other unclosed terms in equations Eq. (1.30) is detailed by Navarro-Martinez et al. (2005). The simulation of a turbulent reacting flow with CMC combines three distinct tasks: (i) LES filtered equations for $\widetilde{\mathbf{u}}$, $\widetilde{Z}$ and $\overline{\rho}$ are solved using conventional closure models; (ii) Conditional means of mass fractions and enthalpy are transported by using Eq. (1.30) and a similar equation for enthalpy; (iii) Unconditional filtered values are computed using a FDF as in Eq. (1.29). A β-PDF is usually used for this purpose. The

variance $\widetilde{Z''^2_{sgs}}$ required for computing the β-PDF can be determined by using an additional transport equation (Giusti and Mastorakos (2017)) or a gradient assumption (Navarro-Martinez et al. (2005)):

$$\widetilde{Z''^2_{sgs}} = C_Z \Delta^2 \left(\frac{\partial \widetilde{Z}}{\partial x_i} \frac{\partial \widetilde{Z}}{\partial x_i} \right) \tag{1.32}$$

where C_Z is a modeling constant usually assumed to be equal to 0.1. CMC can also be adapted to premixed combustion by taking a progress variable as conditioning variable instead of the mixture fraction (Farrace et al. (2017)).

Analysis of CMC modeling Due to its original formulation using mixture fraction as a conditioning variable, CMC-LES models are particularly adapted to non-premixed combustion and most of the reported studies have been tackling such type of flames. These include simulations of bluff body flames (Navarro-Martinez and Kronenburg (2007)), lifted flames (Navarro-Martinez and Kronenburg (2007)), swirling non-premixed flames (Zhang and Mastorakos (2016); Zhang and Mastorakos (2017)) and jet flames (Garmory and Mastorakos (2011); Garmory and Mastorakos (2013); Ayache and Mastorakos (2012)). Each of these studies used Z as a conditioning variable along with a first-order closure for source terms. Some spray flames have also been studied with CMC-LES (Giusti and Mastorakos (2017)), but only few applications of CMC to premixed combustion have been done (Farrace et al. (2017)).

As CMC has not been validated as a method for premixed combustion, it is difficult to draw conclusions about its ability to correctly capture flame propagation. Farrace et al. (2017) reported however large discrepancies on the Flame Surface Density (FSD) predicted by CMC-LES as compared to experimental data for a premixed burner.
The main advantage of CMC methods is the possibility to use detailed chemistry at reasonable computation costs. Many studies use mechanisms with more than 40 species and about 300 reactions (Navarro-Martinez and Kronenburg (2007); Navarro-Martinez and Kronenburg (2007), Ayache and Mastorakos (2012)). This enables extended study of blow-off and ignition (Garmory and Mastorakos (2011); Zhang and Mastorakos (2016); Zhang and Mastorakos (2017)). Accurate predictions of CO have also been reported in the literature for non-premixed cases (Navarro-Martinez and Kronenburg (2009); Navarro-Martinez et al. (2005)). Only minor discrepancies are seen on the rich side of the flames.

A simplification often made in CMC-LES simulations is to assume that conditional averages vary on length scale much bigger than LES scales. For this

reason, two different grids are used in order to reduce computational costs:

- A classical LES grid for transporting $\widetilde{u}$, $\overline{\rho}$ and $\widetilde{Z}$ (and sometimes $\widetilde{Z''^2_{sgs}}$). CMC-LES simulations encountered in the literature report LES meshes containing 1 to 9 millions cells. Grids are on average bigger than grids used in transported FDF methods.

- A coarse CMC grid with a decreased resolution for transporting species conditional means. There are typically between 50 and 200 LES cells for one CMC cell.

Solving species conservation equations on a coarse CMC grid enables simulations with detailed chemical schemes, as mentionned above. Two seperate solvers are often coupled for solving the LES and CMC problems. Further reductions of the CMC grid size can be made by assuming that conditional averages are constants along one direction, leading to 2D-CMC methods (Navarro-Martinez and Kronenburg (2009)). This is however limited to simple academic cases. CMC-LES remains an expensive method, but enables the computation of flames with detailed chemistry on experimental burners. Bigger LES grids and more detailed chemical mechanisms can be used when compared to transported FDF methods. This is however at the expense of strong assumption concerning fluctuations of reactive scalars and is only applicable in perfectly identified regimes.

1.2.2.4 MMC-LES models

Multiple Mapping Conditioning (MMC) is a recent methodology combining the advantages of FDF and CMC methods presented in sections 1.2.2.1 and 1.2.2.3 via the concept of Mapping Closure (Pope (1991b)). In the initial formulation of MMC by Klimenko and Pope (2003), the set of N_S chemical species is divided into two sets of N_m major species and $N_\alpha = N_S - N_m$ minor species, whose fluctuations are assumed to be correlated to the fluctuations of the major species. While complete statistical information is solved for major species, minor species are assumed to be described by conditional means, conditioned by the joint PDF of major species. The concept of MMC has however evolved in time and is rather a modeling framework than a specific combustion model. In its LES formulation (Cleary and Klimenko (2011a)), MMC is used as a new mixing model in conjonction with a full FDF method, and is sometimes referred to as "generalized MMC". The emphasis will be put here on stochastic MMC-LES models. A complete explanation of MMC models and their history can be found in Cleary and Klimenko (2011b) and Cleary and Klimenko (2009). A deterministic version of MMC-LES has been recently developed but very few applications have been reported so far (Devaud et al. (2013)).

Lagrangian MMC The main objective when using MMC in LES is to decrease the computational costs of Lagrangian transported FDF methods. Indeed, the drawback of Lagrangian methods is the high computational cost due to the large number of particles required to reach high accuracy. It has however been argued that much fewer particles can be used to accurately describe the FDF (Cleary and Klimenko (2011a)). The main issue preventing the use of less particles is the constraint imposed by classical mixing models. Indeed, models such as IEM are very sensitive to the localness of particles and require small distances between them, which can only be achieved with a high number of particles. MMC mixing models deal with this problem by enforcing localness in a reference space instead. By doing so, the constraint on physical distance can be relaxed. While initial models used Markov processes to model reference variables, the current trend is to use quantities within the LES flow field (Cleary and Klimenko (2009)). As often done in the literature, the chosen reference variable is here the mixture fraction. Besides the lower computational costs, MMC methods have the advantage of applying mixing equally and linearly to all particles.

Contrarily to IEM models for which mixing is done between a particle and the mean filtered field, MMC mixing is performed between a pair of two mixing particles p and q. Once these particles are selected, mixing is carried out for a step dt as (Cleary and Klimenko (2011a)):

$$\begin{cases} \phi_\alpha^p(t+dt) = \phi_\alpha^p(t) + \mu\left(\overline{\phi}_\alpha^{p,q}(t) - \phi_\alpha^p(t)\right) & \text{(1.33a)} \\ \phi_\alpha^q(t+dt) = \phi_\alpha^q(t) + \mu\left(\overline{\phi}_\alpha^{p,q}(t) - \phi_\alpha^q(t)\right) & \text{(1.33b)} \end{cases}$$

where $\overline{\phi}_\alpha^{p,q}(t)$ is the mean composition between both particles and μ is a relaxation coefficient depending on a mixing time scale. Extensive analysis has been made for the choice of μ, see for example the study of Vo et al. (2017). The enforcement of some localness in mixture fraction space intervenes in the choice of the pairs of mixing particles. A new variable $\widetilde{f}$ emulating mixture fraction is computed on the Eulerian grid and as it is a passive scalar, this variable is mathematically independent of the stochastic composition variables $\mathbf{\Phi}_\alpha$. This new field is used for the purpose of selecting particles pairs only. These are chosen so as to minimize a normalized distance in $\widetilde{f}$ and x spaces (Cleary and Klimenko (2009)):

$$\min_{p,q} \hat{d}^2_{(p,q)} = \frac{1}{1+\lambda^2}\left[\sum_{i=1}^{3}\left(\frac{x_i^{\star(p)} - x_i^{\star(q)}}{L_x}\right)^2 + \lambda^2\left(\frac{\widetilde{f}^{\star(p)} - \widetilde{f}^{\star(q)}}{L_f}\right)^2\right] \quad (1.34)$$

where L_x and L_f are characteristic physical and mixture fraction scales and

λ is a weighting factor for localness in physical and reference spaces. Selecting $\lambda = 0$ means that the closest particles in physical space are chosen while taking $\lambda = \infty$ means that diffusion happens perpendicularly to isocontours of the mixture fraction, as in flamelet modeling. The true mixing happens for a finite value of λ (Cleary and Klimenko (2009)). The value of $\widetilde{f}$ for a particle is obtained by interpolation of the flow field on the particle's position. Details about the methodology for selecting particle pairs and the associated modeling parameters can be found in Cleary and Klimenko (2011a).

The presented methodology can be seen as a blend between FDF methods and mixture-fraction based methods. By coupling the MMC mixing model with Lagrangian FDF methods, fewer particles are used for solving species composition and computational costs are drastically reduced. These methods are often referred to in the literature as sparse Lagrangian FDF methods (as opposed to "intensive" Lagrangian FDF).

Analysis of MMC-LES models The mixture based formulation of sparse Lagragian FDF methods with MMC mixing has led to many simulations on non-premixed configurations. Cleary and Klimenko (2009) and Ge et al. (2011) computed respectively the sandia D and E flames with detailed chemistry, while Sundaram et al. (2016) simulated the Cabra burner and Salehi et al. (2017) a spray flame with a gas-phase modelisation of the liquid using a 106-species scheme. A recent application has also been made on a multi-mode inhomonegeous burner by Galindo et al. (2017).

Similarly to CMC methods, no fully premixed cases have been computed with MMC-LES and no conclusions can be drawn on the ability of the model to capture correctly flame front propagation.
The reduced computational cost of MMC-LES as compared to classical LPEM methods enables the use of more detailed chemical mechanisms. Several studies involved chemical schemes with more than 30 species (Cleary and Klimenko (2009); Ge et al. (2011); Salehi et al. (2017)). In non-premixed cases, CO is well predicted and results are in good accordance with FDF, validating the use of a fewer number of particles. Difficulties are however observed in multi-regime cases. Galindo et al. (2017) under-predict CO mass fractions in all parts of the Sydney inhomogeneous burner (Meares and Masri (2014)), suggesting an inadequacy of current MMC modeling to situations where premixing is present.

As already pointed out, most of the computational work in Lagrangian FDF methods is done for transporting particles on the mesh. The major improvement in sparse Lagrangian MMC methods is the reduced number of particles for describing the FDF. While intensive methods use more particles than LES grid cells (about 5 to 40 particles per LES cell), sparse Lagrangian methods use less particles than cells (1 particle for 8 to 32 LES cell). Reported stud-

ies take advantage of this reduced costs by introducing detailed mechanisms. The Sandia D flame was for exemple computed with a 16-species/12-reactions mechanism by Yaldizli et al. (2010) using traditional FDF, while Cleary and Klimenko (2009) simulated the same flame in an MMC framework with a 34-species/219-reactions scheme.

1.2.3 A multi-scale approach: the LES-ODT model

Another class of methods used for LES of reacting flows are multi-scale approaches. The most popular of such methods are the Linear Eddy Model (LEM) (Smith and Menon (1998); McMurthy et al. (1992); Kerstein (1989); Calhoon and Menon (1996), Menon and Kerstein (2011)) and the One Dimensional Turbulence model (ODT) (Cao and Echekki (2008); Schmidt et al. (2010); Echekki et al. (2011); Park and Echekki (2012)). Both methods treat reaction and diffusion processes in a deterministic way while turbulent transport is incorporated stochastically. LEM-LES and ODT-LES differ in the way the stochastic closure is implemented (see Cao and Echekki (2008) for details).

In the ODT-LES model, premixed flame fronts are solved by using DNS-like resolutions along the normal to the flame.

Description of the ODT-LES model The ODT-LES model is based on the One Dimensional Turbulence model (ODT) developed by Kerstein (1999). The idea in ODT-LES modeling is to perform simultaneously two simulations:

- The first simulation is an LES simulation of the flow on a coarse grid. The filtered momentum and mass conservation equations are solved using standard turbulence models and yield a velocity field $\widetilde{u}_j$, $j = 1, .., 3$.

- The second set of equations, called ODT equations, are solved on 1D elements embedded in the 3D LES grid. The 1D grid resolutions are calibrated so that the LES subgrid-scales physics is solved and are therefore equal to DNS resolutions. An illustration is provided in Fig. 1.2 for a 3D cartesian grid. ODT domains are lines crossing the LES grid nodes in the three directions and intersect at so-called ODT nodes. Conservation equations are solved on each individual ODT element for momentum, energy (or temperature) and species mass fractions. Considering a cartesian grid with directions x_1, x_2 and x_3, the balance equation for a species k on an ODT domain with direction x_1 reads:

$$\frac{\partial Y_k}{\partial t} = \underbrace{\left[\frac{1}{\rho}\frac{\partial \mathcal{J}_{k,1}}{\partial x_1} + \frac{\dot{\omega}_k}{\rho} + \Omega_{Y_k}\right]}_{\text{Resolved on ODT domain}} + \underbrace{\left\{-\widetilde{u}_j\frac{\partial Y_k}{\partial x_j} + \frac{1}{\rho}\left(\frac{\partial \mathcal{J}_{k,2}}{\partial x_2} + \frac{\partial \mathcal{J}_{k,3}}{\partial x_3}\right)\right\}}_{\text{Gradients normal to ODT domain}}$$

(1.35)

Equations for temperature and momentum similar to Eq. (1.35) are also solved on ODT elements and are not shown here. Details can be found in Cao and Echekki (2008). In Eq. (1.35), terms in brackets '[..]' are resolved on the ODT grid while terms in brackets '{..}' require computation of gradients normal to the ODT domain. In particular, the source terms are easily computed as they don't involve gradients. Ω_{Y_k} is the subgrid-scale scalar transport resulting from the residual velocity components (i.e. the difference $u_j - \widetilde{u}_j$ between the velocity u_j and the filtered velocity $\widetilde{u}_j$ obtained from the LES).

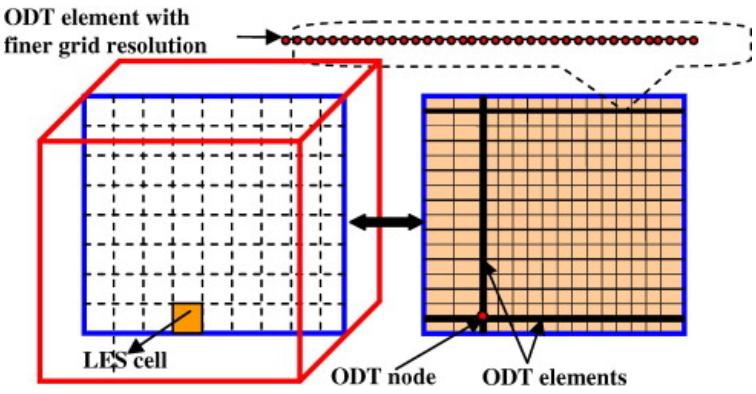

Figure 1.2: *Layout of ODT elements on a cartesian mesh (Park and Echekki (2012)).*

The LES and ODT simulations are coupled at each time step (details about the time-stepping can be found in Cao and Echekki (2008)). The filtered velocity field obtained from the LES simulation is used in the ODT problem and the filtered density in the LES problem is obtained from explicit filtering of the ODT density.

While the LES on the coarse grid is computed using classical models, ODT equations raise several difficulties which have to be tackled. The reaction rates are easily computed on the ODT domain and require no specific treatment. Arrhenius chemistry can be used without theoretical difficulties; only the stiff integration may lead to numerical problems. The terms which need more attention are: (1) the diffusion processes normal to the ODT domain $\frac{\partial \mathcal{J}_{k,2}}{\partial x_2} + \frac{\partial \mathcal{J}_{k,3}}{\partial x_3}$; (2) the subgrid-scale scalar fluxes Ω_{Y_k}; (3) the transport by the Favre-filtered velocities $-\widetilde{u}_j \frac{\partial Y_k}{\partial x_j}$.

Diffusive processes modeling Diffusive processes are closed by supposing 3-D isotropic behavior. Molecular diffusion along x_2 and x_3 are assumed to be

equal to the diffusion along x_1:

$$\frac{\partial \mathcal{J}_{k,2}}{\partial x_2} + \frac{\partial \mathcal{J}_{k,3}}{\partial x_3} = 2\frac{\partial \mathcal{J}_{k,1}}{\partial x_1} \tag{1.36}$$

As emphasized in Cao and Echekki (2008), refinement of this simple assumption may be required if dominant gradients, such as flame brushes, are present.

Subgrid-scale scalar fluxes The SGS scalar fluxes are modeled as stochastic contributions which are represented as discrete stirring events. Turbulent stirring is artificially generated by "triplets maps" (Kerstein (1999)), which mimic the effects of stirring. Piecewise linear functions are used to model the effect of turbulent structures on 1D scalar fields. The sizes of these structures are selected randomly in a given range of turbulent scales. A detailed explanation of the triplet map generation process can be found in Cao and Echekki (2008).

Transport by filtered advection The large-scale advection terms are computed in a two-step process: (1) At a given node (i.e. intersection between three ODT elements, see Fig. 1.2), the scalar value is updated using the three components of the LES filtered velocity field and the scalar values at the three intersecting ODT elements as $\frac{\partial Y_k}{\partial t} = \sum \widetilde{u}_j \frac{\partial Y_k^j}{\partial x_j}$, where j is the direction of the ODT element. Scalar at each nodes are then averaged to keep consistency; (2) For the points between the nodes, scalar values are updated by solving a 1-D relaxation problem.

Details about the closure models for these three terms can be found in Cao and Echekki (2008) and Park and Echekki (2012).

Analysis of ODT-LES Very few simulations with ODT-LES have been published so far. The model has been applied to simple configurations, such as the ignition of non-homogeneous mixtures (Cao and Echekki (2008)) and more recently the interaction between two statistically planar fully premixed flame fronts (Park and Echekki (2012)). In both cases a single-step chemical mechanism is used.

The ability of ODT-LES to capture flame front propagation has been thoroughly discussed by Park and Echekki (2012) who studied the merging of twin flames. Despite minor difference in the merging time between DNS and ODT-LES, results show a good capacity of ODT-LES for predicting transient flame dynamics.
As it has only been tested with single-step chemical mechanisms, no comparisons on pollutants formation is available. ODT-LES has some promising fea-

tures, as it is able to model turbulent combustion with multiple regimes, includes transient effects and the ability to capture differential diffusion. However, the methodology requires testing in more complex cases and coupled to more detailed chemical mechanisms.

Quantification of computational costs associated to ODT-LES is done here by considering the simplified case of a 3-D cartesian grid. A comparison between the number of nodes in an ODT-LES, a LES and a DNS simulation in provided here as a rough estimation of computational costs differences. If the LES grid has N_{LES} points in each direction, and DNS resolutions correspond to N_{DNS} points per direction, the number of ODT points in the whole mesh is $N_{ODT} = 3 \times N_{DNS} \times N_{LES}^2$; and thus the ratio η between the number of points in a ODT-LES simulation ($= N_{LES}^3 + N_{ODT}$) and the amount in an DNS computation ($= N_{DNS}^3$) is:

$$\eta = \left(\frac{N_{LES}}{N_{DNS}}\right)^3 + 3\left(\frac{N_{LES}}{N_{DNS}}\right)^2 \tag{1.37}$$

ODT-LES is hence advantageous compared to a full DNS, but the inclusion of 1-D DNS elements (represented by the second term in the RHS of Eq. (1.37)) makes the simulations much more expensive than a simulation solely done on the LES grid. Since reactive scalars are transported on the ODT grid, the method is expensive for detailed Arrhenius chemistry.

1.2.4 Thickening flame fronts: the Artificially thickened flame model (TFLES)

As emphasized in Sec. 1.2.1.1, a strategy for resolving premixed flames on coarse grids is to artificially thicken the flame front. Initially proposed by Butler and O'Rourke (1977) and O'Rourke and Bracco (1979), flame thickening has been extended in an LES context in the work of Colin et al. (2000), leading to the Thickened Flame model for LES (TFLES).

TFLES modeling A classical result in combustion theory is that the laminar flame thickness and speed are related to the thermal diffusivity D_{th} and the mean reaction rate $\dot{\Omega}$ by (Poinsot and Veynante (2005)):

$$S_l^0 \propto \sqrt{D_{th}\dot{\Omega}} \quad ; \quad \delta_l^0 \propto \sqrt{\frac{D_{th}}{\dot{\Omega}}} \tag{1.38}$$

For defining a flame with an increased thickness and the same burning rate the thermal diffusivity is multiplied by a factor $\mathcal{F}$ while the reaction rate is

divided by $\mathcal{F}$. The flame/turbulence interactions are however modified and the impact of subgrid scale structures on the burning rate has to be modeled. This is done by introducing a subgrid-scale wrinkling factor Ξ_Δ, accounting for the increase in flame propagation speed due to the increased flame surface area at subgrid level. Thermal diffusion and reaction rates contributions are multiplied by Ξ_Δ, so that the flame propagates at the turbulent speed $S_T = \Xi_\Delta S_l^0$ while its thickness stays constant. The balance equation for $\widetilde{Y}_k$ when using the TFLES modeling strategy reads:

$$\frac{\partial \overline{\rho}\widetilde{Y}_k}{\partial t} + \nabla \cdot \left(\overline{\rho}\widetilde{u}\widetilde{Y}_k\right) = \nabla \cdot \left(\Xi_\Delta \mathcal{F} \rho D \nabla \widetilde{Y}_k\right) + \frac{\Xi_\Delta}{\mathcal{F}} \overline{\rho}\widetilde{\dot{\omega}}_k \tag{1.39}$$

The initial TFLES model used a constant $\mathcal{F}$ factor while Legier et al. (2000) pointed out that it leads to an overestimation of the mixing outside the flame region. An alternative method where $\mathcal{F}$ relaxes to one outside of the flame zone has been proposed and renamed as Dynamic Thickened Flame model (DTFLES). The thickening factor can be computed as (Legier et al. (2000)):

$$\mathcal{F} = 1 + (\mathcal{F}_{max} - 1) tanh\left(\beta \frac{\Omega}{\Omega_{max}}\right) \tag{1.40}$$

where Ω is a flame sensor and β is a parameter which controls the transition between thickened and non-thickened areas. The flame sensor Ω is a function who gradually decreases to zero outside the flame zone and is normalized by its maximum value Ω_{max}. The value $\mathcal{F}_{max}$ is the thickening factor in the non-dynamic case. Different definitions can be used for the flame sensor (Legier et al. (2000); Kuenne et al. (2011); Jaravel (2016)). Legier et al. (2000) used for instance an Arrhenius-like formula for defining the sensor. Flame sensors should capture temperature and species gradients at the flame foot to reach a correct flame propagation prediction. Turbulent fluxes, which are modeled in the flame front to retrieve the correct propagation, also require modeling outside the flame zone. This is usually done using a gradient assumption (Kuenne et al. (2012)) and the transport equation for $\widetilde{Y}_k$ in the dynamic case becomes:

$$\frac{\partial \overline{\rho}\widetilde{Y}_k}{\partial t} + \nabla \cdot \left(\overline{\rho}\widetilde{u}\widetilde{Y}_k\right) = \nabla \cdot \left(\left[\Xi_\Delta \mathcal{F} \rho D + (1-\Omega)\frac{\mu_t}{Sc_t}\right] \nabla \widetilde{Y}_k\right) + \frac{\Xi_\Delta}{\mathcal{F}} \overline{\rho}\widetilde{\dot{\omega}}_k \tag{1.41}$$

where μ_t is the turbulent viscosity and Sc_t the turbulent Schmidt number.

Subgrid scale wrinkling modeling A model for the subgrid-scale wrinkling factor Ξ_Δ needs to be specified to close Eq. (1.41). Several algebraic formula have been derived in the literature (Colin et al. (2000); Charlette et al. (2002a)). A commonly used model is the modified Charlette power-law

expression (Wang et al. (2011)):

$$\Xi_\Delta = \left(1 + min\left[\frac{\Delta}{\delta_l^0} - 1, \Gamma_\Delta \frac{u'_\Delta}{S_l^0}\right]\right)^\beta \tag{1.42}$$

where u'_Δ is the subgrid scale turbulent velocity, β the fractal dimension of the flame and Γ_Δ an efficiency function for including straining effects in the model. Details about the derivation of Γ_Δ can be found in Charlette et al. (2002a). Models for the turbulent intensity u'_Δ include the Prandtl-Kolmogorov approach (Kolmogorov (1942)) :

$$u'_\Delta = \sqrt{\frac{2}{3}} \frac{\nu_t}{C_k \Delta_x} \left(\frac{\Delta}{\Delta_x}\right)^{1/3} \tag{1.43}$$

where ν_t is the turbulent viscosity, Δ_x the mesh size, Δ the LES filter scale and C_k a model constant. An alternative is the formula developed by Colin et al. (2000):

$$u'_\Delta = c_2 \Delta_x^3 \mid \nabla^2 (\nabla \times \widetilde{u}) \mid \left(\frac{\Delta}{n_x \Delta_x}\right)^{1/3} \tag{1.44}$$

where $c_2 = 2$ and $n_x = 10$ are model constants.

The fractal dimension β is often taken constant and typically set to 0.3 or 0.5. This factor may also be computed dynamically (Wang et al. (2011); Charlette et al. (2002b)). In this formulation, the wrinkling factor is saturated:

$$\Xi_\Delta = \left(\frac{\Delta}{\delta_l^0}\right)^{\beta_{dyn}} \tag{1.45}$$

and β_{dyn} is computed by using a Germano-like identity. Details can be found in Wang et al. (2011).

Analysis of TFLES modeling The TFLES model is used with both tabulated (Kuenne et al. (2011); Auzillon et al. (2011)) and transported chemistry. In a transported chemistry context, TFLES approaches have successfully been coupled to one-step chemistry (Wang et al. (2011)), global chemistry with intermediate species (Volpiani et al. (2017); Franzelli et al. (2012)) and systematically reduced mechanisms (Franzelli et al. (2013)), including in particular the works on Analytically Reduced Chemistry (ARC) (Jaravel et al. (2017); Schulz et al. (2017); Jaravel et al. (2018); Felden et al. (2018)). Thickening

factors are typically set to reach around 5 points in the flame front thickness (Jaravel (2016)). Several studies of TFLES applied to realistic burners have been reported, as illustrated by the simulations of a premixed swirled burner by Franzelli et al. (2012) and an annular combustor ignition sequence by Philip et al. (2015).

Originally developed for turbulent premixed flames (Colin et al. (2000)), TFLES models include the influence of turbulent structures on flame propagation explicitely by using the sub-grid scale wrinkling term Ξ_Δ. This methodology, also used in other LES closure models (Fiorina et al. (2010); Wang and Bai (2005)), leads to accurate prediction of flame propagation, as observed for instance by Vermorel et al. (2017) who studied the evolution of a flame front for an explosion in a venting chamber, and in the simulation of a semi-industrial gas turbine by Jaravel et al. (2017).
Recent studies showed however that TFLES models lead to mispredictions of the flame structure as compared to LES models based on flame front filtering (Auzillon et al. (2011)). Difficulties are also encountered when accurate CO formation needs to be predicted (Cailler et al. (2017)). Although this can be attributed to the fact that many studies consider 1 to 4 step reduced schemes or tabulated chemistry, additional issues related to flame thickening can be identified. A simplified analysis is done here by computing a 1-D laminar premixed methane flame with the detailed GRI3.0 mechanism at an equivalence ratio $\phi = 0.75$ for different values of the thickening coefficient $\mathcal{F}$. The computation is done using the 1-D flame solver of the YALES2 code (Moureau et al. (2011a)). CO profiles obtained for different values of $\mathcal{F}$ are shown on the left in Fig. 1.3. While the thickness of Y_{CO} is indeed growing as the thickening factor increases, its peak is conserved. The mass of CO present in the laminar flame for a spatial range $[x_1, x_2]$ (sufficiently wide to encapsulate the flame front) is $\mathcal{I}_{CO} = \int_{x_1}^{x_2} \rho Y_{CO} dx$ for the non-thickened flame and $\widetilde{\mathcal{I}}_{CO}^{thickened} = \int_{x_1}^{x_2} \overline{\rho}\widetilde{Y}_{CO} dx$ for thickened flames. The evolution of the CO mass with $\mathcal{F}$ is illustrated in Fig. 1.3 (on the right). A strong increase of the mass with the thickening is observed, and the following relationship is found to hold:

$$\widetilde{\mathcal{I}}_{CO}^{thickened} = \mathcal{F} \times \mathcal{I}_{CO} \tag{1.46}$$

This suggests that flame thickening leads to an over-prediction of CO in the flame front and can be an obstacle to accurate and robust pollutant prediction in LES. Further analysis will be done on 3-D cases in chapter 4.

If transported chemistry is used, computing flames using TFLES model requires the solving of N_S+5 conservations equations on the LES grid (3 for momentum, 1 for mass, 1 for energy and N_S for species). Since the model does not add significant computational costs, these are driven by chemical reaction rates

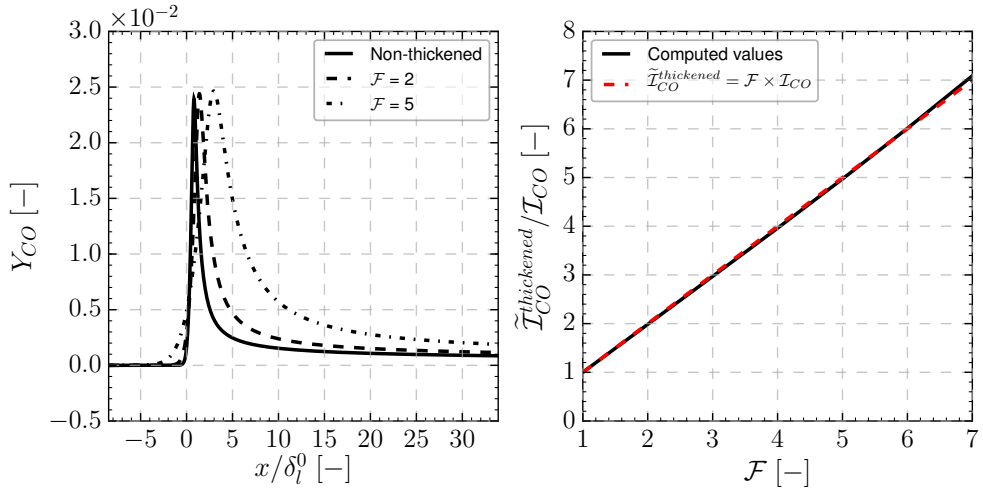

Figure 1.3: *Comparison between reference and thickened Y_{CO} of a 1-D laminar premixed methane flame at an equivalence ratio $\phi = 0.75$. On the left: Y_{CO} profiles for different values of the thickening factor $\mathcal{F}$. On the right: mass of thickened CO $\widetilde{\mathcal{I}}_{CO}^{thickened}$ divided by the non-thickened flame value $\mathcal{I}_{CO}$ as a function of $\mathcal{F}$.*

computation and the transport of chemical species. Computational costs are thus low when reduced chemical schemes are used but lead to prohibitive costs when it comes to including detailed mechanisms. Most of the reported studies use chemical mechanisms with 4 to 13 steps on LES grids containing 5 to 22 millions cells. Recent progress has been made with the work of Jaravel et al. (2017) for instance, who used a 22-species mechanism on a LES mesh with 120 millions elements.

1.2.5 Models based on flame front filtering

An alternative to flame thickening is to resolve the flame front by applying a filtering operator with a characteristic size Δ larger than the mesh size (Fiorina et al. (2010); Fiorina et al. (2014)). The filtering of a CO mass fraction profile obtained with detailed CH_4/air chemistry at an equivalence ratio $\phi = 0.75$ is illustrated in Fig. 1.4 for a filter size $\Delta = \delta_l^0$, $3\delta_l^0$ and $5\delta_l^0$. Filtering broadens the flame front and the flame can thus be resolved on a coarse LES grid. Flame filtering can be related to thickening by determining the parameters $\mathcal{F}$ and Δ leading to the same number of grid points in the flame reactive layer (Auzillon et al. (2011)). The following relationship is derived (Auzillon et al. (2011)):

$$\mathcal{F} = \left(1 + \frac{2\ln(2)}{3}\left(\frac{\Delta}{\delta_r}\right)^2\right)^{\frac{1}{2}} \tag{1.47}$$

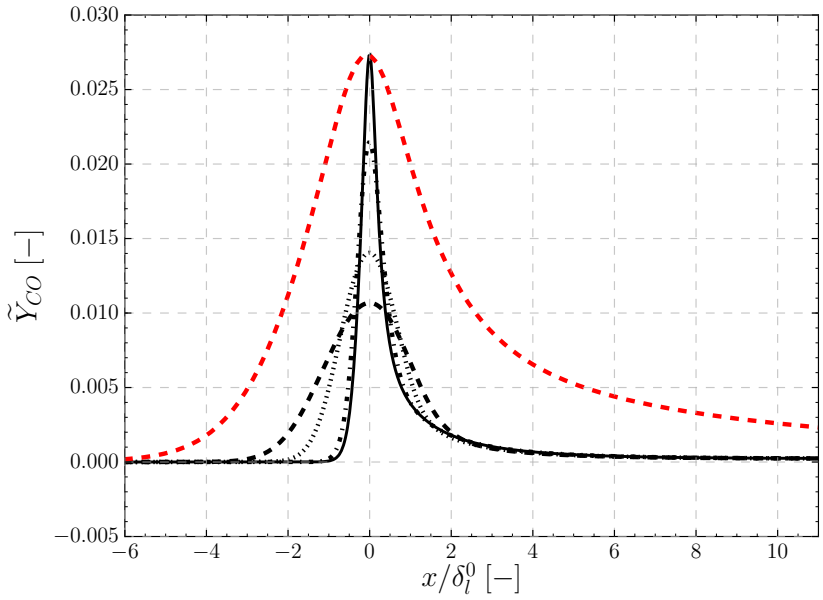

Figure 1.4: *Filtered CO profile of a 1D laminar premixed CH_4/air flame computed with detailed chemistry at an equivalence ratio $\phi = 0.75$. — Fully resolved laminar flame. -.- Flame filtered at $\Delta = \delta_l^0$. . . . Flame filtered at $\Delta = 3\delta_l^0$. - - - Flame filtered at $\Delta = 5\delta_l^0$. - - - Flame thickened with factor $\mathcal{F}$ corresponding to $\Delta = 5\delta_l^0$, as defined by Eq. (1.47).*

where δ_r is the flame reactive thickness, defined as the Full Width at Half Maximum (FWHM) of the CH_4 reaction rate. The thickened CO mass fraction corresponding to $\Delta = 5\delta_l^0$ is added in Fig. 1.4 (red dashed line). While leading to the same flame resolution, filtering and thickening have a significantly different impact on the CO structure. In particular, explicit filtering preserves the mass of CO in the domain: $\widetilde{\mathcal{I}}_{CO}^{filtered} = \mathcal{I}_{CO}$, where $\widetilde{\mathcal{I}}_{CO}^{filtered}$ is the mass of CO defined from an explicitly filtered profile.

Flame filtering has initially been used in a tabulated chemistry context (Fiorina et al. (2010); Auzillon et al. (2011); Moureau et al. (2011b); Nambully et al. (2014b)). The F-TACLES model developed by Fiorina et al. (2010) resolves the premixed flame structure using a mass weighted filtered progress variable $\widetilde{c}$, computed from temperature or species mass fractions. The transport equation of $\widetilde{c}$ is then closed by tabulating unclosed terms with filtered 1-D laminar premixed flames computed with detailed chemistry and transport.

The use of filtered flame fronts in transported chemistry is recent and limited to a few models (Abou-Taouk et al. (2015); Domingo and Vervisch (2014)). Two of these models, deconvolution modeling and optimized filtered chemistry

are described in Sec. 1.2.5.1 and 1.2.5.2, respectively.

1.2.5.1 Deconvolution models

A recent methodology for closing Eq. (1.12) is based on the concept of deconvolution. The idea is to reconstruct reactive scalars from filtered quantities.

Deconvolution modeling Fig. 1.5 shows the different steps in the modeling of the filtered reaction rates using deconvolution: (1) Filtered profiles $\overline{\rho}$, $\overline{\rho Y_k} = \overline{\rho}\widetilde{Y}_k$ and $\overline{\rho h} = \overline{\rho}\widetilde{h}$ are extracted from the LES simulation; (2) Unresolved signals $\rho^\star$, $Y_k^\star$ and $h^\star$ are reconstructed from filtered variables with a deconvolution algorithm; (3) Reaction rates $\dot{\omega}_k^\star$ are computed from reconstructed scalars using Arrhenius laws; (4) Reaction rates are filtered and $\overline{\dot{\omega}_k^\star}$ is injected back in the balance equations.

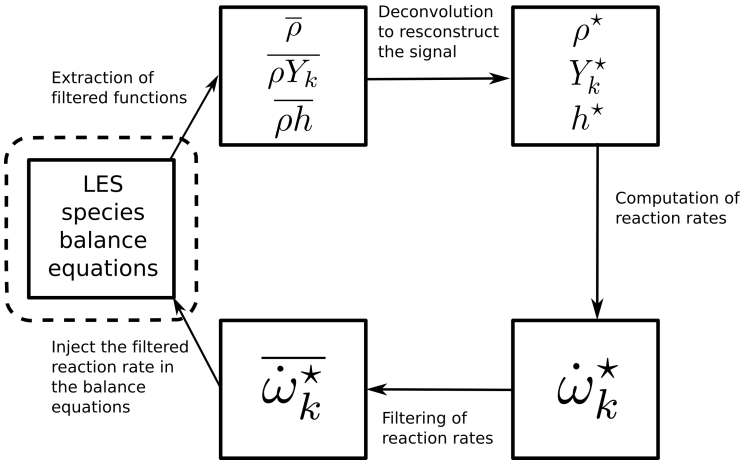

Figure 1.5: *Principle of deconvolution modeling.*

The critical step of the method is the deconvolution algorithm, which aims at recovering small scales information. The application of deconvolution in LES has been pioneered by Stolz and Adams (1999) who developed the Approximate Deconvolution Method (ADM). It has first been designed for the modeling of the subgrid scale Reynolds stresses in non-reacting LES (Stolz et al. (2001a); Stolz et al. (2001b)). A review of deconvolution modeling applied to non-reacting flows can be found in Layton and Rebholz (2012). The first deconvolution methods developed for reacting flows were derived from ADM. A coupling between ADM and a thickened flame has been done in Mathew (2002) and a modification of ADM based on flame similarity has led to a model for premixed flames (Vreman et al. (2009)). A model based on the ADM formalism has also been derived for the specific case of non-premixed combustion (Mellado et al. (2003); Pantano and Sarkar (2001)). More recently, two deconvolution

algorithms have been proposed to tackle the closure of LES equations regardless of the combustion regime. The first one consists in a Taylor expansion of the Gaussian filter (Domingo and Vervisch (2014)) and the second one in a minimization of a constrained quadratic function (Wang and Ihme (2016)). Technical details about the models will be given in chapter 2, were an in-depth analysis will be carried out.

Analysis of deconvolution models As the extension of deconvolution techniques to reacting flows is recent, very few studies have been published. Results include a turbulent Bunsen flame simulated by Domingo and Vervisch (2014) where only a progress variable is transported with the deconvolution model while other scalars were tabulated, leading to bad predictions of pollutant species. Wang and Ihme (2016) simulated a partially premixed flame in decaying turbulence in a DNS context.

The ability of deconvolution models to correctly reproduce flame propagation and pollutants formation has not been validated so far. As deconvolution models are in their formulation independent of the combustion regime, it is essential to check carefully that basic properties of flames are respected. This issue will be addressed in chapter 2, where an in-depth analysis of deconvolution modeling on a laminar premixed flame is done.

As deconvolution methods proposed in the literature are very different from each other, the potential in term of computational cost is heterogeneous. While some methods are linear and directly done on the LES grid (Domingo and Vervisch (2014); Stolz and Adams (1999)), others are implemented by the solving of optimizations problems at least once per solver iteration (Wang and Ihme (2016)). In the latter case, computations are expected to be very expensive.

1.2.5.2 Optimized filtered mechanisms

A new idea recently proposed in the literature is to combine chemical reduction and sub-grid scale modeling in a single step.

Modeling Abou-Taouk et al. (2015) suggest to perform the chemical reduction by optimizing the Arrhenius parameters of the chemical mechanism so that filtered laminar premixed flames are reproduced. Species mass fractions balance equations for are rewritten as:

$$\frac{\partial \overline{\rho}\widetilde{Y_k}}{\partial t} + \nabla \cdot \left(\overline{\rho}\widetilde{u}\widetilde{Y_k}\right) = \nabla \cdot \left(F^{opD}(\widetilde{\phi})\mathcal{J}_k(\widetilde{T}, \widetilde{Y_k})\right) + \dot{\omega}_k^{Op}(\widetilde{T}, \widetilde{Y_k}) \tag{1.48}$$

where F^{opD} is an optimized multiplicative coefficient for diffusive processes depending on the filtered equivalence ratio $\widetilde{\phi}$, and $\dot{\omega}_k^{Op}$ a reaction rate with op-

timized Arrhenius coefficients. The temperature transport equation is modeled in the same way. For these equations to be closed, the Arrhenius parameters and the diffusive multiplicative factor have to be specified. This is done by selecting coefficients so that Eq. (1.48) reproduces a set of filtered laminar premixed flames at several equivalence ratios (denoted in the following by the superscript *ref*). The minimization of the following function $\mathcal{F}_{obj}$ is performed:

$$\mathcal{F}_{obj}\left(\left(A_j(\widetilde{\phi}),\beta_j,E_{a,j},\mu_{i,j}\right)_{j=1..N_R;i=1..N_S},F^{opD}(\widetilde{\phi})\right)= \sum_{l=1}^{N_{fl}}\left[\sum_{i=1}^{N_S}\sum_{k=1}^{N_p}\frac{\mid \widetilde{Y}_i(x_k,l)-\widetilde{Y}_i^{ref}(x_k,l)\mid}{\widetilde{Y}_i^{ref}(x_k,l)}+\beta\left(\frac{\mid S_l^0(l)-S_l^{0,ref}(l)\mid}{S_l^{0,ref}(l)}\right)\right] \tag{1.49}$$

where $(A_j,\beta_j,E_{a,j})$ are constants of Arrhenius laws (see Eq. (1.3)), and $\mu_{i,j}$ the reaction order of the ith species in the jth reaction. Reaction orders can be different from stoechiometric coefficients in non-complete chemistry since reactions are not elementary. β is a weighting factor for the laminar flame speed optimization term, N_p the number of computational nodes in flames and N_{fl} the number of reference flames on which the joint optimization is done. The minimization of Eq. (1.49) is carried out by using a genetic optimization algorithm.

Analysis of the model Abou-Taouk et al. (2015) validated the model on a multi-point swirling injector functioning in a partially premixed regime. Optimization problem 1.49 has been solved for flames with equivalence ratios ranging from 0.4 to 1.2 and filtered with a Gaussian filter. Further investigations have to be led in order to validate the model as a robust alternative in realistic LES, as the simulation done by Abou-Taouk et al. (2015) considered a low filter size and a highly refined grid ($\Delta = 1$mm and typical grid spacing $\Delta_x = 0.3$mm).

The correct propagation of laminar flames is enforced by the second term in optimized function (1.49) and a very good agreement is obtained by Abou-Taouk et al. (2015). However, the modeling in Eq. (1.48) neglects the impact of sub-grid scale wrinkling. In its current form, the model is only applicable to flames which are not wrinkled at sub-grid scales, i.e. very simple configurations or flames computed on a very fine mesh. The ability of the model to capture pollutants, in wrinkled and non-wrinkled cases, has not been studied.

The model is similar in its formulation to TFLES. In particular, the same number of transport equations are solved. Computational costs are hence close to the cost of TFLES and the simulation of realistic burners is thus feasible.

1.3 Conclusions on the LES models and presentation of the thesis objectives

This section synthesizes the information given in the previous parts and presents the modeling routes explored in this thesis.

1.3.1 Conclusions on current LES models

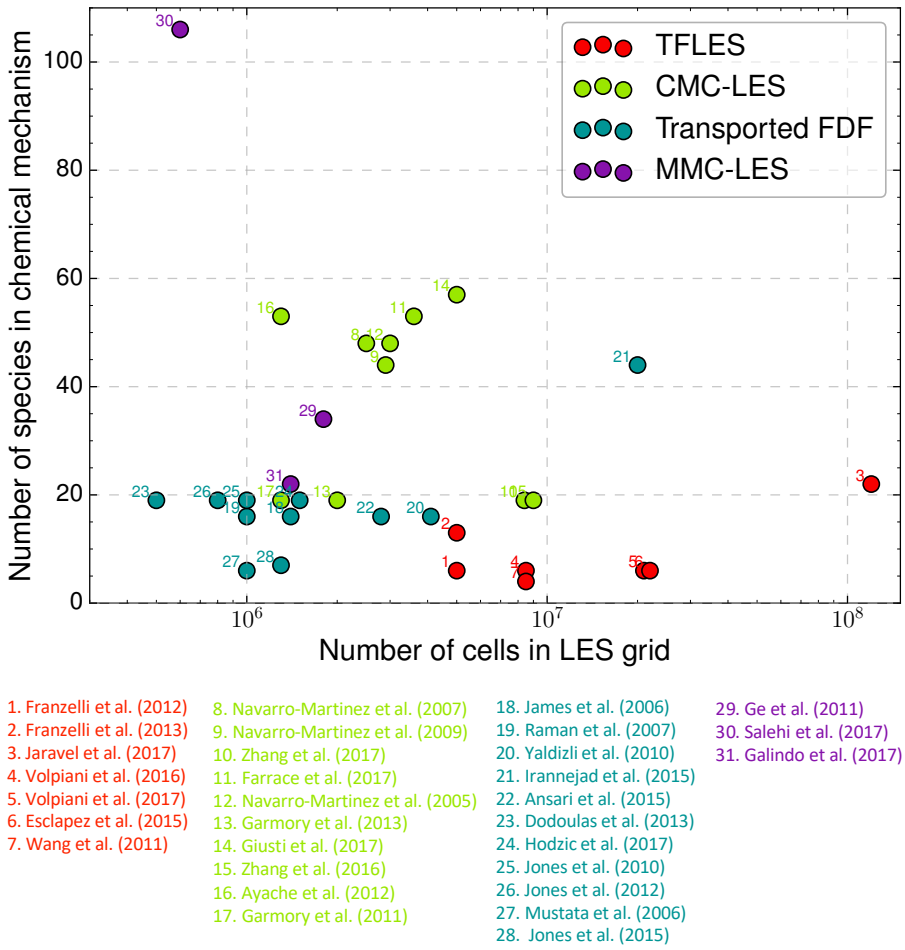

Figure 1.6: *Examples of LES performed with transported chemistry in function of the number of species considered in the chemical mechanism. A log-scale is used for the x-axis.*

Several closure models have been developed over the past decades for LES of turbulent combustion coupled to transported reduced chemical mechanisms. Two challenges have been at the heart of these studies: (i) prediction of flame structure and complex chemistry effects; (ii) coupling between chemical re-

action rates and turbulence. These two issues trigger the need for accurate models. An illustration of LES studies with transported chemistry published in the literature is provided in Fig. 1.6. These methods are classified according to the number of species used in the mechanism and the number of cells in the LES mesh. While this last indicator is not entirely representative of the computational capacities of a model, it is considered to be a good indicator of the possibilities of the LES model in term of mesh size. Only the publications with the most commonly used methods (TFLES, CMC-LES, FDF and to a lesser extent MMC-LES) are considered here. Other methods are either too recent (Deconvolution, Optimized chemistry, ODT) or too restrictive in their potential applications (MILES). The main observations are the following:

- Transported FDF methods (which have arbitrarily been separated from sparse Lagrangian MMC methods to highlight the gain in computational costs reached by MMC-LES) are the most expensive and simulations typically feature less than 20 species and low to medium sized grids.
- The few simulations performed with MMC-LES show that by reducing computational costs with MMC mixing, transported FDF methods can be carried out with a higher number of transported species on similar meshes.
- The assumptions made in CMC through the definition of one or more conditioning variables enable the computation with more detailed mechanisms on slightly bigger meshes.
- TFLES models are widely used with mechanism containing less than 10 species. They are however performed with a significantly higher number of grid elements and enable the computation on complex burners.

These observations corroborate the analysis of combustion models made in section 1.2. The comparison is however flawed since the assumptions made in the different models are not the same.

1.3.2 Contributions of this thesis

The most commonly used LES models (FDF, CMC and TFLES) do not fulfill simultaneously the three following criteria: correct prediction of pollutants, correct flame propagation and low computational costs. With the steady growth of computational capabilities, the use of transported chemistry is expected to increase in the near future. Adequate coupling of transported chemistry with LES is then critical. The focus of the thesis is on the prediction of flame propagation and pollutants formation through the use of transported chemistry in LES of premixed combustion. Current strategies are either not suitable or too expensive to satisfyingly predict pollutants mass fractions. The necessity

of the development of new models has hence become apparent. Two promising modeling routes are selected and explored in this thesis. The main contributions of the work are the following:

- The investigation of turbulent combustion models based on deconvolution algorithms. Selected models from the literature are challenged against a newly developed method. By analyzing a one-dimensional canonical flame, a deep understanding of the behavior of deconvolution models is achieved.

- The development of a new modeling strategy, Filtered Optimized Chemistry (FOC), based on modified chemical mechanisms able to reproduce filtered flame fronts. These mechanisms are designed by optimizing the set of chemical coefficients. The focus is made on the correct prediction of CO formation. In particular, the development of a model for including wrinkling effects on CO formation is proposed. It consists in targeting newly developed filtered wrinkled flamelets (FWF) in the optimization process. Two variants of the FOC model are developed: (i) FOC-FPF, for which optimization is done on filtered planar flames (FPF); (ii) FOC-FWF, involving the use of FWF flamelets in the optimization procedure, so that turbulent combustion modeling is integrated in the chemical formalism. FOC-FPF and FOC-FWF are validated on a turbulent premixed burner.

1.3.3 Structure of the thesis

The structure of the thesis is as follows:

- **In chapter 2**, turbulent combustion models based on deconvolution algorithms are investigated. Deconvolution models are a recently developed strategy for predicting pollutants in LES and few studies have been done in the literature. The problem of deconvolution is first analyzed and insights about ill-posedness of the deconvolution problem are provided. Three models recently introduced in the literature are tested against a new method based on second-order subgrid interpolation and parametric functions. *A priori* and *A posteriori* studies are performed in the case of a 1-D unstrained laminar premixed flame.

- **In chapter 3**, the FOC modeling approach is presented as an alternative to deconvolution methods. The method features an optimization procedure which aims at generating a mechanism able to capture the structure and propagation speed of selected canonical flames (FPF or FWF). Two libraries of canonical flames are used to build the model: (i) a library of 1-D unstrained laminar filtered premixed flames, leading to the FOC-FPF model; (ii) a library of 1-D filtered wrinkled flamelets,

defining the FOC-FWF model. These wrinkled flamelets are generated using a recently proposed methodology and are analyzed in this chapter.

- **In chapter 4**, the FOC-FPF and FOC-FWF models are challenged against data from a laboratory-scale burner experiment. The Cambridge SwB burner in its premixed non-swirled and highly swirled operating conditions is selected to that purpose. The ability of the model to capture flame propagation is studied, along with a thorough analysis of its ability to predict CO in the flame front.

- **In chapter 5**, an analytic formulation of the FOC-FWF model is proposed to simplify the pre-processing step of the model, which involves multiple optimized quantities. The simplified FOC-FWF model is validated on the Cambridge burner.

Chapter 2

Deconvolution applied to Large Eddy Simulation of premixed flames

Contents

A possible modeling approach in Large Eddy Simulation (LES) of reactive flows is to deconvolve resolved scalars. Indeed, by inverting the LES filter, scalars such as mass fractions are reconstructed. This information can be used to close budget terms of filtered species balance equations, such as the filtered reaction rate. Ill-posed in the mathematical sense, the problem is very sensitive to any numerical perturbation. The objective of the present study is to assess the ability of this kind of methodology to capture the chemical structure and flame front consumption speed of premixed flames. For that purpose, three deconvolution methods are tested on a 1-D filtered laminar premixed flame configuration: the Approximate Deconvolution Method (ADM) based on Van Cittert iterative deconvolution, a Taylor decomposition-based method and the Regularized Deconvolution Method (RDM) based on the minimization of a quadratic criterion. The issue of subgrid scale profiles reconstruction is then investigated. Two methodologies are proposed and coupled to the ADM model to study the inclusion of small scales in the modeling: the first one relies on subgrid scale interpolation of deconvolved profiles and the second uses parametric functions to describe small scales. Conducted tests analyze the ability of the method to capture the laminar chemical filtered flame structure and the laminar front propagation speed.

2.1 Motivations

2.1.1 Objectives

Combustion models based on deconvolution have recently been suggested in the literature (see Sec. 1.2.5.1 for a bibliographical review). Deconvolution models are attractive as they enable the closure of LES equations without any assumption on the combustion regime. The objective of the study in this chapter is to investigate deconvolution modeling as a new method for LES simulations with transported chemistry.

2.1.2 Introduction to deconvolution modeling

According to Mellado et al. (2003), LES signals decompose into three parts: (1) the resolved signal which corresponds to filtered quantities represented on the LES grid; (2) the under-resolved scales for which frequency components are smaller than the cut-off frequency given by the LES filter size (approximately the grid size); (3) the unresolved scales which correspond to the scales smaller than the cut-off length-scale, or also called sub-grid scales. The challenge of deconvolution in practical LES grid is to recover the full signal composed of parts (1), (2) and (3) from the only data available at each LES iteration, i.e. the resolved signal (1). Deconvolution models recently introduced in the literature - ADM (Stolz and Adams (1999)), Approximate Deconvolution Method

and Explicit flame Filtering (Domingo and Vervisch (2014)), and the Regularized Deconvolution Method (RDM) (Wang and Ihme (2016)) - are designed to recover under-resolved scales (2) from resolved quantities (1). Additional effort is needed to include unresolved contributions (3).

Even though many studies of deconvolution applied to LES of reactive flows have been carried out on 3-D configurations, the ability of this methodology to capture the laminar flame propagation speed and the chemical structure has never been investigated. Situations where the sub-grid flame wrinkling is close to unity are common in practice and it is hence essential that a combustion model retrieves the correct flame dynamics in a laminar regime (Fiorina et al. (2010); Fiorina et al. (2014)). The suitability of existing methodologies will be challenged on the simple 1-D freely propagating flame configuration. The intend of this work is not to provide the ultimate solution for applying deconvolution to combustion LES, but to analyze related issues. In particular, we aim to determine the importance of accounting for unresolved contribution (3) in the deconvolution process.

In Sec. 2.2, the problem of deconvolution is presented and analyzed. The chosen grid resolutions are representative of realistic LES meshes. The resolved (1), under-resolved (2) and unresolved (3) contributions are illustrated through a laminar flame post-processing. Several deconvolution methods are then exposed. Existing methods designed to recover under-resolved quantities (2) are first presented. Then, we propose two strategies to include unresolved contribution (3). The first one is simply based on interpolation whereas the second includes small scales with a parametric model. All deconvolution methods are challenged on the 1-D freely propagating laminar premixed flame configuration in *a priori* and *a posteriori* analyses in Sec. 2.3. An in-depth study of the laminar flame speed and its variation in time on a 1-D freely propagating CH_4/air flame is done to highlight the importance of including small scales in the modeling.

2.2 Deconvolution problem

2.2.1 The mono-dimensional filtered freely propagating flame configuration

The unstretched 1-D filtered laminar premixed flame configuration challenges the ability of LES combustion model to capture the flame front propagation speed in situations where no wrinkling occurs at the subgrid scale. Under unity Lewis number assumption and for isobaric conditions, the flame governing

equations read:

$$\frac{\partial \rho}{\partial t} + \frac{\partial \rho u}{\partial x} = 0 \tag{2.1}$$

$$\rho \frac{\partial Y_k}{\partial t} + \rho u \frac{\partial Y_k}{\partial x} = \frac{\partial}{\partial x}\left(\rho D \frac{\partial Y_k}{\partial x}\right) + \dot{\omega}_k(Y_k, T) \tag{2.2}$$

$$\rho \frac{\partial h}{\partial t} + \rho u \frac{\partial h}{\partial x} = \frac{\partial}{\partial x}\left(\rho D \frac{\partial h}{\partial x}\right) + \dot{Q} \tag{2.3}$$

where x is the direction normal to the flame front, ρ is the density, Y_k is the species k mass fraction, D the diffusivity coefficient, u the flow speed, T the temperature and h the mixture enthalpy per unit mass. $\dot{Q}$ is a energy heat losses term, neglected in the present work. These governing equations are filtered in an LES context, leading to:

$$\frac{\partial \overline{\rho}}{\partial t} + \frac{\partial \overline{\rho}\widetilde{u}}{\partial x} = 0 \tag{2.4}$$

$$\overline{\rho}\frac{\partial \widetilde{Y_k}}{\partial t} + \overline{\rho}\widetilde{u}\frac{\partial \widetilde{Y_k}}{\partial x} = \overline{\frac{\partial}{\partial x}\left(\rho D \frac{\partial Y_k}{\partial x}\right)} + \overline{\dot{\omega}_k(Y_k, T)} + \overline{\tau}_c^k \tag{2.5}$$

$$\overline{\rho}\frac{\partial \widetilde{h}}{\partial t} + \overline{\rho}\widetilde{u}\frac{\partial \widetilde{h}}{\partial x} = \overline{\frac{\partial}{\partial x}\left(\rho D \frac{\partial h}{\partial x}\right)} + \overline{\tau}_c^h + \overline{\dot{Q}} \tag{2.6}$$

The overbar denotes the spatial filtering operation $\overline{\upsilon} = \int_{\mathbb{R}} G(x-u)\upsilon(u)\mathrm{d}u$, where υ is any thermo-chemical or flow quantity. G is called the filter kernel and is considered to be Gaussian throughout this chapter, so that $G(x) = \sqrt{\frac{6}{\pi\Delta^2}} exp\left(\frac{-6x^2}{\Delta^2}\right)$. Details about the implementation of the filter are given in appendix C. The tilde operator denotes the density weighted filtering defined by $\overline{\rho}\widetilde{\varphi} = \overline{\rho\varphi}$. Under ideal gas assumption, the filtered density relates to the temperature T and the constant pressure p as follow: $\overline{\rho} = p/\widetilde{rT}$, where r is the specific gas constant.
$\overline{\tau}_c^k$ and $\overline{\tau}_c^h$, the unresolved convective terms of species and energy balance equations, read respectively as:

$$\overline{\tau}_c^k = \frac{\partial}{\partial x}\left(\overline{\rho}\left(\widetilde{u}\widetilde{Y_k} - \widetilde{uY_k}\right)\right) \tag{2.7}$$

$$\overline{\tau}_c^h = \frac{\partial}{\partial x}\left(\overline{\rho}\left(\widetilde{u}\widetilde{h} - \widetilde{uh}\right)\right) \tag{2.8}$$

The diffusivity $\rho D = \lambda / C_p$ is modeled using Sutherland's type law: $D_T = \frac{\mu_0}{Pr}\left(\frac{T}{T_0}\right)^{\alpha}$, where $\alpha = 0.682$, $T_0 = 300\ K$, $\mu_0 = 1.8071 \times 10^{-4}\ kg.s^{-1}.m^{-1}$ and $Pr = 0.68$.

Chemical reaction rates are modeled by using the two-steps methane mechanism described in Bibrzycki and Poinsot (2010):

$$\begin{aligned} CH_4 + \frac{3}{2}O_2 &\longrightarrow CO + 2H_2O \\ CO + \frac{1}{2}O_2 &\longleftrightarrow CO_2 \end{aligned} \tag{2.9}$$

This 5-species/2-steps mechanism is very simple but includes the main type of species encountered in most chemical mechanisms: reactants (CH_4 and O_2), products (H_2O and CO_2) and CO, which is both an intermediate and a final product species.

2.2.2 Challenges for deconvolution of flames

2.2.2.1 Modeling and numerical issues

In a combustion LES context, the issues are to close Eqs. (2.4)–(2.6). The task is especially challenging for the filtered chemical reaction rates $\overline{\omega}_k(Y_k, T)$, as kinetic constants are described by Arrhenius-type laws. By consequence, even in the present 1-D laminar problem, where the wrinkling of the flame by turbulence is not considered, the high non-linearity of reaction rates induces critical issues.
This is illustrated in Fig. 2.1, which shows the filtered chemical reaction rate of species CH_4 across a steady state 1-D premixed laminar flame (the fresh gas velocity exactly compensates the flame consumption speed in the reference frame of the flame). The dimensionless filter size is defined as $\gamma = \Delta/\delta_r$, where δ_r, the reactive flame thickness is defined as the Full Width at Half Maximum (FWHM) of the methane chemical reaction rate. The reference solutions (solid lines) are obtained by *a priori* filtering the chemical reaction rate extracted from the solution of the non-filtered flames equations (Eqs. (2.1)–(2.3)) for γ=4. This solution is compared against a first-order approximation, where the chemical reaction rate is directly approximated from the resolved thermochemical quantities (Duwig et al. (2011); Duwig and Fuchs (2008)):

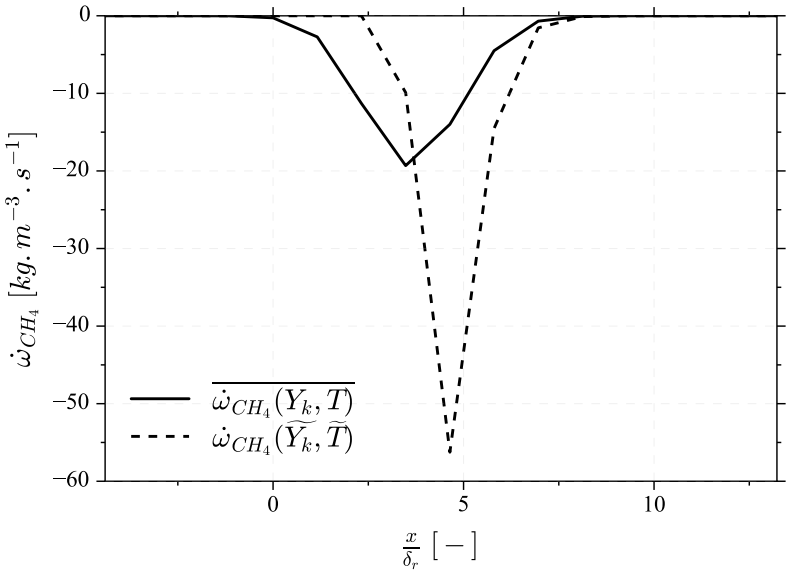

Figure 2.1: *Comparison between the reference filtered reaction rate and the filtered reaction rate without model for CH_4 and $\gamma = 4$. Solid lines: $\overline{\dot{\omega}_{CH_4}(Y_k,T)}$. Dashed lines: $\dot{\omega}_{CH_4}(\widetilde{Y_k},\widetilde{T})$.*

$\overline{\dot{\omega}}_{CH_4}(Y_k,T) \approx \dot{\omega}_{CH_4}(\widetilde{Y_k},\widetilde{T})$ (dashed lines in Fig. 2.1). Important discrepancies are observed between the reference and the first-order assumption, leading to a misprediction of the flame consumption speed of 46.7%.

When the LES grid is uniform of spacing $\overline{\Delta_x}$, the flame front resolution is defined as $\overline{n_0} = \overline{\delta_r}/\overline{\Delta_x}$, where $\overline{\delta}_r$ is the filtered reactive flame thickness. As $\overline{\Delta_x}$ is typically larger than the flame thickness δ_r Poinsot and Veynante (2005), deconvolved flame profiles are not sufficiently discretized on the filtered simulation grid. Two methods are then possible: i) use the same grid for LES and the deconvolution procedure (Domingo and Vervisch (2014); Mathew (2002); Wang and Ihme (2016)). Numerical diffusion will then compensate under-resolution of deconvolved profiles. ii) introduce a finer additional grid, only dedicated to the deconvolution procedure. This has been applied in the context of LES for non-reacting flows (Domaradzki and Loh (1999); Domaradzki et al. (2002)) but has never been investigated in a combustion context where the phenomena taking place at small scales are even more essential. This procedure will be investigated in the present work. The mesh is assumed uniform, of grid spacing Δ_x^*. The deconvolved flame front resolution is then quantified by the parameter n_0^* defined as $n_0^* = \delta_r/\Delta_x^*$.

The following analysis is conducted to highlight the impact of the deconvolved grid resolution on the flame structure: reference temperature and species mass fraction solutions, obtained by solving the system of Eqs. (2.1)-(2.3), are interpolated on grids with varying spacings Δ_x^* to mimic different deconvolved

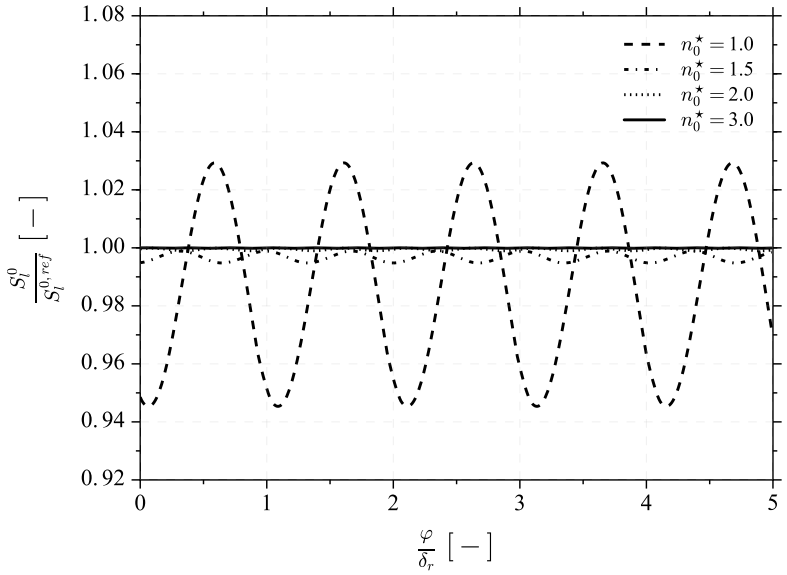

Figure 2.2: A priori *computations of filtered flame propagation speed obtained from the integration of CH_4 filtered reaction rate $\overline{\dot{\omega}}_{CH_4}$ profiles, as given by Eq. (2.10). Each curve corresponds to a given deconvolution profile resolution n_0^*. Results are plotted as a function of φ/δ_r, the dimensionless position of the flame relative to the grid cells.*

profile resolutions. The methane chemical reaction rate is filtered and integrated across the spatial direction to estimate the filtered flame consumption speed:

$$S_c^\Delta = \frac{1}{\rho_u(Y_{CH_4}^b - Y_{CH_4}^u)} \int_{-\infty}^{+\infty} \overline{\dot{\omega}}_{CH_4}(x)dx \tag{2.10}$$

In unsteady reactive computations, the flame position relative to the grid changes. Numerical resolution conditions may then evolve with time, especially when the reactive layer is under-resolved. To mimic a moving 1-D flame in the present *a priori* tests, the coarse mesh is shifted relative to the flame position by an offset distance φ. The filtered flame consumption speed is plotted as a function of φ/δ_r for four different grids on figure 2.2. The flame speed varies periodically when n_0^* is low, meaning that the deconvolved profile resolution is not sufficient. Conversely, when n_0^* grows the impact of the grid is decreased. This highlights the importance of using a sufficient number of points for the deconvolved functions.

2.2.2.2 Filter and conditioning

The filtering operation is linear and expresses as a matrix-vector multiplication $\overline{\rho Y_k} = M(\rho Y_k)$, where M is the filtering matrix. A perturbation $\delta(\overline{\rho Y_k})$ results

in a perturbation $\delta\left(\rho Y_k\right)^*$ of the deconvolved function bounded by the following inequality:

$$\frac{\|\delta\left(\rho Y_k\right)^*\|}{\|\left(\rho Y_k\right)^*\|} \leq \kappa(M) \frac{\|\delta\overline{(\rho Y_k)}\|}{\|\overline{\rho Y_k}\|} \tag{2.11}$$

where the filter condition number $\kappa(M) = \|M\|\|M^{-1}\|$ measures the sensitivity of the deconvolution to a perturbation of the initial filtered function. If the condition number is close to 1, the inversion of the filter is numerically stable. On the other hand, if it is larger than 1, a perturbation of the initial filtered variable will cause a larger discrepancy on the deconvolved function. Figure 2.3 plots the condition number of M in terms of the dimensionless filter size γ for different grids resolutions n_0^*. The condition number grows rapidly when the filter size increases, meaning that the problem is ill-conditioned. In addition numerical stabilities issues are amplified when the resolution of the deconvolved profile increases.

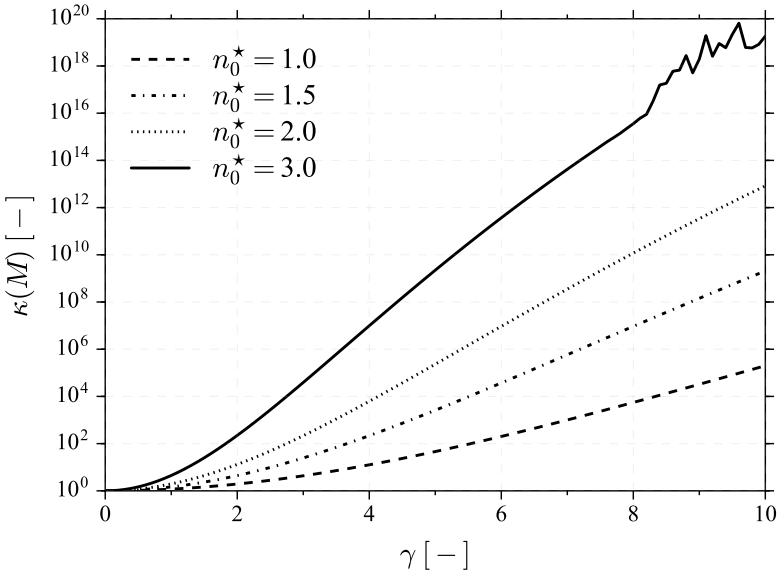

Figure 2.3: *Computation of the condition number of M as a function of γ for different values of grid resolution n_0^*. A log scale is used for the condition number axis.*

2.2.2.3 Fourier analysis of the filtering operator

An analysis of LES filtering in terms of Discrete Fourier Transforms (DFT) is proposed to understand modeling issues related to deconvolution methods. The analysis is done here using the CH_4 mass fraction. The DFT vector for a

given discretization is given by the points :

$$\widehat{(\rho Y_i)}_n = \sum_{m=0}^{N-1} (\rho Y_i)_m \, exp\left(-2\pi i \frac{mn}{N}\right) \tag{2.12}$$

where N is the number of points in the spatial grid. Similar formula can be derived for filtered functions, hence enabling to compare their frequency content. The filtering operator corresponds to a multiplication in Fourier space, therefore a transfer function is associated to each filter kernel. For the Gaussian filter, the DFT reads:

$$\widehat{\overline{\rho Y_i}}(k) = e^{-\Delta^2 k^2} \widehat{\rho Y_i}(k) \tag{2.13}$$

where k is the wavenumber. Figure 2.4 plots the one-dimensional spectrum of both reference and filtered CH_4 mass fractions, extracted from a 1-D methane/air flame (with $\phi = 0.8$) in terms of the normalized wave number $\delta_r k$. Low frequencies are almost unaffected by the filtering operation whereas high frequencies are damped. The unresolved part of the signal, or sub-grid contribution, is shown by the area highlighted in Fig. 2.4. As discussed in Mellado, Sarkar, and Pantano (2003), two distinct contributions are identified: scales located to the left of the LES filter size wave number (area with stripes) are damped by the filtering operation but are *recoverable* on the LES grid, whereas scales located to the right (area with points) contain high frequency components and are *unrecoverable* from the filtered LES signal.

2.2.3 Deconvolution methods

This section is dedicated to the presentation of deconvolution methods. Techniques designed to reconstruct the under-resolved part of the signal are described in Section 2.2.3.1 and methodologies to include unresolved contributions are discussed in Section 2.2.3.2.

2.2.3.1 Deconvolution of under-resolved contributions

Approximate Deconvolution Method (ADM) One of the earliest attempts to use deconvolution in LES is the Approximate Deconvolution Method (ADM), originally proposed by Stolz and Adams (1999). It is based on Van Cittert's algorithm and has been developed for non-reactive LES. It focuses on the reconstruction of the *recoverable* part of the signal. This method, iterative and initialized using transported filtered quantities, reads:

$$\begin{cases} [\rho Y_k]_0 = \overline{\rho Y_k} & \text{(2.14a)} \\ [\rho Y_k]_{n+1} = [\rho Y_k]_n + (\overline{\rho Y_k} - M\,[\rho Y_k]_n) & \text{(2.14b)} \end{cases}$$

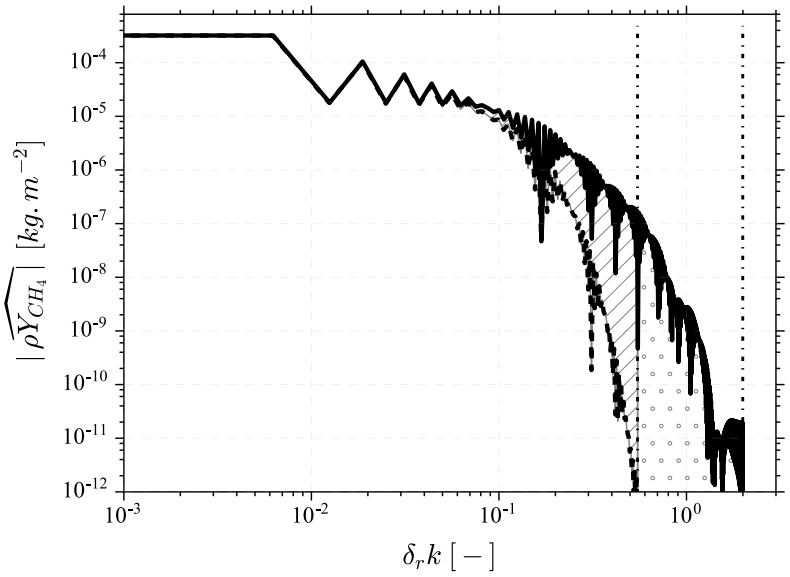

Figure 2.4: *Filtered and resolved CH_4 mass fraction in Fourier space ($\gamma = 5$). Solid line: resolved function $|\ \widehat{\rho Y_{CH_4}}\ |$. Dashed line: filtered function $|\ \widehat{\overline{\rho Y_{CH_4}}}\ |$. Area with stripes: under-resolved part of the signal. Area with points: unresolved part of the signal.*

where n refers to the iteration number. The deconvolved variables are approximated by:

$$(\rho Y_k)^* = [\rho Y_k]_{N_{ADM}} \tag{2.15}$$

where N_{ADM} is the total number of iterations. In the variable density case treated here the filtered density $\overline{\rho}$ is deconvolved in a similar manner. As discussed in Stolz and Adams (1999), $N_{ADM} = 5$ has been retained in a good compromise between the computational cost and the accuracy of the model. The Approximate Deconvolution Method is a deconvolution method regularized by truncating the series. Indeed, low frequencies of the signal are recovered first and by stopping the series we avoid getting high frequencies, more sensitive to undesired perturbations.

Taylor decomposition of the filter Domingo and Vervisch (2014) proposed a deconvolution method based on a Taylor-decomposition of the Gaussian filter. It aims at retrieving the *recoverable* part of scalars using the following deconvolution formulae:

$$(\rho Y_k)^* = \overline{\rho Y_k} - \frac{\Delta^2}{24}\frac{\partial^2 \overline{\rho Y_k}}{\partial x^2} \tag{2.16}$$

$$(\rho)^* = \overline{\rho} - \frac{\Delta^2}{24}\frac{\partial^2 \overline{\rho}}{\partial x^2} \tag{2.17}$$

Eq. (2.17) is computed in practice by solving the anti-diffusion equation, explicitly or implicitly. The method, called Approximate Deconvolution and Explicit flame Filtering (ADEF), is a non-regularized method in the sense that no assumption is made about the deconvolved function.

Regularized deconvolution method Deconvolution can also be performed by an optimization process which aims at minimizing a quadratic criterion (Wang and Ihme (2016)):

$$Y_k^* = \min_{Y_k s.t.\ Y_k^- \leq Y_k \leq Y_k^+} \|\widetilde{Y}_k - \widetilde{G} * Y_k\|^2 + \alpha_{RDM}\|Y_k - \widetilde{Y}_k\|^2 \tag{2.18}$$

The density is deconvolved by minimizing $\|\overline{\rho} - G * \rho\|^2$. The deconvolution function is constrained and a regularization is performed via the addition of a penalization term in the objective function. The approach is similar to a Tikhonov method (Tikhonov (1963); Tikhonov and Arsenin (1978)). The regularization is based on the assumption that $\widetilde{Y}_k$ is an *a priori* assumed solution for the deconvolved function Y_k^*. A similar approach has been used in a Conditional Source-term Estimation (CSE) context by Labahn et al. (2014). Although this method was tested on the post-processing of a 3-D DNS, it will here be challenged on a coarse grid. The L-BFGS-B algorithm has been used to solve the optimization problem (2.18) (Byrd et al. (1995); Zhu et al. (1997)).

2.2.3.2 Extension to unresolved signal deconvolution

As discussed in Section 2.2.2.1, the reconstruction of the unresolved part of a signal requires a reconstruction grid finer than the LES grid. Two alternatives are proposed to reconstruct this signal on the reconstruction grid: The first is a second order interpolation, whereas the second extrapolates small scale information by using a parametric model. The two strategies discussed in the following section are compatible with any of the deconvolution methods presented in Section 2.2.3.1. The methods described in Section 2.2.3.1 will also be referred to as explicit deconvolution methods in the next sections.

Second order interpolation of the reconstructed signal Second order interpolation inside each grid cell has been done in combination with ADEF deconvolution method in the work of Domingo and Vervisch (2014) and has also been studied in a TFLES context by Kuenne et al. (2017). A quadratic interpolation method will be used in the following of the paper.

Parametric reconstruction of subgrid scales Quality of the second order interpolation can be improved by compensating the remaining reconstruction error by a parametric model. The model relies on the self-similar properties of laminar flames, observed in multiple configurations, including premixed laminar (Ribert, Gicquel, Darabiha, and Veynante (2006)) and premixed turbulent flames (Veynante, Fiorina, Domingo, and Vervisch (2008), Fiorina et al. (2009)). These self-similar properties suggest that subgrid scales flame structures could be modeled by parametric analytical functions.

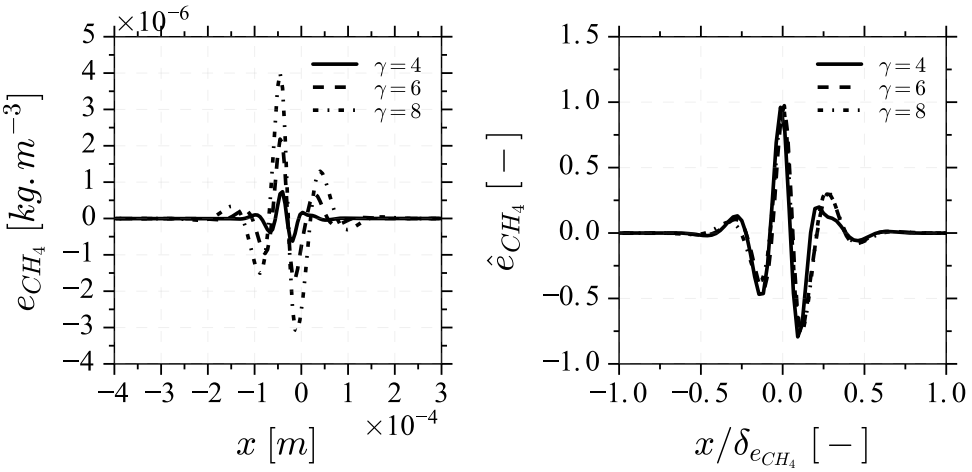

Figure 2.5: *Remaining error on CH_4 density-weighted mass fraction after application of ADM deconvolution method. On the left: absolute value. On the right: normalized value. Solid lines: $\gamma = 4$. Dashed lines: $\gamma = 6$. Dash-dotted lines: $\gamma = 8$.*

Density-weighted mass fractions obtained after explicit deconvolution and second-order interpolation are written $(\rho Y_k)^{*,i}$. The method introduces an analytical function $\mathcal{M}_{p_k}$ to model the remaining error $e_k = \rho Y_k - (\rho Y_k)^{*,i}$. Similar patterns are observed when computing e_k for different values of γ. This is illustrated in Fig. 2.5, which shows on the left the reconstruction error for ρY_{CH_4} obtained after application of the ADM deconvolution method. The normalized error $\hat{e}_{CH_4} = e_{CH_4}/max(e_{CH_4})$ is plotted on the right in Fig. 2.5 as a function of a dimensionless spatial coordinate $x/\delta_{e_{CH_4}}$. The curves superimpose, meaning that a parametric model could be appropriate. The Gaussian modulated sine function is retained to model $\mathcal{M}_{p_k}$:

$$\mathcal{M}_{p_k}(x) = Ae^{-b(x-x_0)^2}\sin\left(2\pi f x + 2\pi\varphi\right) \tag{2.19}$$

where x is the spatial direction. x_0, A, b, f and φ constitutes a set of parameters which characterize $\mathcal{M}_{p_k}$. These variables are identified during the deconvolution process by minimizing α, the difference between $\mathcal{M}_{p_k}$ and the

error e_k:

$$\alpha = \min_{p_k} \|e_k - \mathcal{M}_{p_k}\|^2 \tag{2.20}$$

As e_k is unknown, this optimization process cannot be performed directly. However, as the filtered variables are known, this optimization step can be modified so that $\overline{\alpha}$ is minimized:

$$\overline{\alpha} = \min_{p_k} \|\overline{e_k} - \overline{\mathcal{M}_{p_k}}\|^2 \tag{2.21}$$

where $\overline{e_k} = \overline{\rho Y_k} - \overline{(\rho Y_k)^{*,i}}$. The final deconvolved function is then $(\rho Y_k)^* = (\rho Y_k)^{*,i} + \mathcal{M}_{p_k}$. This optimization step is performed using a Newton Conjugate Gradient algorithm (Nocedal and Wright (1999)) on the fine grid of resolution n_0^*.

2.2.4 *A priori* analysis of deconvolution models

The deconvolution models are now challenged by post-processing the solutions of a filtered 1-D freely propagating laminar flame, discretized on a coarse grid in order to mimic realistic LES grid conditions.
The challenge of deconvolution is that the frequency range represented by the coarse grid is not large enough to capture the high frequencies contained in deconvolved functions. The *a priori* tests consist in post-processing a filtered laminar flame solution. In a first step, instantaneous solutions of the system of Eqs. (2.1)–(2.3) are selected as reference resolved data. In a second step, these solutions are filtered using the Gaussian filter operator. Finally, in a third step, the filtered data are deconvolved using one of the algorithms. Deconvolved data are then compared against the resolved reference solution. As *a priori* tests aim to evaluate the loss of information due to grid resolution and its impact on filtered reaction rates, it is especially important to use two different grids: a fine grid with spacing Δ_x for the variables used as the reference resolved solution and a coarse grid with spacing $\overline{\Delta}_x$ for the filtered data. The coarse grid spacing $\overline{\Delta}_x$ is defined so that $\overline{\Delta}_x = \overline{\delta}_r/3$, where $\overline{\delta}_r$ is the thickness of the filtered CH_4 reaction rate. This flame resolution is chosen to ensure a proper prediction of the flame speed without introducing numerical artifacts. As the filtered flame thickness grows with the filter size, $\overline{\Delta}_x$ increases as well.
If the same grid was used, the inversion of perfectly filtered data using the same algorithm than the filter operator would lead to fake positive results. This numerical phenomenon, often referred in the literature as *inverse crime*, has to be considered when testing a deconvolution method (Kaipio and Somersalo (2005)). A way of tackling the issue is to use an additive noise (Labahn et al. (2014)). In our case, as tests are done in realistic LES conditions (i.e. with a

coarse grid for filtered variables) and artificial noise is not needed.

The deconvolution models for under-resolved part of signals are first tested and the impact of unresolved scales modeling via interpolation and parametric functions is then studied.

2.2.4.1 Deconvolution of under-resolved contributions

The dimensionless filter size is first set to $\gamma = 4$. Deconvolved mass fractions of methane and carbon monoxide are compared against resolved reference solutions in Fig. 2.6. While the three deconvolution methods recover fairly well the reference solution for Y_{CH_4}, only ADM and ADEF enable to correctly reproduce the CO peak. The damping of Y_{CO} peak in RDM solution may be due to the regularizing term in Eq. (2.18). This is demonstrated in Fig. 2.8 where the solution for $\alpha_{RDM} = 0.1$ is compared to the solution with $\alpha_{RDM} = 0$ (no regularizing term).
Further post-processing is performed to evaluate the ability of the methods to model the filtered chemical reaction rates, a key unclosed quantity. For that purpose, deconvolved reaction rates are first computed as $\dot{\omega}_k^* = \dot{\omega}_k(Y_k^*, T^*)$ and filtered to obtain $\overline{\dot{\omega}}_k^*$. This filtered chemical reaction rate issued from the deconvolution procedure is compared to the reference one, obtained by filtering the reference resolved chemical reaction rate in Fig. 2.7 for both CH_4 and CO. It shows that the three algorithms recover the correct shape of the filtered methane reaction rate, though they slightly under-predict the peak. The task is more challenging for the CO chemical reaction rate, which exhibits both positive (production) and negative (consumption) contributions. ADM and ADEF do not even reproduce the shape of the profile. RDM succeeds to reproduce the shape, with however a misprediction of the negative peak.
Results are then shown for a higher filter size value, corresponding to $\gamma = 8$. CH_4 and CO mass fractions are plotted in Fig. 2.9, whereas CH_4 and CO chemical reaction rates are plotted in Fig. 2.10. In terms of mass fractions, none of the methods is able to predict the CO peak. CH_4 reaction rates are globally well captured while big discrepancies are exhibited for CO reaction rates.
To quantify the impact of the deconvolution errors on the flame front propagation, the deconvolved consumption speed is introduced:

$$S_c^* = \frac{1}{\rho_u(Y_{CH_4}^b - Y_{CH_4}^u)} \int_{-\infty}^{+\infty} \dot{\omega}_{CH_4}^*(x)dx \tag{2.22}$$

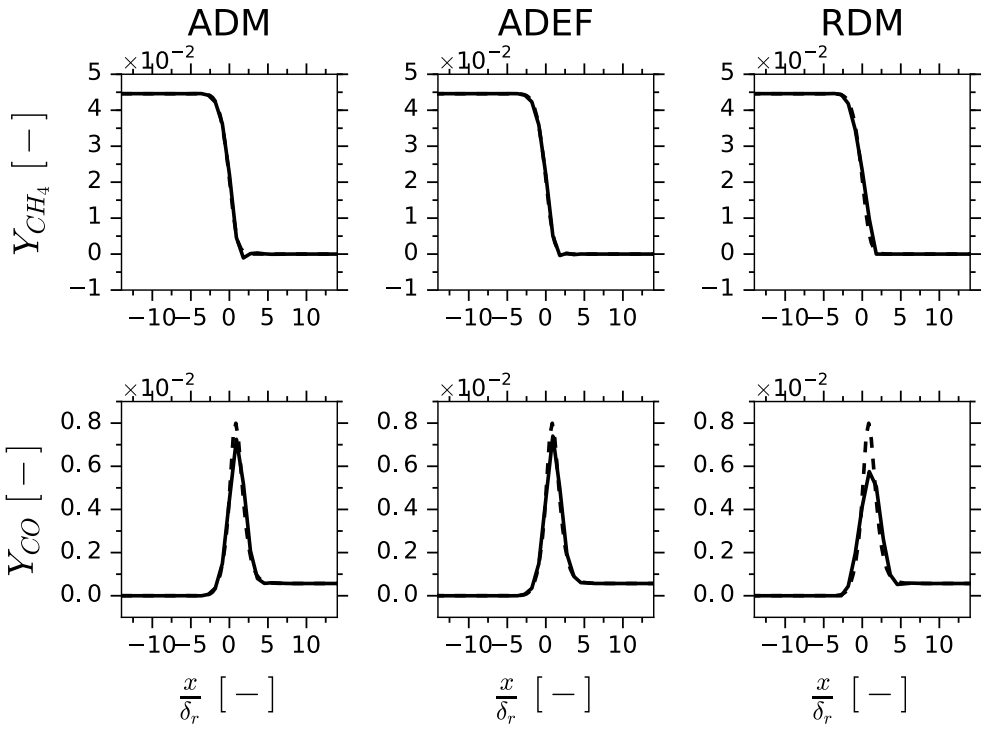

Figure 2.6: *Deconvolved CH_4 and CO mass fractions for the three explicit deconvolution methods ($\gamma = 4$). Solid lines: deconvolved term Y_k^*. Dashed lines: reference term Y_k.*

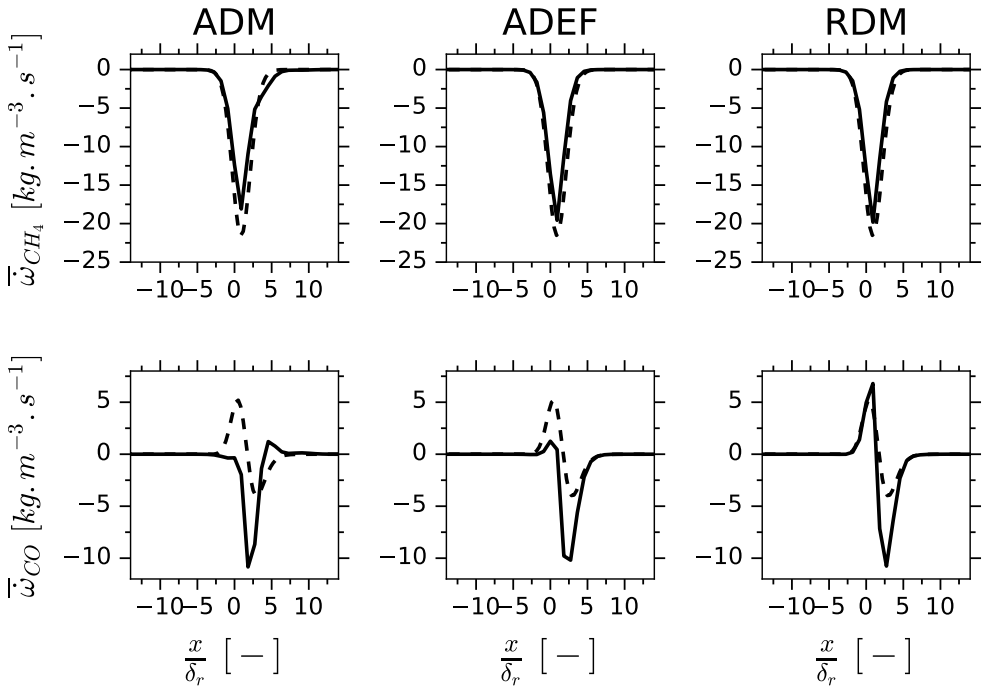

Figure 2.7: *Modelled CH_4 and CO reaction rates for the three explicit deconvolution methods ($\gamma = 4$). Solid lines: modelled term $\overline{\dot{\omega}}_k^*$. Dashed lines: reference term $\overline{\dot{\omega}}_k$.*

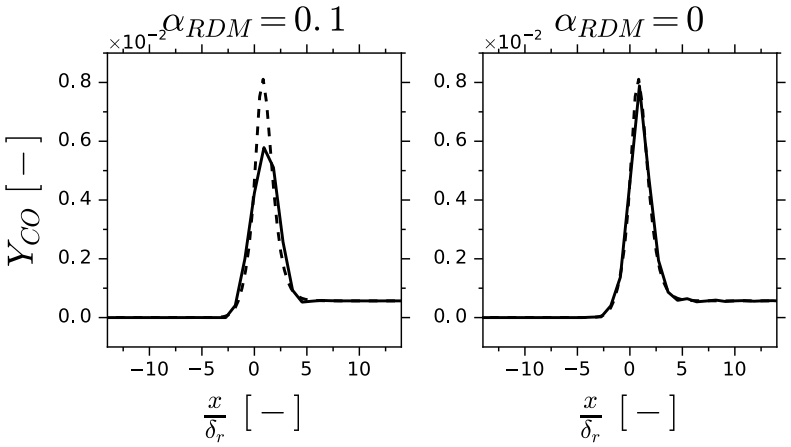

Figure 2.8: *Deconvolved CO mass fraction for the RDM deconvolution method with* $\alpha = 0.1$ *(left) and* $\alpha = 0$ *(right) for* $\gamma = 4$*. Solid lines: deconvolved term* Y_k^**. Dashed lines: reference term* Y_k*.*

The error (in %) on the laminar flame consumption speed is evaluated as:

$$\varepsilon = 100 \times \frac{\mid S_c^* - S_l^{0,ref} \mid}{S_l^{0,ref}} \tag{2.23}$$

The evolution of ε with respect to the filter size γ is plotted on Figure 2.11. All methods behave correctly when γ is small. When γ increases, the flame speed is very sensitive to the loss of information due to filtering. For $\gamma > 4$ the evolution of the error is unstable. This is explained by the ill-conditioned nature of deconvolution: for different values of gamma different perturbations are seen by the algorithm and hence a high variability is observed in the results.

2.2.4.2 Deconvolution with unresolved scales modeling

The same analysis is now carried out to study the effect of including information about fine scales using subgrid scale interpolation and parametric functions. The small scales extrapolation is done on a fine mesh of resolution $n_0^* = 3$. As pointed out in the previous part, the methodology can be applied to any of the three explicit methods. Amongst the three methods presented previously, ADM is retained to retrieve under-resolved contributions.
The impact of the parametric model is studied separately by first performing a deconvolution with subgrid scales interpolation only and then a second deconvolution with subgrid scales interpolation and parametric modeling of reconstruction errors. Deconvolved CH_4 and CO mass fractions are shown in Fig. 2.12 for $\gamma = 4$ while the corresponding reaction rates are plotted in Fig. 2.13. Filtering is applied on the fine reconstruction grid. While the inclusion of the unresolved

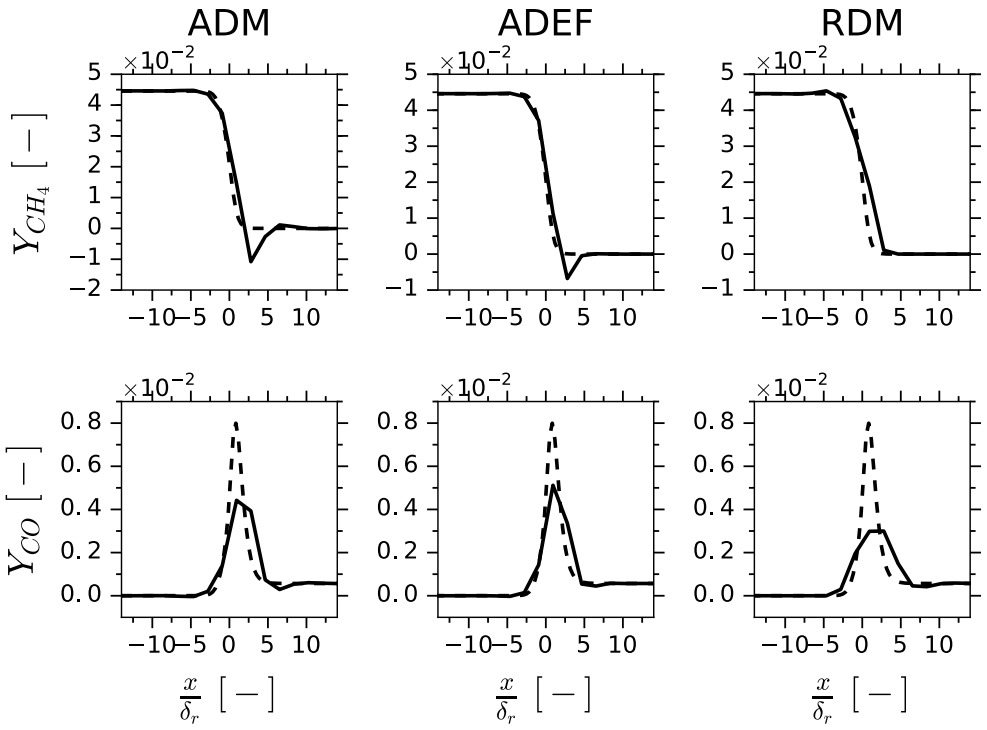

Figure 2.9: *Deconvolved CH_4 and CO mass fractions for the three explicit deconvolution methods ($\gamma = 8$). Solid lines: deconvolved term Y_k^*. Dashed lines: reference term Y_k.*

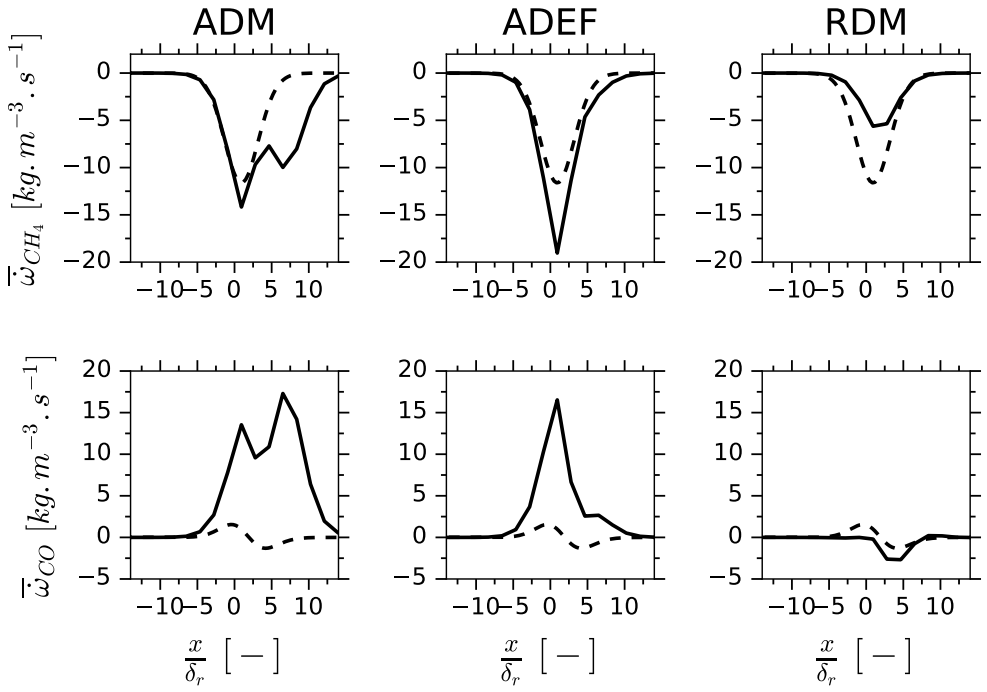

Figure 2.10: *Modelled CH_4 and CO reaction rates for the three explicit deconvolution methods ($\gamma = 8$). Solid lines: modelled term $\overline{\dot{\omega}}_k^*$. Dashed lines: reference term $\overline{\dot{\omega}}_k$.*

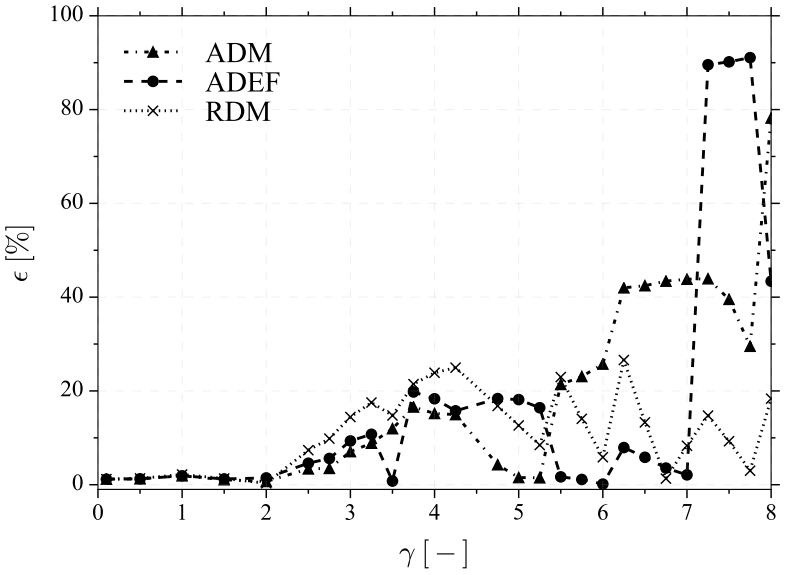

Figure 2.11: *Error on laminar flame speed as a function of the filter size γ obtained after an* a priori *analysis of explicit deconvolution methods. Triangles: Approximate Deconvolution Method. Circles: Taylor decomposition method. Crosses: Regularized Deconvolution Method.*

part of the signal with only second order interpolation gives results similar to the method with no subgrid scales modeling, the compensation of reconstruction error by a parametric model improves both CH_4 reaction rate peak and CO reaction rate prediction.
Similar conclusions are observed when considering a higher filter size ($\gamma = 8$) as shown in Figs. 2.14 and 2.15. CO mass fraction peak and CH_4 reaction rate are better approximated by the inclusion of a parametric function. This is not the case for the CO reaction rate, for which even the unresolved scales modeling via parametric function cannot predict the correct shape. As γ increases, the conditioning of the deconvolution problem is affected and the unresolved part of the signal grows.
Finally, the impact of unresolved scales modeling on the *a priori* laminar flame speed is illustrated. ε, as defined in Eq. (2.23) is plotted against γ in Fig. 2.16. The addition of unresolved contribution to the reconstructed under-resolved signal with either second order interpolation or parametric modeling tends to improve the prediction of the flame consumption speed.

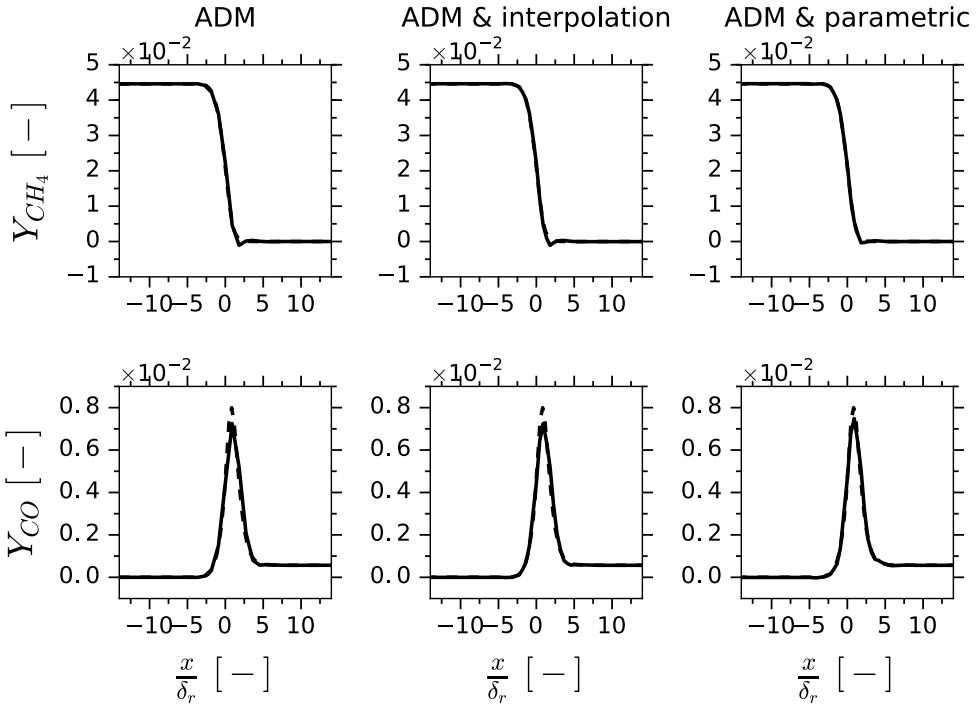

Figure 2.12: *Deconvolved CH_4 and CO mass fractions for ADM (left), ADM with interpolation (middle) and ADM with parametric model (right) ($\gamma = 4$). Solid lines: deconvolved term Y_k^*. Dashed lines: reference term Y_k.*

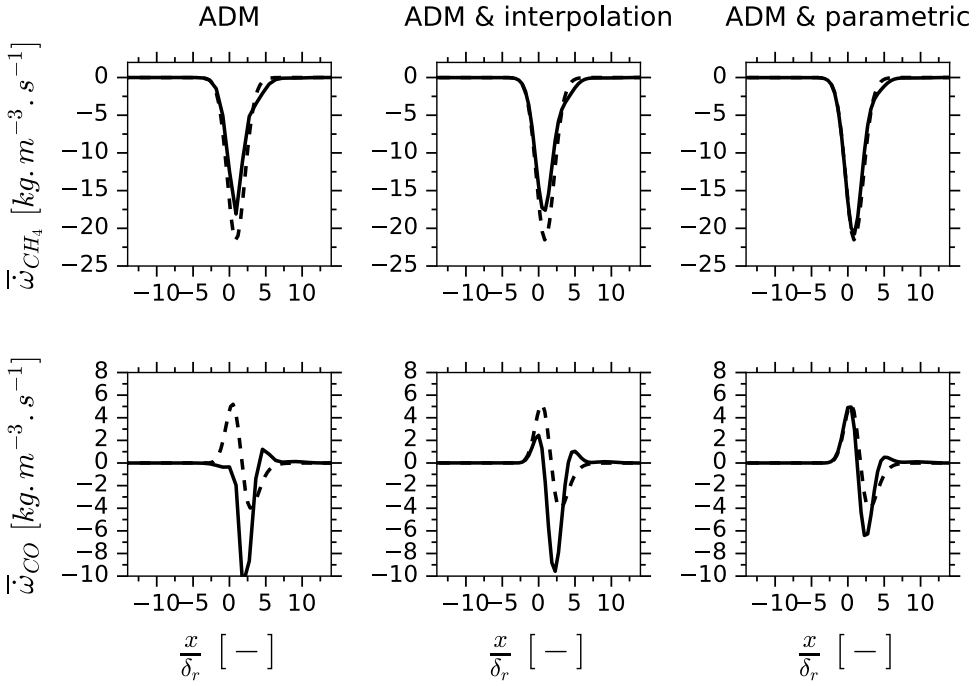

Figure 2.13: *Modelled CH_4 and CO reaction rates for ADM (left), ADM with interpolation (middle) and ADM with parametric model (right) ($\gamma = 4$). Solid lines: modelled term $\overline{\dot{\omega}}_k^*$. Dashed lines: reference term $\overline{\dot{\omega}}_k$.*

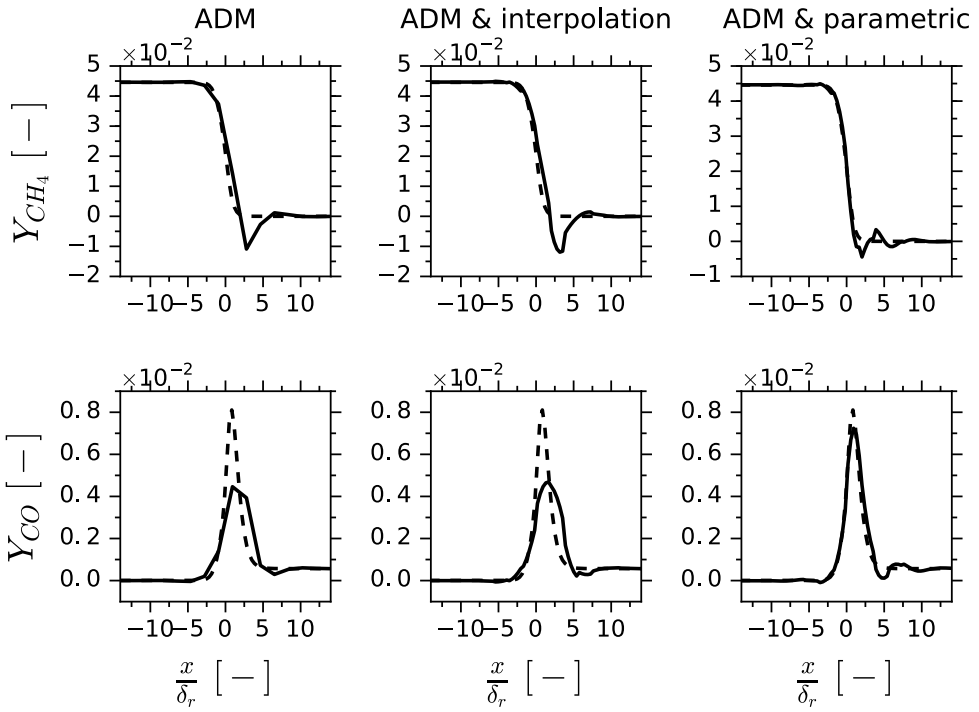

Figure 2.14: *Deconvolved CH_4 and CO mass fractions for ADM (left), ADM with interpolation (middle) and ADM with parametric model (right) ($\gamma = 8$). Solid lines: deconvolved term Y_k^*. Dashed lines: reference term Y_k.*

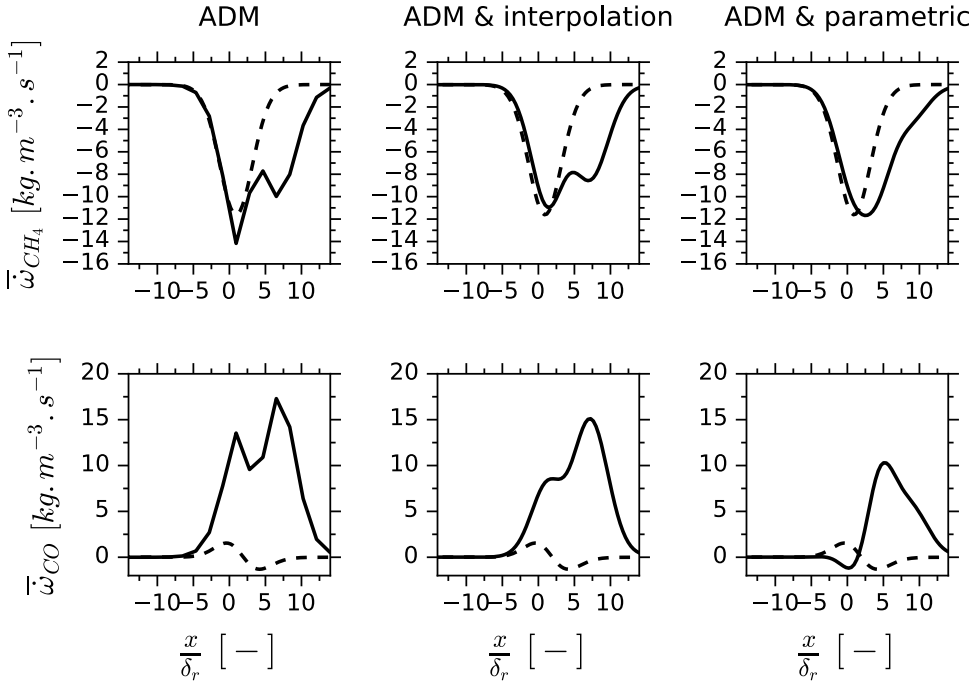

Figure 2.15: *Modelled CH_4 and CO reaction rates for ADM (left), ADM with interpolation (middle) and ADM with parametric model (right) ($\gamma = 8$). Solid lines: modelled term $\overline{\dot{\omega}}_k^*$. Dashed lines: reference term $\overline{\dot{\omega}}_k$.*

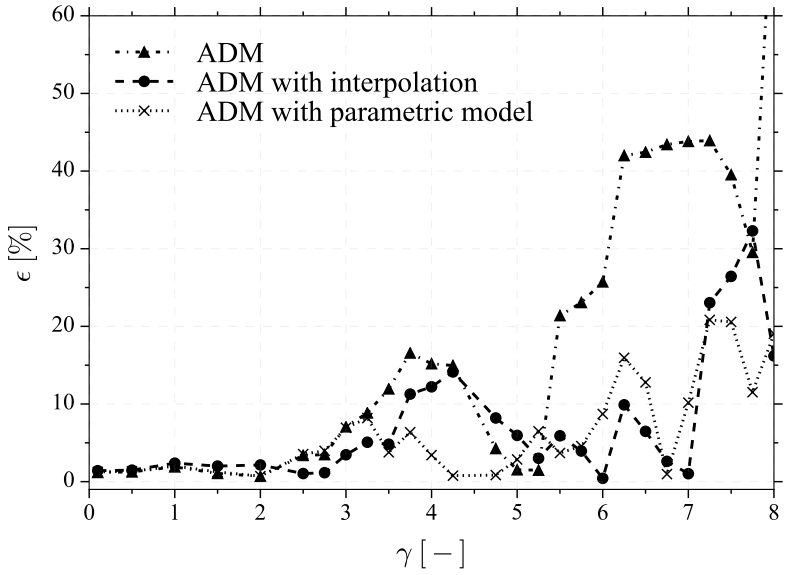

Figure 2.16: *Error on laminar flame speed as a function of the filter size γ obtained after an* a priori *analysis of deconvolution methods with unresolved scales modeling. Triangles: Approximate Deconvolution Method. Circles: Approximate Deconvolution Method with SGS interpolation. Crosses: Approximate Deconvolution Method with SGS interpolation and parametric model.*

2.3 Filtered flame simulations using deconvolution algorithms

This section discusses the practical implementation of deconvolution algorithms to perform filtered flame simulations. The closure of the filtered reactive flow balance equations is given for one spatial dimension. Then simulation results of 1-D freely propagating filtered premixed laminar flames are shown and discussed.

2.3.1 Closing filtered species and energy balance equation using deconvolution

The RHS of the filtered species mass fractions balance equation (Eq. (2.5)) is composed of three terms: the filtered chemical reaction rate, the unresolved convective fluxes and the filtered molecular diffusion. The RHS of the filtered energy equation (Eq. (2.6)), written under unity Lewis assumption, contains the filtered diffusion and the unresolved convective fluxes. To close species and energy balance equation budgets, filtered thermo-chemical variables $\overline{\rho Y}_k$, $\overline{h}$, and $\overline{\rho}$ are first deconvolved to compute Y_k^*, ρ^* and h^* by using one of the reconstruction algorithms described in Sec. 2.2.3. The deconvolved temperature T^* is obtained from the deconvolved enthalpy h^* and the species mass frac-

tions Y_k^* by inverting the relationship $h^* = \sum_{k=1}^{N} h_k^*(T^*)Y_k^*$ by using a Newton method. RHS terms are then closed by using the reconstructed thermo-chemical variables as discussed below.

Filtered chemical reaction rate $\overline{\dot{\omega}}_k$ The species chemical reaction rate is first *reconstructed* at the subgrid scale by expressing chemical Arrhenius laws in terms of deconvolved variables:

$$\dot{\omega}_k = \dot{\omega}_k(T^*, Y_k^*) \tag{2.24}$$

The filtered species chemical reaction rates of Eq.(2.5) is then estimated by filtering explicitly the *reconstructed* chemical reaction rate :

$$\overline{\dot{\omega}(T, Y_k)} = \overline{\dot{\omega}(T^*, Y_k^*)} \tag{2.25}$$

Filtered laminar diffusive terms $\overline{\frac{\partial}{\partial x}\left(\rho D \frac{\partial Y_k}{\partial x}\right)}$ and $\overline{\frac{\partial}{\partial x}\left(\rho D \frac{\partial h}{\partial x}\right)}$ The diffusive terms of species Eq. (2.5) and energy Eq. (2.6) are estimated by the explicit filtering of the gradient of deconvolved variables Y_k^*, $h^*$and D^* as follows:

$$\begin{cases} \overline{\dfrac{\partial}{\partial x}\left(\rho D \dfrac{\partial Y_k}{\partial x}\right)} = \overline{\dfrac{\partial}{\partial x}\left((\rho D)^* \dfrac{\partial Y_k^*}{\partial x}\right)} & \text{(2.26a)} \\ \overline{\dfrac{\partial}{\partial x}\left(\rho D \dfrac{\partial h}{\partial x}\right)} = \overline{\dfrac{\partial}{\partial x}\left((\rho D)^* \dfrac{\partial h^*}{\partial x}\right)} & \text{(2.26b)} \end{cases}$$

The deconvolved molecular diffusivity is expressed as a function of a Prandtl number Pr and the flow viscosity μ: $D = \mu/Pr$. By modeling the viscosity with Sutherland law, it comes:

$$D^* = \frac{\mu_0}{Pr}\left(\frac{T^*}{T_0}\right)^{\alpha} \tag{2.27}$$

where $T_0 = 300\ K$ is a reference temperature and $\alpha = 0.682$.

Filtered laminar unresolved convective fluxes $\overline{\tau}_c^k$ and $\overline{\tau}_c^h$ The relative local flame displacement speed S_d defined as the difference between the absolute flow speed u and the absolute flame front speed w is introduced:

$$S_d = u - w \tag{2.28}$$

As the absolute flame front speed w remains constant across the flame brush

the filtered laminar species convective terms reads:

$$\overline{\tau}_c^k = \frac{\partial}{\partial x}\left(\overline{\rho}\left(\widetilde{S}_d\widetilde{Y_k} - \widetilde{S_dY_k}\right)\right) \tag{2.29}$$

By assuming that steady state regime is satisfied in the flame coordinate system, mass conservation implies the following relation between the laminar flame speed S_l^0, the fresh gas mixture density ρ_0 and the local displacement speed :

$$\rho S_d = \rho_0 S_l^0 \tag{2.30}$$

This can be used to compute the terms in Eq. (2.29): $\overline{\rho}\widetilde{S}_d\widetilde{Y_k} = \rho_0 S_l^0\widetilde{Y_k}$ and $\overline{\rho}\widetilde{S_dY_k} = \overline{\rho S_dY_k} = \rho_0 S_l^0\overline{Y_k}$. By introducing Y_k^*, the filtered species unresolved laminar fluxes are finally modeled as follows:

$$\overline{\tau}_c^k = \frac{\partial}{\partial x}\left(\rho_u S_l^0\left(\widetilde{Y}_k - \overline{Y_k^*}\right)\right) \tag{2.31}$$

By analogy the unresolved laminar fluxes of the energy balance equation reads:

$$\overline{\tau}_c^h = \frac{\partial}{\partial x}\left(\rho_u S_l^0\left(\widetilde{h} - \overline{h^*}\right)\right) \tag{2.32}$$

Summary of the model equations The mass, species and energy equations are finally modeled as:

$$\frac{\partial\overline{\rho}}{\partial t} + \frac{\partial\overline{\rho}\widetilde{u}}{\partial x} = 0 \tag{2.33}$$

$$\overline{\rho}\frac{\partial\widetilde{Y}_k}{\partial t} + \overline{\rho}\widetilde{u}\frac{\partial\widetilde{Y}_k}{\partial x} = \overline{\frac{\partial}{\partial x}\left((\rho D)^*\frac{\partial Y_k^*}{\partial x}\right)} + \overline{\dot{\omega}_k(T^*, Y_k^*)} + \frac{\partial}{\partial x}\left(\rho_u S_l^0\left(\widetilde{Y}_k - \overline{Y_k^*}\right)\right) \tag{2.34}$$

$$\overline{\rho}\frac{\partial\widetilde{h}}{\partial t} + \overline{\rho}\widetilde{u}\frac{\partial\widetilde{h}}{\partial x} = \overline{\frac{\partial}{\partial x}\left((\rho D)^*\frac{\partial h^*}{\partial x}\right)} + \frac{\partial}{\partial x}\left(\rho_u S_l^0\left(\widetilde{h} - \overline{h^*}\right)\right) \tag{2.35}$$

These equations are implemented into an in-house 1D flame solver, which is 1^{st} order explicit in time and 2^{nd} order in space.

2.3.2 Results

Flame solutions obtained with methods for recovering the under-resolved part (2) of the signal are analyzed first, while results which account for the unresolved part (3) of the signal are presented in a second part.

2.3.2.1 Deconvolution of under-resolved contributions

The fresh gas velocity is set to 0 at the inlet of the domain. The grid is uniform of spacing $\overline{\Delta}_x = \overline{\delta_r}/3$. The system of filtered balance equations (2.33)-(2.35) is solved in time. The computation is initialized with a filtered 1D resolved flame. The analysis focuses on three quantities: the flame consumption speed S_c^{Δ}, the filtered thermal thickness $\widetilde{\delta}_{th}$ and the maximal value of CO mass fraction $\widetilde{Y}_{CO_{max}}$.

These three quantities are plotted as a function of the dimensionless time $\tau = \delta_r / S_l^{0,ref}$ (where the reference flame velocity $S_l^{0,ref}$ is estimated from the laminar resolved flame solution) for $\gamma = 1$ and $\gamma = 5$ in Figs. 2.17, 2.18 and 2.19 for the three deconvolution methods recovering only under-resolved signals. At small filter size, the evolution of the three quantities in time is almost constant regardless of the deconvolution method used. Only small variations are observed on the thermal thickness and the maximal CO mass fraction: relative variations of respectively 2.6% and 2.7% are for example observed for thermal thickness and maximal CO mass fraction when using ADM method. The variations of the different quantities in time are significantly amplified when γ increases. The simulations exhibit spurious fluctuations up to 60 % of the flame consumption speed. This is also the case for the CO mass fraction peak and the thermal thickness. These non-physical oscillations on flame speed, CO mass fraction peak and thermal thickness when the filter size increases are due to the inability of ADM, RDM and ADEF to reconstruct enough frequencies to accurately define the deconvolved reaction rates.

The performances of the deconvolution methods are then assessed for filter sizes in the range $1 < \gamma < 10$. To simplify the analysis by still taking into account the unsteadiness of instantaneous quantities, a time-averaged flame consumption speed is hence defined:

$$< S_c^{\Delta} >= \frac{1}{T} \int_0^T S_c^{\Delta}(t) dt \tag{2.36}$$

where T is an integration time sufficiently large for $< S_c^{\Delta} >$ to be statistically converged. Note that time integration starts when the variation of flame consumption speed in time reaches a steady state. The error on the average flame

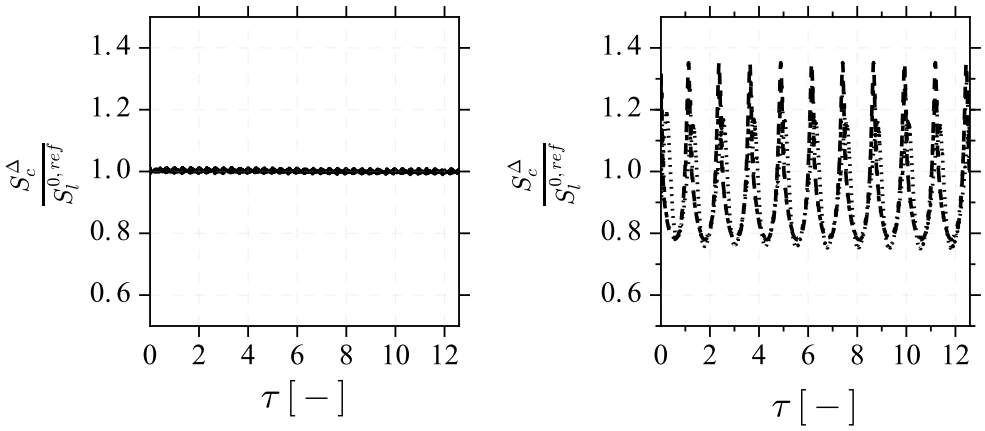

Figure 2.17: *Flame consumption velocity as a function of time for under-resolved signal deconvolution. Left:* $\gamma = 1$*. Right:* $\gamma = 5$*. Dashed lines: ADEF. Dashed-dotted lines: ADM. Dotted lines: RDM.*

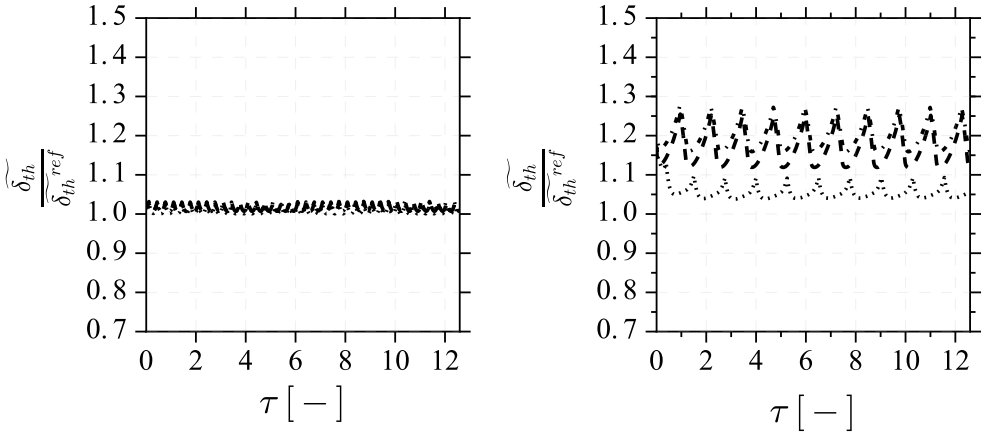

Figure 2.18: *Flame thermal thickness as a function of time for under-resolved signal deconvolution. Left:* $\gamma = 1$*. Right:* $\gamma = 5$*. Dashed lines: ADEF. Dashed-dotted lines: ADM. Dotted lines: RDM.*

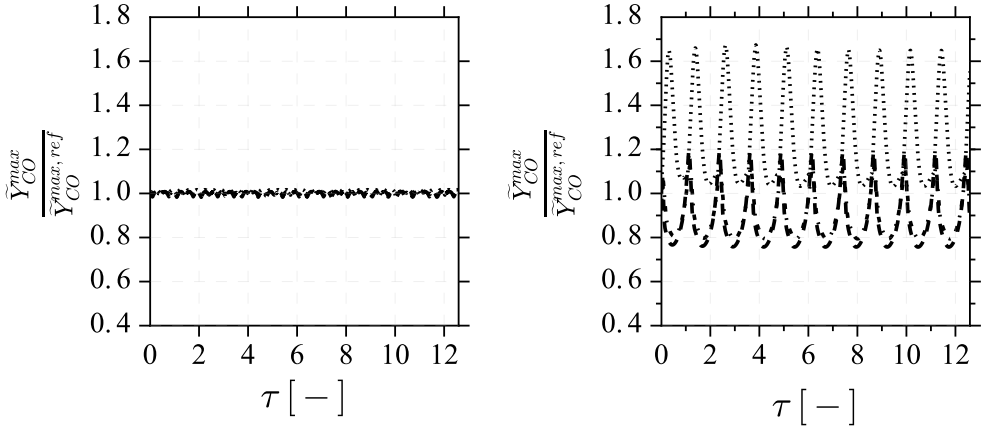

Figure 2.19: *Maximum of CO mass fraction as a function of time for under-resolved signal deconvolution. Left:* $\gamma = 1$*. Right:* $\gamma = 5$*. Dashed lines: ADEF. Dashed-dotted lines: ADM. Dotted lines: RDM.*

consumption speed with respect to the reference speed is computed as follows:

$$\varepsilon^{\Delta} = \frac{|< S_c^{\Delta} > - S_l^{0,ref}|}{S_{l,ref}^0} \tag{2.37}$$

The relative peak to peak variation of consumption speed over time is also introduced:

$$\delta S_c^{\Delta} = \frac{max\left[S_c^{\Delta}(t)\right] - min\left[S_c^{\Delta}(t)\right]}{S_{l,ref}^0} \tag{2.38}$$

As discussed in Sec. 2.2.2.1, δS_c^{Δ} is directly related to the flame resolution and is expected to increase when the flame front resolution decreases.

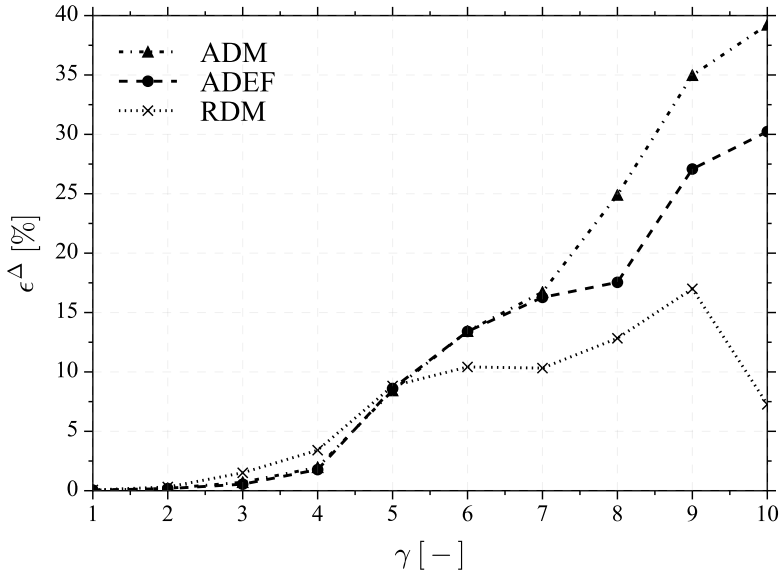

Figure 2.20: *Error on flame consumption speed ε^{Δ} as a function of γ obtained by the simulation of a one-dimensional laminar premixed flame. Triangles: Approximate Deconvolution Method. Circles: Taylor decomposition method. Cross: Regularized Deconvolution Method.*

In Fig. 2.25 and 2.26, ε^{Δ} and δS_c^{Δ}, respectively, are plotted as functions of the dimensionless flame filter size γ. When $\gamma < 4$, the methods lead to a good estimation of the mean flame speed $< S_l^0 >$, with an error below 5%. When $\gamma > 4$, the average consumption speeds predicted by ADM, ADEF and RDM deviate from the reference speed and the propagation is strongly affected by the modeling. When it comes to peak to peak flame speed fluctuations, the conclusions are similar. For $\gamma < 3$, δS_c^{Δ} is lower than 8%, meaning that it

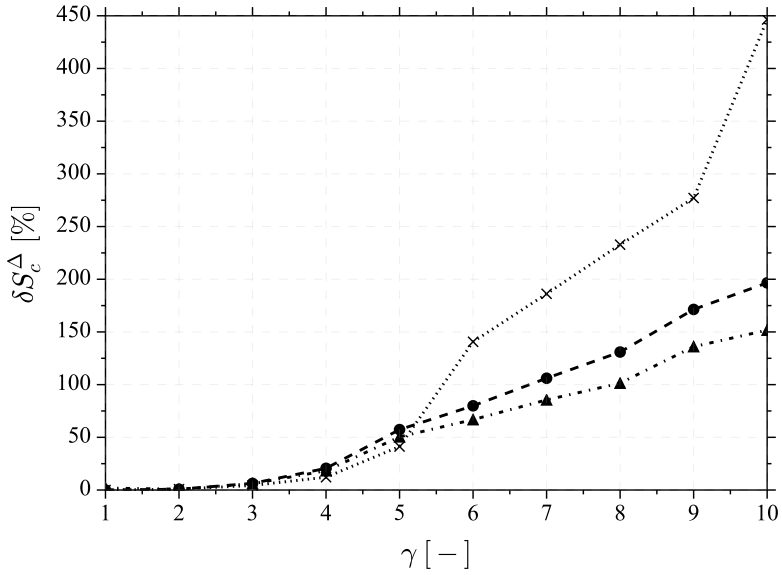

Figure 2.21: *Peak to peak variation of flame consumption speed δS_c^{Δ} as a function of γ obtained by the simulation of a 1D laminar premixed flame. Triangles: Approximate Deconvolution Method. Circles: Taylor decomposition method. Cross: Regularized Deconvolution Method. Squares: Parametric model.*

is acceptable to consider the laminar flame speed quasi-constant in time. It increases sharply for ADM, ADEF and RDM when $\gamma > 3$. Regardless of the deconvolution method used, no satisfying results are obtained for $\gamma > 4$.
A closer look at the performance of the different deconvolution methods reveals a similar behavior between ADM and ADEF. This is explained by the fact that the grids used in the simulation are coarse and only permit the representation of low frequencies. The coarse grid regularizes the deconvolution operation and the effect of the additional regularization introduced by ADM is not significant. Only a slight advantage of ADEF over ADM is seen on figure 2.26. The RDM method shows a better agreement with the average flame consumption speed but its evolution in time become very unstable as soon as $\gamma > 6$. A probable explanation lies in the ill-conditioning of the deconvolution, which makes the numerical optimization of the regularized quadratic objective function 2.18 very difficult.
It should be noted that an important difference with the article of Wang and Ihme (2016) and their implementation of the RDM methodology is the type of filter: a top-hat filter is used instead of the Gaussian filter. The condition number of the top-hat filter is very much lower than that of the Gaussian filter and hence the numerical resolution is faster and more accurate. The drawback of the box filter is that it separates low and high frequencies less efficiently than the Gaussian filter, so that in realistic LES conditions many points are still required to correctly represent filtered functions.

2.3.2.2 Deconvolution with unresolved scales modeling

Second order interpolation of the reconstructed signal Figs. 2.22, 2.23 and 2.24 compare the evolution in time of S_c^Δ, $\widetilde{\delta}_{th}$ and $\widetilde{Y}_{CO_{max}}$, respectively, when using ADM and ADM with second order interpolation at the subgrid scales. Results for $\gamma = 1$ are shown on the left of the figures while results for $\gamma = 5$ are on the right. The use of a fine reconstruction grid for representing small scales is important, as it limits the flame speed oscillations when the reactive layer crosses grid points. This corroborates the observations made on Fig. 2.2. Additionally, a stabilization of the CO peak is also seen, while it is less pronounced for the flame thermal thickness.
The effect of SGS interpolation for different filter size values is analyzed by studying the evolution of ε^Δ and δS_c^Δ with γ in Figs. 2.25 and 2.26. Deconvolution with unresolved scales modeling leads to a better prediction of the average flame speed, which remains almost constant as γ increases. Variations are also dramatically decreased, but become however non negligible when the filter size is large ($\delta S_c^\Delta \approx 20\%$ for $\gamma = 7$). Indeed, when the filter size grows, interpolation at the subgrid scales is not sufficient to represent the unresolved signal.

Parametric reconstruction of subgrid scales The temporal variations of S_c^Δ, $\widetilde{\delta}_{th}$ and $\widetilde{Y}_{CO_{max}}$ are shown in Figs. 2.27, 2.28 and 2.29. The results obtained with the parametric model are very close to the results with interpolation only, suggesting that the flame propagation improvement is due to the interpolation on the fine grid.
Error on flame consumption speed and peak to peak fluctuations are added in Fig. 2.26 and Fig. 2.25, respectively. Improvements of the results by parametric modeling observed in the *a priori* study are not significant. In practice, ill-conditioning of the deconvolution problem implies discontinuities in time of the reconstruction parameters.
Finally, the ability of deconvolution to capture the correct flame structure is studied. Steady state solutions for the flame simulations with unresolved scales modeling are shown on Fig. 2.30, 2.31 and 2.32 for $\gamma = 2$, 5 and 10 respectively. The classical ADEF, ADM and RDM deconvolution methods are very unsteady and are hence not considered here. Only the flames modeled with SGS modeling, which present low oscillations, are compared against the reference solutions. The simulations are analyzed for a physical time $t \approx 10\tau$. The comparison is made between the filtered flame computed with the deconvolution model and a filtered reference flame. All flames have been centered at $x = 0$.
For low filter sizes (case $\gamma = 2$), the flame structure is perfectly recovered. When the filter size has a medium value ($\gamma = 5$), the results are also good and

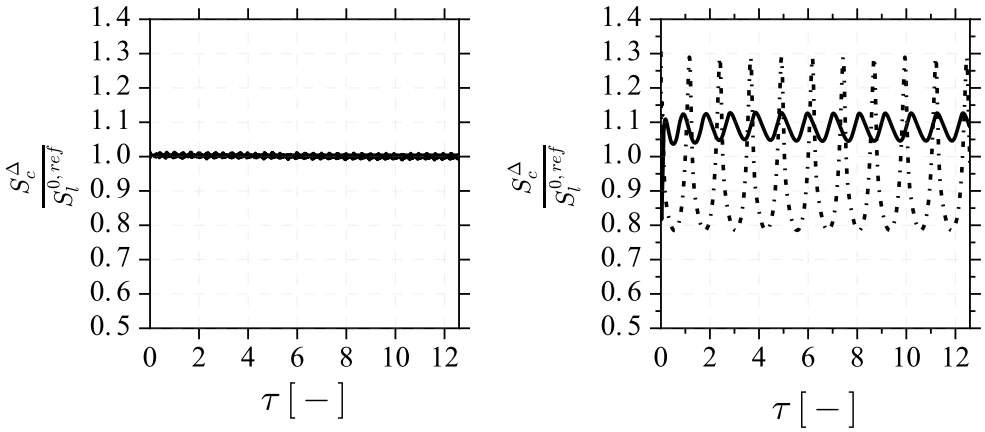

Figure 2.22: *Flame consumption velocity as a function of time for ADM method with and without SGS interpolation. Left: $\gamma = 1$. Right: $\gamma = 5$. Dashed-dotted lines: ADM. Solid lines: ADM with SGS interpolation.*

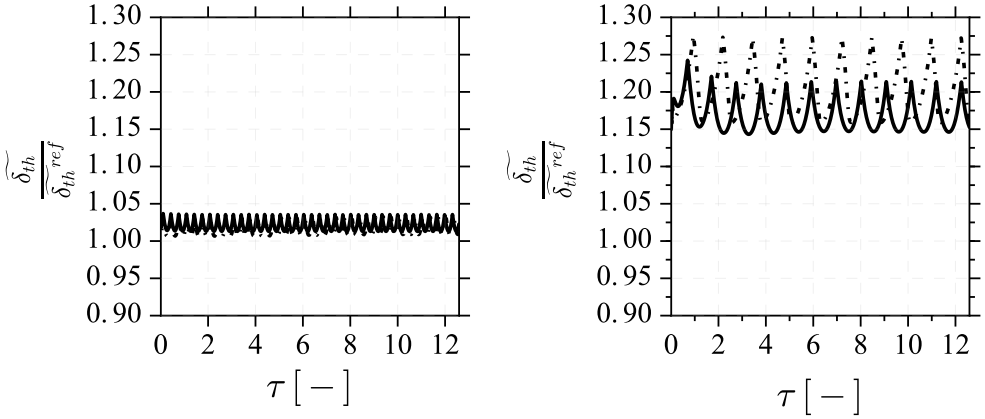

Figure 2.23: *Flame thermal thickness as a function of time for ADM method with and without SGS interpolation. Left: $\gamma = 1$. Right: $\gamma = 5$. Dashed-dotted lines: ADM. Solid lines: ADM with SGS interpolation.*

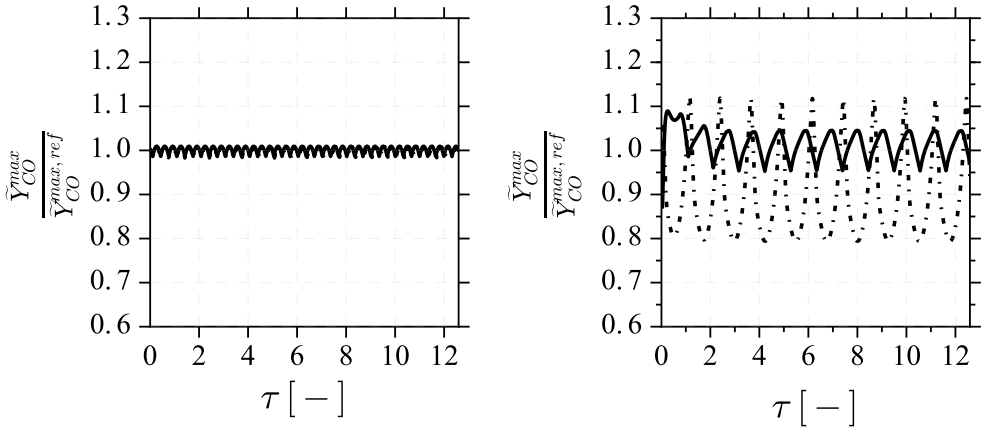

Figure 2.24: *Maximum of CO mass fraction as a function of time for ADM method with and without SGS interpolation. Left: $\gamma = 1$. Right: $\gamma = 5$. Dashed-dotted lines: ADM. Solid lines: ADM with SGS interpolation.*

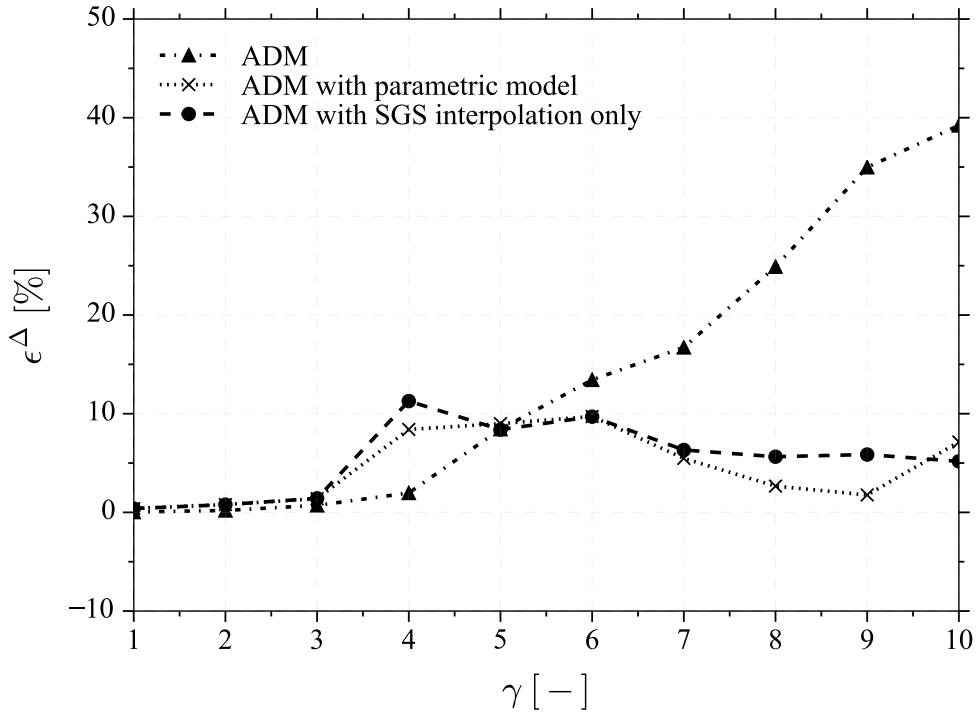

Figure 2.25: *Error on flame consumption speed ε^{Δ} as a function of γ obtained by the simulation of a one-dimensional laminar premixed flame. Triangles: Approximate Deconvolution Method. Circles: Approximate Deconvolution Method with SGS interpolation. Crosses: Approximate Deconvolution Method with SGS interpolation and the parametric model.*

both models are able to predict the correct flame. When the filter size becomes too high ($\gamma = 10$), there are strong discrepancies between the simulated and the filtered reference mass fractions. In particular, the CH_4 mass fraction takes negative values (computation is made possible by clipping these negatives values) and is hence non-physical. This is the case for SGS interpolation alone and for the parametric model. In the case of parametric modeling, errors on CO are even more important, showing that at these values of filter size, ill-conditioning of the optimization problem leads to a deterioration of the results. Larger filter sizes lead to even lower negative values. This corroborates the observations made on Fig. 2.26, where the difficulties encountered with deconvolution were revealed by the high value of δS_c^{Δ}.

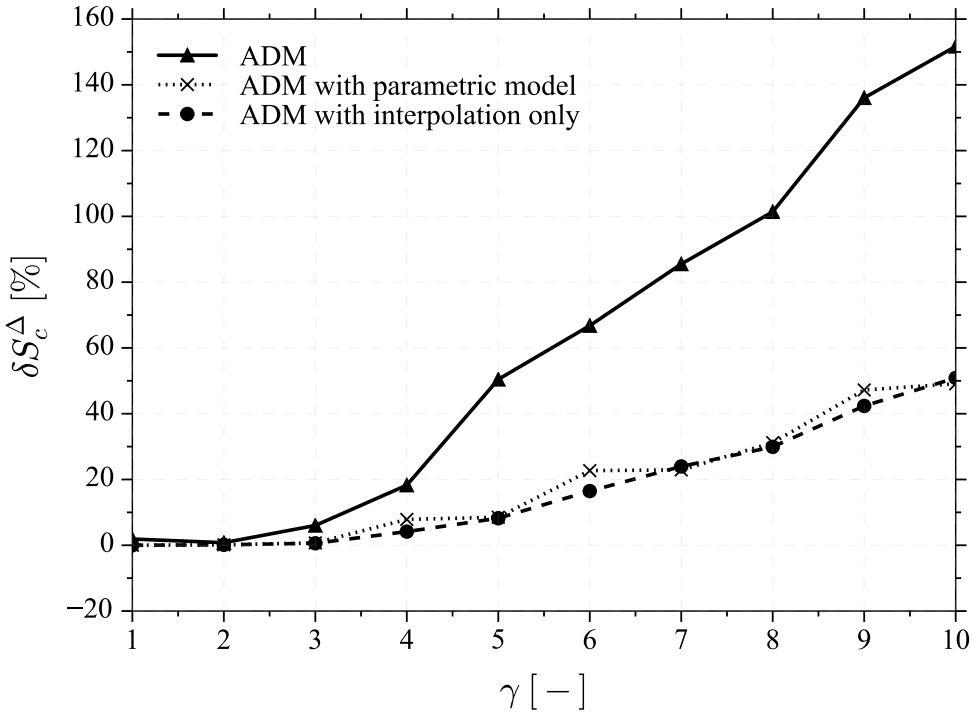

Figure 2.26: *Peak to peak variation of flame consumption speed δS_c^Δ as a function of γ obtained by the simulation of a one-dimensional laminar premixed flame. Triangles: Approximate Deconvolution Method. Circles: Approximate Deconvolution Method with SGS interpolation. Crosses: Approximate Deconvolution Method with SGS interpolation and the parametric model.*

2.4 Conclusion on the suitability of deconvolution for turbulent combustion modeling

The objective of this chapter is to assess the ability of deconvolution to capture the flame propagation and chemical structure of laminar flames in an LES context. Approximation of non-filtered reactive scalars are found by applying a deconvolution algorithm to their transported (filtered) counterparts. The analysis focuses on the deconvolution algorithm which is the critical modeling step in this new approach. It has been identified as a mathematically ill-posed problem characterized by a high condition number. For that purpose, three reconstructions methods have been challenged. The first method proposed was designed for the modeling of the sub-grid scale Reynolds stresses in non reactive LES and its extension to combustion has been tested here. Two other methods were specifically created for the closure of transport equations in a combustion context. The ADEF method uses the inversion of a Taylor decomposition of a Gaussian filter, whereas the RDM methodology solves a set of constrained and penalized quadratic functions at each iteration. These methods have been

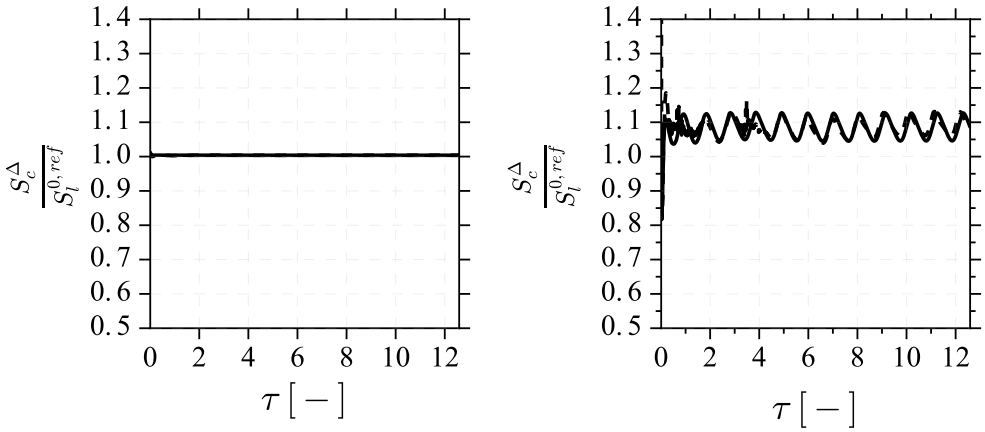

Figure 2.27: *Flame consumption velocity as a function of time for ADM method with and without parametric model. Left: $\gamma = 1$. Right: $\gamma = 5$. Dotted line: ADM with SGS interpolation only. Solid line: ADM with SGS interpolation and parametric modeling.*

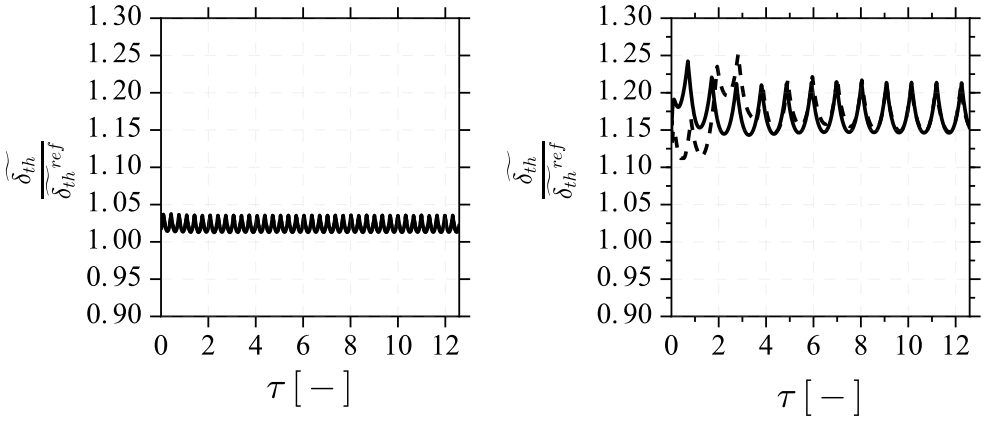

Figure 2.28: *Flame thermal thickness as a function of time for ADM method with and without parametric model. Left: $\gamma = 1$. Right: $\gamma = 5$. Dotted line: ADM with SGS interpolation only. Solid line: ADM with SGS interpolation and parametric modeling.*

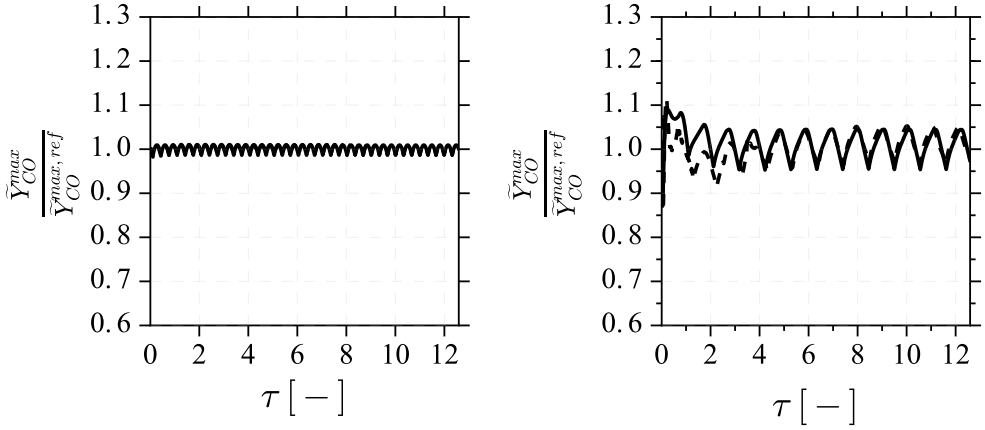

Figure 2.29: *Maximum of CO mass fraction as a function of time for ADM method with and without parametric model. Left: $\gamma = 1$. Right: $\gamma = 5$. Dotted line: ADM with SGS interpolation only. Solid line: ADM with SGS interpolation and parametric modeling.*

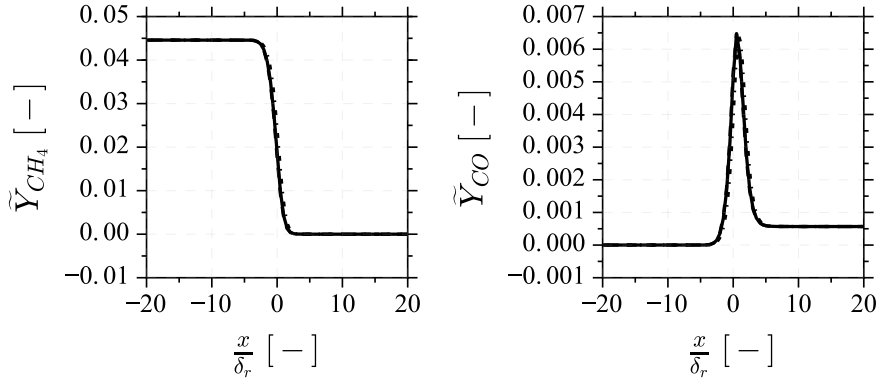

Figure 2.30: *Comparison of filtered reference and deconvolved CH_4 (left) and CO (right) mass fractions for $\gamma = 2$ and $t \approx 10\tau$. Solid lines: ADM with parametric modeling. Dashed lines: ADM with SGS interpolation only. Dashed-dotted lines: filtered reference flame.*

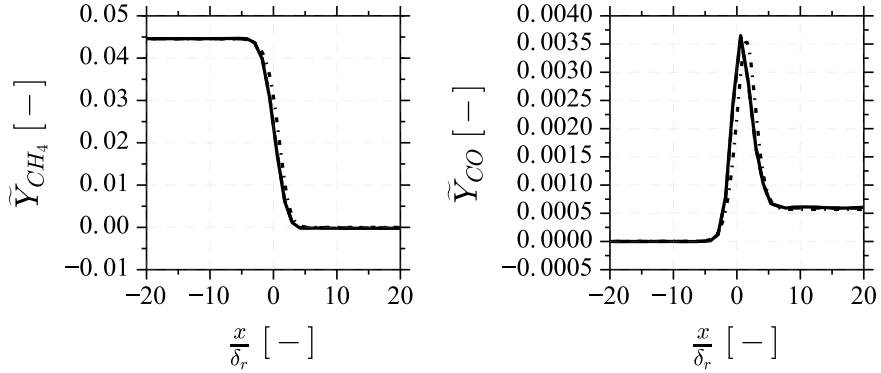

Figure 2.31: *Comparison of filtered reference and deconvolved CH_4 (left) and CO (right) mass fractions for $\gamma = 5$ and $t \approx 10\tau$. Solid lines: ADM with parametric modeling. Dashed lines: ADM with SGS interpolation only. Dashed-dotted lines: filtered reference flame.*

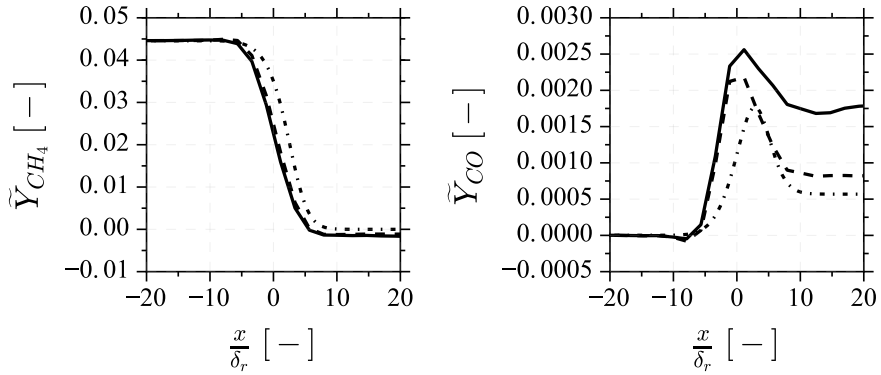

Figure 2.32: *Comparison of filtered reference and deconvolved CH_4 (left) and CO (right) mass fractions for $\gamma = 10$ and $t \approx 10\tau$. Solid lines: ADM with parametric modeling. Dashed lines: ADM with SGS interpolation only. Dashed-dotted lines: filtered reference flame.*

designed to retrieve the under-resolved part of a signal. New methodologies including the influence of small scales are proposed. The main idea is to use a specific refined grid for representing deconvolved functions. A first methodology is based on the interpolation of deconvolved variables on the fine grid. An extension is then proposed, where a parametric model for small scales is added to compensate for the remaining errors.

A laminar 1D premixed flame has been used to challenge the deconvolution methods. This simple configuration enables us to study the non-linearities due to the flame front independently from any turbulent effect. An *a priori* analysis was conducted first and showed a strong influence of the filter size on the results. When used on coarse LES grids with deconvolution methods intended to recover only the under-resolved signals, the flame propagation speed and structure deviates from the reference value when the normalized filter size γ increases. Approximation of unresolved scales by interpolation improves the result even though it mostly fails at predicting the correct flame shapes. The parametric method shows a better agreement and is in particular able to get a better prediction of the CO peak and the species reaction rates. *A priori* flame propagation predictions are however similar when using second-order interpolation or parametric modeling. *A posteriori* analysis conducted on 1-D premixed flame simulations suggest the same conclusions for the three methods that do not include small scales (RDM, ADEF and ADM). They show large variation of flame consumption speed, CO peak and thermal thickness over time. These variations increase with the flame filter size. This is explained by the under-resolution of the LES grid and its inability to represent frequencies above its Nyquist frequency. Including unresolved information using second-order interpolation and a fine grid improves the stability of the flame front propagation, even though the method fails for large filter widths. Second-order interpolations are not significantly improved by the additional parametric compensation of the error.

The main conclusion of this chapter is that unresolved scales have to be accounted for in the deconvolution process in order to retrieve the laminar flame structure. As these small scales can only be represented on fine grids, the introduction of an intermediate refined grid for deconvolved variables is necessary. Several challenges are yet to be solved to extend deconvolution to complex 3-D LES:

- The methodology presented in this chapter is valid for laminar flamelets. The implementation of small scales reconstruction in turbulent 3-D cases is an additional modeling challenge to overcome.

- Reconstruction of subgrid scales in 3-D requires the representation of deconvolved quantities on a refined grid with a DNS resolution. In

addition to expensive deconvolution and filtering steps on the refined grid, the storage of these quantities requires a large amount of memory, which will certainly be an issue.

- Modeling of subgrid scale chemistry/turbulence interactions has not been investigated here and is a key challenge for turbulent premixed combustion modeling.

In the light of these issues, an alternative methodology to include Gaussian filtering in a transported chemistry formalism is investigated in the next chapter. This methodology is based on a chemical mechanism reduction in a preprocessing step and it does not need the small scales to be reconstructed at each iteration.

Chapter 3

Filtered Optimized Chemistry

Contents

The difficulties encountered when modeling sub-grid scale contributions to balance equations with deconvolution techniques trigger the need for a more robust alternative. A new model for premixed combustion designed to reproduce filtered canonical flames is considered in this chapter. It consists in modifying the Arrhenius parameters in a suitable way by using optimization tools. Two different types of canonical flames are used in this work: the first are the widely used 1-D laminar premixed flames while the second are newly developed 1-D filtered wrinkled flamelets. A general formulation of the closure model is first presented and a focus on the specific cases of laminar premixed flamelets and filtered wrinkled flamelets is then made.

3.1 Introduction

A novel turbulent combustion modeling strategy based on deconvolution has been investigated in chapter 2. It provides a closure methodology for unclosed LES terms in a transported chemistry context with explicit Gaussian filtering of the flame front. Results showed that modeling small scales is mandatory. Such operation is feasible but too expensive in terms of computational costs for practical applications. This stems from the fact that small scales reconstructed with deconvolution require a highly refined grid to be accurately represented.

An alternative to deconvolution is presented in this chapter. The method, called Filtered Optimized Chemistry (FOC), is based on the inclusion of the filtering operation directly in the chemical mechanism. The model, summarized in Fig. 3.1, involves the following steps:

- **Step 1:** A set of reference filtered flames is built by explicitly filtering, in a pre-processing step, a library of 1-D canonical flames computed with detailed chemistry.
- **Step 2:** A reduced mechanism is selected and its Arrhenius coefficients are optimized to reproduce the set of reference filtered flames.
- **Step 3:** The LES 3-D transport equations are solved using the reduced mechanism defined by the optimized coefficients.

The flame archetype selected in **Step 1** must be representative of combustion processes taking place in the simulated 3-D systems and its choice is thus critical. Abou-Taouk et al. (2015) recently proposed to optimize the coefficients of a reduced mechanism by targeting a set of spatially filtered 1-D laminar unstretched premixed flames. The approach has been successfully validated on an industrial gas turbine in stratified flame conditions. The model of Abou-Taouk et al. (2015) is limited to well resolved LES. In particular, flame wrinkling is

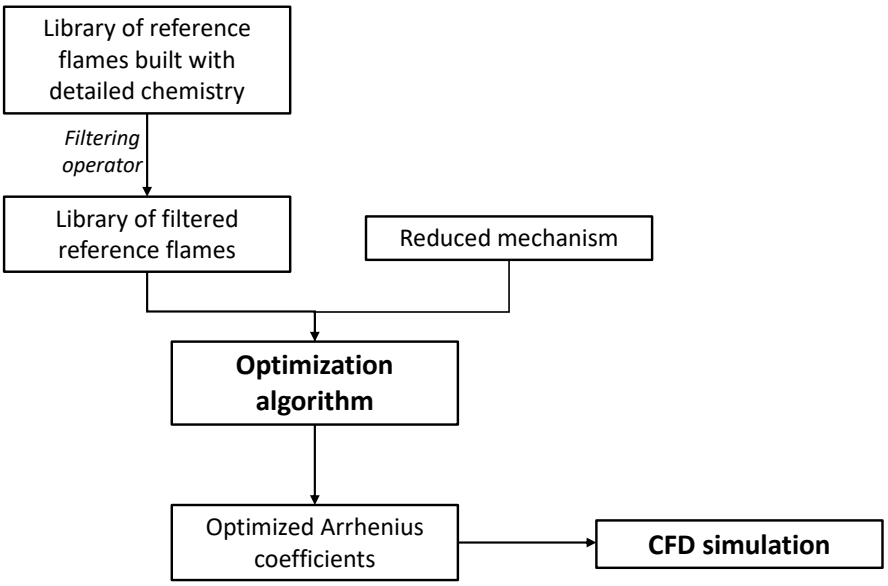

Figure 3.1: *Principle of Filtered Optimized Chemistry (FOC)*

fully resolved and the effects of subgrid scale wrinkling on the filtered flame are thus not considered in the modeling.

In practice however, LES grids are coarse and the impact of SGS flame wrinkling on the flame propagation and structure is significant (Mercier et al. (2015); Vermorel et al. (2017)). The FOC modeling approach aims at including SGS wrinkling effects on the filtered flame and thus extends the strategy of Abou-Taouk et al. (2015) to more realistic LES simulations. Unresolved wrinkling leads to an underprediction of the flame surface area and is typically tackled in premixed combustion by increasing the flame propagation speed by a wrinkling factor Ξ_Δ (Colin et al. (2000); Charlette et al. (2002a)). However, studies also suggest a strong influence of SGS wrinkling on pollutants formation (Nilsson and Bai (2002); Mercier et al. (2018)). Simulations of the swirling stabilized Cambridge flame (Sweeney et al. (2012a); Sweeney et al. (2012b)) by Mercier et al. (2018) showed that accounting for sub-filter flame wrinkling on the chemical flame structure is mandatory to predict intermediate species such as CO. The focus in this chapter is hence on the accurate prediction of intermediate pollutants formation, in particular CO, in situation where SGS wrinkling is important. Two strategies are challenged:

- **Strategy 1:** In the FOC-FPF strategy, filtering and modeling of SGS wrinkling effects are treated separately: (i) optimization is done using the FOC strategy on Filtered Planar Flames (FPF) obtained from the filtering of 1-D unstretched laminar premixed flames; (ii) the SGS

wrinkling is included ad-hoc in the transport equations by multiplying diffusive and reactive terms by a wrinkling factor Ξ_Δ.

- **Strategy 2:** The recent work developed by Mercier et al. (2018) includes effects of unresolved wrinkling on pollutant formation by defining a new flame archetype, which takes sub-grid scale flame wrinkling intrinsically into account. The model relies on the Filtered Wrinkled Flamelets (FWF) archetype, obtained first by manufacturing 2-D wrinkled flames and then by filtering them at the LES filter size. FWF has been used to build-up a filtered chemical look-up table in order to model the unclosed terms of the filtered progress variable equation. The second strategy, FOC-FWF, extends the method of Mercier et al. (2018) in a transported chemistry context by performing the mechanism reduction on FWF flames.

The FOC modeling framework is detailed in Sec. 3.2 and the FOC-FPF and FOC-FWF strategies are explained in Sec. 3.3 and 3.4, respectively. Finally, a summary of the model equations used in this work is provided in Sec. 3.5.

3.2 Filtered Optimized Chemistry for LES of turbulent flames

The model equations of the FOC strategy are presented in this section. The general formulation is detailed in Sec. 3.2.1. The chemical formalism used in this work is then presented in Sec. 3.2.2, and the FOC model is consequently adapted to account for the specific assumptions made in this formalism.

3.2.1 General methodology

3.2.1.1 Transport equations

A Low-Mach number assumption is used throughout the work and equations are written in this context. The flow field is computed with standard techniques using a LES solver. Scalars are transported using the following filtered equations:

$$\frac{\partial \overline{\rho}\widetilde{Y_k}}{\partial t} + \nabla \cdot \left(\overline{\rho}\widetilde{u}\widetilde{Y_k}\right) = \overline{\mathrm{RHS}_k(\mathbf{\Phi})} \tag{3.1}$$

$$\frac{\partial \overline{\rho}\widetilde{h}}{\partial t} + \nabla \cdot \left(\overline{\rho}\widetilde{u}\widetilde{h}\right) = \overline{\mathrm{RHS}_h(\mathbf{\Phi})} \tag{3.2}$$

where $\mathbf{\Phi} = (P, T, Y_1, ..., Y_N)$ is the thermo-chemical state. The unclosed filtered

Right Hand Sides $\overline{\mathrm{RHS}_k(\mathbf{\Phi})}$ and $\overline{\mathrm{RHS}_h(\mathbf{\Phi})}$ read:

$$\overline{\mathrm{RHS}_k(\mathbf{\Phi})} = \overline{\nabla \cdot (\rho D_k \nabla Y_k)} + \overline{\tau}_c^k + \overline{\rho}\widetilde{\dot{\omega}}_k \tag{3.3}$$

$$\overline{\mathrm{RHS}_h(\mathbf{\Phi})} = \overline{\nabla \cdot \left(\lambda \nabla T + \sum_{k=1}^{N_S} \rho D_k h_k \nabla Y_k \right)} + \overline{\tau}_c^h \tag{3.4}$$

Where the unclosed convective terms $\overline{\tau}_c^k$ and $\overline{\tau}_c^h$ are:

$$\overline{\tau}_c^k = -\nabla \cdot \left(\overline{\rho u Y_k} - \overline{\rho}\widetilde{u}\widetilde{Y}_k \right) \tag{3.5}$$

$$\overline{\tau}_c^h = -\nabla \cdot \left(\overline{\rho u h} - \overline{\rho}\widetilde{u}\widetilde{h} \right) \tag{3.6}$$

The set of Arrhenius parameters defining the reactions rates $\dot{\omega}_k$ ($k = 1..N_S$) is formally written $\mathcal{A}$ and the exact filtered reaction rate is expressed as:

$$\overline{\rho}\widetilde{\dot{\omega}}_k = \overline{\rho}\widetilde{\dot{\omega}}_k^{\mathcal{A}} = \overline{W_i \sum_{j=1}^{N_R} A_j \left(\nu_{kj}^b - \nu_{kj}^f \right) \prod_{i \in \mathcal{S}_j} \left(\frac{\rho Y_i}{W_i} \right)^{n_{ij}} \exp\left(\frac{-E_{a,j}}{\mathcal{R}T} \right)} \tag{3.7}$$

where $\mathcal{A} = [A_j, n_{ij}, E_{a,j}]$ contains the pre-exponential factors, the activation energies and the reaction orders defining the mechanism. Because of non-linearity of the terms that compose Eqs. (3.3) and (3.4), the RHS cannot be directly estimated from the filtered thermochemical variable (Poinsot and Veynante (2005)): $\overline{\mathrm{RHS}_k(\mathbf{\Phi})} \neq \mathrm{RHS}_k(\overline{\mathbf{\Phi}})$ and $\overline{\mathrm{RHS}_h(\mathbf{\Phi})} \neq \mathrm{RHS}_h(\overline{\mathbf{\Phi}})$. The concept of Filtered Optimized Chemistry (FOC) is to identify functions RHS_k^* and RHS_h^*, which verify $\overline{\mathrm{RHS}_k(\mathbf{\Phi})} = \mathrm{RHS}_k^*(\overline{\mathbf{\Phi}})$ and $\overline{\mathrm{RHS}_h(\mathbf{\Phi})} = \mathrm{RHS}_h^*(\overline{\mathbf{\Phi}})$. The following formulations of the RHS are retained for that purpose:

$$\mathrm{RHS}_k^* = \nabla \cdot \left(\overline{\rho}\alpha^* \widetilde{D}_k \nabla \widetilde{Y}_k \right) + \overline{\rho}\widetilde{\dot{\omega}}_k^{\mathcal{A}^*} \tag{3.8}$$

$$\mathrm{RHS}_h^* = \nabla \cdot \left(\alpha^* \widetilde{\lambda} \nabla \widetilde{T} + \sum_{k=1}^{N_S} \overline{\rho}\alpha^* \widetilde{D}_k h_k \nabla \widetilde{Y}_k \right) \tag{3.9}$$

with

$$\overline{\rho}\widetilde{\dot{\omega}}_k^{\mathcal{A}^*} = W_i \sum_{j=1}^{N_R} A_j^* \left(\nu_{kj}^b - \nu_{kj}^f\right) \prod_{i \in \mathcal{S}_j} \left(\frac{\overline{\rho}\widetilde{Y}_i}{W_i}\right)^{n_{ij}^*} \exp\left(\frac{-E_{a,j}^*}{\mathcal{R}\widetilde{T}}\right) \tag{3.10}$$

Variables with * superscripts are model parameters: α^* is constant in space and identical for each species and $\mathcal{A}^* = (A_j^*, E_{a,j}^*, n_{ij}^*)$ where A_j^* are the pre-exponential constants, $E_{a,j}^*$ the activation energies and n_{ij}^* the reaction orders of the modeled chemical mechanism. The final set of equations reads:

$$\frac{\partial \overline{\rho}\widetilde{Y}_k}{\partial t} + \nabla \cdot \left(\overline{\rho}\widetilde{u}\widetilde{Y}_k\right) = \nabla \cdot \left(\overline{\rho}\alpha^* \widetilde{D}_k \nabla \widetilde{Y}_k\right) + \overline{\rho}\widetilde{\dot{\omega}}_k^{\mathcal{A}^*} \tag{3.11}$$

$$\frac{\partial \overline{\rho}\widetilde{h}}{\partial t} + \nabla \cdot \left(\overline{\rho}\widetilde{u}\widetilde{h}\right) = \nabla \cdot \left(\alpha^* \widetilde{\lambda} \nabla \widetilde{T} + \sum_{k=1}^{N_S} \overline{\rho}\alpha^* \widetilde{D}_k h_k \nabla \widetilde{Y}_k\right) \tag{3.12}$$

This system of equations is closed if models for the Arrhenius coefficients $\mathcal{A}^*$ and the diffusive correction term α^* are provided. A methodology is proposed in the following section to estimate $\mathcal{A}^*$ and α^*.

3.2.1.2 Optimization of model parameters

Optimization problem The model parameters $\mathcal{A}^*$ and α^* are optimized with a genetic algorithm (Cailler et al. (2017)). A library of reference filtered flames is assumed to be dependent on a set of parameters $\mathbf{p} = (p_1, p_2, ...)$. Reference flames are written with a superscript *ref*. The objective function for a flame defined by parameters $\mathbf{p}$ reads:

$$\begin{aligned}\mathcal{F}_{\mathbf{p}}\left(\mathcal{A}^*(\mathbf{p}), \alpha^*(\mathbf{p})\right) = & \underbrace{\sum_{\varphi} \frac{\|\widetilde{\varphi}\left(\mathcal{A}^*(\mathbf{p}), \alpha^*(\mathbf{p})\right) - \widetilde{\varphi}^{ref}(\mathbf{p})\|_2}{\|\widetilde{\varphi}^{ref}(\mathbf{p})\|_2}}_{\text{Fit on thermo-chemical variables}} \\ & + \underbrace{\beta \sum_{f_\varphi} \frac{\mid \widetilde{f}_\varphi\left(\mathcal{A}^*(\mathbf{p}), \alpha^*(\mathbf{p})\right) - f_\varphi^{ref}(\mathbf{p}) \mid}{f_\varphi^{ref}(\mathbf{p})}}_{\text{Fit on variables properties}}\end{aligned} \tag{3.13}$$

where φ are targeted thermo-chemical variables, such as temperature or mass fractions, and f_φ are properties related to thermo-chemical variables, such as the maximal value of a pollutant or the flame consumption speed. The second term in Eq. (3.13) is used to enforce specific physical constraints on the

optimized flames. The minimization problem to solve is then:

$$\min_{(\mathcal{A}^*(\mathbf{p}),\alpha^*(\mathbf{p}))} \mathcal{F}_{\mathbf{p}}\left(\mathcal{A}^*(\mathbf{p}),\alpha^*(\mathbf{p})\right) \tag{3.14}$$

There are two ways for evaluating the parameters: (i) solve separately the optimization problems (3.14) for each value of $\mathbf{p}$; (ii) solve a joint problem where the optimization on the whole set of reference flames defined by parameters $\mathbf{p}$ is done in a single step. In the latter case, the minimization formally reads:

$$\min_{(\boldsymbol{\mathcal{A}}^*,\boldsymbol{\alpha}^*)} \sum_{\mathbf{p}} \mathcal{F}_{\mathbf{p}}\left(\mathcal{A}^*(\mathbf{p}),\alpha^*(\mathbf{p})\right) \tag{3.15}$$

where $\boldsymbol{\mathcal{A}}^*$ and $\boldsymbol{\alpha}^*$ are matrices of parameters with columns respectively filled with $\mathcal{A}^*(\mathbf{p})$ and $\alpha^*(\mathbf{p})$ for each flame parameter $\mathbf{p}$. Separate solving of the optimization problems has been retained throughout this work in order to simplify the algorithmic implementation.

Optimization tool As classically done in combustion kinetics, optimization problem (3.14) is solved using genetic optimization (Cailler et al. (2017); Harris et al. (2000); Polifke et al. (1998)). The genetic optimization algorithm, developed by Cailler et al. (2016), is coupled to the 1-D flame solver REGATH in order to compute the flame thermo-chemical variables in the objective function (3.13).

3.2.2 Chemical scheme formalism

The virtual chemical mechanism is retained as a basis for the optimization procedure detailed in Sec. 3.2.1. This new type of chemistry description, initially proposed by Cailler et al. (2016), recovers only thermo-chemical variables of interest, reducing the complexity of the optimization problem (3.14). The specific case of CH_4/air mixtures combustion is considered here.

The chemical scheme developed by Cailler et al. (2017) is composed of a main mechanism for temperature and heat release predictions and complementary independent virtual sub-mechanisms devoted to the prediction of pollutant species such as CO, NOx or soot precursors (PAH). By dedicating each sub-mechanism to a unique pollutant prediction, this approach enables an efficient separation between slow and rapid chemical time scales. The specific case of CO prediction is treated here (Cailler et al. (2018)).

Main mechanism The main scheme is designed to reproduce temperature profiles and laminar flame speed of flames computed with detailed chemistry.

The reference flames are computed with differential diffusion so that the resulting flame speeds include the influence of this phenomenon. The scheme consists in the following two-step mechanism:

$$\alpha_F F + \alpha_{Ox} Ox \rightarrow \alpha_I I \tag{R1}$$

$$\alpha_I I \rightarrow \sum_{k=1}^{N_p} \alpha_{P_k} P_k \tag{R2}$$

where N_p is the number of products, which will be set to 4 in this work. This choice enables to correctly capture laminar flame speeds over a wide range of equivalence ratios (Cailler et al. (2016)). The reactive mixture is composed of the fuel (F), the oxidizer (Ox) and an inert dilutant (D). Products of the reaction are a set of virtual species (P_k). The rates of progress w_1 and w_2 of reactions (R1) and (R2), respectively, are expressed as:

$$\begin{cases} w_1 = k_1 [F]^{F_{F,1}} [Ox]^{F_{Ox,1}} & \text{(3.16a)} \\ w_2 = k_2 [I]^{F_{I,2}(\phi)} & \text{(3.16b)} \end{cases}$$

with

$$\begin{cases} k_1 = A_1(\phi) exp\left(\dfrac{-E_{a,1}}{RT}\right) & \text{(3.17a)} \\ k_2 = A_2 exp\left(\dfrac{-E_{a,2}}{RT}\right) & \text{(3.17b)} \end{cases}$$

where A_r and $E_{a,r}$ are the pre-exponential constant and the activation energy of reaction r, and $F_{k,r}$ is the forward reaction order of species k in reaction r. The pre-exponential constant A_1 and $F_{I,2}$ are varying functions of the equivalence ratio ϕ (alternatively the mixture fraction) in order to capture the flame profiles and flame speeds over a wide range of operating conditions.
The thermo-chemical parameters of the virtual species are set so that global properties of mixtures match the temperature dependent properties of corresponding real reactive mixtures. For fuel, oxidizer and dilutant, the real thermodynamic and transport properties are attributed. As for the products, the stoechiometric coefficients α_k and the thermo-chemical parameters are optimized so that equilibirum mean properties of the mixture are retrieved. Details for the design of the virtual mechanism can be found in Cailler et al. (2016) and Cailler et al. (2018). Regarding transport properties, the diffusivity is modelled with a unity Lewis assumption $\rho D_k = \rho D = \lambda / C_p$. D is computed using a Sutherland's type law: $D = \frac{\mu_0}{Pr} \left(\frac{T}{T_0}\right)^{\alpha}$, where $\alpha = 0.682$, $T_0 = 300\ K$,

$\mu_0 = 1.8071 \times 10^{-4}\ kg.s^{-1}.m^{-1}$ and $Pr = 0.68$.

CO sub-mechanism A sub-mechanism for CO has been recently introduced by Cailler et al. (2018). A modified version of this mechanism considering two steps instead of three is used here (Cailler et al. (2017)). This choice is justified by the fact that the third reaction aims at improving predictions in rich and purely non-premixed conditions, which will not be considered in this work. The set of reactions reads:

$$\alpha_F F + \alpha_{Ox} Ox \rightarrow CO \tag{R3}$$
$$CO \rightleftharpoons V_1 \tag{R4}$$

Where V_1 is a virtual species. The rate of progress of reaction (R3) is identical to the one of reaction (R1) to enforce consistency between main and secondary mechanisms. The rates of progress w_3 and w_4 of reactions (R3) and (R4) read:

$$\begin{cases} w_3 = k_3 [F]^{F_{F,3}} [Ox]^{F_{Ox,3}} & \text{(3.18a)} \\ w_4 = k_4 \left([CO]^{F_{CO,4}} [V1]^{F_{V1,4}} - \dfrac{[CO]^{R_{CO,4}} [V1]^{R_{V1,4}}}{K_{e,4}} \right) & \text{(3.18b)} \end{cases}$$

with

$$\begin{cases} k_3 = A_3(\phi) exp\left(\dfrac{-E_{a,3}}{RT} \right) & \text{(3.19a)} \\ k_4 = A_4(\phi) exp\left(\dfrac{-E_{a,4}}{RT} \right) & \text{(3.19b)} \end{cases}$$

where A_r and $E_{a,r}$ are the pre-exponential constant and activation energy of reaction r, and $F_{k,r}$, $R_{k,r}$ are respectively the forward and reverse reaction order of species k in reaction r. $K_{e,4}$ is the equilibrium constant of (R4). Its derivation is detailed in Cailler et al. (2018). The fuel and oxidizer species involved in reaction (R4) are assumed equal to their counterparts in reaction (R1) and hence the following equalities hold: $A_3 = A_1$, $E_{a,3} = E_{a,1}$, $F_{F,3} = F_{F,1}$ and $F_{Ox,3} = F_{Ox,1}$. Reaction orders are moreover linked together by the following relations: $R_{CO,4} = F_{CO,4} - 1$ and $R_{V1,4} = F_{V1,4} + 1$ (Cailler et al. (2018)).

3.2.3 FOC modeling applied to virtual chemistry

The specific modeling choices related to the coupling between the general Filtered Optimized Chemistry model presented in Sec. 3.2.1 and virtual chemistry are provided in this section. In particular, the optimization procedure is split into two parts: (i) parameters of the filtered main scheme are computed; (ii)

parameters of the filtered CO sub-scheme are computed. Premixed flames are considered in this thesis, therefore a consumption speed may be defined.

Optimization of main scheme The main scheme parameters are optimized to fit Favre-filtered temperature and propagation speed of a series of filtered reference flames computed with the detailed GRI3.0 mechanism. This leads to the following objective function:

$$\mathcal{F}_{\mathbf{p}}^{T}\left(\mathcal{A}_T^*(\mathbf{p}),\alpha_T^*(\mathbf{p})\right) = \frac{\|\widetilde{T}\left(\mathcal{A}_T^*(\mathbf{p}),\alpha_T^*(\mathbf{p})\right)-\widetilde{T}^{ref}(\mathbf{p})\|_2}{\|\widetilde{T}^{ref}(\mathbf{p})\|_2} + \beta_T \frac{\mid S_c\left(\mathcal{A}_T^*(\mathbf{p}),\alpha_T^*(\mathbf{p})\right)-S_c^{ref}(\mathbf{p})\mid}{S_c^{ref}(\mathbf{p})} \quad (3.20)$$

where the superscript T refers to parameters related to the main mechanism and S_c and S_c^{ref} are respectively the optimized and reference flame consumption speeds, defined as

$$S_c^{ref} = \frac{1}{\rho_u(Y_{fuel}^b - Y_{fuel}^u)}\int_{-\infty}^{+\infty}\overline{\rho}^{ref}\widetilde{\dot{\omega}}_{fuel}^{ref}(x)dx \quad (3.21)$$

$$S_c = \frac{1}{\rho_u(Y_{fuel}^b - Y_{fuel}^u)}\int_{-\infty}^{+\infty}\overline{\rho}\widetilde{\dot{\omega}}_{fuel}^{\mathcal{A}_T^*}(x)dx \quad (3.22)$$

where $\widetilde{\dot{\omega}}_{fuel}^{ref}$ and $\widetilde{\dot{\omega}}_{fuel}^{\mathcal{A}_T^*}$ are the fuel reaction rates of respectively the reference filtered flame and the optimized filtered flame. The propagation speeds are not necessarily equal to the laminar flame speed and may include the influence of subgrid scale wrinkling. β_T is set to 0.01. The Arrhenius constants and reaction orders to optimize are:

$$\mathcal{A}_T^* = \left(A_1^*, E_{a,1}^*, F_{F,1}^*, F_{Ox,1}^*, A_2^*, E_{a,2}^*, F_{I,2}^*\right) \quad (3.23)$$

This set of 7 parameters, along with diffusive correction α_T^* are optimized with a genetic algorithm.

Optimization of CO sub-scheme A second optimization is performed to select CO sub-scheme parameters. In this optimization, the Favre-filtered CO mass fraction is set as a target, and the prediction of the peak is enforced by an additional term:

$$\mathcal{F}_{\mathbf{p}}^{CO}\left(\mathcal{A}_{CO}^{*}(\mathbf{p}),\alpha_{CO}^{*}(\mathbf{p})\right)=\frac{\|\widetilde{Y}_{CO}\left(\mathcal{A}_{CO}^{*}(\mathbf{p}),\alpha_{CO}^{*}(\mathbf{p})\right)-\widetilde{Y}_{CO}^{ref}(\mathbf{p})\|_2}{\|\widetilde{Y}_{CO}^{ref}(\mathbf{p})\|_2} + \beta_{CO}\frac{|\left[\widetilde{Y}_{CO}\right]^{max}\left(\mathcal{A}_{CO}^{*}(\mathbf{p}),\alpha_{CO}^{*}(\mathbf{p})\right)-\left[\widetilde{Y}_{CO}^{ref}(\mathbf{p})\right]^{max}|}{\left[\widetilde{Y}_{CO}^{ref}(\mathbf{p})\right]^{max}} \quad (3.24)$$

where $[Y_{CO}]^{max}$ refers to the maximal value of the CO mass fraction profile. β_{CO} is set to 1. The optimized Arrhenius parameters are:

$$\mathcal{A}_{CO}^{*}=\left(A_4^{*},E_{a,4}^{*},F_{CO,4}^{*},F_{V1,4}^{*}\right) \quad (3.25)$$

Note the diffusive correction α_{CO}^{*} different from α_T^{*}, allowed to account for differences in the thickening effect of the filter on T and Y_{CO}.

3.2.4 Choice of reference flames archetypes

The choice of the reference canonical filtered flames used for optimizing the model parameters $\mathcal{A}^{*}$ and α^{*} is at the heart of the model. These flames are defined by a set of parameters $\boldsymbol{p}$. The model performance and its suitability to different configurations is expected to depend strongly on the choice of the reference flame library. Two flame archetypes are retained in this work:

- **Filtered Planar Flames (FPF):** They are obtained from the explicit filtering of laminar 1-D unstretched premixed flames. Within this approach, the set of parameters defining the reference filtered flames is reduced to the equivalence ratio: $\boldsymbol{p}=\phi$. The FPF flame archetype has previously been used as an optimization target in the work Abou-Taouk et al. (2015) for a stratified flame in a semi-industrial gas turbine and has led to promising results in a situation where flame front wrinkling is fully resolved. The detailed description of the FPF reference library and optimization results in 1-D are provided in Sec. 3.3.

- **Filtered Wrinkled Flamelets (FWF):** FWF flamelets are proposed in the work of Mercier et al. (2018) and are representative of the sub-grid turbulent flame structure encountered for various level of sub-grid flame wrinkling. The FWF flame archetype is defined by the equivalence ratio and by parameters describing the flame subgrid wrinkling patterns. FWF flames are further described in Sec. 3.4 along with results on 1-D cases.

3.3 Filtered Optimized Chemistry with Filtered Planar Flames (FOC-FPF)

The first solution to build-up the filtered optimized scheme is to isolate the impact of sub-grid scale wrinkling from the filtering process. The identification of diffusion and kinetic rate parameters is then split in two steps:

- A collection of 1-D freely propagating laminar flames is first computed for various equivalence ratios ϕ by using a detailed chemical scheme and then filtered in the spatial dimension with a Gaussian filter of size Δ. This collection of Filtered Planar Flames (FPF) provides the filtered reference thermo-chemical quantities $\widetilde{\varphi}_{\text{FPF}} = \widetilde{\varphi}_{\text{FPF}}(x, \phi, \Delta)$ on which the filtered optimized scheme is trained. This step leads to the identification of parameters $\mathcal{A}^*_{\text{FPF}} = (A^*_{j,\text{FPF}}, E^*_{a,j,\text{FPF}}, n^*_{ij,\text{FPF}})$ and α^*_{FPF}, function of ϕ and Δ.

- The introduction of sub-grid scale flame wrinkling Ξ_Δ is done *a posteriori* by multiplying pre-exponential constants and the diffusive correction coefficient by Ξ_Δ: $\mathcal{A}^* = (\Xi_\Delta A^*_{j,\text{FPF}}, E^*_{a,j,\text{FPF}}, n^*_{ij,\text{FPF}})$ and $\alpha^* = \Xi_\Delta \alpha^*_{\text{FPF}}$. This operation, which is common in many turbulent LES combustion model (Poinsot and Veynante (2005); Colin et al. (2000)) does not affect the filtered flame structure but ensures that the filtered flame front propagates at a speed $S_c = \Xi_\Delta S^0_l$, where S^0_l is the unstretched laminar flame speed. However, as pointed out in Mercier et al. (2018), this assumption includes biases in the prediction of some pollutant, such as CO. To address this issue, the wrinkling patterns can be included in the filtering process, as proposed in Sec. 3.4.

The reference FPF library creation is detailed in Sec. 3.3.1, while the optimization results and comparison with 1-D reference flames are provided in Sec. 3.3.2. Some elements for analysing the newly developed mechanism are given in Sec. 3.3.3. The methodology for including subgrid scale wrinkling effects which will be assessed on a 3-D case in chapter 4 is finally illustrated in Sec. 3.3.4.

3.3.1 Building Filtered Planar Flames (FPF) reference library

The reference FPF flames are solved by considering the following 1-D steady-state equations:

$$\rho u = cte = \rho_u S^0_l \tag{3.26}$$

$$\rho u \frac{dY_k}{dx} = \frac{d}{dx}\left(\rho D_k \frac{dY_k}{dx}\right) + \rho \dot{\omega}_k \tag{3.27}$$

$$\rho u \frac{dh}{dx} = \frac{d}{dx}\left(\lambda \frac{dh}{dx}\right) + \frac{d}{dx}\left(\sum_{k=1}^{N_S} \rho D_k h_k \frac{dY_k}{dx}\right) \tag{3.28}$$

Reaction rates are computed with the GRI3.0 mechanism. Detailed transport coefficients, including the effect of differential diffusion, are used. The flame propagates at the laminar flame speed S_l^0 and no information about subgrid scale wrinkling is taken into account in FPF. Computations are performed with the REGATH solver (Darabiha (1992)).

The FPF flame structure is then estimated by filtering the 1-D laminar premixed flame with the Gaussian filter $G_\Delta(\mathbf{x}) = \sqrt{\frac{6}{\pi\Delta^2}} exp\left(\frac{-6\mathbf{x}^2}{\Delta^2}\right)$:

$$\widetilde{Y}_k = \frac{G_\Delta * (\rho Y_k)}{G_\Delta * \rho} \tag{3.29}$$

$$\widetilde{T} = \frac{G_\Delta * (\rho T)}{G_\Delta * \rho} \tag{3.30}$$

3.3.2 FPF library optimization

Computing filtered flames during optimization The optimization procedure is illustrated in Fig. 3.2. Repeated calls to the 1-D flame solver REGATH are done during the optimization step. The following steady state equations are solved:

$$\overline{\rho}\widetilde{u} = cte = \rho_u S_l^0 \tag{3.31}$$

$$\overline{\rho}\widetilde{u}\frac{d\widetilde{Y}_k}{dx} = \frac{d}{dx}\left(\overline{\rho}\alpha^* \widetilde{D}_k \frac{d\widetilde{Y}_k}{dx}\right) + \overline{\rho}\widetilde{\dot{\omega}}_k^{\mathcal{A}^*} \tag{3.32}$$

$$\overline{\rho}\widetilde{u}\frac{d\widetilde{h}}{dx} = \frac{d}{dx}\left(\alpha^* \widetilde{\lambda}\frac{d\widetilde{h}}{dx}\right) + \frac{d}{dx}\left(\sum_{k=1}^{N_S} \overline{\rho}\alpha^* \widetilde{D}_k h_k \frac{d\widetilde{Y}_k}{dx}\right) \tag{3.33}$$

where the reaction rates are evaluated using the virtual mechanism and transport coefficient are computed assuming unity Lewis numbers.

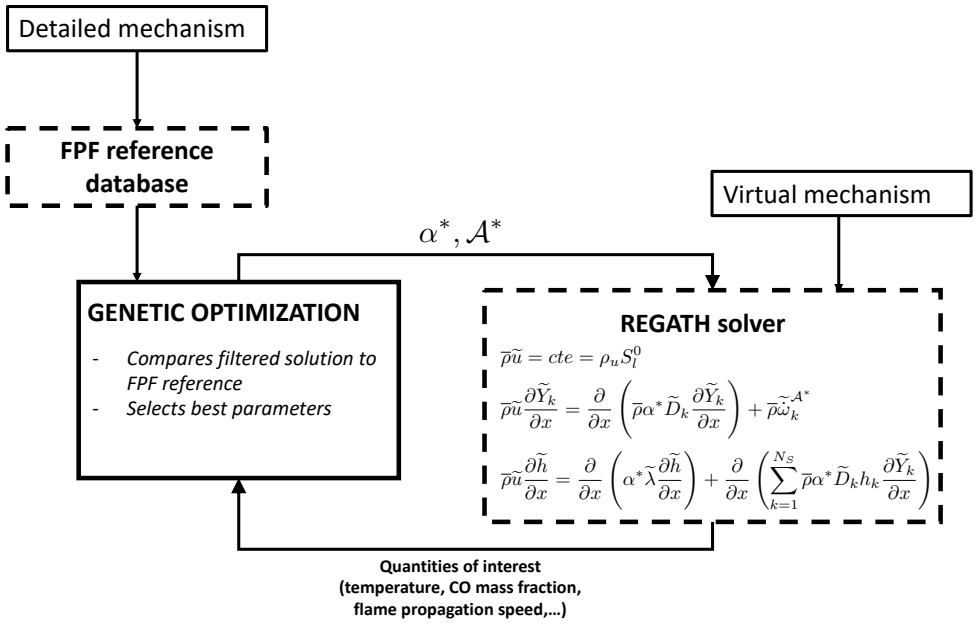

Figure 3.2: *Scheme of the parameters optimization procedure.*

Temperature optimization The mechanism is first optimized for an equivalence ratio $\phi = 0.75$[1]. The resulting parameters are shown in Tab. 3.1. The associated diffusive correction is $\alpha_T^{*,\mathrm{FPF}}(\phi = 0.75) = 3.3$. Superscripts FPF refer to values obtained by targeting Filtered Planar Flames.

Table 3.1: *Filtered temperature mechanism for* $\Delta = 4\delta_l^0$ *and* $\phi = 0.75$.

	Arrhenius constants		Reaction orders	
Reaction	$\boldsymbol{A_i^{*,\mathrm{FPF}}}$	$\boldsymbol{E_{a,i}^{*,\mathrm{FPF}}}$	**Name**	**Value**
(R1)	1.47×10^{18}	4.25×10^4	$\boldsymbol{F_{F,1}^{*,\mathrm{FPF}}}$	1.81
			$\boldsymbol{F_{Ox,1}^{*,\mathrm{FPF}}}$	0.64
(R2)	4.39×10^{18}	8.37×10^4	$\boldsymbol{F_{I,2}^{*,\mathrm{FPF}}}$	1.78

[1]This value is selected as it corresponds to the mean equivalence ratio of the Cambridge burner simulated in chapter 4.

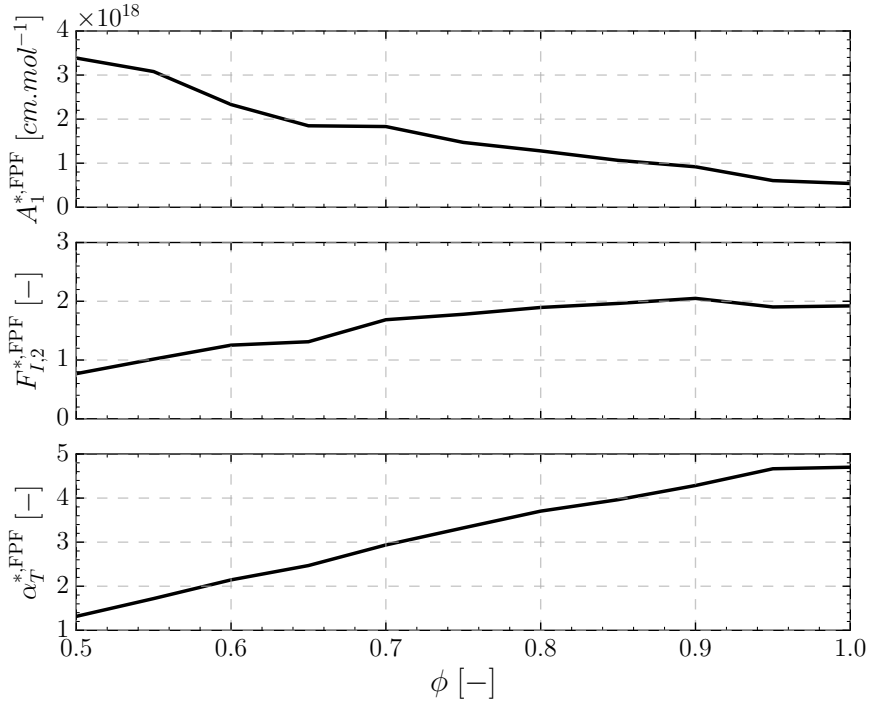

Figure 3.3: *Evolution of main mechanism parameters with the equivalence ratio ϕ.*

As the work is focused on burners in lean to stoechiometric conditions, the mechanism is optimized on the equivalence ratio range $\phi \in [0.5, 1.0]$. To prevent discontinuities in the evolution of optimized parameters with ϕ, only a subset of the parameters are allowed to vary with the equivalence ratio. It is found that varying $A_1^{*,\mathrm{FPF}}$, $F_{I,2}^{*,\mathrm{FPF}}$ and $\alpha_T^{*,\mathrm{FPF}}$ leads to accurate flame propagation and structure. The evolution of the parameters is shown in Fig. 3.3. The functions are continuous and thus the accuracy of the interpolation between the discrete optimized points is satisfying. Being directly related to the flame thickness, the diffusive correction factor $\alpha_T^{*,\mathrm{FPF}}$ increases with the equivalence ratio until $\phi = 1$. The pre-exponential coefficient $A_1^{*,\mathrm{FPF}}$ decreases, thus ensuring a correct flame propagation speed.

Fig. 3.4 shows that a perfect agreement between the laminar flame speeds obtained with the reference and optimized mechanisms is achieved for the whole range of equivalence ratios. Profiles of temperature are compared in Fig. 3.5 for different values of ϕ. The flame structure computed with the optimized mechanism is in good agreement with reference flames and only minor discrepancies are observed for $\phi = 1$.

CO optimization Similarly to the main mechanism optimization, the filtered CO scheme is first determined for $\phi = 0.75$. Results are shown in Tab. 3.2. The

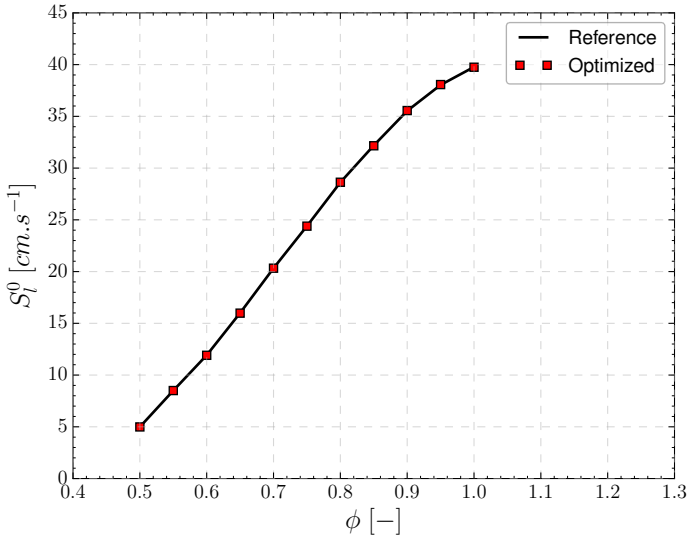

Figure 3.4: *Laminar flame speed S_l^0 as a function of the equivalence ratio ϕ. Line: flame speeds obtained with the reference mechanism. Dots: flame speeds obtained with optimized mechanism.*

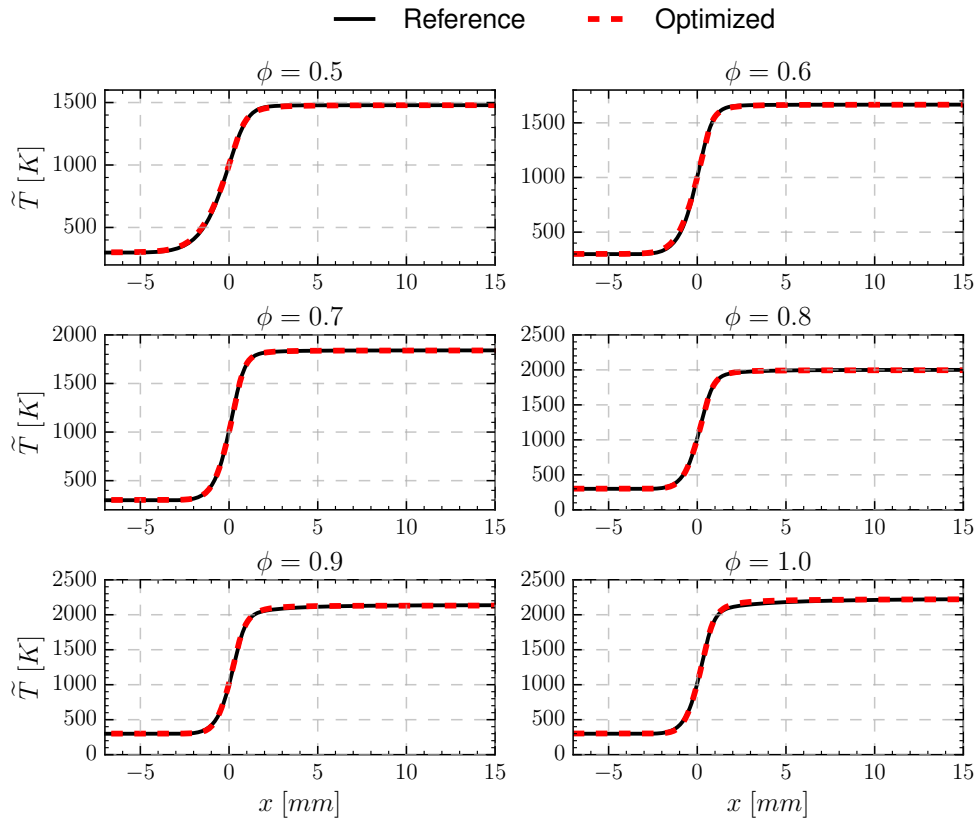

Figure 3.5: *Favre-filtered flame temperature profiles for a filter size $\Delta = 4\delta_l^0$ and different values of ϕ. Legend: — Reference, - - Optimized.*

Table 3.2: *Filtered CO mechanism for* $\Delta = 4\delta_l^0$ *and* $\phi = 0.75$.

Reaction	Arrhenius constants		Reaction orders	
	$\boldsymbol{A_i^{*,\mathrm{FPF}}}$	$\boldsymbol{E_{a,i}^{*,\mathrm{FPF}}}$	Name	Value
(R3)	1.47×10^{18}	4.25×10^4	$\boldsymbol{F_{F,1}^{*,\mathrm{FPF}}}$	1.81
			$\boldsymbol{F_{Ox,1}^{*,\mathrm{FPF}}}$	0.64
(R4) forward	2.90×10^{19}	2.41×10^4	$\boldsymbol{F_{CO,2}^{*,\mathrm{FPF}}}$	2.61
			$\boldsymbol{F_{V1,2}^{*,\mathrm{FPF}}}$	0.48
(R4) reverse	-	-	$\boldsymbol{R_{CO,2}^{*,\mathrm{FPF}}}$	1.61
			$\boldsymbol{R_{V1,2}^{*,\mathrm{FPF}}}$	1.48

diffusive correction is $\alpha_{CO}^{*,\mathrm{FPF}}(\phi = 0.75) = 5.8$.

$A_4^{*,\mathrm{FPF}}$, $F_{CO,4}^{*,\mathrm{FPF}}$, $F_{V1,4}^{*,\mathrm{FPF}}$ and $\alpha_{CO}^{*,\mathrm{FPF}}$ depend on ϕ to capture the CO flame structure for the equivalence ratio range $[0.5, 1.0]$. Selecting fewer varying coefficients leads to deteriorated results when reaching stoechiometry ($\phi = 1$). Coefficients evolutions obtained from the genetic optimization are displayed in Fig. 3.6. The functions are less continuous than for temperature optimization as the fit to reference data is more difficult to reach for CO. Resulting CO mass fraction profiles are shown in Fig. 3.7 for several equivalence ratios. The overall agreement is very satisfactory, despite some issues for predicting the correct structure when $\phi = 0.5$ and the post-flame region at stoechiometry. The CO peak, an explicit constraint for the optimization objective function, is perfectly retrieved for any value of the equivalence ratio.

3.3.3 Analysis of the filtered scheme

The filtered mechanism built from Filtered Planar Flames using the optimization procedure is here analyzed in the light of the following elements:

- The reaction rates profiles are analyzed for assessing the stiffness of the new mechanism.
- A Damköhler number is evaluated by carrying out an analysis of the flame response to a perturbation. This is done practically by computing the transient evolution of a 1-D flame towards its steady state solution.

Reaction rates stiffness Fuel and CO reaction rates of the optimized mechanism are compared to the reaction rates of the reference mechanism in Fig. 3.8. The explicitly filtered reaction rates are added to the figures. The computation is done for $\Delta = 4\delta_l^0$ and $\phi = 0.75$.

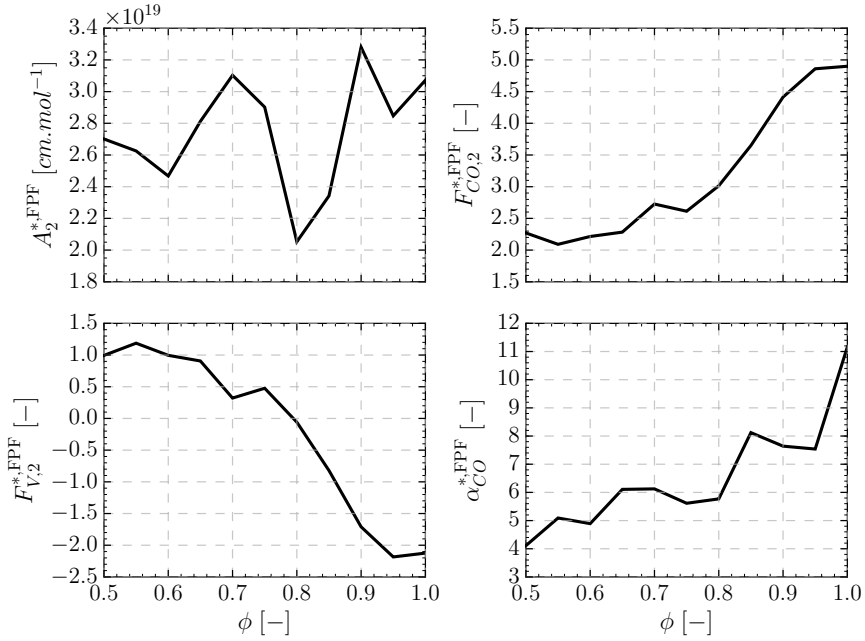

Figure 3.6: *Evolution of CO mechanism parameters with the equivalence ratio ϕ.*

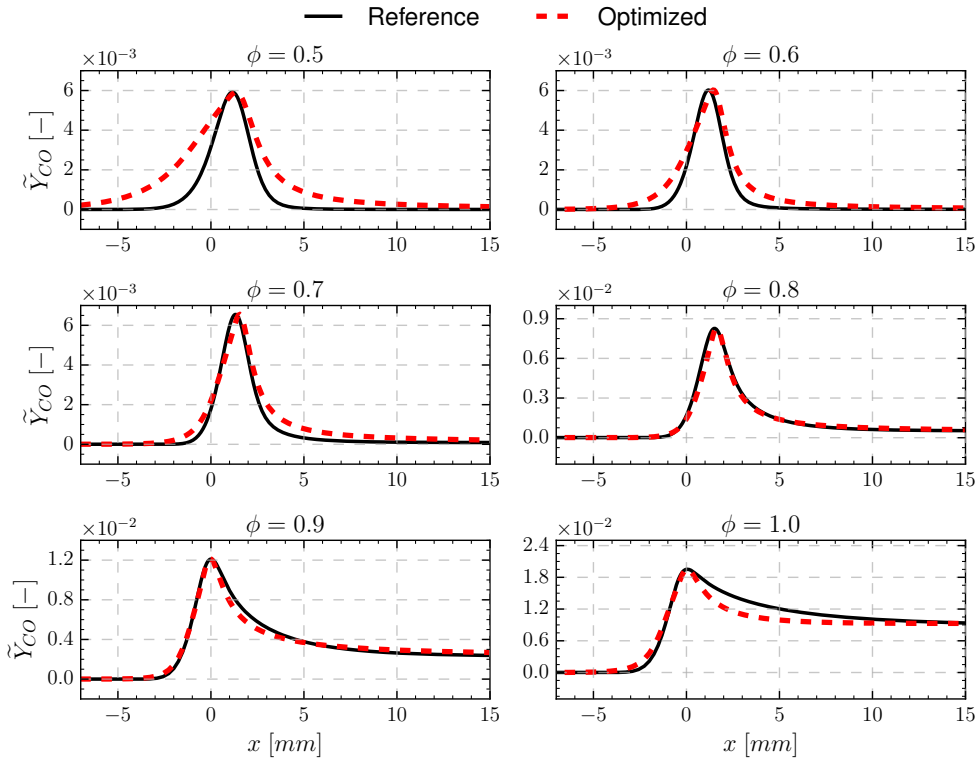

Figure 3.7: *Favre-filtered CO mass fraction profiles for a filter size $\Delta = 4\delta_l^0$ and different values of ϕ. Legend: — Reference, - - Optimized.*

The optimized mechanism features a higher reactive flame thickness and lower reaction rate peaks than the non-filtered reference scheme. This is consistent with the optimization methodology as filtered flame structures are targeted. It enables simulations on coarser grids using stiff chemistry solvers. The optimized reaction rates are however stiffer than explicitly filtered reaction rates. This stems from the fact that no optimization target has been set explicitly on the reaction rate thickness and peak. Adding information related to the reaction rate in the optimization problem may be a way to further decrease the scheme's stiffness.

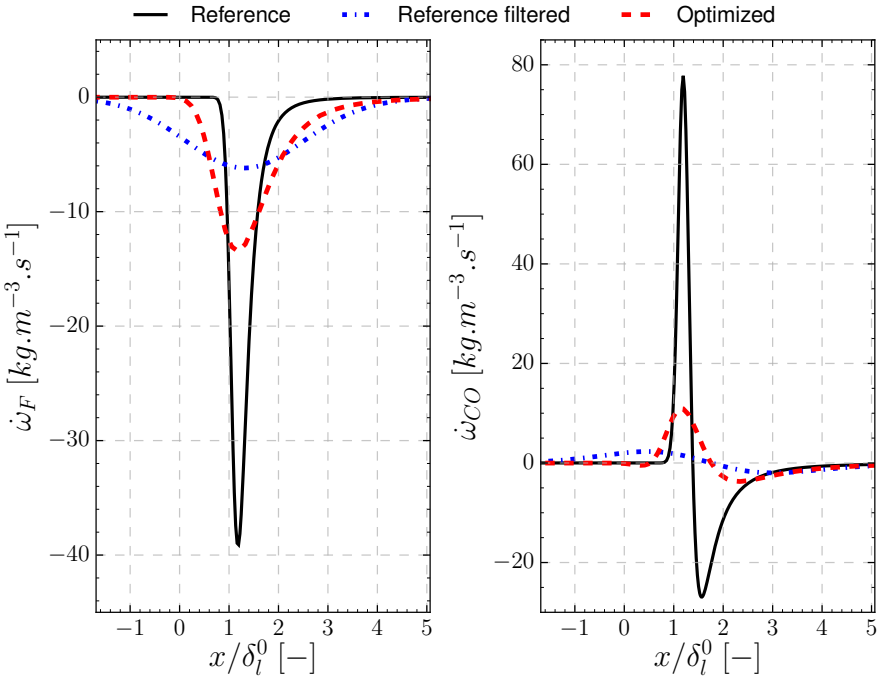

Figure 3.8: *Fuel (left) and CO (right) reaction rates for a filter size* $\Delta = 4\delta_l^0$*. Solid lines: reference mechanism. Dash-dotted lines: explicitly filtered reference mechanism. Dashed lines: optimized mechanism. Legend: — Reference flame. -.- Explicitly filtered reference flame. - - Flame obtained with optimized model.*

Relaxation time analysis Combustion models modify the flame response to turbulent structures (Colin et al. (2000)). A simplified 1-D analysis is proposed here to study the response of the optimized filtered scheme built with laminar premixed flame to a perturbation and compare it to the response of a resolved (non-filtered) flame. The following steps are performed:

- An initial solution far enough from the steady-state solution is built

analytically. Transported thermo-chemical variables are initialized as:

$$\varphi_{ini} = \left[1 - \frac{1}{2}\left(1 + \tanh\left(\frac{x - x_f}{\delta_f}\right)\right)\right]\varphi_u + \frac{1}{2}\left(1 + \tanh\left(\frac{x - x_f}{\delta_f}\right)\right)\varphi_b \tag{3.34}$$

where $\varphi = Y_k$, ρ or h. φ_u is the value of φ in fresh gases and φ_b in burnt gases. x_f and δ_f are the flame position and the flame thickness, respectively. Their values are set to $x_f = 0\ m$ and $\delta_f = 5 \times 10^{-3}\ m$, which is close to the laminar flame thickness of the considered flame.

- Numerical solution of a 1-D freely propagating flame at $\phi = 0.75$ is computed using the YALES2 explicit solver (Moureau et al. (2011a)). Two computations are done with (i) the reference mechanism and (ii) the optimized filtered scheme. The analysis is focused on the physical time spent in each simulation to reach the steady-state thermal thickness.

- A characteristic relaxing time is defined as the time required for a flame to reach 95 % of its steady state thickness value, relatively to its thickness at $t = 0$. This time is written t_c^{DNS} for the reference mechanism and t_c^{Opt} for the optimized mechanism.

Fig. 3.9 shows the time evolution of flame thermal thickness for DNS and optimized filtered simulations. The time is normalized by the laminar flame characteristic time $t_l^0 = \delta_l^0/S_l^0$. The thickness is written δ_l and its equilibrium value[2] δ_l^{eq}. The main observation is that the optimized filtered flame answers more slowly to perturbations than the resolved flame. This is consistent with previous studies which showed that the flame thermal thickness broadening acts as a low-pass filter and thus the broader flame takes more time to respond to a perturbation (Auzillon et al. (2011); Auzillon (2012)). Practically, this suggests that the optimized filtered flames will be less sensitive to turbulence. The characteristic time of the resolved flame is $t_c^{DNS} = 0.86\tau_c$ while for the optimized flame it is $t_c^{Opt} = 1.86\tau_c$. This can be expressed using a Damköhler number, which is defined as $Da = \tau_{turb}/\tau_{chem}$ where τ_{chem} is a characteristic chemical time scale and τ_{turb} a turbulent time scale. At given turbulence level, the resolved Damköhler number can be related to the optimized filtered Damköhler as $Da^{Opt} = (t_c^{DNS}/t_c^{Opt})Da^{DNS} \approx Da^{DNS}/2$ for this particular case ($\Delta = 4\delta_l^0$).

3.3.4 Subgrid scale wrinkling effects modeling

The optimization of $\mathcal{A}^*$ and α^* using Filtered Planar Flames leads to a formulation only valid in situations where wrinkling is fully resolved. Subgrid scale

[2] $\delta_l^{eq} = \delta_l^0$ for the resolved flame and $\delta_l^{eq} = \overline{\delta}_l$ for the optimized filtered flame

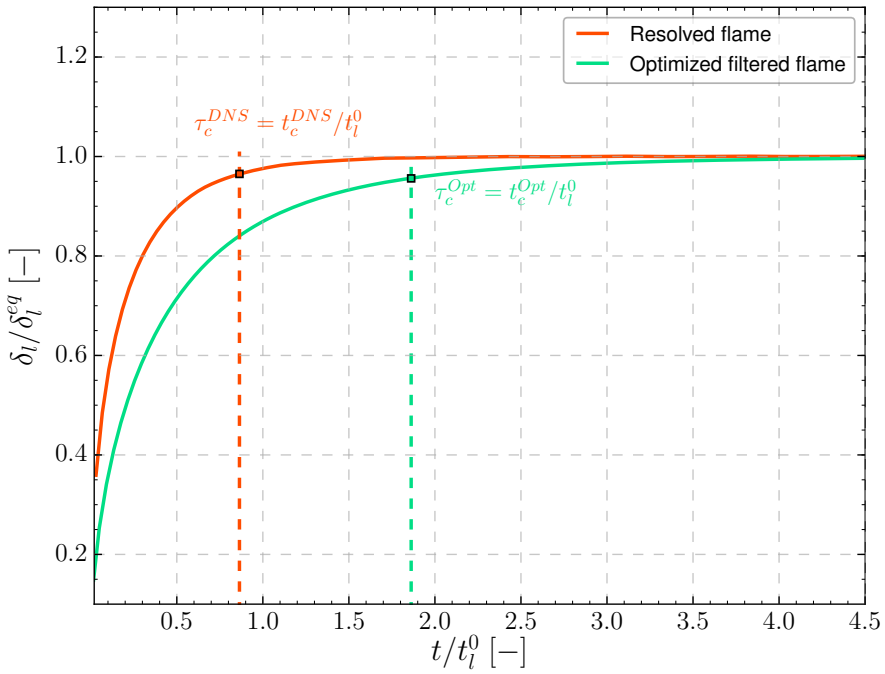

Figure 3.9: *Evolution of flame thickness in time for the 1-D explicit simulation of a freely propagating premixed flame with* $\phi = 0.75$. *Legend:* — *Reference flame thickness.* — *Optimized filtered flame thickness* ($\Delta = 4\delta_l^0$).

(SGS) flame wrinkling increases however the flame surface and hence the flame propagation speed. This effect has been widely studied and is explicitly integrated in models such as TFLES through the introduction of an efficiency factor Ξ_Δ (Colin et al. (2000); Charlette et al. (2002a); Charlette et al. (2002b)). The introduction of Ξ_Δ is done *a posteriori* by multiplying diffusive and reactive terms by Ξ_Δ. Using this strategy, sub-grid scale turbulence is assumed to have an impact on the flame propagation speed only, leaving the filtered flame structure unaffected. The reaction rates $\widetilde{\dot{\omega}}_k$ and diffusive correction term α^* of the temperature scheme read:

$$\begin{cases} \overline{\rho}\widetilde{\dot{\omega}}_k = \Xi_\Delta \overline{\rho}\widetilde{\dot{\omega}}_k^{\mathcal{A}_T^{*,\mathrm{FPF}}(\phi)} & \text{(3.35a)} \\ \alpha^* = \Xi_\Delta \alpha_T^{*,\mathrm{FPF}}(\phi) & \text{(3.35b)} \end{cases}$$

And for the CO sub-mechanism:

$$\begin{cases} \overline{\rho}\widetilde{\dot{\omega}}_k = \Xi_\Delta \overline{\rho}\widetilde{\dot{\omega}}_k^{\mathcal{A}_{CO}^{*,\mathrm{FPF}}(\phi)} & \text{(3.36a)} \\ \alpha^* = \Xi_\Delta \alpha_{CO}^{*,\mathrm{FPF}}(\phi) & \text{(3.36b)} \end{cases}$$

where superscript *FPF* refers to values obtained by optimization on Filtered Planar Flames.

3.4 Filtered Optimized Chemistry with Filtered Wrinkled Flamelets (FOC-FWF)

The FOC-FPF modeling strategy neglects the impact of SGS wrinkling on the filtered flame structure. Some studies have however shown that it has a significant impact on pollutants formation, and CO in particular (Nilsson and Bai (2002); Mercier et al. (2018)). For integrating these effects in turbulent combustion modeling, a strategy based on analytical subgrid scale wrinkling patterns has recently been developed (Mercier et al. (2018)). It relies on the building of mono-dimensional Filtered Wrinkled Flamelets (FWF) and has led to excellent results in a tabulated chemistry context. The present work proposes to use these newly defined flames as optimization targets in the FOC modeling approach.

3.4.1 Building a set of 1D manufactured wrinkled flames

3.4.1.1 Manufactured 2-D wrinkling patterns

A 2-D wrinkled flame pattern, shown in Fig. 3.10, is manufactured by approximating the flame front position by a sinusoidal function of amplitude A and wavelength P. Embedded in a 2-D square of size Δ to mimic a sub-filter scale domain, this flame pattern of wrinkling Ξ_Δ contains a number of wavelengths $n_\Delta = \Delta/P$. n_Δ can be interpreted as an average number of flame crossings per unit distance Δ (Bray and Moss (1977)). Assuming that the flame is in the flamelet regime, the 2-D flame structure is manufactured from a 1-D laminar premixed flame computed with detailed chemistry. The flame front position is given by:

$$x_{(T=T_i)} = A sin\left(\frac{2\pi y_{(T=T_i)}}{P}\right) \tag{3.37}$$

where T_i is the value of the temperature at the inflection point of a laminar one-dimensional premixed flame. This point is chosen to approximate the position of the thin reaction zone[3]. Assuming that the sub-filter flame is in flamelet regime, a 2-D flame is created by mapping a 1-D flame to the analytic sinusoidal pattern. The value of any thermo-chemical variable φ in the sub-filter box is reconstructed from the 1-D laminar solution by knowing the distance $\mathcal{D}$ between

[3] An alternative is to set the maximal heat release point on the sine. A small impact on results is however observed in the present work.

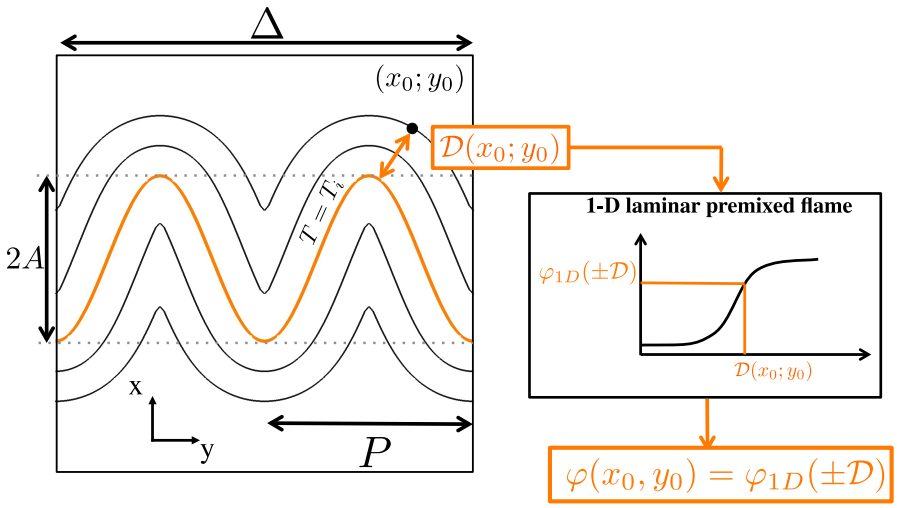

Figure 3.10: *Schematical view of sub-filter sinusoidal flame pattern*

the point (x, y) and the sine (i.e. the flame front):

$$\varphi(x, y) = \varphi_{1D}(\pm\mathcal{D}(x, y)) \tag{3.38}$$

The distance is defined as positive when the point is in the burnt gases and negative in the fresh gases. The temperature inflection point of the 1-D laminar flamelet is located at $\mathcal{D} = 0$. This is the first step of the Filtered Wrinkled Flamelet library generation, as illustrated in Fig. 3.11. A representation of the 2-D manufactured flame is shown in Fig. 3.12 for parameters $\Delta/\delta_l^0 = 4$, $n_\Delta = 2$ and $A = 2\delta_l^0$. Temperature, density, CO mass fraction and fuel reaction rate 2-D fields computed with virtual chemistry are illustrated.

3.4.1.2 Generation of 1-D wrinkled flamelets

Definition of a non-isotropic filtering operator The filters used in LES are usually isotropic. A new filter is constructed here to account for asymmetry in premixed combustion processes: a preferential direction for flame propagation is indeed introduced by boundary conditions of the considered system. By considering a local referential to the flame as in Fig. 3.10, the direction x is the propagation direction of the flame and y its normal. A Gaussian kernel is used along x while a box filter is considered for the y direction so that a filtered quantity φ reads:

$$\overline{\varphi}^{2D}(x, y) = \int_{x'=-\infty}^{+\infty} G_\Delta(x' - x) \left(\int_{y'=-\infty}^{+\infty} B_\Delta(y' - y)\varphi(x', y')dy' \right) dx' \tag{3.39}$$

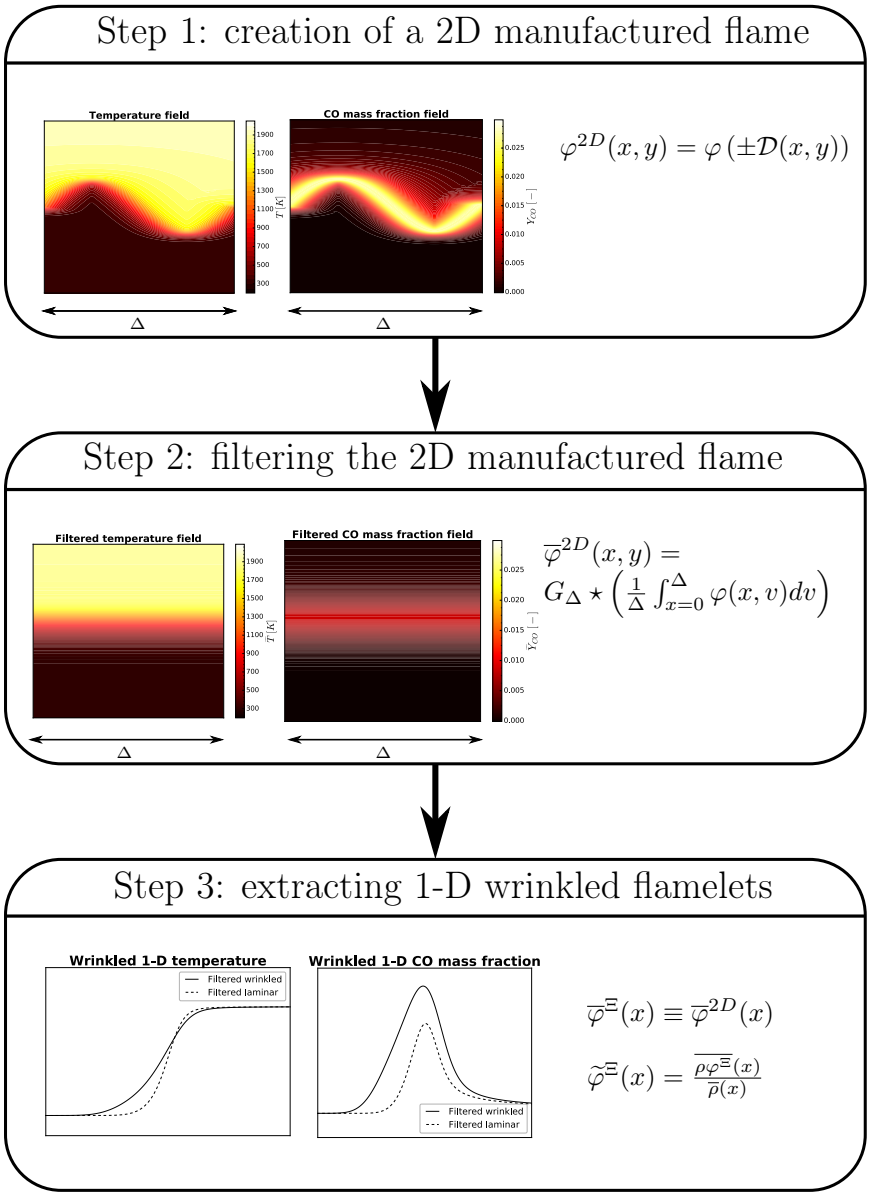

Figure 3.11: *Principle of 1-D wrinkled flame generation.*

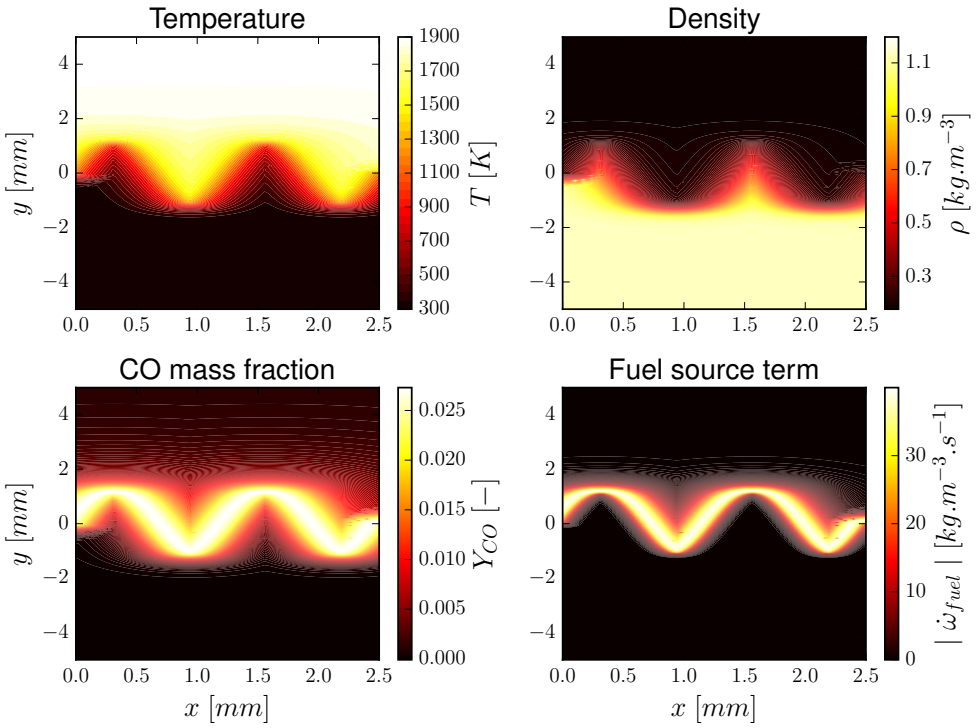

Figure 3.12: *Representation of 2-D manufactured thermo-chemical variables for* $\Delta/\delta_l^0 \approx 4$, $n_\Delta = 2$ *and* $A = 2\delta_l^0$. *The virtual chemical scheme is used. Top left: temperature field* T. *Top right: density field* ρ. *Bottom left: CO mass fraction* Y_{CO}. *Bottom right: fuel reaction rate* $\mid \dot{\omega}_{fuel} \mid$.

where G_Δ is a Gaussian kernel and B_Δ a box kernel. This approach is similar to anisotropic diffusion encountered in optics (Perona and Malik (1990)).

Filtering sub-grid flame patterns Eq. (3.39) can be rewritten as:

$$\overline{\varphi}^{2D}(x,y) = \int_{x'=-\infty}^{+\infty} G_\Delta(x'-x)\overline{\varphi}^{y}(x',y)dx' \tag{3.40}$$

Where $\overline{\varphi}^{y}$ is the filtering operation with kernel B_Δ on the y-axis. Since the box has a size Δ, it reduces to:

$$\overline{\varphi}^{y}(x,y) = \frac{1}{\Delta}\int_{v=0}^{\Delta} \varphi(x,v)dv \tag{3.41}$$

As the flame pattern is $n_\Delta P$-periodic at the sub-filter scale in the y direction, the filtering along y reduces to a single variable function: $\overline{\varphi}^{y}(x,y) \equiv \overline{\varphi}^{y}(x)$. Finally, wrinkled thermo-chemical variables $\overline{\varphi}^{\Xi}$, depending only on space variable

x, are estimated as:

$$\overline{\varphi}^{\Xi}(x) = \int_{x'=-\infty}^{+\infty} G_{\Delta}(x'-x)\overline{\varphi}^{y}(x')dx' \tag{3.42}$$

Superscript Ξ denotes here variables obtained from the filtering of a 2-D manufactured wrinkling pattern. The non-isotropic filtering operator is thus able to transform rigorously the 2-D wrinkled patterns presented in the previous section into 1-D flames and hence encapsulating the wrinkling information along one space dimension. Favre-filtered wrinkled quantities can then be defined as:

$$\widetilde{\varphi}^{\Xi}(x) = \frac{\overline{\rho\varphi}^{\Xi}(x)}{\overline{\rho}^{\Xi}(x)} \tag{3.43}$$

A summary of the filtering procedure is provided in Fig. 3.11. In the context of virtual chemistry, the strategy is applied to obtain the wrinkled temperature $\widetilde{T}^{\Xi}(x)$, the wrinkled CO mass fraction $\widetilde{Y}_{CO}^{\Xi}(x)$ and the wrinkled fuel reaction rate $\overline{\rho}^{\Xi}\widetilde{\dot{\omega}}_{fuel}^{\Xi}(x)$. In addition, wrinkled mass fractions of other species are also computed to initialize the 1-D flame solver involved in the optimization process.

3.4.1.3 Extraction of flame properties

Turbulent flame speed and SGS flame wrinkling The turbulent propagation speed of the wrinkled flame front is defined from the filtered fuel reaction rate as:

$$S_T^{\Xi} = \frac{-1}{\rho_u \left(Y_{fuel}^u - Y_{fuel}^b\right)} \int_{-\infty}^{+\infty} \overline{\rho}^{\Xi}\widetilde{\dot{\omega}}_{fuel}^{\Xi}(x)dx \tag{3.44}$$

where ρ_u is the fresh gas density, and Y_{fuel}^u, Y_{fuel}^b are respectively the fresh and burnt fuel mass fractions. The subgrid scale flame wrinkling is then computed as the ratio of the turbulent flame speed to the laminar flame speed:

$$\Xi_{\Delta} = \frac{S_T^{\Xi}}{S_l^0} \tag{3.45}$$

The wrinkling depends on n_{Δ} and A, which have been omitted in the notations for clarity.

Wrinkled flame thickness The thickness $\overline{\delta}_\Xi$ of the wrinkled flamelets is defined from the temperature gradient:

$$\overline{\delta}_\Xi = \frac{\widetilde{T}_b^\Xi - \widetilde{T}_u^\Xi}{max\left(\left|\frac{\partial \widetilde{T}^\Xi}{\partial x}\right|\right)} \tag{3.46}$$

where $\widetilde{T}_u^\Xi$ and $\widetilde{T}_b^\Xi$ are respectively the fresh and burnt gas temperature.

3.4.1.4 Analytic expression for Ξ_Δ in the case of an infinitely thin flame

Under the infinitely thin flame flame front assumption ($\delta_l^0 \ll \Delta$), an analytic expression is derived for the SGS flame wrinkling. In such situation, the wrinkling factor is defined as:

$$\Xi_\Delta = \frac{\mathcal{L}}{\Delta} \tag{3.47}$$

where $\mathcal{L}$, the arc-length of the sine, reads:

$$\mathcal{L} = \int_0^\Delta \sqrt{1 + \left(\frac{dx_{(T=T_i)}}{dy_{(T=T_i)}}\right)^2}\, dy \tag{3.48}$$

After some mathematical operations, the wrinkling factor is estimated as:

$$\Xi_\Delta = \frac{2}{\pi}\sqrt{1 + \frac{4\pi^2 A^2 n_\Delta^2}{\Delta^2}}\, E\left(\sqrt{\frac{1}{1 + \frac{\Delta^2}{4\pi^2 A^2 n_\Delta^2}}}\right) \tag{3.49}$$

where E is the complete elliptic integral of the second kind.

3.4.2 Flame regime and parameters range

The construction of wrinkled flamelets presented above is only valid for flames which have a laminar inner structure. This is the case for wrinkled and corrugated flame regimes, and to some extent for thin reaction zones regime, where only the thermal flame layer is affected by turbulent eddies.

Range of n_Δ In the flamelet regime, the size of the smallest eddies able to wrinkle the flame front is given by the Gibson length l_G:

$$l_G = l_t \left(\frac{S_l^0}{u'} \right)^3 \tag{3.50}$$

where l_t is the turbulent integral length scale and u' the turbulent velocity, determined experimentally. The flame wrinkling pattern period P is therefore larger than $2l_G$. Additionally, P should also be larger than $2\delta_l^0$ to avoid the overlap of two sine branches. Hence, the number of sine periods in the sub-filter box is limited by n_Δ^{max} defined as:

$$n_\Delta^{max} = \min \left[n_{\Delta,\delta}^{max}, n_{\Delta,l_G}^{max} \right] \tag{3.51}$$

where $n_{\Delta,\delta}^{max}$ and n_{Δ,l_G}^{max} are the maximal sine periods based on laminar flame thickness and Gibson lengths respectively, and are defined as:

$$n_{\Delta,\delta}^{max} = int \left(\frac{\Delta}{2l_G} \right) \tag{3.52}$$

$$n_{\Delta,l_G}^{max} = int \left(\frac{\Delta}{2\delta_l^0} \right) \tag{3.53}$$

Range of sine amplitudes The local flame front curvature κ should remain small to keep an unaltered flame structure in the flamelet regime. The radius of curvature of the flame $R = 1/\kappa$ must be larger than the flame cut-off thickness δ. As the flame front is assimilated to a sine pattern of normal $\mathbf{n}$, the curvature is estimated as:

$$\kappa = \nabla \cdot \mathbf{n} = \frac{A \left(\frac{2\pi}{P}\right)^2 \left| sin\left(\frac{2\pi}{P} y\right) \right|}{\left(1 + A^2 \left(\frac{2\pi}{P}\right)^2 cos\left(\frac{2\pi}{P} y\right)^2\right)^{3/2}} \tag{3.54}$$

The maximal curvature κ_{max} occurs at $y = P/4$ (modulo $P/2$) and reads:

$$\kappa_{max} = A \left(\frac{2\pi}{P} \right)^2 \tag{3.55}$$

The flamelet condition $R > \delta$ thus leads to the following maximal value for the

sine pattern amplitude (Mercier et al. (2018)):

$$A_{max} = \frac{P^2}{4\pi^2\delta} \tag{3.56}$$

3.4.3 Analysis of the manufactured wrinkled flamelet library

The wrinkled flamelet library is here illustrated for an equivalence ratio $\phi = 0.75$.

Wrinkling factor effects on flame profiles Selected wrinkled temperature and CO mass fraction profiles are shown in Fig. 3.13 for parameters $\Delta = 2.5\text{mm} = 4\delta_l^0$ and $n_\Delta = 1$ and 2. The first observation is that wrinkling thickens the filtered flame profiles. This is caused by the increased space occupied by the wrinkled flame, as illustrated in Fig. 3.12. For a given SGS wrinkling, the temperature and CO mass fraction profiles are also thicker for $n_\Delta = 1$ than for $n_\Delta = 2$. CO peak quantity is also increased by wrinkling, and the overall CO quantity in the flame front grows with Ξ_Δ. This is explained by the higher flame area and hence the enhanced amount of pollutants produced in the sub-filter box. The CO peak is higher for $n_\Delta = 2$ than for $n_\Delta = 1$.

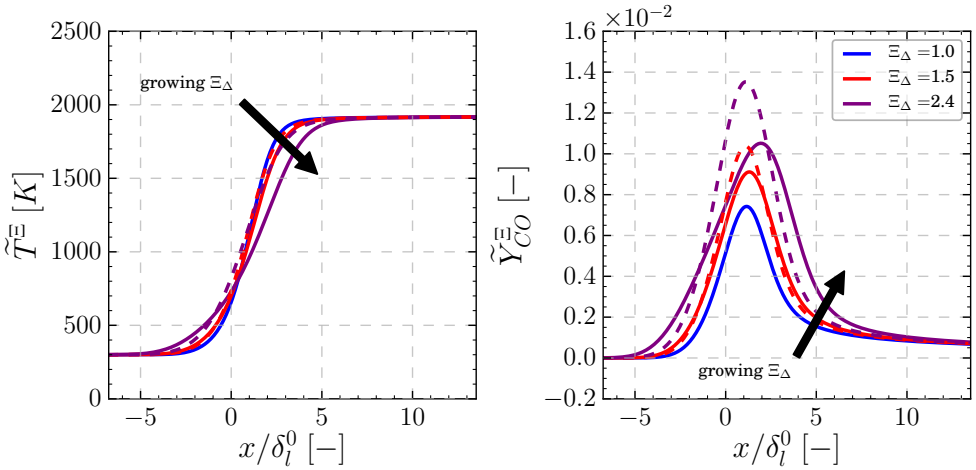

Figure 3.13: *Illustration of the FWF flamelet library for different wrinkling factors for $\phi = 0.75$, $\Delta = 2.5mm$ and $n_\Delta = 1$ and 2. Profiles for $n_\Delta = 1$ are represented in solid lines while $n_\Delta = 2$ profiles are in dashed lines. On the left: filtered temperature. On the right: filtered CO mass fraction.*

Wrinkling factors are shown as a function of the normalized sine pattern amplitude A/δ_l^0 for three filter sizes ($\Delta = 2\delta_l^0$, $4\delta_l^0$ and $8\delta_l^0$) in Fig. 3.14 (top row). The wrinkling factor as well as the flame surface increase with the amplitude. For a given A/δ_l^0, the SGS wrinkling grows with n_Δ. The modeling degenerates

well to DNS when the filter size Δ tends to zero: indeed when Δ is lower than the flame thickness δ_l^0, the sine can no longer be defined and the flame reduces to a plane laminar filtered flame. Wrinkled flame thickness is also plotted in Fig. 3.14 for the three same filter sizes (bottom row). Observations made in Fig. 3.13 are emphasized since the thickness grows with the wrinkling. For a given wrinkling factor, wrinkled flame thickness is higher for $n_\Delta = 1$ than for $n_\Delta = 2$. An explanation is that a higher value of A has to be reached for $n_\Delta = 1$ than for $n_\Delta = 2$ to obtain the same wrinkling factor Ξ_Δ. The flame front then spreads over a larger area in the sub-filter box and the thickness of the filtered wrinkled flame is increased. Comparisons between numerically computed and analytic wrinkling under infinitely thin flame assumption (defined by Eq. (3.49)) are included in Fig. 3.14 for $\Delta = 2\delta_l^0$, $4\delta_l^0$ and $8\delta_l^0$.

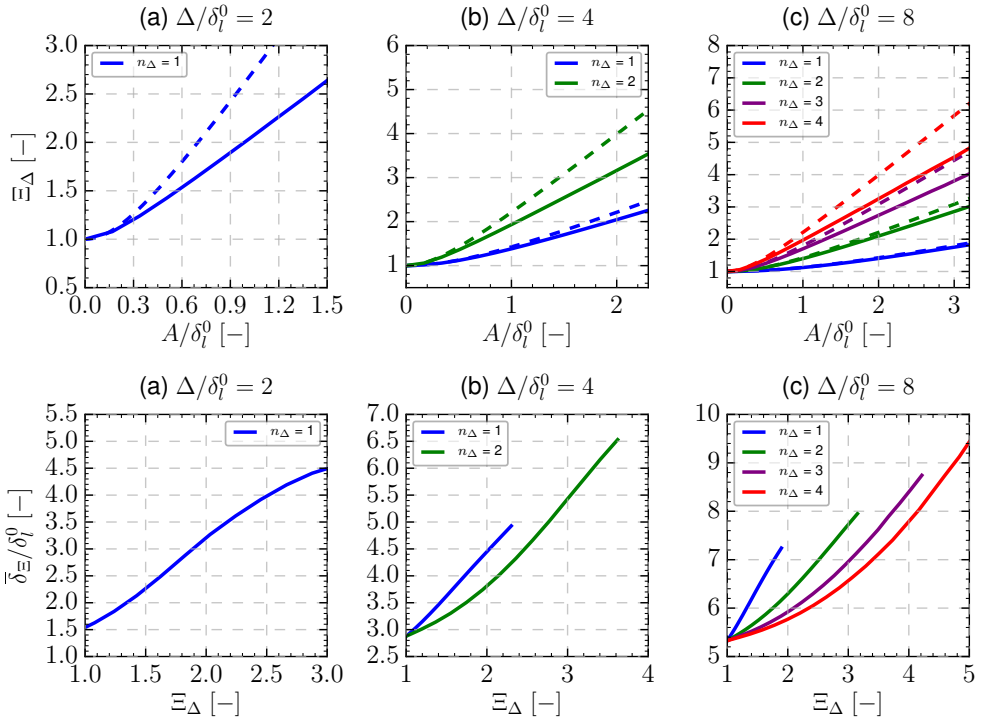

Figure 3.14: *Flame wrinkling factors and wrinkled flame thickness for $\phi = 0.75$ and three different filter sizes $\Delta = 2\delta_l^0$, $4\delta_l^0$ and $8\delta_l^0$. Top row: wrinkling factor Ξ_Δ as a function of the normalized sine amplitude A/δ_l^0; dotted lines are the wrinkling factors under infinitely thin flame assumption (Eq. (3.49)). Bottom: wrinkled flame thickness $\overline{\delta}_\Xi$. Legend: — $n_\Delta = 1$, — $n_\Delta = 2$, — $n_\Delta = 3$, — $n_\Delta = 4$.*

Analysis of CO quantity in the LES sub-filter surface The analysis of the effect of subgrid-scale wrinkling on CO mass fraction is given in Fig. 3.15. On the bottom of the figure, the peak of CO mass fraction $[\widetilde{Y}_{CO}^{\Xi}]^{max}$, normalized

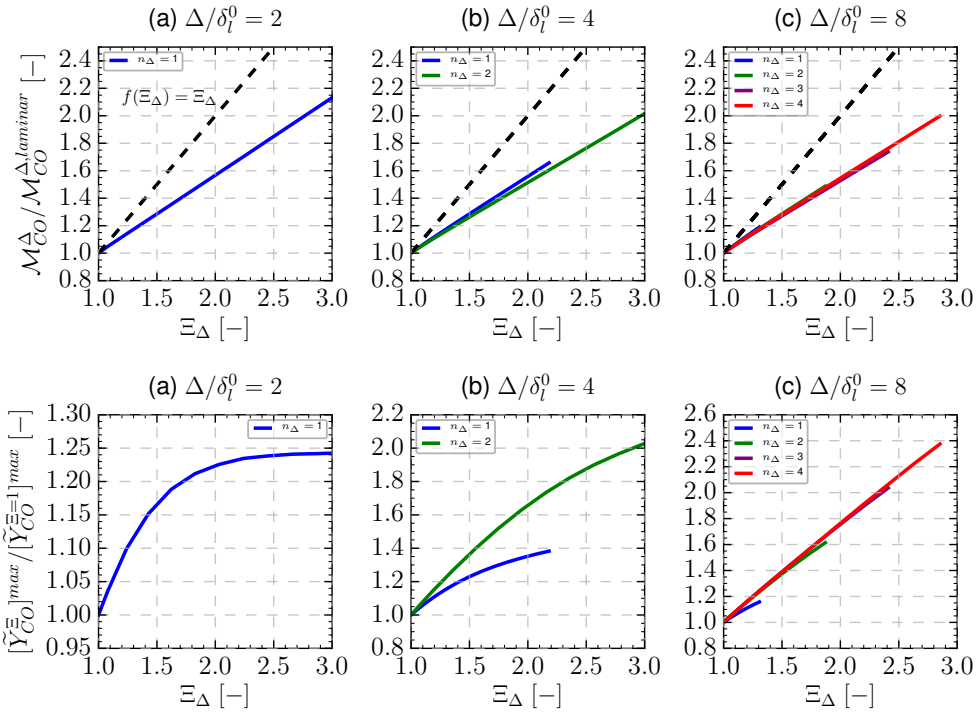

Figure 3.15: *Analysis of wrinkled CO for $\phi = 0.75$ and three different filter sizes $\Delta \approx 2\delta_l^0$, $4\delta_l^0$ and $8\delta_l^0$. Top row: normalized CO peak in function of the wrinkling factor. Bottom row: normalized mass of CO in a sub-filter box in function of the wrinkling ratio Ξ_Δ. Legend: — $n_\Delta = 1$, — $n_\Delta = 2$, — $n_\Delta = 3$, — $n_\Delta = 4$.*

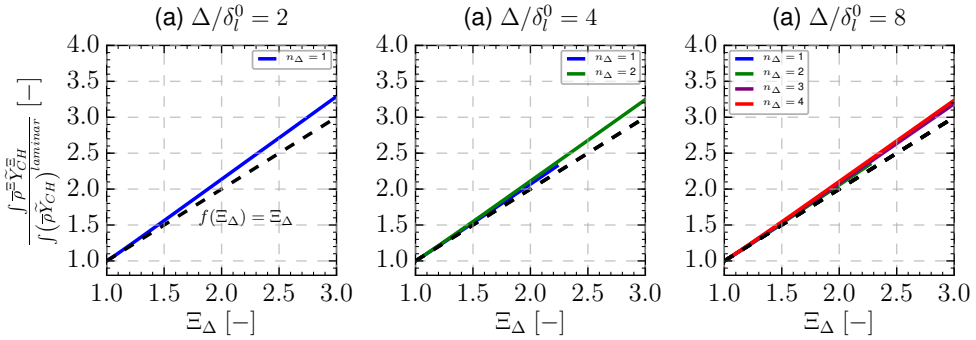

Figure 3.16: *Normalized mass of CH in a sub-filter box as a function of the SGS wrinkling Ξ_Δ for $\phi = 0.75$ and three different filter sizes $\Delta \approx 2\delta_l^0$, $4\delta_l^0$ and $8\delta_l^0$. Legend: — $n_\Delta = 1$, — $n_\Delta = 2$, — $n_\Delta = 3$, — $n_\Delta = 4$.*

by its laminar value $[\widetilde{Y}_{CO}^{\Xi=1}]^{max}$, is plotted in terms of the wrinkling factor Ξ_Δ for the three filter size values. The peak increases with Ξ_Δ, and at a given wrinkling ratio, it is higher for high n_Δ values. $\mathcal{M}_{CO}^{\Delta}$, the CO mass in a sub-filter box of surface S, is defined as:

$$\mathcal{M}_{CO}^{\Delta}(\Xi_\Delta) = \iint_S \rho Y_{CO} dS = \int_{x=-\Delta/2}^{\Delta/2} \int_{y=0}^{\Delta} (\rho Y_{CO})(x,y) dy dx \tag{3.57}$$

The mass conservation property of the LES filter leads to:

$$\mathcal{M}_{CO}^{\Delta}(\Xi_\Delta) = \int_{x=-\Delta/2}^{\Delta/2} \int_{y=0}^{\Delta} \left(\overline{\rho}\widetilde{Y}_{CO}\right)(x,y) dy dx \tag{3.58}$$

Besides, in the FWF formalism, $(\overline{\rho}\widetilde{Y}_{CO})(x,y) = (\overline{\rho}^{\Xi}\widetilde{Y}_{CO}^{\Xi})(x)$. Hence:

$$\mathcal{M}_{CO}^{\Delta}(\Xi_\Delta) = \Delta \times \left(\int_{x=-\Delta/2}^{\Delta/2} \overline{\rho}^{\Xi}\widetilde{Y}_{CO}^{\Xi}(x) dx \right) \tag{3.59}$$

The mass of CO in the filter domain normalized by its laminar value $\mathcal{M}_{CO}^{\Delta,laminar} = \mathcal{M}_{CO}^{\Delta}(\Xi_\Delta = 1)$ is shown on the top of Fig. 3.15 as a function of the SGS wrinkling Ξ_Δ. The mass of CO increases significantly with the wrinkling factor. For example, in a situation representative of practical LES ($\Xi_\Delta = 2$, $\Delta = 4\delta_l^0$), the SGS flame wrinkling enhances by 50 % the mass of CO in comparison with a planar flame. The integral is however almost insensitive to the value of n_Δ. This suggest than the increase of CO quantity in the box is mostly dependent on the wrinkling factor, regardless of the flame front period.

Under the infinitely thin flame front assumption, the following model for the CO mass in the sub-filter box is derived:

$$\mathcal{M}_{CO}^{\Delta}(\Xi_\Delta) = \Xi_\Delta \mathcal{M}_{CO}^{\Delta,laminar} \tag{3.60}$$

This simplified model is added in Fig. 3.15 (shown by dotted lines). The CO mass computed from Eq. (3.59) stays significantly below this line for the whole set of parameters $\left(\Delta/\delta_l^0, n_\Delta\right)$ and thus Eq. (3.60) is not satisfied. This departure of CO mass compared to the infinitely thin flame front assumption is mainly due to the non-zero Y_{CO} value in the burnt gases which implied that some mass of CO is located outside the filter volume where the wrinkled flamelet is manufactured. A complementary analysis is made by manufacturing a 2-D CH mass fraction field (computed with the GRI3.0 mechanism). Since CH has an equilibrium value equal to zero and a thin structure, it is an appropriate

choice for providing further insight. The mass of CH in a sub-filter box is illustrated in Fig. 3.16 and the relationship $\mathcal{M}_{CH}^{\Delta} = \Xi_{\Delta}\mathcal{M}_{CH}^{\Delta,laminar}$ is satisfyingly verified.

3.4.4 FWF library optimization

The optimization procedure previously applied to Filtered Planar Flames is here adapted to the wrinkled flamelets library. The FWF database serves as an ensemble of targets for the filtered optimized scheme. This step leads to the identification of parameters $\mathcal{A}^* = (A^*_{j,\mathrm{FWF}}, E^*_{a,j,\mathrm{FWF}}, n^*_{ij,\mathrm{FWF}})$ and $\alpha^* = \alpha^*_{\mathrm{FWF}}$. Wrinkled temperature and CO mass fraction, as plotted in Fig. 3.13 for instance, are targeted in the optimization process. The flame defining parameters vector is here $\boldsymbol{p} = (\phi, \Xi_{\Delta}, n_{\Delta})$. The flame consumption speed is set to $S_c = S_T^{\Xi}$.

The filter size is $\Delta = 2.5\mathrm{mm} = 4\delta_l^0$ and values of n_{Δ} are limited to 1 and 2, in accordance with bounds given by Eq. (3.51). The sine amplitude range is set to $A = [0; 3\delta_l^0]$ and the range of wrinkling factors is defined accordingly by the relationship $\Xi_{\Delta} = \Xi_{\Delta}(n_{\Delta}, A)$. As in the case of laminar premixed flame optimization, temperature and CO optimization are performed in the following two separate steps.

Temperature optimization As in Sec. 3.3.2, a selection of optimized Arrhenius coefficients are dependent on the wrinkling factor in order to ensure sufficient continuity of the coefficients in terms of Ξ_{Δ}. To be consistent with the results already presented in section 3.3.2, the parameters corresponding to $\Xi_{\Delta} = 1$ are the one obtained for planar premixed flames. As a reminder, these parameters are written:

$$\mathcal{A}_T^{*,\mathrm{FPF}} = \left(A_1^{*,\mathrm{FPF}}, E_{a,1}^{*,\mathrm{FPF}}, F_{F,1}^{*,\mathrm{FPF}}, F_{Ox,1}^{*,\mathrm{FPF}}, A_2^{*,\mathrm{FPF}}, E_{a,2}^{*,\mathrm{FPF}}, F_{I,2}^{*,\mathrm{FPF}}\right) \quad (3.61)$$

The diffusive correction factor in the planar case is written $\alpha_T^{*,\mathrm{FPF}}$. For capturing the correct wrinkled flame propagation and structure, it is found that varying A_1^* and α_T^* in terms of Ξ_{Δ} is sufficient to obtain accurate results. Parameters $\alpha_T^{*,\mathrm{FWF}}$ and $\mathcal{A}^{*,\mathrm{FWF}}$ are decomposed as:

$$\begin{cases} \alpha_T^{*,\mathrm{FWF}}(\phi, \Xi_{\Delta}, n_{\Delta}) = \xi_1^T(\Xi_{\Delta}, n_{\Delta})\, \alpha_T^{*,\mathrm{FPF}}(\phi) & (3.62a) \\ A_1^{*,\mathrm{FWF}}(\phi, \Xi_{\Delta}, n_{\Delta}) = \xi_2^T(\Xi_{\Delta}, n_{\Delta})\, A_1^{*,\mathrm{FPF}}(\phi) & (3.62b) \end{cases}$$

where ξ_1^T and ξ_2^T are dimensionless factors for defining the coefficients variation with the wrinkling parameters.

Computed values of these two factors using the genetic optimization tool are

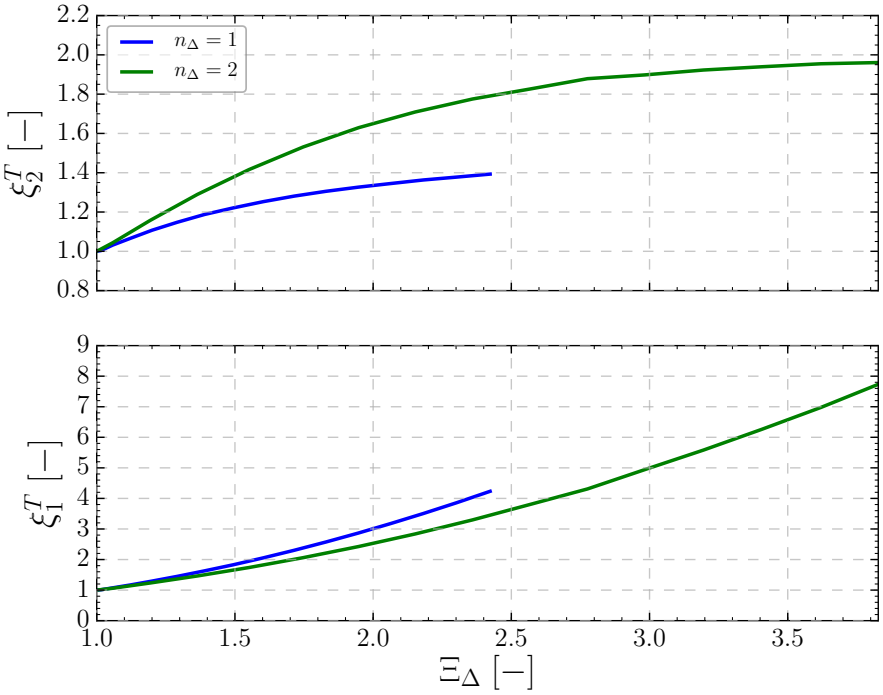

Figure 3.17: *Dimensionless factors* ξ_1^T *and* ξ_2^T *for* $\phi = 0.75$ *and* $\Delta = 4\delta_l^0$. *Legend:* — $n_\Delta = 1$, — $n_\Delta = 2$.

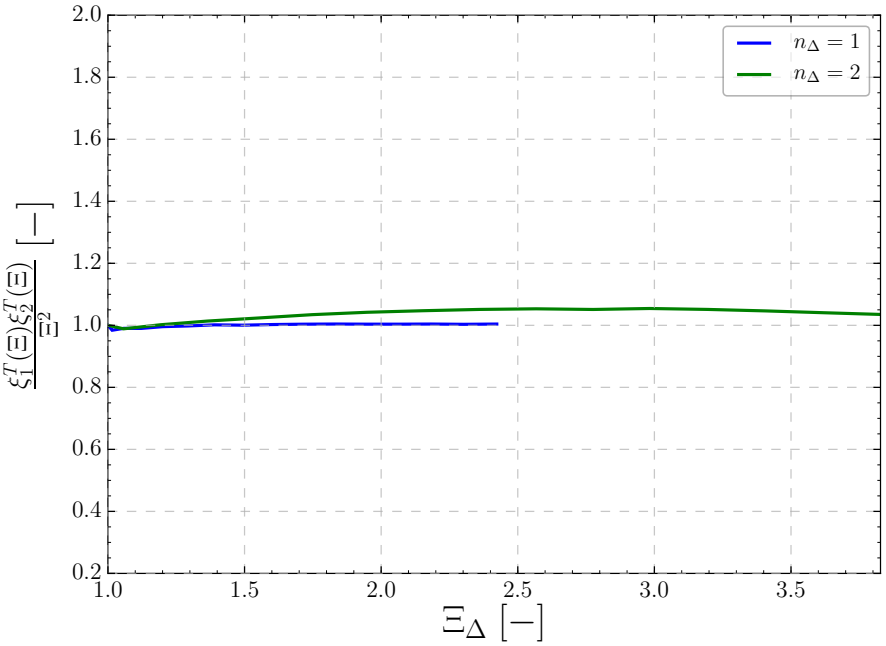

Figure 3.18: *Ratio* $\xi_1^T(\Xi_\Delta)\xi_2^T(\Xi_\Delta)/\Xi_\Delta^2$ *computed as a function of the wrinkling factor* Ξ_Δ *for* $\phi = 0.75$ *and* $\Delta = 2.5mm$. *Legend:* — $n_\Delta = 1$, — $n_\Delta = 2$.

shown in Fig. 3.17 for $\phi = 0.75$ and $\Delta = 4\delta_l^0$. The resulting functions are continuous for each value of n_Δ. Differences between the $n_\Delta = 1$ and $n_\Delta = 2$ cases are due to the different flame structures at a given SGS wrinkling factor. ξ_1^T is lower for $n_\Delta = 2$ than for $n_\Delta = 1$ because at a given wrinkling factor, the $n_\Delta = 1$ flame is thicker than the $n_\Delta = 2$ flame (see Fig. 3.14).

When it comes to propagation, the turbulent speed of a FWF flame scales as:

$$S_T^\Xi \propto \sqrt{\alpha_T^{*,\mathrm{FWF}} \widetilde{D}\overline{\dot{\Omega}}} \tag{3.63}$$

where $\overline{\dot{\Omega}}$ is the mean filtered reaction rate of the FWF flame, scaling as $\overline{\dot{\Omega}} \propto A_1^{*,\mathrm{FWF}}$. Substituting Eqs. (3.62b) and (3.62a) in Eq. (3.63):

$$S_T^\Xi \propto \sqrt{\xi_1^T \xi_2^T} \underbrace{\sqrt{\alpha_T^{*,\mathrm{FPF}} \widetilde{D} A_1^{*,\mathrm{FPF}}}}_{S_T^\Xi(\Xi_\Delta=1)=S_l^0} \tag{3.64}$$

Since $S_T^\Xi = \Xi_\Delta S_l^0$, the following relationship is obtained:

$$\frac{\xi_1^T\left(\Xi_\Delta, n_\Delta\right) \xi_2^T\left(\Xi_\Delta, n_\Delta\right)}{\Xi_\Delta^2} = 1 \tag{3.65}$$

This relationship is verified for optimized values of ξ_1^T and ξ_2^T in Fig. 3.18. This implies that the flame propagation is *a priori* well captured by the optimization procedure.

The ability of the optimized mechanism to capture flame structure is now *a posteriori* verified by comparing reference (wrinkled) and optimized flame solutions for different values of the wrinkling factor. This is illustrated in Fig. 3.19 for $\phi = 0.75$ and $\Delta = 4\delta_l^0$. The case $\Xi_\Delta = 1$ corresponds to the optimization on laminar premixed flames, highlighting the consistency between the models proposed in this chapter. An excellent agreement is moreover obtained with the optimized scheme for $\Xi_\Delta = 1.5$ and 2. In particular, the thermal flame thickness is very well predicted.

CO optimization An identical strategy is used to design the CO wrinkled optimized mechanism. The optimized coefficients of the CO sub-scheme for the laminar premixed flame ($\Xi_\Delta = 1$) are written:

$$\mathcal{A}_{CO}^{*,\mathrm{FPF}} = \left(A_4^{*,\mathrm{FPF}}, E_{a,4}^{*,\mathrm{FPF}}, F_{CO,2}^{*,\mathrm{FPF}}, F_{V1,2}^{*,\mathrm{FPF}}\right) \tag{3.66}$$

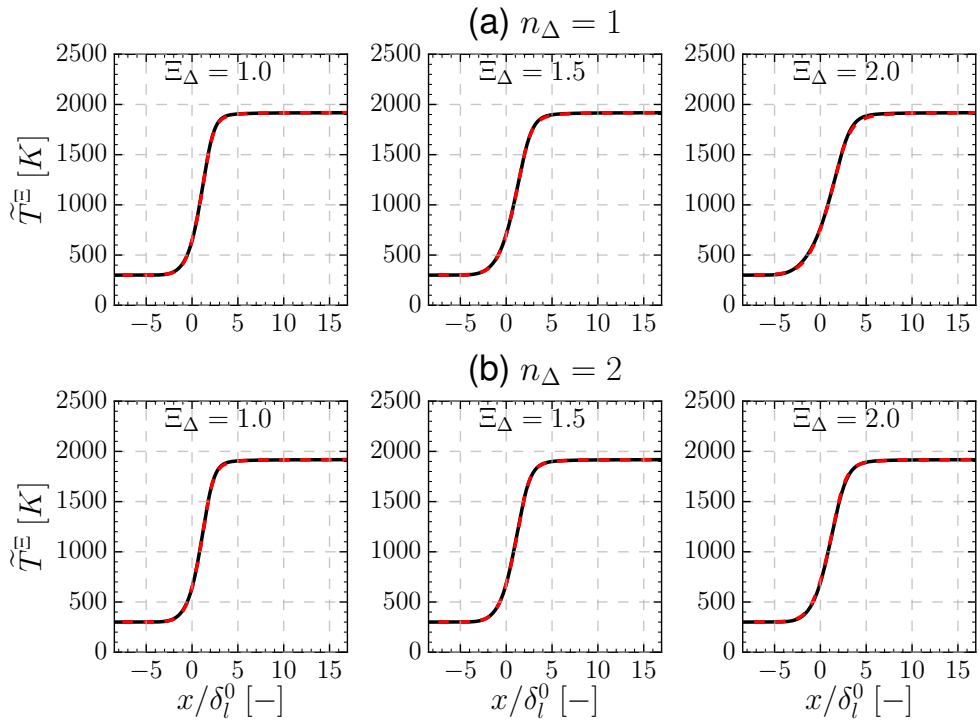

Figure 3.19: *Comparison between reference (wrinkled) and optimized temperature profiles for* $\phi = 0.75$ *and* $\Delta = 2.5mm$. *Legend:* — *Reference,* - - *Optimized.*

with a diffusive correction factor $\alpha_{CO}^{*,\mathrm{FPF}}$. The dependence of the mechanism on the wrinkling factors is done through the variation of A_4^* and α_{CO}^* as:

$$\begin{cases} \alpha_{CO}^{*,\mathrm{FWF}}(\phi, \Xi_\Delta, n_\Delta) = \xi_1^{CO}(\Xi_\Delta, n_\Delta)\, \alpha_{CO}^{*,\mathrm{FPF}}(\phi) & \text{(3.67a)} \\ A_4^{*,\mathrm{FWF}}(\phi, \Xi_\Delta, n_\Delta) = \xi_2^{CO}(\Xi_\Delta, n_\Delta)\, A_4^{*,\mathrm{FPF}}(\phi) & \text{(3.67b)} \end{cases}$$

where ξ_1^{CO} and ξ_2^{CO} are dimensionless factors. Resulting values of both factors are shown in Fig. 3.20. The continuity of the coefficients with Ξ_Δ is not as good as in the case of the main mechanism but still satisfying. As for temperature, differences in functions between $n_\Delta = 1$ and $n_\Delta = 2$ cases are due to differences in flame structure and the balance of local CO production/consumption.
Performance of the optimization is illustrated in Fig. 3.21 where reference and optimized CO mass fractions are compared for different value of the wrinkling factor and for flame sub-filter parameters $n_\Delta = 1$ and $n_\Delta = 2$. The optimized mechanism is very accurate for the whole range of computed flames. In particular, CO peaks and CO thicknesses are well recovered.

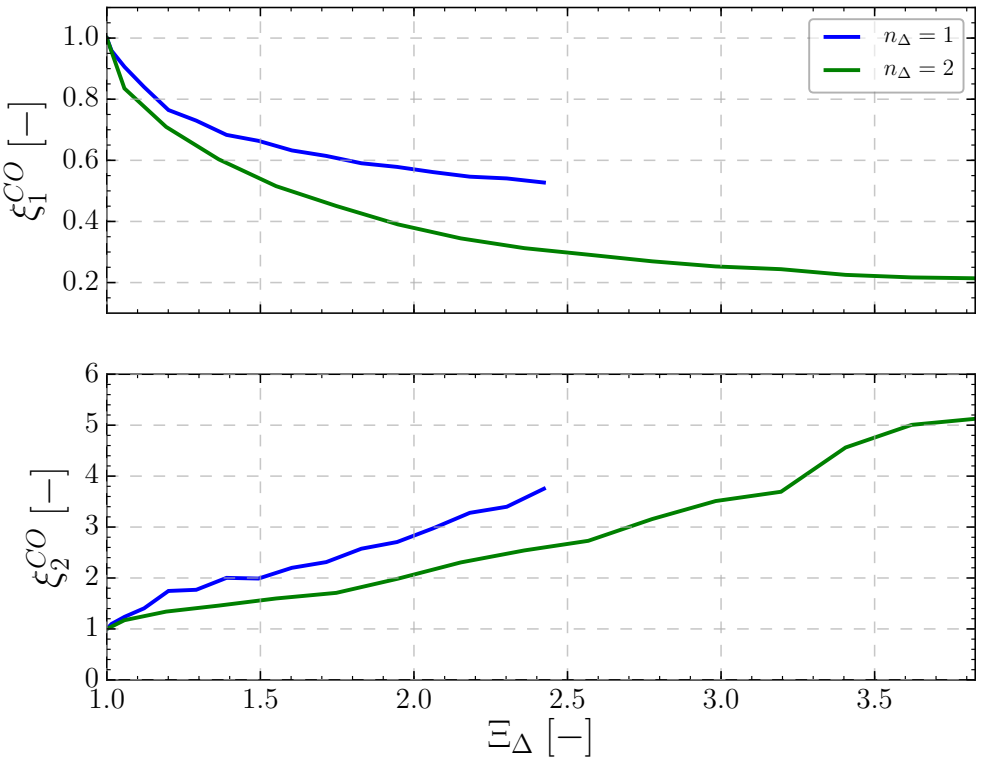

Figure 3.20: *Dimensionless factors* ξ_1^{CO} *and* ξ_2^{CO} *for* $\phi = 0.75$ *and* $\Delta = 2.5mm$. *Legend:* — $n_\Delta = 1$, — $n_\Delta = 2$.

3.5 Summary of equations of Filtered Optimized Chemistry model

In this chapter, a new modeling strategy baptized Filtered Optimized Chemistry has been proposed. It is based on the modification of Arrhenius parameters of existing chemical mechanisms. Coefficients are optimized by targeting filtered canonical flame. Two variants of the model have been suggested: (i) coefficients are calculated by using Filtered Planar Flames (FPF), leading to the FOC-FPF model; (ii) coefficients are computed by targeting newly developed mono-dimensional Filtered Wrinkled Flamelets (FWF), leading to the FOC-FWF model. In the former case, the influence of SGS wrinkling effects is modeled separately while in the latter the effects of SGS wrinkling on the flame structure is directly incorporated in the Arrhenius coefficients. This crucial distinction is highlighted in Fig. 3.22. A detailed summary of the model equations for turbulent premixed combustion in both cases is shown in this section.

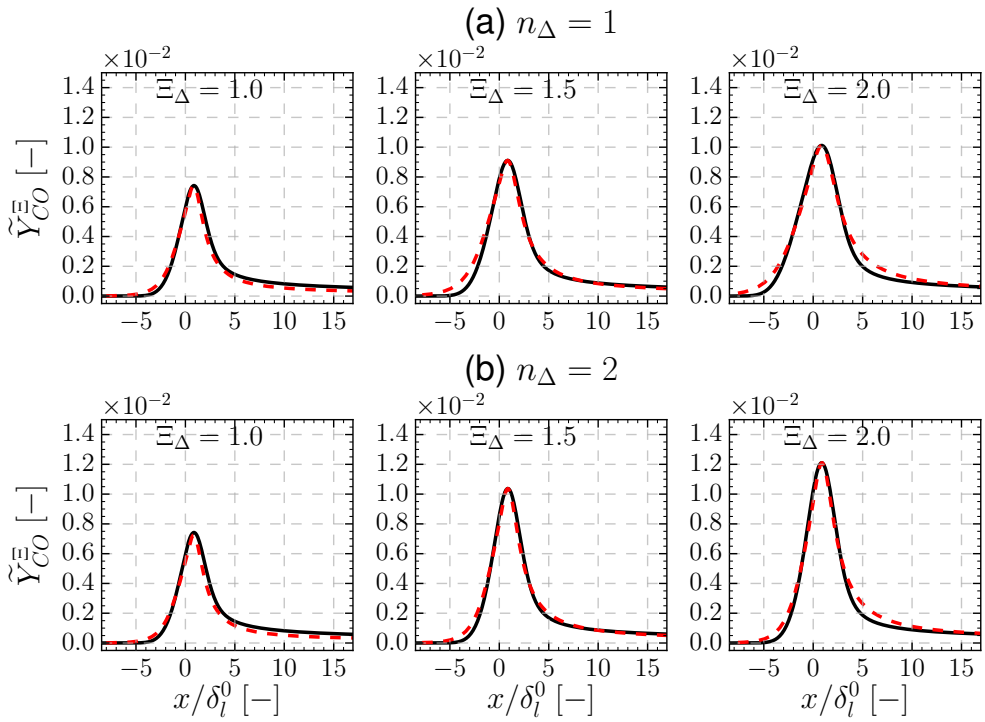

Figure 3.21: *Comparison between reference (wrinkled) and optimized CO mass fraction profiles for $\phi = 0.75$ and $\Delta = 2.5mm$. Legend: — Reference, - - Optimized.*

3.5.1 FOC-FPF model

When laminar premixed flames as used as optimization targets, scalars conservation equations in a low Mach and unity Lewis context read:

$$\begin{aligned}
&\frac{\partial \overline{\rho}\widetilde{Y_k}}{\partial t} + \nabla \cdot \left(\overline{\rho}\widetilde{u}\widetilde{Y_k}\right) = \nabla \cdot \left(\Xi_\Delta \alpha^{*,\mathrm{FPF}}(\phi)\overline{\rho}\widetilde{D}\nabla\widetilde{Y_k}\right) + \Xi_\Delta \overline{\rho}\widetilde{\dot{\omega}}_k^{\mathcal{A}^{*,\mathrm{FPF}}(\phi)} \\
&\frac{\partial \overline{\rho}\widetilde{h}}{\partial t} + \nabla \cdot \left(\overline{\rho}\widetilde{u}\widetilde{h}\right) = \nabla \cdot \left(\Xi_\Delta \alpha^{*,\mathrm{FPF}}(\phi)\widetilde{\lambda}\nabla\widetilde{T}\right) \\
&+ \nabla \cdot \left(\sum_{k=1}^{N_S} \overline{\rho}\Xi_\Delta \alpha^{*,\mathrm{FPF}}\widetilde{D}_k h_k \nabla\widetilde{Y_k}\right)
\end{aligned} \tag{3.68}$$

This set of equation is completed with a perfect gas equation: $p_0 = \overline{\rho}\widetilde{r}\widetilde{T}$ where p_0 is the thermodynamic pressure. Wrinkling is included by multiplying diffusive and reactive terms by the wrinkling factor Ξ_Δ. Ξ_Δ is computed using a Charlette model (Charlette et al. (2002a)).

3.5.2 FOC-FWF model

Alternatively, if wrinkled flamelets are used as optimization targets, conservation equations are:

$$\begin{aligned}
&\frac{\partial \overline{\rho}\widetilde{Y_k}}{\partial t} + \nabla \cdot \left(\overline{\rho}\widetilde{u}\widetilde{Y_k} \right) = \nabla \cdot \left(\alpha^{*,\mathrm{FWF}}(\phi, \Xi_\Delta, n_\Delta) \overline{\rho}\widetilde{D}\nabla\widetilde{Y_k} \right) + \overline{\rho}\widetilde{\dot{\omega}}_k^{\mathcal{A}^{*,\mathrm{FWF}}(\phi,\Xi_\Delta,n_\Delta)} \\
&\frac{\partial \overline{\rho}\widetilde{h}}{\partial t} + \nabla \cdot \left(\overline{\rho}\widetilde{u}\widetilde{h} \right) = \nabla \cdot \left(\alpha^{*,\mathrm{FWF}}(\phi, \Xi_\Delta, n_\Delta) \widetilde{\lambda}\nabla\widetilde{T} \right) \\
&+ \nabla \cdot \left(\sum_{k=1}^{N_S} \overline{\rho}\alpha^{*,\mathrm{FWF}}(\phi, \Xi_\Delta, n_\Delta) \widetilde{D}_k h_k \nabla\widetilde{Y_k} \right)
\end{aligned} \tag{3.69}$$

The perfect gas equation still holds as $p_0 = \overline{\rho}\widetilde{r}\widetilde{T}$. The wrinkling Ξ_Δ is again computed using a Charlette model but the inclusion in the conservation equations is directly done through the optimized Arrhenius and diffusive corrective factor optimization.

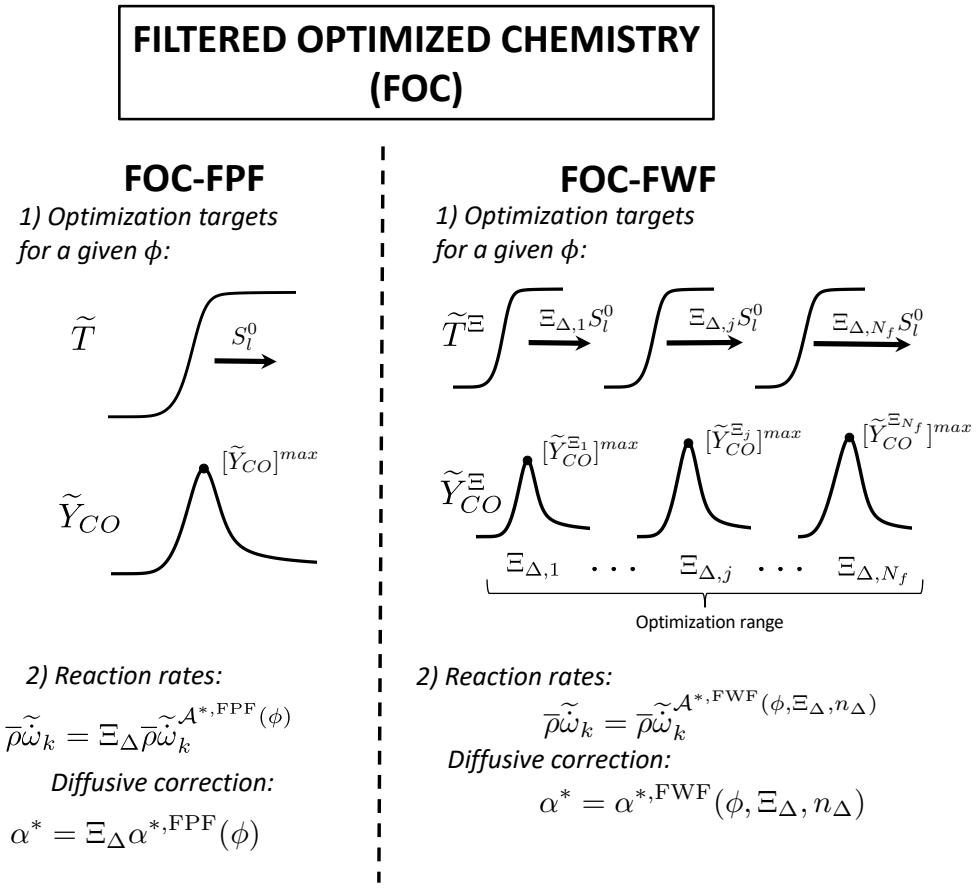

Figure 3.22: *Summary of Filtered Optimized Chemistry model.*

Chapter 4

Application to a premixed swirled burner

Contents

The FOC modeling strategy is validated on a turbulent premixed configuration. The Cambridge swirled burner is selected to challenge the model. The non-swirled configuration is simulated by using (i) the thickened flame model; (ii) the FOC-FPF model; (iii) the FOC-FWF. The same methodology is then applied in highly swirled operating conditions. The central role of wrinkling modeling to predict pollutants in the flame front is highlighted.

4.1 Presentation of the set-up

THE ability of a combustion model to capture flame propagation and structure is critical in turbulent premixed flames. The Filtered Optimized Chemistry (FOC) model has been shown to perform well in laminar premixed configurations and is now challenged on a 3-D turbulent configuration. The Cambridge swirled burner, jointly studied by teams in Cambridge University and Sandia National Laboratories (Sweeney et al. (2012a); Sweeney et al. (2012b)), has been selected in its premixed configuration to test the new modeling strategy. In this section, the burner is first presented and the choices made regarding the numerical set-up are then detailed.

4.1.1 Cambridge SwB burner

Burner geometry The Cambridge SwB burner is a bluff-body stabilized swirled burner which has been initially developed to improve knowledge about stratified combustion in situation where the swirl number is close to values found in industrial burners. Measures have been performed for three levels of stratification and three levels of swirl. Several measurement campaigns have led to data about flow fields (Zhou et al. (2013)), scalars, temperature, thermal gradients and flame curvature (Sweeney et al. (2012a); Sweeney et al. (2012b)) and wall temperature at the bluff-body (Euler et al. (2014)). The latter enables the inclusion of heat-losses effect in numerical models.

The burner is represented in Fig. 4.1 and is composed of a central bluff-body and two concentric annular tubes in which CH_4/air mixtures are flowing. A mixture with mean velocity U_i and equivalence ratio ϕ_i flows in the inner tube while a mixture of mean velocity U_o and equivalence ratio ϕ_o flows through the outer one. A much higher value is used for U_i than for U_o, giving rise to a strong shear layer promoting turbulence in the flame. In order to avoid entrainment effects, the burner is isolated from ambient air by a large co-flow with mean velocity U_{cf}. Varying swirl is generated by allowing part of the outer annulus mixture to flow through a swirl plenum prior to flowing in injection tubes. Both Cartesian and cylindrical coordinates systems are used in the work and are illustrated in Fig. 4.1. The burner axial coordinate is written z. The origin $z = 0$ is located at the burner nozzle. Planes perpendicular to the main axis

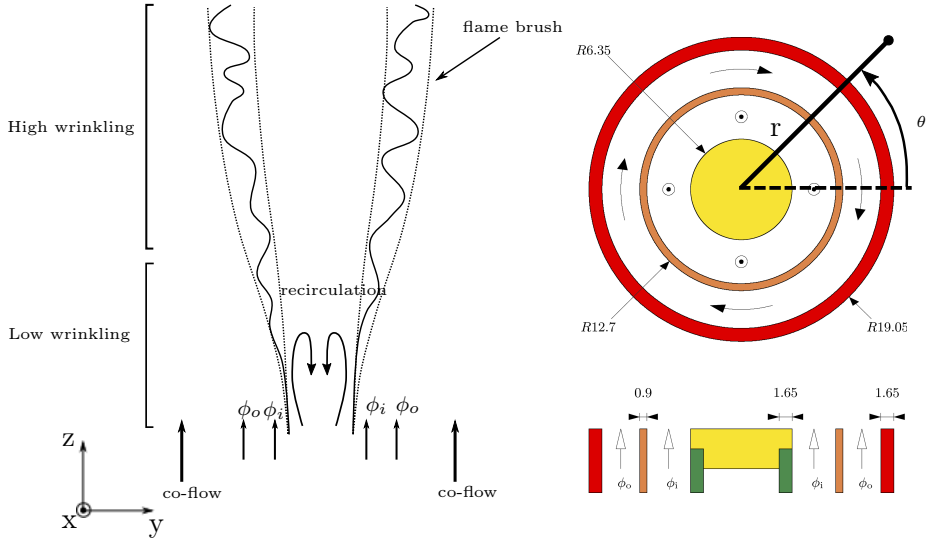

Figure 4.1: *Representation of the Cambridge SwB burner. On the left: sketch of the flame anchored at the burner. On the right: scheme representing the burner nozzle on top and side views.*

z are characterized by (x, y) in Cartesian coordinate system or equivalently by (r, θ) in cylindrical coordinate system.

Cambridge swirled burner in previous numerical works The large set of available experimental data and the complexity of physical phenomena taking place in the Cambridge SwB burner make it an ideal test case for LES combustion models. Recent simulations include the works of Nambully et al. (2014a) who tested a filtered laminar flame PDF closure model, Mercier et al. (2015) who used a tabulated filtered laminar flamelets model, Brauner et al. (2016) a transported FDF model and Proch and Kempf (2014) who used TFLES combined with tabulated chemistry. Most of the works exclusively focus on the non swirled cases (Mercier et al. (2015); Proch and Kempf (2014); Proch et al. (2017)) and only Brauner et al. (2016) and Mercier et al. (2018) have considered the swirling cases. Inclusion of stratification effects in LES has been tackled (Nambully et al. (2014b)), as well as the study of non-adiabatic effects (Mercier (2016)). A parametric study of wrinkling modeling on the non-swirled cases has also been carried out by Mercier et al. (2015).

Most of the LES studies of the Cambridge burner considered tabulated chemistry to include chemical effects. Only Brauner et al. (2016) reported results using transported chemistry and a 19-species mechanism coupled to a FDF transport closure strategy. While results are globally satisfying, transported FDF methods remain very expensive as explained in chapter 1.

Turbulent combustion parameters An analysis of the Cambridge burner features is provided by studying the turbulent parameters of the flow for the different operating conditions. These parameters have been experimentally measured by Zhou et al. (2013) using Laser Doppler Anemometry (LDA) near the burner exit and at the middle of the outer flow/outer tube and outer tube/inner tube shear layers (corresponding approximately to $z = 30$mm). The shear layer measures have been used to characterize the flame regime. This is illustrated in Fig. 4.2 where the reacting operating conditions are shown on a modified Borghi combustion diagram. It reveals that the flame operates in a thin reaction zone regime, where small eddy are unable to disrupt the reactive layers but are able to interact with thermal layers of flames. This physical feature often leads to increased flame thicknesses.

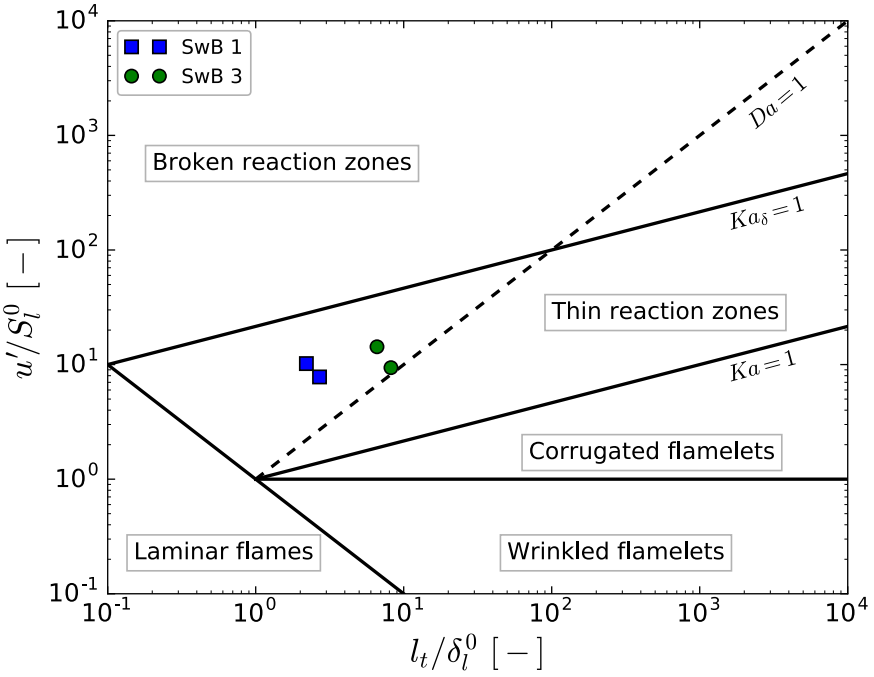

Figure 4.2: *Modified Borghi diagram illustrating the turbulent regimes of the SwB burner for SwB1 (squares) and SwB3 (circles) cases. Turbulent parameters are extracted at $z = 30mm$ for two different radius in each case (Zhou et al. (2013)).*

4.1.2 Numerical set-up and simulated operating conditions

Simulated cases The work in this chapter focuses on premixed operating conditions of the Cambridge burner. Simulations are performed for the corresponding non-swirled and highly swirled cases, as summarized in Tab. 4.1. SR stands for Stratification Ratio and is defined as $SR = \phi_i/\phi_o$. SFR is the Swirl Flow Ratio and measures the ratio of outer annulus flow passing through

a swirl plenum relative to the total flow in the outer annulus.

Table 4.1: *Simulated configurations of the SwB burner and associated parameters.*

	Flow				Mixtures		
Case	SFR (%)	U_i (m/s)	U_o (m/s)	U_{cf} (m/s)	SR (-)	ϕ_i (-)	ϕ_o (-)
cSwB1	0	8.31	18.7	0.4	-	0	0
SwB1	0	8.31	18.7	0.4	1	0.75	0.75
cSwB3	33	8.31	18.7	0.4	-	0	0
SwB3	33	8.31	18.7	0.4	1	0.75	0.75

LES solver The low Mach number code YALES2 (Moureau et al. (2011a)) is retained to perform computations. The solver features a fourth-order finite volume discretization for spatial integration and a fourth-order time integration using an explicit temporal scheme. Artificial viscosity is introduced in the solving where required in order to stabilize the computation. This is done through introducing a fourth order dissipation term as proposed by Cook and Cabot (2004).

Meshes Two different meshes are used for the simulation of the swirled and non-swirled cases. The reason is twofold:

- The flame shape varies significantly between swirled and non-swirled cases, as seen in the experimental works of Sweeney et al. (2012b) and Zhou et al. (2013). The non-swirled flame is similar to a jet flame while the swirled flame has a conical shape with a wide opening angle.
- Experimental mean and RMS flow fields obtained by Zhou et al. (2013) are shown in Fig. 4.3 for SwB1 and SwB3 cases. The recirculation zone of the flow is contained in a small region downstream the burner in non-swirling flow while it opens up in the reacting swirling case (bottom right of Fig. 4.3). This recirculation pattern triggers the need for a larger domain in the swirling operating condition to diminish the influence of side walls boundary conditions.

Both meshes have the same resolution $\Delta_x = 0.5$mm within the flame front. As $\Delta_x \approx \delta_l^0(\phi = 0.75)$ for a CH_4/air flame, the flame front is unresolved on the LES grid and an artificial broadening is required. The refined mesh region has a constant radius in the non swirled case and a radius increasing with z in the swirled case. Both meshed domains are axi-symmetric and in the swirled case the computed volume is larger than in the non-swirled case to avoid undesired effects due to the large zone of gas recirculation. The flow is computed in the tubes upstream the burner exit from $z = -120$mm, while it develops from

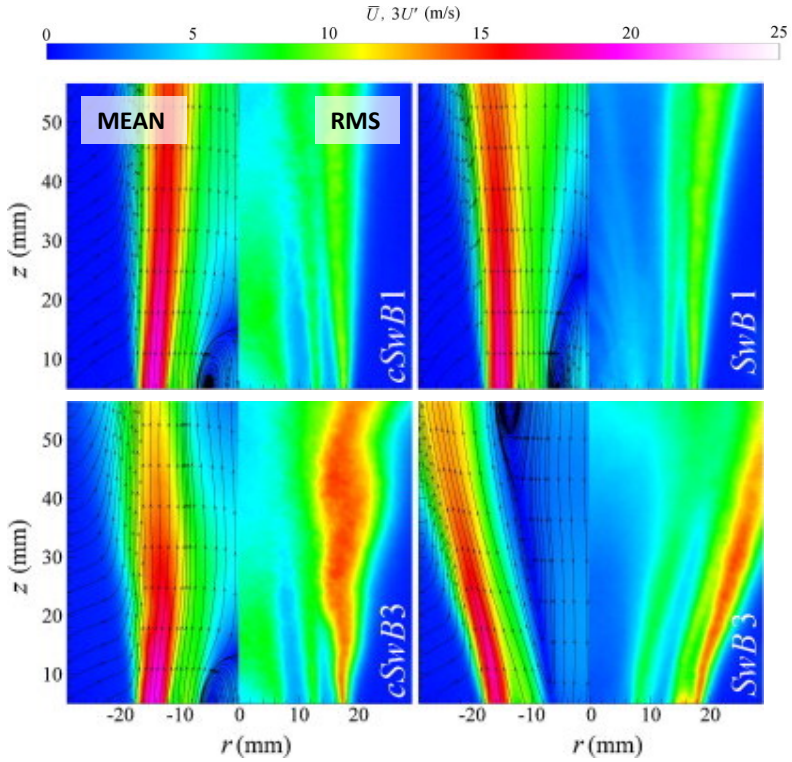

Figure 4.3: *Experimental mean ($r < 0$mm) and fluctuating ($r > 0$mm) velocities for non-swirling (top) and highly swirling (bottom) premixed operating conditions. Left column is non-reacting and right is reacting. (Zhou et al. (2013))*

$z \approx -250$mm in the experiment. Characteristics of the two meshes M30 and M100, dedicated to SwB1 and SwB3 cases respectively, are given in Tab.4.2. A x-normal slice is illustrated in Fig. 4.4 and highlights the conically shaped refined area of the M100 mesh.

Table 4.2: *Meshes used for the simulation of the Cambridge burner.*

Mesh	Cases	Nb of cells	Nb of nodes	Δ_x in flame front
M30	SwB1c, SwB1	30 Millions	6 Millions	0.5mm
M100	SwB3c, SwB3	97 Millions	18 Millions	0.5mm

Boundary conditions The flow through inlet boundaries is assumed axi-symmetric and the mean field is thus written $(U_r(r), U_\theta(r), U_z(r))$ in polar coordinates. The following parabolic laws are used to prescribe the axial inlet

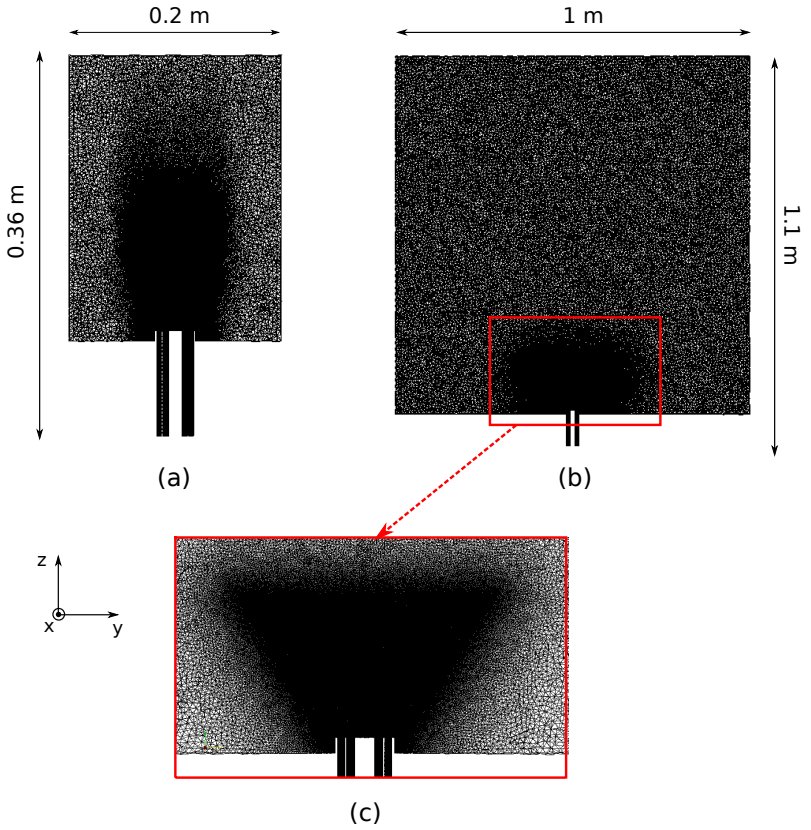

Figure 4.4: *X-normal slice of the M30 and M100 meshes. (a) M30 mesh. (b) M100 mesh. (c) zoom on the conical refined area of M100.*

flow field:

$$U_z(r) = U_z^{max}\left(1 - \left(\frac{2d(r)}{r_o - r_i}\right)^4\right) \tag{4.1}$$

where,

$$d(r) = r - \frac{r_i + r_o}{2} \tag{4.2}$$

where r_i and r_o are respectively the radius of the inner and outer walls of the considered injection stream. U_z^{max} is 10.5 m/s in the inner tube and 22.4 m/s in the outer tube. In non-reacting and reacting swirling cases SwB3c and SwB3, a parabolic function is also used for defining the tangential velocity field in the

outer tube:

$$U_\theta(r) = U_\theta^{max}\left(1 - \left(\frac{2d(r)}{r_o - r_i}\right)^4\right) \tag{4.3}$$

U_θ^{max} is set to 18 m/s. In both SwB1 and SwB3 cases, $U_r(r) = 0$. Homogeneous isotropic turbulence is added at the inlet to match the experimental fluctuation values at the burner exit measured at $z = 2$mm (See profiles in Fig. 4.8). The turbulent intensity is set to 10 % while the integral length scale is $L_t = 3$mm (approximately one fourth of the hydraulic diameter of the system).

Heat losses at the burner bluff body Heat losses have been reported at the bluff body of the Cambridge burner, and detailed measurements using phosphor thermometry have been carried out (Euler et al. (2014)). Heat losses are significantly more important for the SwB3 case than for SwB1 and are thus only taken into account for the former case in this study. The evolution of the surface temperature with the radius is well reproduced by a linear function which is easily imposed as a boundary condition in the 3-D computation:

$$T_{bb}(r) = T_1 + \frac{T_2 - T_1}{R_{bb}} r \tag{4.4}$$

where T_{bb} is the bluff-body surface temperature, $R_{bb} = 6.35$mm the bluff-body radius, and $T_1 = 590K$ and $T_2 = 540K$ are respectively the approximated temperatures at the center and at the outer edge of the bluff body for the SwB3 case.

Turbulence closure Turbulence closure is performed by using the Sigma model developed by Nicoud et al. (2011), which has led to good results on this configuration in previous studies (Mercier et al. (2015)).

4.2 Comparison between LES and experimental statistics

Statistics of thermo-chemical fields - mean and variance - are conventionally selected to perform model validations. Some definitions are provided in Sec. 4.2.1, along with some elements about the comparison between simulation and experimental datasets in Sec. 4.2.2. A particular effort is done in this work to compare experimental and numerical pollutants mass fraction fields in a consistent way.

4.2.1 Definitions

LES statistical means A Reynolds average in time is obtained by averaging Favre filtered thermo-chemical quantities $\widetilde{\varphi}$ over a period T:

$$\langle\widetilde{\varphi}\rangle(\mathbf{x}) = \frac{1}{T}\int_0^T \widetilde{\varphi}(\mathbf{x},t)dt \tag{4.5}$$

A mass weighted Favre-average $\{\widetilde{\varphi}\}$ in time is also defined as:

$$\{\widetilde{\varphi}\}(\mathbf{x}) = \frac{\langle\overline{\rho}\widetilde{\varphi}\rangle(\mathbf{x})}{\langle\overline{\rho}\rangle(\mathbf{x})} \tag{4.6}$$

Experimental statistical means The spatial resolution of experimental data is given by the size of the probes used to perform measures. Probe volumes indeed act as spatial filters characterized by an averaging radius, written Δ_{exp}, which depends on the instrumentation. In the case of the Cambridge burner, temperature and major species measurements are limited by the sampling resolution of $103\mu m \approx \delta_l^0/5$ and the laser beam diameters of $220\mu m \approx \delta_l^0/2$ (Sweeney et al. (2012b)). As $\Delta = 4\delta_l^0$ is used for model validation, the LES filter size is significantly larger than the experimental averaging radius ($\Delta >> \Delta_{exp}$). The experimental filtering is thus neglected and instantaneous experimental thermo-chemical variables are written φ_{exp}.

The selected experimental techniques also influence the nature of statistical time averaging. Kamal et al. (2015) have for example shown that for velocity fields measurements, Laser Doppler Anemometry (LDA) corresponds to Favre averages in time $\{\varphi_{exp}\}$ while Particle Image Velocimetry (PIV) corresponds to Reynolds averages $< \varphi_{exp} >$. This is due to the physical principles involved in the measurement process: in LDA bursts of particles are detected and the measure is hence proportional to a local density, while in PIV images are averaged and thus only the number of particle is significant.

LES and experimental variances The local statistical mass weighted variance of a quantity φ is defined as $\{\varphi^2\} - \{\varphi\}^2$. In LES, the variance is split into resolved and sub-grid contributions (Veynante and Knikker (2006)):

$$\{\varphi^2\} - \{\varphi\}^2 \approx \underbrace{\frac{1}{\langle\overline{\rho}\rangle}\left(\langle\overline{\rho}(\widetilde{\varphi})^2\rangle - \frac{\langle\overline{\rho}\widetilde{\varphi}\rangle^2}{\langle\overline{\rho}\rangle}\right)}_{\text{Resolved}} + \underbrace{\frac{1}{\langle\overline{\rho}\rangle}\left\langle\overline{\rho}\left(\widetilde{\varphi^2} - (\widetilde{\varphi})^2\right)\right\rangle}_{\text{Subgrid}} \tag{4.7}$$

As only the resolved contribution is computed in the present work, variances estimated from LES are expected to be smaller than experimental values.

4.2.2 Comparison between LES and experimental means

When the filter size Δ is not small compared to the mean flame brush, the effect of the LES filter on the averaged quantities is not negligible. The issue is presented here and a methodology for comparing LES and experimental means in those situations is proposed. The focus is made on CO mass fractions.

A major issue is the rigorous comparison between averaged filtered LES quantities and averaged experimental quantities. Favre averages in time and space are here considered. $\{\widetilde{\varphi}\}$ is computed in LES while in experiments $\{\widetilde{\varphi}_{exp}\} \approx \{\varphi_{exp}\}$ is measured. Veynante and Knikker (2006) state that if the LES filter size is small compared to the mean flame brush δ_T ($\delta_T >> \Delta$), the filter influence can be neglected in LES:

$$\{\widetilde{\varphi}\}(\mathbf{x}) \approx \{\varphi\}(\mathbf{x}) \tag{4.8}$$

and thus $\{\widetilde{\varphi}\}$ and $\{\varphi_{exp}\}$ can be compared to validate models.

A mean flame brush δ_T^{exp} is defined as the thickness of the mean experimental temperature for the Cambridge burner[1]. δ_T^{exp} is shown in Fig. 4.5 for SwB1 and SwB3 flame configurations at different positions z. The filter size $\Delta = 4\delta_l^0 =$ 2.5mm is added on the figure. The condition $\delta_T^{exp} >> \Delta$ holds for any position in the SwB3 case except $z = 10$mm, but not for the SwB1 operating conditions where the mean flame brush is of the order of magnitude of Δ. Issues thus arise for the comparison between experimental and LES statistics and the effects of LES filtering on time averages have to be assessed.

Manufactured 1-D flame brush. An analysis derived from the study of Vervisch et al. (2010) is performed to evaluate the impact of LES filtering on time averages. A mean turbulent flame brush is mimicked by using 1-D unstrained premixed laminar flames. These flames are randomly generated over a spatial domain having a size equal to a turbulent flame brush δ_T, and consequently averaged. Instantaneous CO mass fraction and density profiles are defined for that purpose as:

$$\begin{cases} Y_{CO}(x,t) = Y_{CO,L}\left(x - x_L(t)\right) & \text{(4.9a)} \\ \rho(x,t) = \rho_L\left(x - x_L(t)\right) & \text{(4.9b)} \\ x_L(t) = x_0 + \mathcal{N}(t)\delta_T & \text{(4.9c)} \end{cases}$$

[1] Thickness is here defined by the spatial length where the flame mean temperature evolves between 5 % and 95 % of $T_{eq} - T_0$, where T_{eq} is the equilibrium value and T_0 the fresh gases temperature.

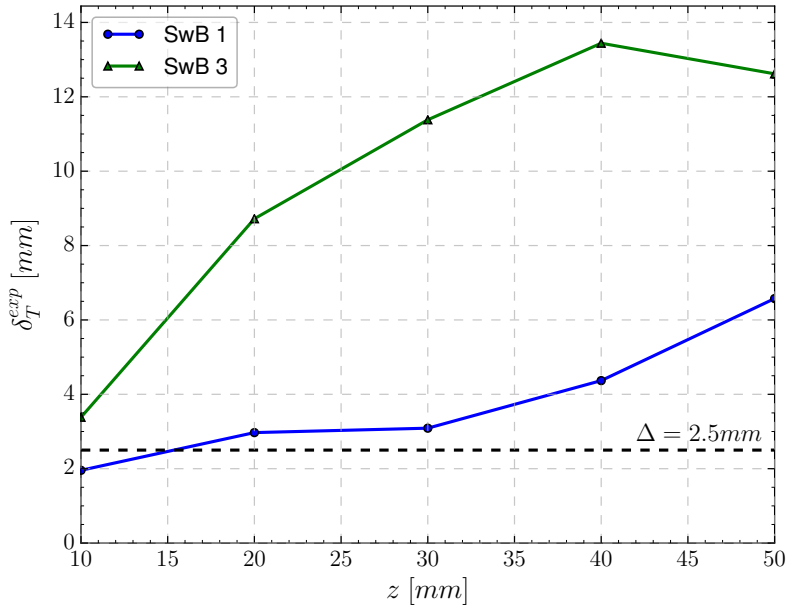

Figure 4.5: *Flame brush as a function of the axial distance to the burner nozzle z for cases SwB1 and SwB3. Legend: ●—● SwB1. ▲—▲ SwB3.*

where $Y_{CO,L}$ and ρ_L are respectively the CO mass fraction and density obtained from the computation of a 1-D laminar unstretched premixed flame using detailed chemistry and detailed transport. x_0 is the mean flame position and $\mathcal{N}(t)$ a truncated normal distribution. Favre averaged CO mass fraction $\{Y_{CO}\}$ is computed from the manufactured instantaneous $Y_{CO}(x,t)$ and $\rho(x,t)$ profiles. Additionally, a flame brush of Favre-filtered CO mass fraction and Reynolds filtered density is constructed as:

$$\begin{cases} \widetilde{Y}_{CO}(x,t) = \widetilde{Y}_{CO,L}\left(x - x_L(t)\right) & \text{(4.10a)} \\ \overline{\rho}(x,t) = \overline{\rho}_L\left(x - x_L(t)\right) & \text{(4.10b)} \end{cases}$$

The time averaged quantity $\{\widetilde{Y}_{CO}\}$ mimics a LES mean profile while $\{Y_{CO}\}$ mimics a Favre averaged experimental profile.

The manufactured flame brush is built for $\delta_T \approx 4\Delta/5$, which corresponds to the mean flame brush of the SwB1 case at $z = 10$mm. The generated flame brush is illustrated in Fig. 4.6, where dashed lines represent instantaneous flame fronts built with the methodology described above. The time averaged statistics $\{\widetilde{Y}_{CO}\}$ and $\{Y_{CO}\}$ are added on the figure. It is observed that $\{\widetilde{Y}_{CO}\} \neq \{Y_{CO}\}$. This highlights the difficulties for comparing simulated and experimental data when the condition $\delta_T >> \Delta$ is not satisfied.

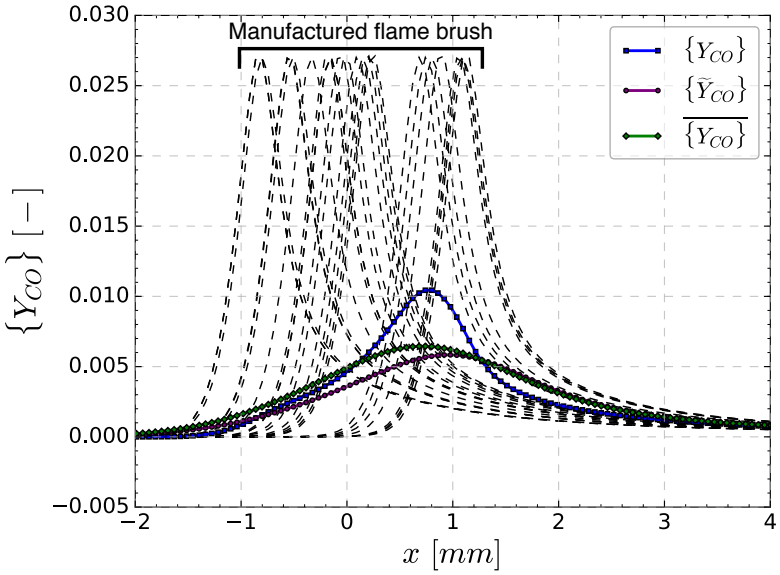

Figure 4.6: *Manufactured Y_{CO} flame brush using 1-D unstrained laminar flames at $\phi = 0.75$ and associated non-filtered and filtered mean quantities. Legend:* **- -** *Samples of 1-D unstrained flames.* ■—■ *Mean of unstrained flames $\{Y_{CO}\}$.* ●—● *Mean of Favre-filtered unstrained flames $\{\widetilde{Y}_{CO}\}$.* ♦—♦ *Reynolds-filtered mean of unstrained flames $\overline{\{Y_{CO}\}}$.*

Methodology for comparing experimental and simulated data The average $\{Y_{CO}\}$ is then filtered with the Gaussian LES filter to get $\overline{\{Y_{CO}\}}$, which is added in Fig. 4.6. The $\overline{\{Y_{CO}\}}$ profile is close to $\{\widetilde{Y}_{CO}\}$. The following approximation is thus proposed:

$$\{\widetilde{Y}_{CO}\} \approx \overline{\{Y_{CO}\}} \tag{4.11}$$

As $\{Y_{CO}\}$ mimics experimental measures, Eq. (4.11) suggests that filtered experimental statistics are a good approximation to LES statistics when δ_T is close to Δ. The experimental profiles of the Cambridge burner will hence be filtered to conduct model validation.

4.3 Non-swirled premixed operating condition (SwB1)

The non-swirled premixed configuration SwB1 is first investigated. It has been the focus of several numerical studies using different turbulent combustion models (Proch et al. (2017); Proch and Kempf (2014); Nambully et al. (2014b)). The non-reacting case is simulated in Sec. 4.3.1 and the reacting case results are then presented in Sec. 4.3.2 and 4.3.3 for simulations using (i) a dynamic TFLES model; (ii) the FOC-FPF model and (iii) the FOC-FWF model.

4.3.1 Non-reacting case

The non-reacting case SwB1c is computed on the M30 mesh. The mesh resolution is sufficient to capture flow field statistics and mixing according to the mesh refinement analysis done by Mercier (2016).
Mean and RMS flow statistics are shown respectively in Fig. 4.7 and 4.8 for $z = 2$, 10, 30 and 50mm. A good overall agreement is obtained for mean values. Only a small over-estimation of axial velocity is observed for $z = 30$mm and $z = 50$mm. Radial velocities are slightly over-estimated as well. The narrow recirculation zone observed in experiments, typical of bluff-bodies, is well-predicted as seen on the $z = 10$mm plot of axial velocity.
RMS values also show a good overall agreement with however some inaccuracies far from the burner nozzle for axial and radial velocities, and close to the burner for tangential velocities. This validates the level of turbulent fluctuations imposed at the tube inlets.

4.3.2 Reacting SwB1 case with FOC-FPF

The FOC-FPF model presented in Sec. 3.3 is first challenged. It is based on the optimization of Arrhenius and diffusive correction parameters on filtered 1-D unstrained laminar premixed flames computed using a virtual mechanism for temperature and CO prediction. Wrinkling is included separately by multiplying both diffusive and reactive contribution by a wrinkling factor as indicated in Sec. 3.3.4.

4.3.2.1 Modeling details

Filtered chemical mechanism The LES filter size is set to $\Delta = 4\delta_l^0$. Chemistry is introduced in the simulation using the virtual chemical mechanism. The optimized chemistry model has been built for $\phi = 0.5$ to 0.75 to account for dilution effects far from burner exit. As argued in experimental analyses (Sweeney et al. (2012a)), internal structures of flames conditioned on equivalence ratio are well approximated by unstrained laminar premixed flames. Equivalence ratio sub-grid fluctuations are thus neglected here, so that $\mathcal{A}^*(\phi) = \mathcal{A}^*(\widetilde{\phi})$ and $\alpha^*(\phi) = \alpha^*(\widetilde{\phi})$.

Sub-grid scale wrinkling model Sub-grid scale wrinkling is modeled using the modified Charlette model (Wang et al. (2011)):

$$\Xi_\Delta = \left(1 + min\left[\frac{\Delta}{\delta_l^0} - 1, \Gamma_\Delta \frac{u'_\Delta}{S_l^0}\right]\right)^\beta \tag{4.12}$$

with $\beta = 0.5$ and a Prandt-Kolmogorov model for u'_Δ.

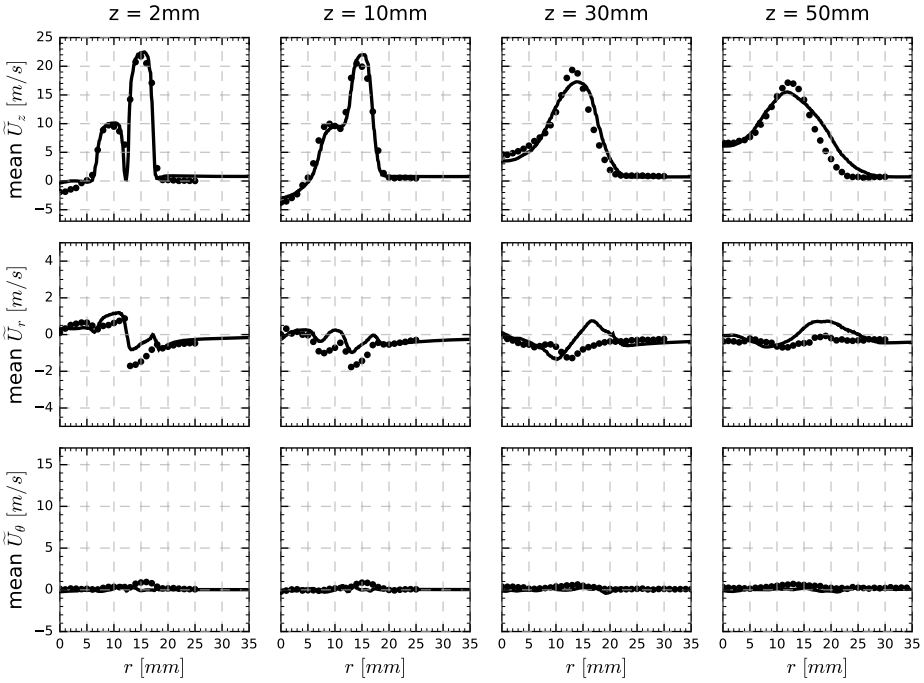

Figure 4.7: *Radial profiles of mean axial, radial and tangential velocities for the non-reacting case SwB1c at z=2, 10, 30 and 50mm from the burner nozzle. Legend: — Simulated profiles on mesh M30. • • Experimental data.*

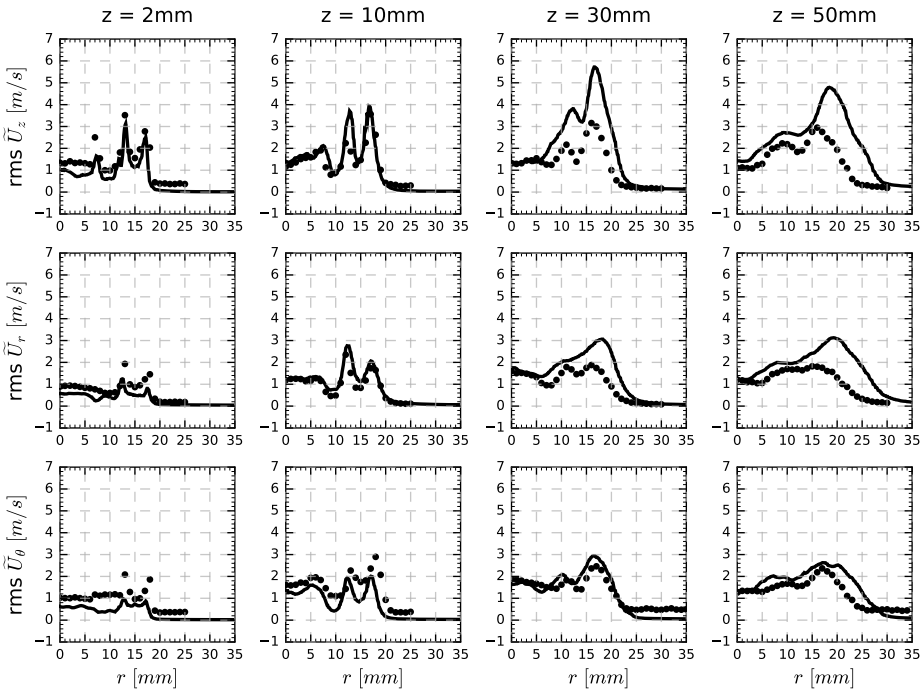

Figure 4.8: *Radial profiles of RMS axial, radial and tangential velocities for the non-reacting case SwB1c at z=2, 10, 30 and 50mm from the burner nozzle. Legend: — Simulated profiles on mesh M30. • • Experimental data.*

Comparison with the TFLES modeling strategy The FOC-FPF model is compared to the TFLES model using the virtual chemical mechanism for temperature and CO. A dynamic formulation is used and the thickening factor is computed from mesh resolution (Legier et al. (2000)). The M30 mesh yields values around 4 to 5 for the thickening factor $\mathcal{F}$ in the flame front.

4.3.2.2 Results

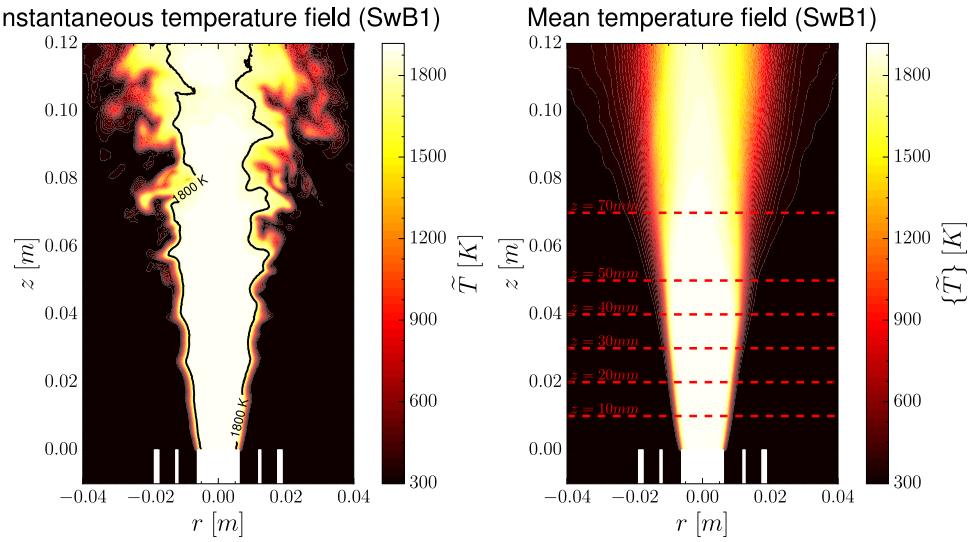

Figure 4.9: *2-D fields of instantaneous and averaged temperature for SwB1 case with FOC-FPF modeling. These fields are obtained by $\theta = 0$. On the left: instantaneous temperature field for a given time. On the right: averaged temperature field.*

An illustration of the flame computed with the FOC-FPF model is provided in Fig. 4.9, where a 2-D representation of the flame in the plane defined by $x = 0$ is proposed. An instantaneous temperature field is shown on the left while the averaged temperature field is shown on the right. Locations of the available experimental statistics for scalars is highlighted. As seen on the instantaneous temperature field, the simulated flame front is quasi-laminar upstream and wrinkled downstream. The flame has the shape of a jet flame with a small opening angle.

Simulated mean components of the velocity field are displayed in Fig. 4.10 and associated RMS in Fig. 4.11. TFLES and FOC-FPF models yield similar results when it comes to mean and RMS flow features. The simulated axial velocities are well captured for $z > 10$mm. For $z = 2$mm and $z = 10$mm, the magnitude of the axial velocity is well predicted but the strength of the recirculation zone, located in the region $r < 5$mm, is under-predicted. Radial mean velocities predictions are above experimental values in the outer region of the flow. RMS

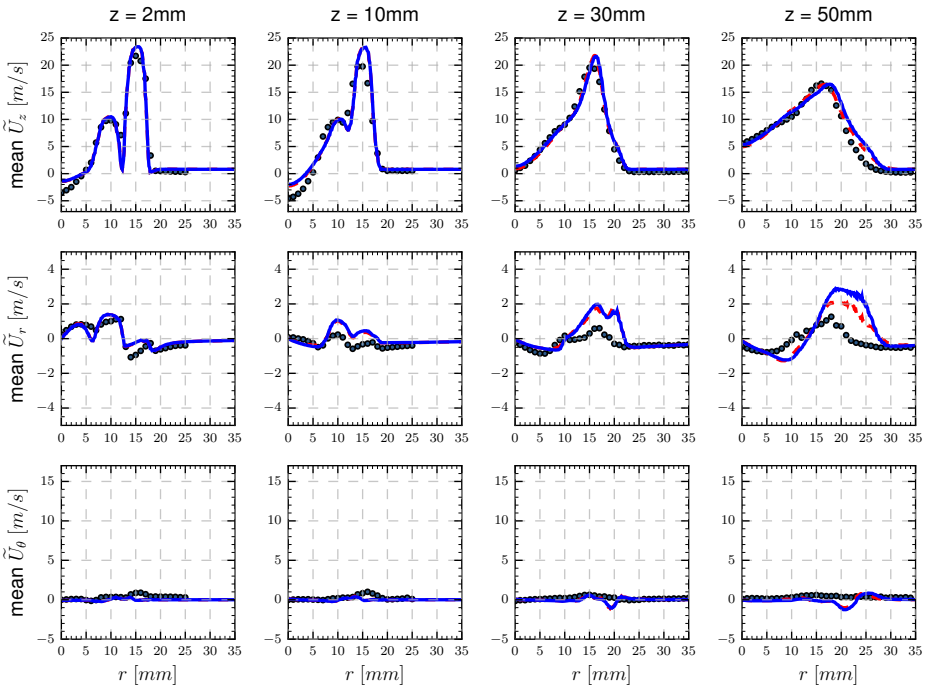

Figure 4.10: *Radial profiles of mean axial, radial and tangential velocities for the reacting non-swirled case SwB1 at z=2, 10, 30 and 50mm from the burner nozzle. Legend: • • Experimental data. - - TFLES model. — FOC-FPF model.*

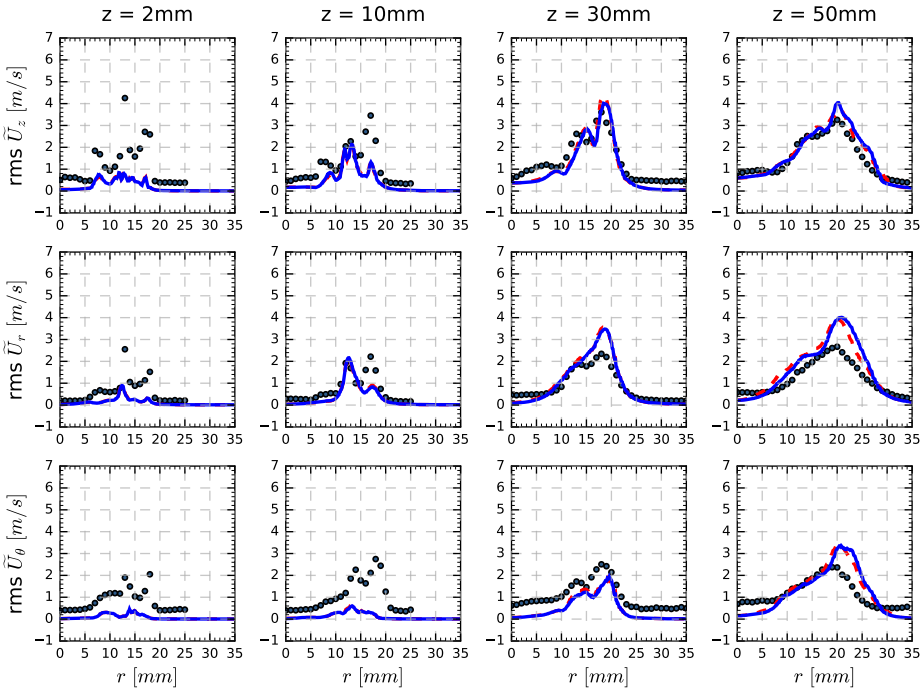

Figure 4.11: *Radial profiles of RMS axial, radial and tangential velocities for the reacting non-swirled case SwB1 at z=2, 10, 30 and 50mm from the burner nozzle. Legend: • • Experimental data. - - TFLES model. — FOC-FPF model.*

value are weaker than experimental measures close to the burner nozzle but fluctuation levels tend to be correctly predicted for $z > 10$mm.

The mean and RMS temperature fields obtained with TFLES and the FOC-FPF models are illustrated in Figs. 4.12 and 4.13. Experimental and simulated RMS have been each divided by the maximal mean temperature, so that they are expressed as a fraction of this maximal temperature[2]. The flame opening angle is well predicted by both models, with only a slight over-estimation when using the FOC-FPF model, and thus suggest a correct estimation of flame propagation speeds. Regarding the flame structure, TFLES predicts a larger post-flame zone. This is especially visible for axial positions $z = 10$ to 30mm. This feature has been reported on other configurations simulated with the TFLES model (Auzillon et al. (2011)). The temperature is incorrectly captured for $z = 70$mm regardless of the combustion model. This suggests an inadequate modeling of the flame/turbulence interaction in this flow region and may be attributed to the too coarse grid elements. A similar behavior has been observed in Nambully et al. (2014b) using a filtered based flamelet model. Simulated RMS temperature levels plotted in Fig. 4.13 underestimate experimental data. This is consistent with the fact that the sub-grid scales fluctuations in Eq. (4.7) are not included in the numerical solution. Fluctuations are however much smaller than experimental values in the near flame zone while they are of the same order of magnitude than experiments downstream.
Finally, mean CO mass fraction profiles are shown in Fig. 4.14 for TFLES and FOC-FPF models. Note that the experimental profiles have been explicitly filtered following the methodology described in Sec. 4.2.2. A non-filtered experimental profile is added for $z = 10$mm to highlight the difference (green squares). The main observation is that TFLES widely over-estimates experimental CO levels, whether filtered or non-filtered, while FOC-FPF under-estimates them. A significant improvement of CO mean prediction is however reached with the FOC-FPF model. The over-estimation of CO in TFLES simulation is in line with the analysis made in Sec. 1.2.4, where it has been shown that thickening a flame causes the amount of CO to be multiplied by the thickening factor $\mathcal{F}$. It is here emphasized by adapting the flame brush analysis made in Sec. 4.2.2 to thickened flames:

- An experimental flame brush is mimicked by Favre-averaging a set of randomly positioned premixed laminar flames obtained with detailed chemistry and detailed transport at equivalence ratio $\phi = 0.75$. This leads to a Favre average $\{Y_{CO}\}$ (black color in Fig. 4.15).

[2]Since maximal temperature are the same for TFLES and FOC-FPF, the relative difference between RMS is not affected. This is however not the case for pollutants RMS where maximal pollutant values depend strongly on the model and comparing non-normalized profiles can mislead the modeller.

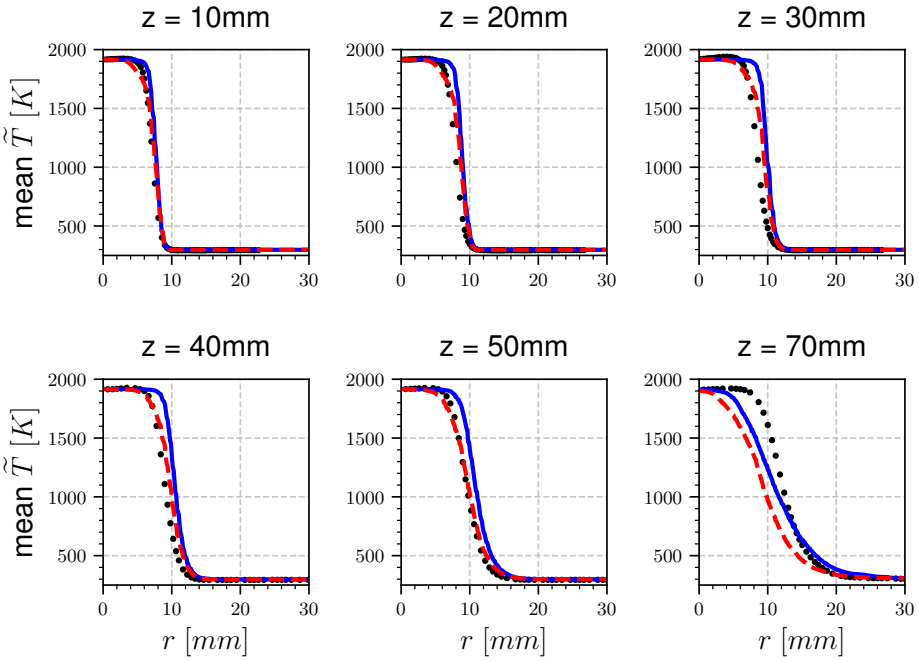

Figure 4.12: *Radial profiles of mean temperature for the reacting non-swirled case SwB1 at z=10, 20, 30, 40, 50 and 70mm from the burner nozzle. Legend: • • Filtered experimental data. - - TFLES model. — FOC-FPF model.*

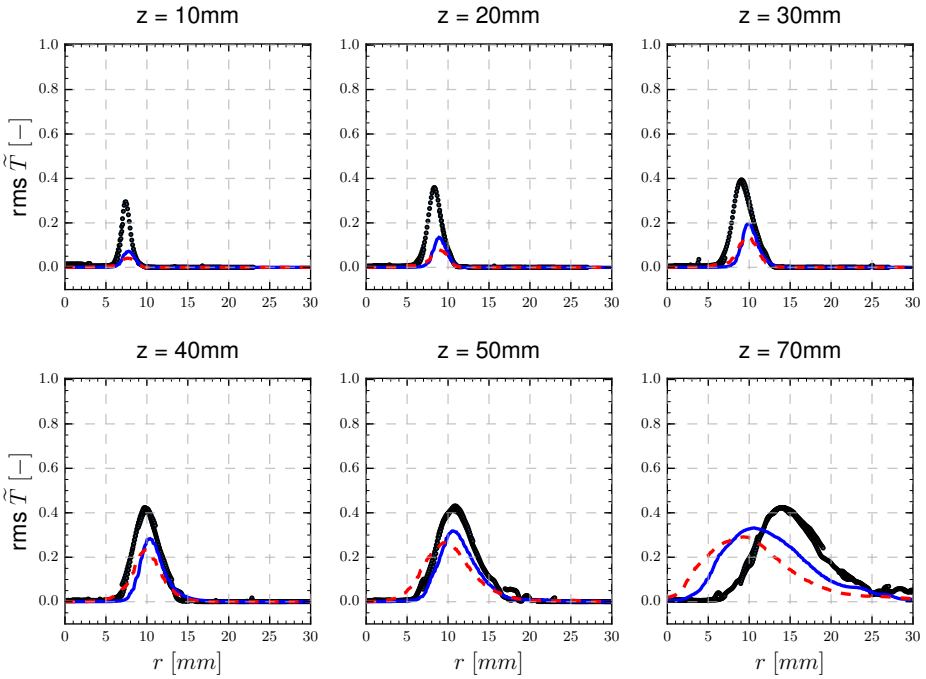

Figure 4.13: *Radial profiles of RMS temperature for the reacting non-swirled case SwB1 at z=10, 20, 30, 40, 50 and 70mm from the burner nozzle. Legend: • • Experimental data. - - TFLES model. — FOC-FPF model.*

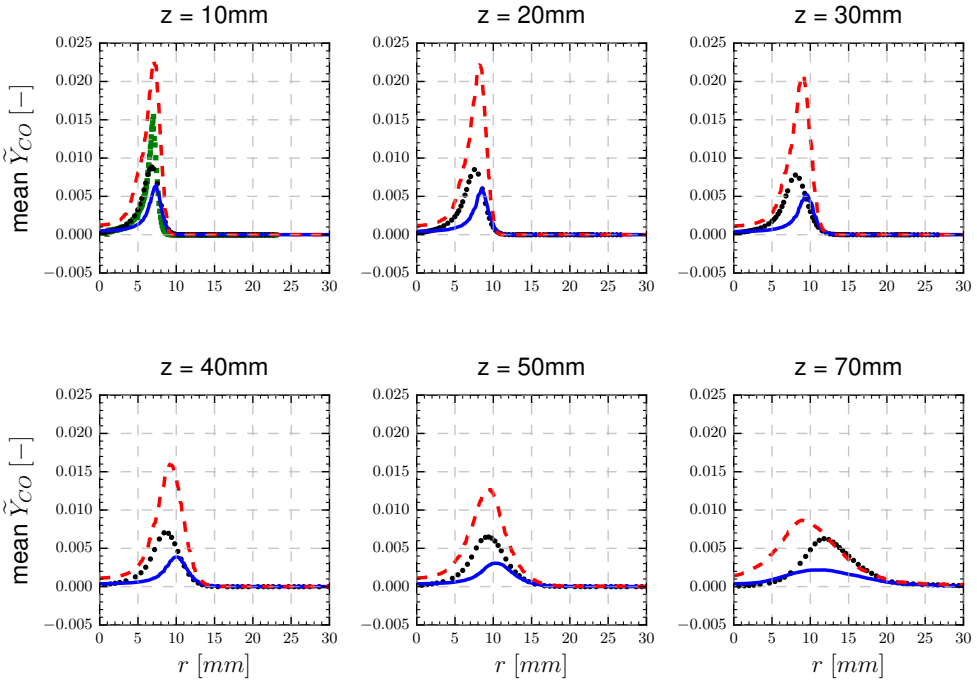

Figure 4.14: *Radial profiles of mean CO mass fraction for the reacting non-swirled case SwB1 at z=10, 20, 30, 40, 50 and 70mm from the burner nozzle. Legend:* ■ ■ *Non-filtered experimental data.* • • *Filtered experimental data.* - - *TFLES model.* — *FOC-FPF model.*

- Averages obtained from a simulation using the TFLES model are mimicked by Favre-averaging artificially thickened laminar flames. Thickening factor $\mathcal{F} = 2$ (blue color) and $\mathcal{F} = 4$ (red color) are used to conduct the study.

Fig. 4.15 evidences an over-estimation of mean CO profiles when the flame is thickened. This effect is amplified when the thickening factor $\mathcal{F}$ increases. Nevertheless, thicknesses and peaks of CO profiles obtained with FOC-FPF model are underestimated. This triggers the need for a deeper analysis of the inclusion of SGS wrinkling on CO formation.

4.3.2.3 Analysis of classical wrinkling formulation for CO predictions

As exposed in Sec. 3.5.1, accounting for sub-grid scale wrinkling in the CO equation when using the FOC-FPF model is achieved by multiplying diffusive and reactive terms by Ξ_Δ. This strategy is challenged here. An interesting feature of the present virtual chemical mechanism is that separate schemes are used for temperature and CO predictions. It is hence mathematically possible

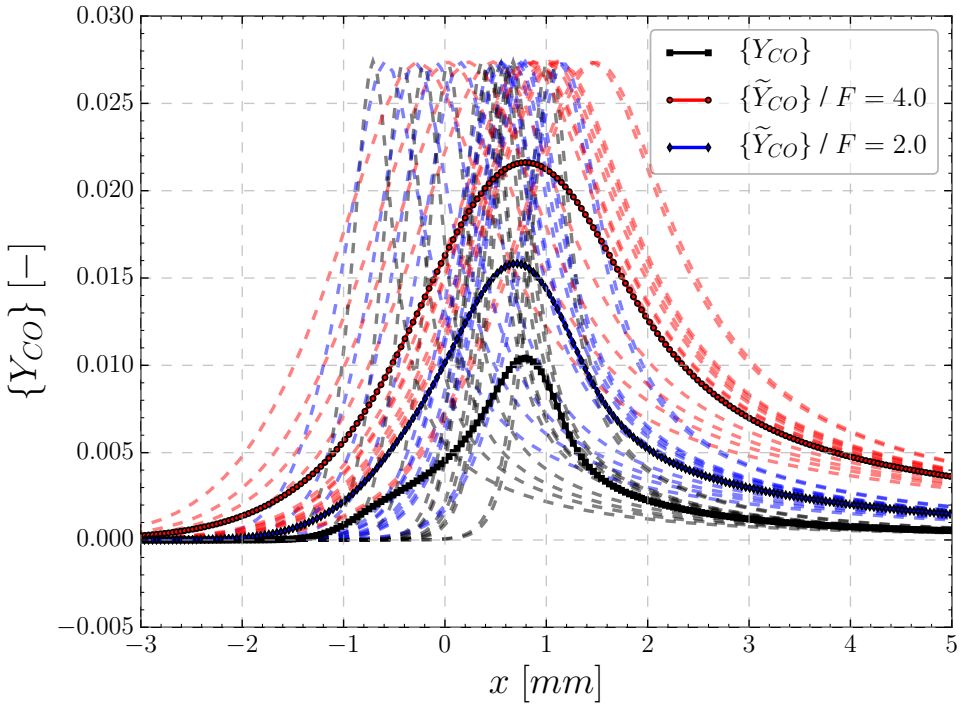

Figure 4.15: *Manufactured Y_{CO} flame brush using 1-D unstrained laminar flames at $\phi = 0.75$ and associated thickened mean quantities. Legend: - - Samples of 1-D unstrained flames. - - Samples of 1-D unstrained flames thickened with factor $\mathcal{F} = 2$. - - Samples of 1-D unstrained flames thickened with factor $\mathcal{F} = 4$. ■—■ Mean of unstrained flames $\{Y_{CO}\}$. ●—● Mean of thickened unstrained flames $\{\widetilde{Y}_{CO}\}$ ($\mathcal{F} = 2$). ♦—♦ Mean of thickened unstrained flames $\{\widetilde{Y}_{CO}\}$ ($\mathcal{F} = 4$).*

to include a wrinkling factor in the main mechanism equations and to omit it on the CO scheme transport equations. Flame propagation is given by the first mechanism and hence the impact of multiplying budget terms of CO mechanism by Ξ_Δ can be investigated separately. Two computations are hence challenged:

- In the first case, sub-grid-scale wrinkling is included via the conventional method of multiplication of diffusive and reactive terms by Ξ_Δ in the CO sub-mechanism species transport equations (solid lines).
- In the second case, no impact of wrinkling on the species of the CO sub-mechanism is considered. This corresponds to $\Xi_\Delta = 1$ in the CO scheme's equations (dashed lines).

The mean CO profiles, displayed in Fig. 4.16, do not differ between both computations. It means that accounting for SGS wrinkling by multiplying budget terms with the wrinkling factor does not affect pollutants predictions. As dis-

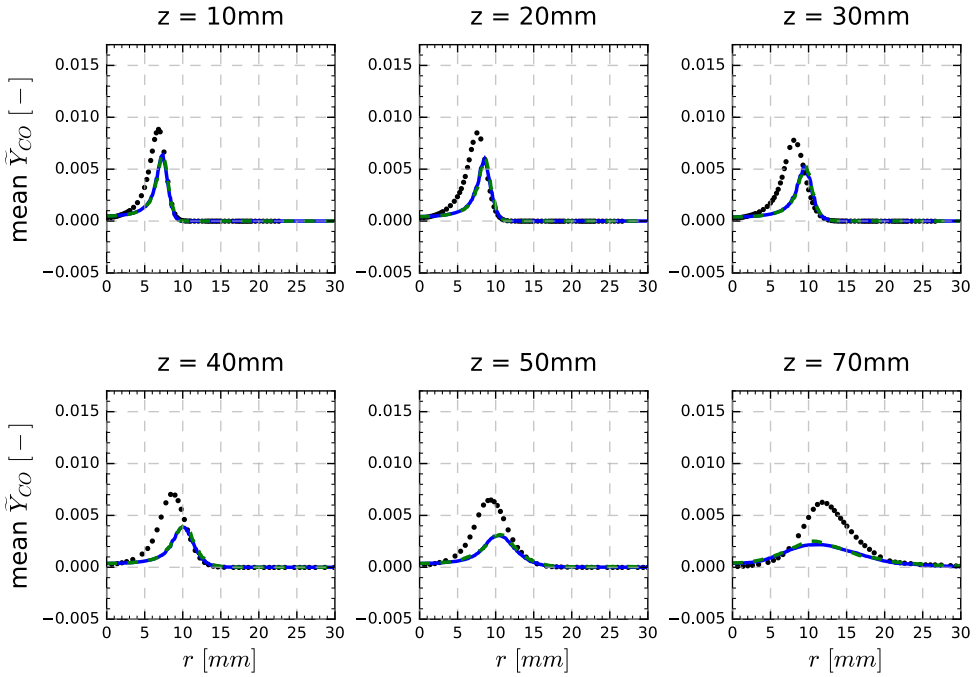

Figure 4.16: *Radial profiles of mean CO mass fraction with and without wrinkling factor Ξ_Δ in the modeling for the reacting non-swirled case SwB1 at z=10, 20, 30, 40, 50 and 70mm from the burner nozzle. Legend: • • Filtered experimental data. - - Without Ξ_Δ in $\widetilde{Y}_{CO}$ transport equation. — With Ξ_Δ in $\widetilde{Y}_{CO}$ transport equation.*

cussed in Colin et al. (2000), it modifies the flame propagation but does not affect the chemical flame structure.

A one-dimensional analysis is carried out to shed light on the issue. We consider a stationary 1-D flame in two situations:

- A laminar flame computed with FOC-FPF. A stationary solution is obtained in the frame moving at speed S_l^0 and is written $\widetilde{Y}_{CO}^l$.
- A 1-D pseudo-turbulent flame computed with the laminar FOC-FPF mechanism and the multiplication of diffusive and reactive terms by a spatially constant value Ξ. A stationary solution is obtained in the frame moving at speed $S_T = \Xi S_l^0$ and is written $\widetilde{Y}_{CO}^{\Xi}$.

The equation verified by $\widetilde{Y}_{CO}^l$ in the steady state coordinate system reads:

$$\rho_0 S_l^0 \frac{d}{dx}\left(\widetilde{Y}_{CO}^l\right) = \frac{d}{dx}\left(D_{opt}\frac{\lambda}{C_p}\frac{d\widetilde{Y}_{CO}^l}{dx}\right) + \overline{\rho}\widetilde{\dot{\omega}}_{CO}^l \tag{4.13}$$

And the balance equation for $\widetilde{Y}_{CO}^{\Xi}$ is:

$$\rho_0 \underbrace{\Xi S_l^0}_{S_T} \frac{d}{dx}\left(\widetilde{Y}_{CO}^{\Xi}\right) = \frac{d}{dx}\left(\Xi D_{opt} \frac{\lambda}{C_p} \frac{d\widetilde{Y}_{CO}^{\Xi}}{dx}\right) + \Xi \overline{\rho}\widetilde{\dot{\omega}}_{CO}^{l} \tag{4.14}$$

Eqs. (4.13) and (4.14)/Ξ are equivalent and have the same solutions as the boundary conditions of $\widetilde{Y}_{CO}^{l}$ and $\widetilde{Y}_{CO}^{\Xi}$ are identical. It corroborates the observations made in Fig. 4.16. This shows that the classical wrinkling inclusion strategy does not impact the CO structure and is hence not suitable.

4.3.3 Reacting SwB1 case with FOC-FWF

Alternatively to Filtered Planar Flames, the filtered wrinkled flamelets (FWF) described in Sec. 3.4.1 are used as optimization targets in the newly developed combustion modeling formalism. The FOC-FWF model is detailed in Sec. 3.4 and an application on the SwB1 reacting case is performed in this section.

4.3.3.1 Modeling details

FOC-FWF model parameters The same LES filter with characteristic size $\Delta = 4\delta_l^0$ is considered. The wrinkled flamelet database has been built using the strategy presented in Sec. 3.4.1 and for two values of the number per sine pattern in a sub-filter box: $n_\Delta = 1$ and $n_\Delta = 2$. These values satisfy the flame cut-off bound defined in chapter 3 as $n_\Delta^{max} = \Delta/2\delta_l^0$ ($= 2.11$ for $\phi = 0.75$). The second bound based on the Gibson length, computed as $n_{\Delta,Gibson}^{max} = \Delta/2l_G$, depends on the local turbulent parameters flow properties. By using the data gathered by Zhou et al. (2013) on non-reacting flows, table 4.3 shows computed values of Gibson lengths and resulting bounds on n_Δ for different position in the flow. These bounds are very high and confirm that for the Cambridge SwB1 configuration n_Δ is limited by the flame cut-off. The bound on the sine amplitude is not enforced directly in the simulation and deviations from the flamelet regime are allowed.

Table 4.3: *Maximal values of n_Δ at different positions in the SwB1 non-reacting flow.*

Axial position	Radial position	Gibson length (μm)	Maximal n_Δ based on l_G	Maximal n_Δ based on δ_l^0
$z = 2$mm	Inner annulus	44	28.4	2.11
$z = 2$mm	Outer annulus	29	43.1	2.11
$z = 30$mm	$r = 11$mm	3.4	367.6	2.11
$z = 30$mm	$r = 16$mm	1.2	1041.7	2.11

Sub-grid scale wrinkling model As in Sec. 4.3.2, wrinkling factors are computed using a modified Charlette model with $\beta = 0.5$. The saturated wrinkling factor value is defined as $\Xi_\Delta^{sat} = (\Delta/\delta_l^0)^\beta$ and is equal to $\Xi_\Delta^{sat} = 2.05$.

4.3.3.2 Results

FOC-FWF results The mean temperature computed with the FOC-FWF model is compared in Fig. 4.17 against the results previously obtained with TFLES and the FOC-FPF model. The mean profiles obtained with FOC-FWF are very close to the results of FOC-FPF. This is expected since modification of the main mechanism parameters shown in Fig. 3.17 are well approximated by $\xi_1^T(\Xi_\Delta) \approx \Xi_\Delta$ and $\xi_2^T(\Xi_\Delta) \approx \Xi_\Delta$ for $\Xi_\Delta \leq \Xi_\Delta^{sat}$.

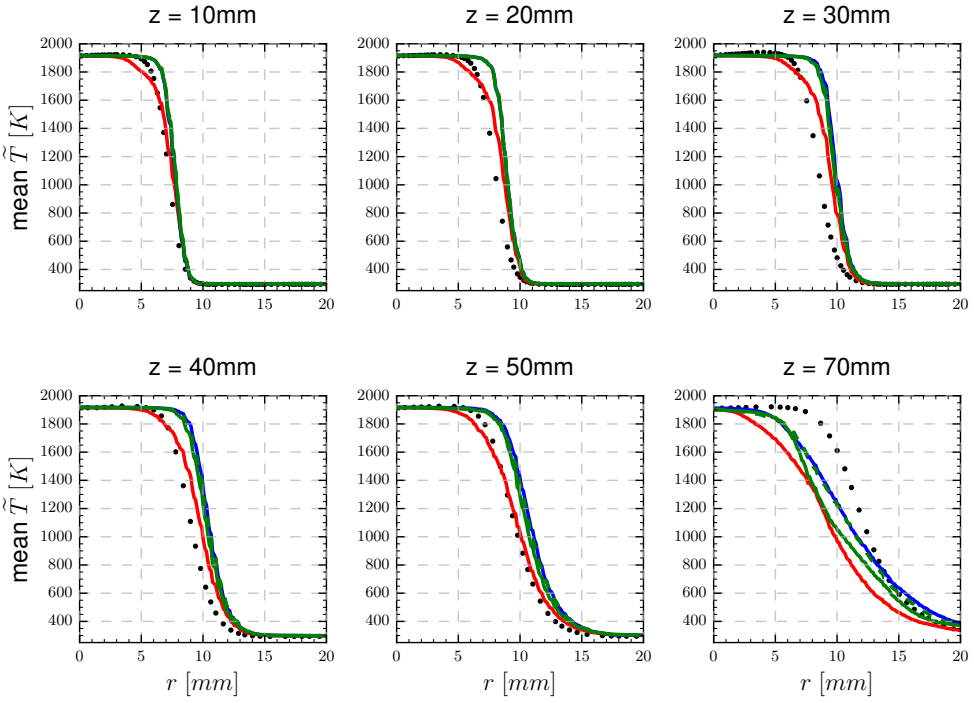

Figure 4.17: *Radial profiles of mean temperature for the reacting non-swirled case SwB1 at z=10, 20, 30, 40, 50 and 70mm from the burner nozzle. Legend: • • Filtered experimental data. — TFLES model. — FOC-FPF model. — FOC-FWF model with* $n_\Delta = 1$. - - - *FOC-FWF model with* $n_\Delta = 2$.

Major differences are however observed in the behavior of simulated CO mass fractions. Fig. 4.18 shows instantaneous fields of $\widetilde{Y}_{CO}$ and Ξ_Δ. On the left, a comparison between an instantaneous $\widetilde{Y}_{CO}$ field obtained with the FOC-FPF model against a field obtained with the FOC-FWF model is done. On the right, the Ξ_Δ field is confronted to $\widetilde{Y}_{CO}$ in the case of FOC-FWF. It is seen that a

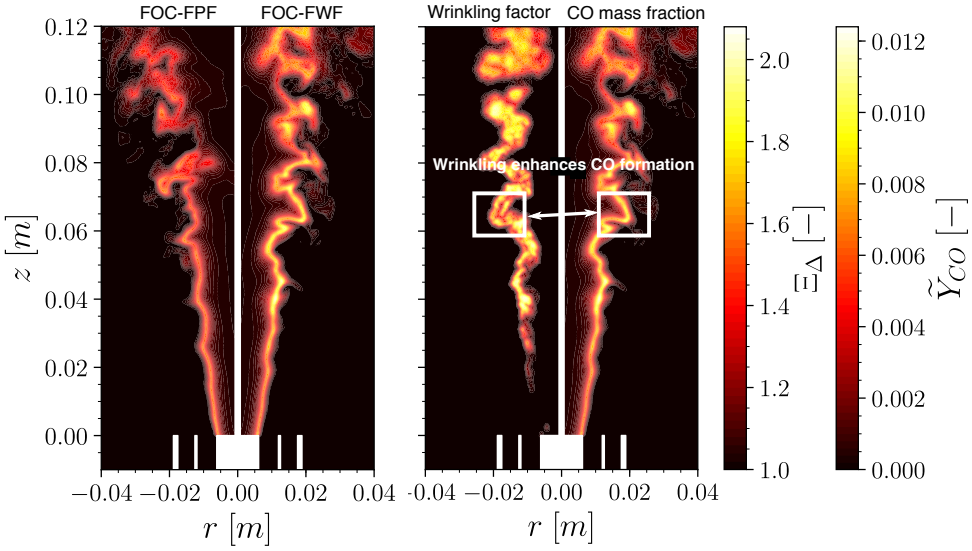

Figure 4.18: *Comparison of 2-D fields for SwB1 simulated with FOC-FPF and FOC-FWF for $n_\Delta = 1$. These fields are obtained by $\theta = 0$. On the left: comparison between $\widetilde{Y}_{CO}$ field obtained with FOC-FPF (left) and FOC-FWF (right) models. On the right: comparison between Ξ_Δ (left) and $\widetilde{Y}_{CO}$ (right) obtained with filtered wrinkled model.*

higher quantity of CO is produced when using filtered wrinkled flamelets as optimization targets. This higher value is linked in Fig. 4.18 (right) to the level of sub-grid scale wrinkling. CO mean radial profiles are shown in Fig. 4.19. The peak values and the thickness of predicted profiles increase when using the wrinkled optimized model for $z \geq 30$mm, which corresponds to the region where sub-grid scale wrinkling is significant. The numerical values remain however lower than the experimental measures. These discrepancies may be related to complex differential diffusion effects. Indeed, a strong influence of differential diffusion effects for these operating conditions have been reported in the literature (Barlow et al. (2012)). Proch et al. (2017) showed that even in a highly resolved LES, where the flame wrinkling is fully resolved, CO profiles remain lower and thinner than measured profiles when differential diffusion is not modeled. A qualitative assessment of these effects will be further investigated in Sec. 4.3.3.3.

Analysis of the impact of n_Δ Predicted mean CO profiles for $n_\Delta = 2$ are added in Fig. 4.19. It does not show any influence of the parameter n_Δ. It is consistent with Fig. 3.15, where it is seen that for $\Delta = 4\delta_l^0$, the quantity of CO in the sub-filter box as evaluated by a 2-D integral is similar for $n_\Delta = 1$ and $n_\Delta = 2$.

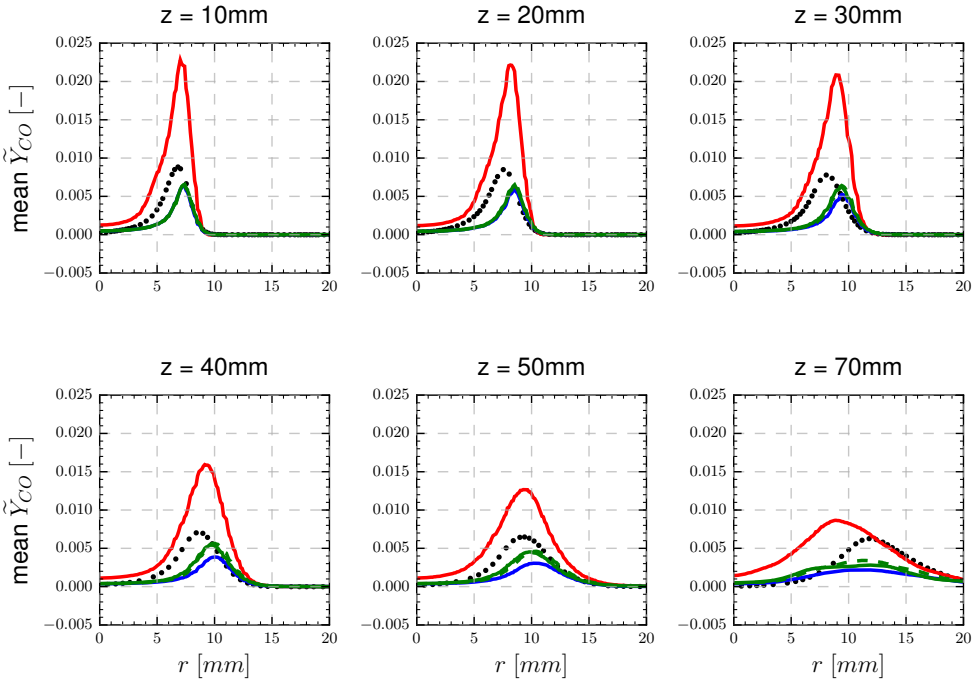

Figure 4.19: *Radial profiles of mean CO mass fraction for the reacting non-swirled case SwB1 at z=10, 20, 30, 40, 50 and 70mm from the burner nozzle. Legend:* • • *Filtered experimental data.* — *TFLES model.* — *FOC-FPF model.* — *FOC-FWF model with* $n_\Delta = 1$. - - - *FOC-FWF model with* $n_\Delta = 2$.

Analysis of CO formation due to subgrid scale wrinkling The following post-processing aims at removing the error induced by the omission of differential diffusion effects in the present simulations. The simulated and experimental mean scalar fields are assumed to be axisymmetric. The LES and experimental mass of CO per unit of axial length are computed for that purpose in cylindrical coordinates as follows:

$$\mathcal{I}^{z=z_0}_{CO,sim} = \int_{\theta=0}^{2\pi} \left(\int_{r=0}^{R} r\{\widetilde{Y}_{CO,sim}\}(r,\theta)\mathrm{d}r \right) \mathrm{d}\theta = 2\pi \int_{r=0}^{R} r\{\widetilde{Y}_{CO,sim}\}(r)\mathrm{d}r \tag{4.15}$$

$$\mathcal{I}^{z=z_0}_{CO,exp} = \int_{\theta=0}^{2\pi} \left(\int_{r=0}^{R} r\overline{\{Y_{CO,exp}\}}(r,\theta)\mathrm{d}r \right) \mathrm{d}\theta = 2\pi \int_{r=0}^{R} r\overline{\{Y_{CO,exp}\}}(r)\mathrm{d}r \tag{4.16}$$

where R is a radius covering the entire reaction zone up to the co-flow where $\widetilde{Y}_{CO}$ vanishes. Experiments show that the equivalence ratio variation along r induced by differential diffusion remains roughly identical at any axial locations (Barlow et al. (2012)). This is illustrated in Fig. 4.21, where the measured

equivalence ratio is plotted for different z. By selecting as a reference the plane located at $z = 10$mm, where the sub-grid scale flame wrinkling is resolved ($\Xi_\Delta \approx 1$), the relative mass of CO per unit of axial length is therefore defined as $\delta\mathcal{I}^z_{CO} = \mathcal{I}^z_{CO} - \mathcal{I}^{z=10mm}_{CO}$.

$\delta\mathcal{I}^z_{CO}$ is plotted against z for experimental data and each of the simulations in Fig. 4.20. While TFLES over-estimates the CO integral evolution, the FOC-FPF model under-estimates it because the influence of growing sub-grid scale flame wrinkling is not considered. Note that FOC-FPF still predicts an increasing amount of CO as z increases since the flame is radially expanding. Adding the wrinkling influence in the target flame archetype (FOC-FWF) leads to an excellent agreement with experimental data. It is moreover interesting to note that for $z = 10$mm (i.e. in the quasi-laminar part of the flame) $\mathcal{I}^{TFLES}_{CO} = 4 \times \mathcal{I}^{laminar}_{CO}$, where $\mathcal{I}^{TFLES}_{CO}$ is the CO integral computed with TFLES and $\mathcal{I}^{laminar}_{CO}$ the integral with the FOC-FPF model. This relationship is consistent with the thickening factor of $\mathcal{F} \approx 4.5$ found in the flame front.

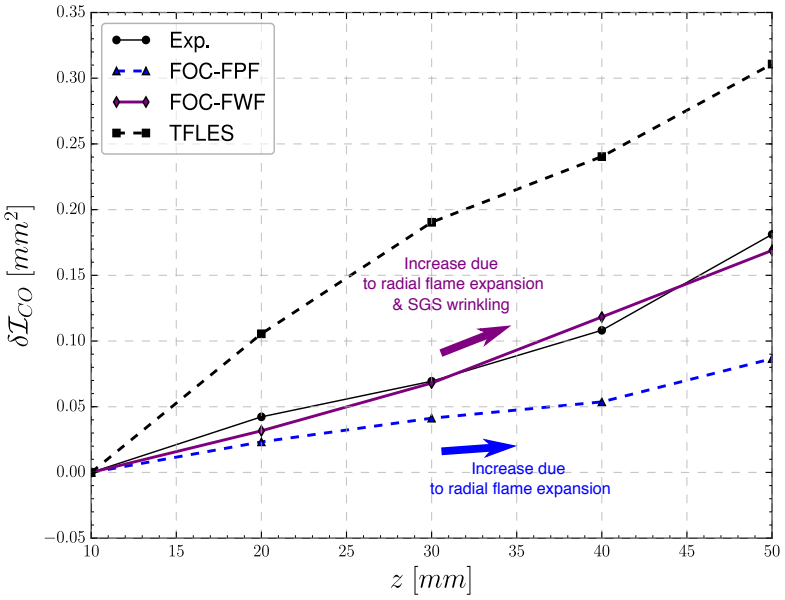

Figure 4.20: *Integral of CO mass fractions $\mathcal{I}_{CO}$ in planes (r, θ) as a function of the axial positions z. Legend: ●—● Experimental data. ▲- - -▲ FOC-FPF model. ♦—♦ FOC-FWF model. ■- - -■ TFLES model.*

4.3.3.3 Analysis of differential diffusion effects on the CO profiles

A significant influence of differential diffusion on experimental scalar fields has been reported in the literature (Barlow et al. (2012)). As illustrated in Fig. 4.21, differential diffusion gives rise to a jump of the mean equivalence

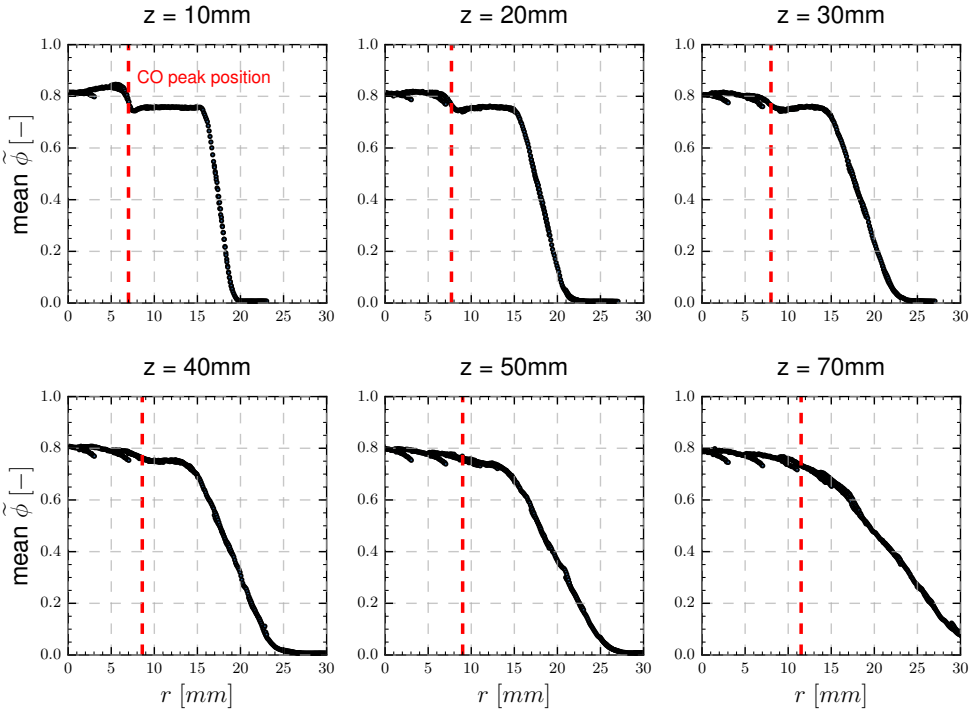

Figure 4.21: *Experimental values of the equivalence ratio at the different axial positions of the burner in non-swirled premixed operating conditions SwB1. Legend:* ●- -● *Experimental data.*

ratio[3] from $\phi = 0.75$ to 0.8 across the flame front. An *a priori* analysis of the impact of this equivalence ratio variation on CO mass fraction is carried out by performing a 1-D manufactured flame brush analysis, following the methodology presented in Sec. 4.2.2. Two flames brushes, mimicking experimental profiles, are generated using 1-D unstrained flames with equivalence ratios respectively equal to 0.75 and 0.8. Fig. 4.22 shows the averaged CO mass fractions using the flame brush thickness of the SwB1 burner at $z = 10$mm. It is observed that the mean profile with $\phi = 0.8$ is thicker and with a higher peak than the $\phi = 0.75$ mean profiles. This is in qualitative agreement with the discrepancies observed in Fig. 4.19. The analysis is however insufficient to carry out a quantitative assessment and further investigations have to be led. In particular, the coupling of the new wrinkling model with a scheme capable of predicting non-unity Lewis effects would lead to valuable information.

[3]The equivalence ratio is here defined from an atomic balance.

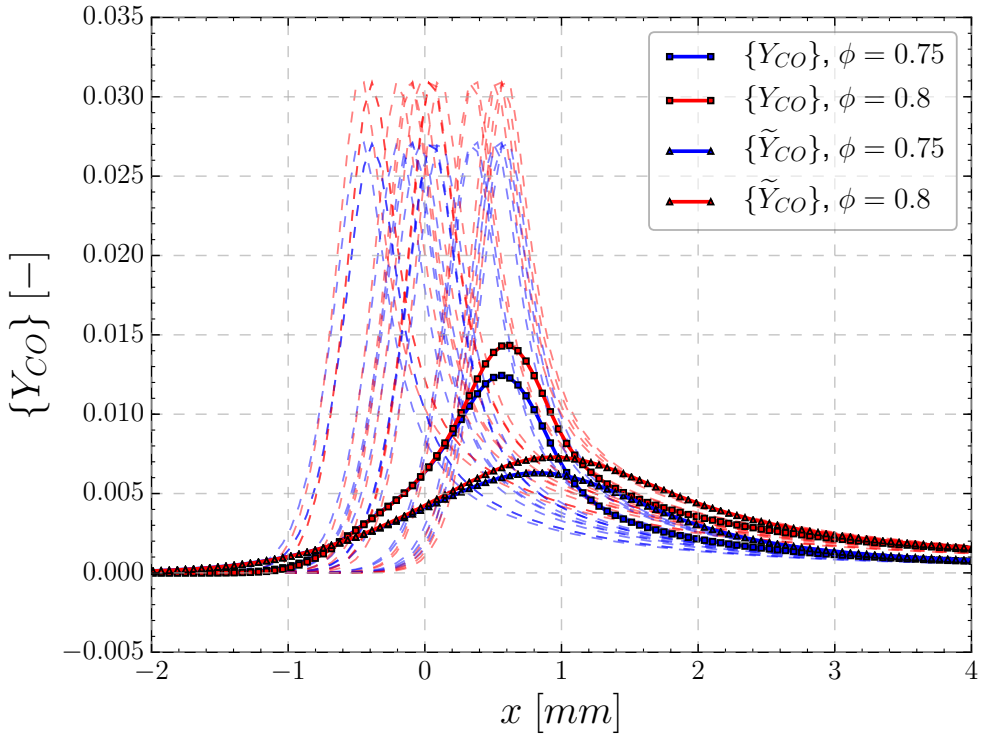

Figure 4.22: *Manufactured Y_{CO} flame brush using 1-D unstrained laminar flames at $\phi = 0.75$ and $\phi = 0.8$ and associated non-filtered and filtered mean quantities. Legend: - - Samples of 1-D unstrained flames at $\phi = 0.75$. - - Samples of 1-D unstrained flames at $\phi = 0.8$. ■—■ Mean of unstrained flames $\{Y_{CO}\}$ at $\phi = 0.75$. ■—■ Mean of unstrained flames $\{Y_{CO}\}$ at $\phi = 0.8$. ▲—▲ Mean of Favre-filtered unstrained flames $\{\widetilde{Y}_{CO}\}$ at $\phi = 0.75$. ▲—▲ Mean of Favre-filtered unstrained flames $\{\widetilde{Y}_{CO}\}$ at $\phi = 0.8$.*

4.3.3.4 Concluding remarks on the non-swirled premixed Cambridge simulation

The Cambridge SwB1 configuration has been simulated with the dynamic thickened flame model (TFLES), the FOC-FPF model and the FOC-FWF model. While the three models predicts similar flow and temperature statistical fields, large discrepancies are obtained regarding CO predictions. The outcomes of the work are the following:

- The thickened flame model largely over-predicts CO formation in the flame front. This corroborates the analysis made on laminar flames which showed that the mass of CO in the flame front multiplied by the thickening factor $\mathcal{F}$ when the flame is thickened.

- The FOC-FPF model leads to significant improvement of mean CO

prediction when compared to TFLES. It nevertheless under-predicts CO formation. By assessing the impact of classical wrinkling modeling on CO, it is suggested that inadequate inclusion of subgrid scale wrinkling influence on CO is partly responsible for their low level.

- Including subgrid scale wrinkling effects on CO formation through the use of the FOC-FWF model improves predictions. It is however insufficient to entirely explain the discrepancies. A phenomenon impacting CO quantity is differential diffusion, which has been reported in the literature and is not accounted for by the virtual chemical mechanism.

- To further assess the performance of wrinkling modeling on CO, the integral of CO mass fraction in planes (r, θ) has been studied. By subtracting the integral of Y_{CO} in the laminar part of the flame, influence of differential diffusion on results is diminished and an excellent agreement between the CO increase due to wrinkling is obtained between experimental and simulated data.

4.4 Swirled premixed operating condition (SwB3)

The premixed highly swirled configuration (SwB3) is the second targeted validation configuration for the newly developed model. It is characterized by a Swirl Flow Ratio of 33%, representative of swirl levels found in industrial applications (Sweeney et al. (2012b)). The swirl is added in the simulation by modifying the boundary condition (4.3), where the parameter U_θ^{max} has been adjusted to retrieve the tangential velocity profiles at $z = 2$mm. The configuration has been experimentally studied by Sweeney et al. (2012b) and has two interesting features in comparison with the non-swirled case:

- The turbulent levels in the swirled case are higher, and the sub-grid scale flame wrinkling is also expected to be more important. This will help to discriminate even more than in the SwB1 case the impact of wrinkling on CO levels.

- A wide and opened recirculation zone is located in the wake of the bluff-body. The strength of the recirculation is much weaker than in the non-swirled case and it has been observed experimentally that differential diffusion effects have a minor influence on scalar fields (Sweeney et al. (2012b)).

The non-reacting simulation is presented in Sec. 4.4.1. Reacting computations focus on the ability of the FOC-FWF model to capture the correct CO level. Results are shown and examined in Sec. 4.4.2. The configuration is performed on the M100 mesh.

4.4.1 Non-reacting case

Mean velocity profiles obtained at axial distances $z = 2$, 10, 30 and 50mm are illustrated in Fig. 4.23 and the corresponding RMS values in Fig. 4.24. An excellent overall agreement is obtained for mean velocities and the recirculation zone is correctly captured. This is for instance observed on the $\widetilde{U}_z$ profile at $z = 10$mm when $r \leq 5$mm. The azimuthal velocity $\widetilde{U}_\theta$ at $z = 2$mm shows a nearly perfect agreement with the experimental data, thus validating the analytic formulation chosen for the inlet boundary condition. A slight shift in azimuthal velocities is nevertheless seen for $z \geq 30$mm. Experimental RMS profiles are also satisfyingly recovered (see Fig. 4.24), despite some inaccuracies. Profiles in the near burner region are adequately retrieved while over estimation of the RMS of axial and radial velocities occur for $z = 30$mm and $z = 50$mm.

4.4.2 Filtered Optimized Chemistry model with FOC-FWF

4.4.2.1 Modeling details

FOC modeling parameters Similarly to the previous simulations on the non-swirled operating conditions, a filter size $\Delta = 4\delta_l^0$ is used for the swirled burner since the mesh resolution in the flame front is identical. The FOC model is built for $\phi = 0.5$ to 0.75 and the approximations $\mathcal{A}^*(\phi) = \mathcal{A}^*(\widetilde{\phi})$ and $\alpha^*(\phi) = \alpha^*(\widetilde{\phi})$ are considered for taking into account dilution effects far from the burner nozzle.

As shown in Sec. 4.3.3.2, the parameter n_Δ has a negligible influence on the predicted levels of CO. A single parameter value $n_\Delta = 2$ is hence considered in the present case. This parameter is in agreement with the bounds imposed by Gibson lengths as illustrated in Tab. 4.4.

Sub-grid scale wrinkling model Mercier et al. (2015) showed that the SGS wrinkling factor model has a strong influence on predicted statistical quantities in the non-swirling operating conditions of the Cambridge burner. A parametric study is here provided for the SwB3 case by selecting three algebraic models:

- **Model 1**: Modified charlette model Eq. (4.12) with $\beta = 0.5$ and a Prandtl-Kolmogorov model for u'_Δ.
- **Model 2**: Saturated Charlette model $\Xi_\Delta = \left(\Delta/\delta_l^0\right)^\beta$ with $\beta = 0.5$.
- **Model 3**: Modified Charlette model (Eq. 4.12) with $\beta = 0.9$ and a Prandtl-Kolmogorov model for u'_Δ.

Model 1, 2 and 3 will be challenged on their ability to capture flame propagation and CO mass fraction levels. The saturated SGS wrinkling factor for models 1 and 2 is $\Xi_\Delta^{sat,i} = 2.05$ $(i = 1, 2)$ and for model 3 it is $\Xi_\Delta^{sat,3} = 3.67$.

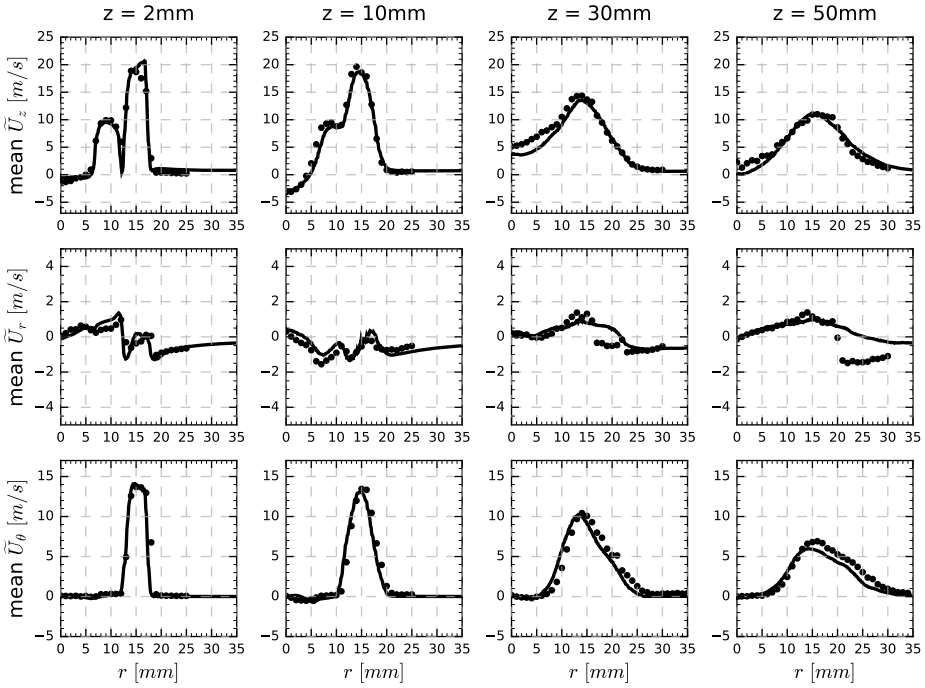

Figure 4.23: *Radial profiles of mean axial, radial and tangential velocities for the non-reacting case SwB3c at z=2, 10, 30 and 50mm from the burner nozzle. Legend: — Simulated profiles on mesh M100. • • Experimental data.*

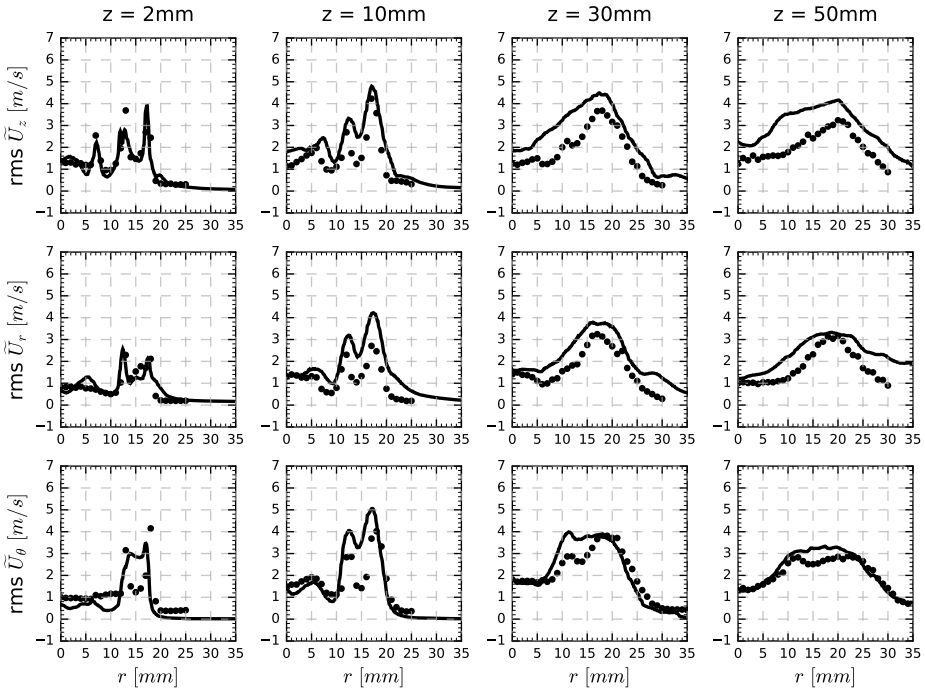

Figure 4.24: *Radial profiles of RMS axial, radial and tangential velocities for the non-reacting case SwB3c at z=2, 10, 30 and 50mm from the burner nozzle. Legend: — Simulated profiles on mesh M100. • • Experimental data.*

Table 4.4: *Gibson length at different positions in the SwB3 non-reacting flow.*

Axial position	Radial position	Gibson length (μm)	Maximal n_Δ based on l_G	Maximal n_Δ based on δ_l^0
$z = 2$mm	Inner annulus	54	23.1	2.11
$z = 2$mm	Outer annulus	12	104.2	2.11
$z = 30$mm	$r = 11$mm	5.8	215.5	2.11
$z = 30$mm	$r = 16$mm	1.3	961.5	2.11

Comparison with a TFLES modeling strategy As for the non-swirled simulation, the new modeling strategy will be compared to a classical dynamic thickened flame model. The SGS wrinkling is in this case computed with the modified Charlette model (Eq. (4.12)) and $\beta = 0.5$ (Model 1).

4.4.2.2 Results

Five computations are carried out to assess CO predictions on the SwB3 burner. Three simulations using FOC-FWF with each of the three SGS wrinkling models are performed to make a parametric analysis. They are compared to a simulation with TFLES modeling and a simulation with FOC-FPF. Both of these two last computations are done with the wrinkling model 1.

Flow field Mean and RMS flow fields are plotted in Figs. 4.25 and 4.26 respectively. The mean velocities are accurately reproduced in the region close to the burner nozzle ($z = 2$mm and $z = 10$mm), while a slight shift is observed for higher values of axial positions. This shift suggests that the expansion of hot products tends to be under-estimated. The wrinkling model has a low influence on the flow field as computed results are sensibly the same for any of the simulations. The wide and open re-circulation zone is predicted in computations though its width is lower than the experimentally measured recirculation zone. Similar conclusions are reached for RMS profiles, for which a shift is observed and correlated to the shift of corresponding mean values. RMS peaks are under-estimated for $z = 2$mm and correctly reproduced downstream this location.

Flame shape and temperature field An instantaneous temperature field obtained with the FOC-FWF model coupled to SGS wrinkling model 3 is shown on the bottom left in Fig. 4.27 and the corresponding mean field is on the bottom right. While the separation between a weakly wrinkled region downstream the flame and a highly wrinkled region upstream still holds, the swirled flame has a wider opening angle than the non-swirling SwB1 flame.

Mean and RMS temperature fields are plotted in Fig. 4.28 and Fig. 4.29, respectively. No significant differences in temperature predictions are observed

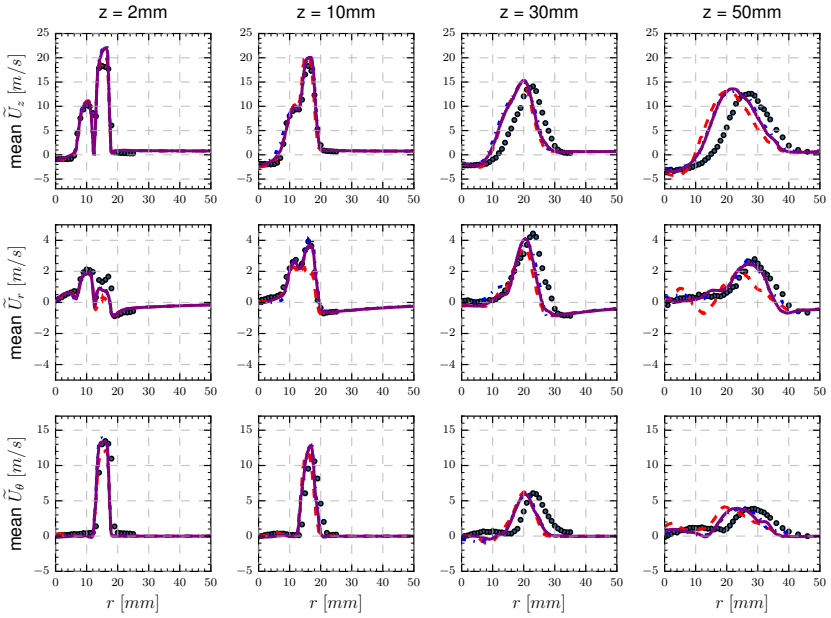

Figure 4.25: *Radial profiles of mean axial, radial and tangential velocities for the reacting non-swirled case SwB3 at z = 2, 10, 30 and 50mm from the burner nozzle. Legend: • • Experimental data. - - - FOC-FWF model with wrinkling model 1. -.- FOC-FWF model with wrinkling model 2. — FOC-FWF model with wrinkling model 3.*

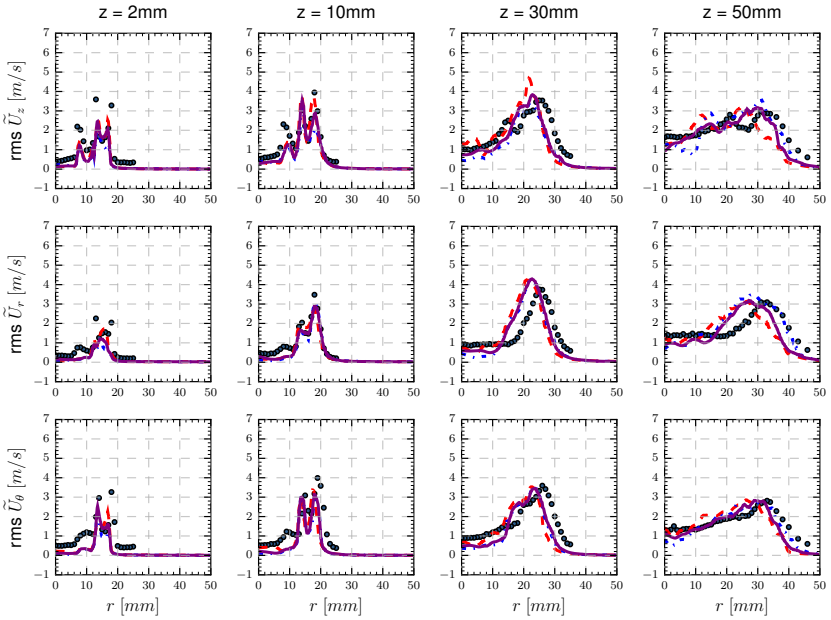

Figure 4.26: *Radial profiles of RMS axial, radial and tangential velocities for the reacting non-swirled case SwB3 at z = 2, 10, 30 and 50mm from the burner nozzle. Legend: • • Experimental data. - - - FOC-FWF model with wrinkling model 1. -.- FOC-FWF model with wrinkling model 2. — FOC-FWF model with wrinkling model 3.*

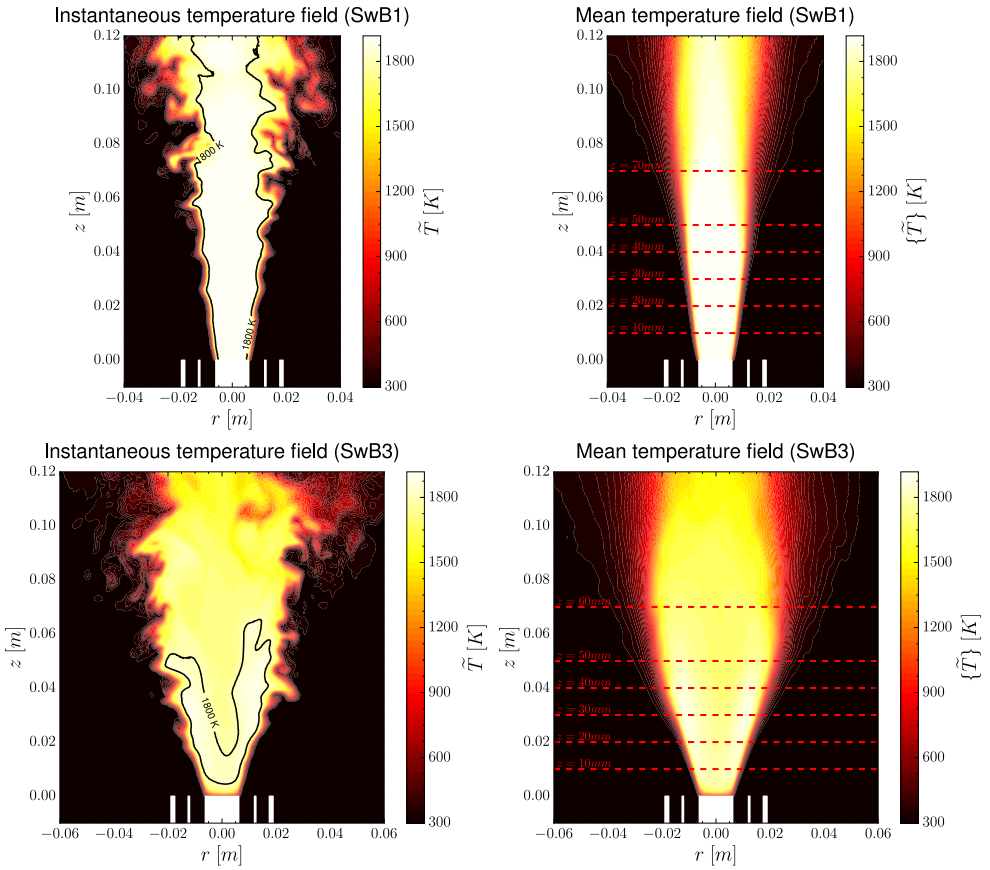

Figure 4.27: *2-D fields of instantaneous and averaged temperature fields for SwB1 (top) and SwB3 (bottom) cases. In the SwB3 case, FOC-FWF model coupled to SGS wrinkling model 3 is used. These fields are obtained in the plane $x = 0$ (also defined by $\theta \equiv 0$ $[\pi]$). On the left: instantaneous temperature field for a given time. On the right: averaged temperature field.*

between any of the models. Similarly to the mean flow field, the opening angle is underpredicted. This highlights the difficulties encountered by the models to accurately predict the flame opening angle and thus its propagation in the current grid resolution conditions. A slight improvement is observed for wrinkling models 2 and 3, which tend to predict a higher mean SGS wrinkling factor than model 1. This is illustrated in Fig. 4.30 where the mean wrinkling factor obtained from the three model formulations is plotted for $z = 10$, 30 and 50mm. The difficulties are explained by the low resolved wrinkling in the simulations, which is attributed to the use of a coarse grid coupled to a relatively high LES filter size. Reported studies have indeed shown the limits of algebraic SGS wrinkling models in such situations (Mercier et al. (2015)). A solution for recovering the correct flame angle is to use a finer grid as discussed in Mercier et al. (2018), who showed that a fine grid is required to retrieve the

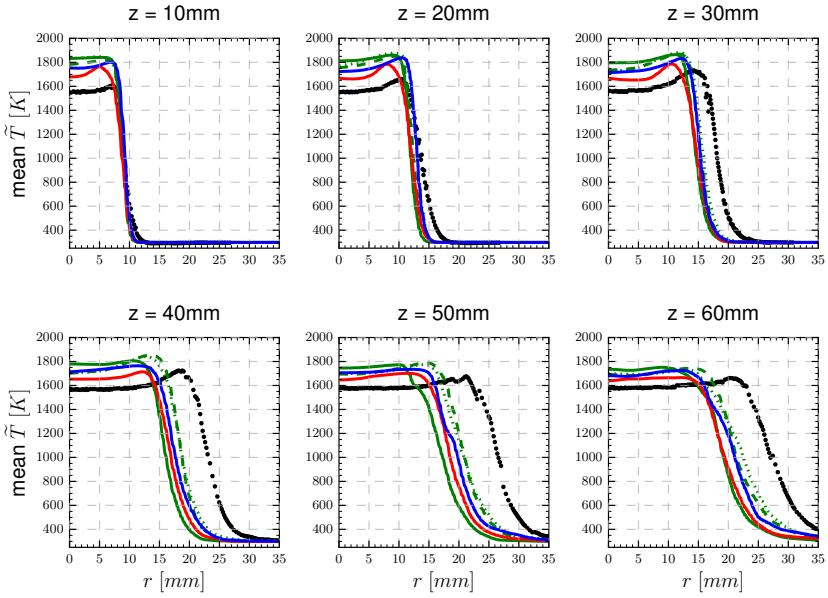

Figure 4.28: *Radial profiles of mean temperature for the reacting highly swirled case SwB3 at z=10, 20, 30, 40, 50 and 60mm from the burner nozzle. Legend: • • Experimental data. — TFLES model with wrinkling model 1. — FOC-FPF model with wrinkling model 1. — FOC-FWF model with wrinkling model 1. . . . FOC-FWF model with wrinkling model 2. - - - FOC-FWF model with wrinkling model 3.*

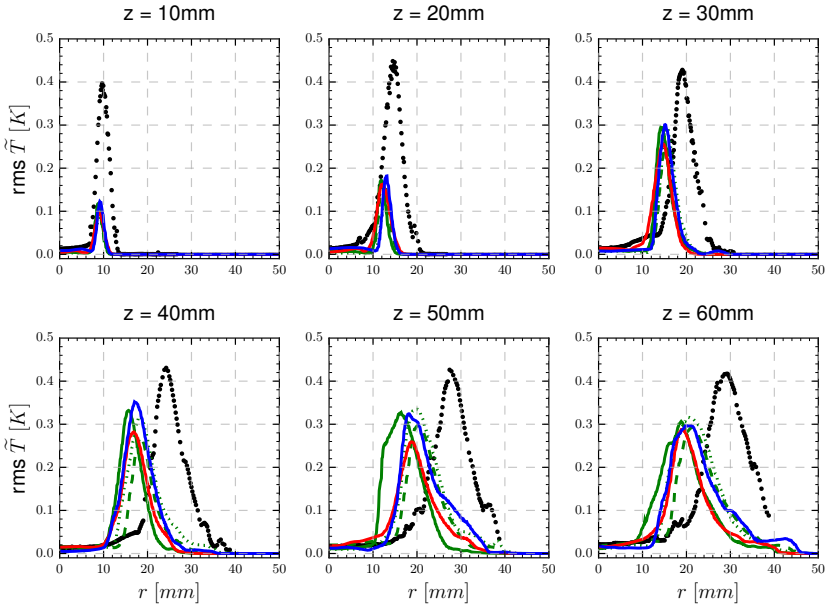

Figure 4.29: *Radial profiles of rms temperature for the reacting highly swirled case SwB3 at z=10, 20, 30, 40, 50 and 60mm from the burner nozzle. Legend: • • Experimental data. — TFLES model with wrinkling model 1. — FOC-FPF model with wrinkling model 1. — FOC-FWF model with wrinkling model 1. . . . FOC-FWF model with wrinkling model 2. - - - FOC-FWF model with wrinkling model 3.*

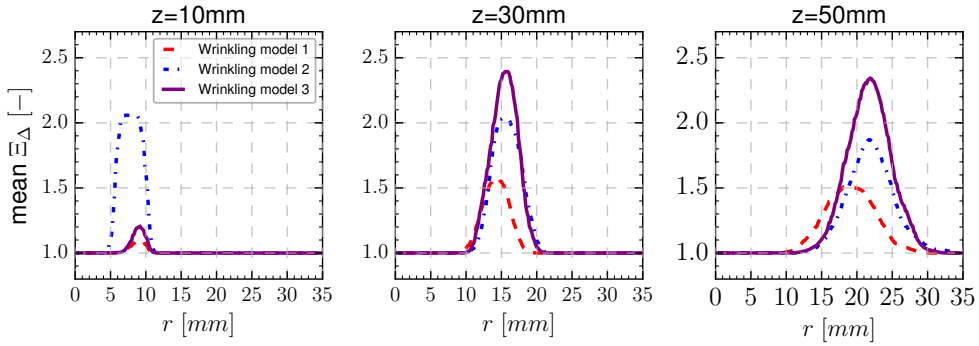

Figure 4.30: *Radial profiles of mean wrinkling factor Ξ_Δ for the reacting highly swirled case SwB3 at z=10, 30 and 50mm from the burner nozzle. The results are shown for the wrinkled optimized model with each of the three SGS wrinkling models. Legend: • • Experimental data. - - - FOC-FWF model with wrinkling model 1. -.- FOC-FWF model with wrinkling model 2. — FOC-FWF model with wrinkling model 3.*

correct hot gas expansion. For CPU time reasons, the parametric analysis on CO formation is carried out on the coarse mesh, where the FOC-FWF model is challenged against TFLES and FOC-FPF models.
The relatively low temperature measured near the burner centerline, as compared to the adiabatic flame temperature at $\phi = 0.75$ (estimated as $T_{adiab} = 1920K$), has been pointed out by Sweeney et al. (2012b). This behavior is explained by the recirculation of both air and cooler combustion products from downstream the burner, due to the wide and open re-circulation zone. The physical phenomenon is not correctly predicted in the simulations as the computed center-line temperatures in Fig. 4.28 are higher than experimental values for any of the considered models. Recent studies (see 2018 TNF workshop) suggest that long statistical convergence times, as compared to the time used in the present study, should be used on the SwB3 case to correctly capture the temperature statistics.

CO formation Major differences between combustion models are observed in the prediction of CO mass fractions. Mean profiles $\{\widetilde{Y}_{CO}\}$ are shown in Fig. 4.31 for $z = 10$ to 60mm. The TFLES solution severely over-predicts CO for any of the axial locations. This corroborates the analysis made on the SwB1 non-swirled burner. The over-prediction is likely due to the multiplication of the computed CO mass by the thickening factor, as in the current case $\mathcal{F} \approx 5$ in the flame front. Indeed at the axial location $z = 10$mm, the SGS wrinkling effects are low ($\Xi_\Delta \approx 1$), and the relationship $\mathcal{I}_{CO}^{TFLES} = 3.9\mathcal{I}_{CO}^{laminar}$, where $\mathcal{I}_{CO}^{laminar}$ is the value of CO integral computed with the FOC-FPF model, is obtained. The ratio between CO integrals of flames respectively computed in the thickened and filtered formalisms is hence of the same order of magnitude

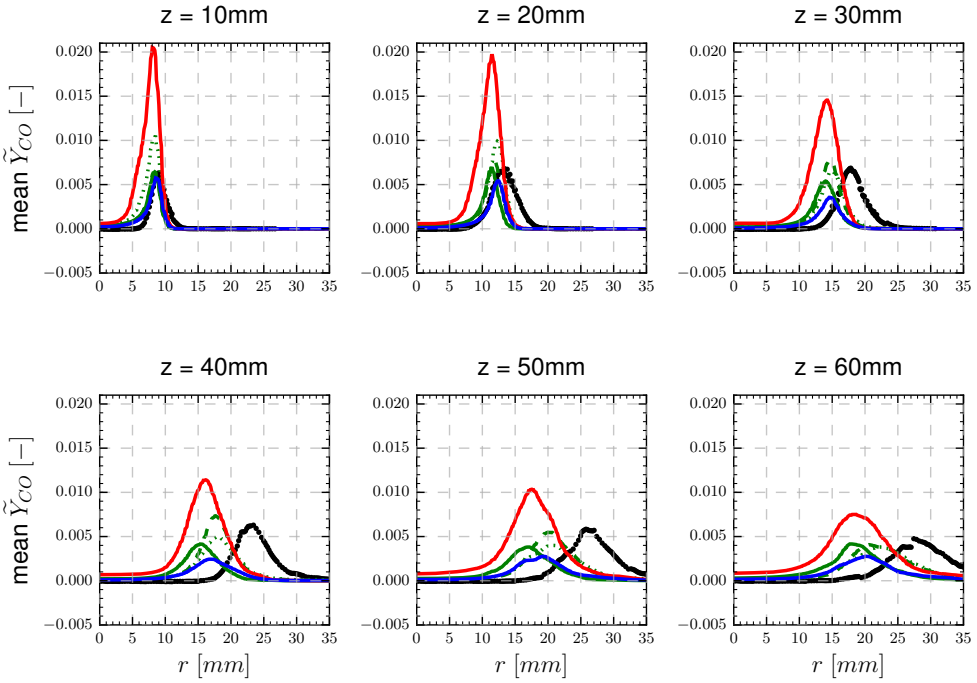

Figure 4.31: *Radial profiles of mean CO mass fraction for the reacting highly swirled case SwB3 at z=10, 20, 30, 40, 50 and 60mm from the burner nozzle. Legend:* • • *Experimental data.* — *TFLES model with wrinkling model 1.* — *FOC-FPF model with wrinkling model 1.* — *FOC-FWF model with wrinkling model 1.* . . . *FOC-FWF model with wrinkling model 2.* - - - *FOC-FWF model with wrinkling model 3.*

than $\mathcal{F}$.

As shown in Fig. 4.31, The FOC-FPF model is able to predict accurately the mean CO mass fraction for $z = 10$mm. As the SGS wrinkling model 1 is used, the computed SGS wrinkling factor satisfies $\Xi_\Delta \approx 1$ at this axial location. For $z \geq 20$mm, the CO mass fractions are however under-predicted. This corresponds to the flame regions where the wrinkling factor is significantly larger than one.

A comparison between instantaneous $\widetilde{Y}_{CO}$ fields computed using the FOC-FPF model (with SGS wrinkling model 1) and the FOC-FWF model (with SGS wrinkling model 3) is shown in Fig. 4.32. As observed for SwB1, a significantly increased amount of CO is predicted by FOC-FWF, due to the influence of Ξ_Δ on $\widetilde{Y}_{CO}$. Challenging the computations done with each of the three SGS wrinkling models (see Fig. 4.31) highlights the strong influence of the SGS wrinkling model on the predicted $\{\widetilde{Y}_{CO}\}$. In the quasi-laminar part of the flame ($z = 10$mm), models 1 and 3 are in agreement with experimental data

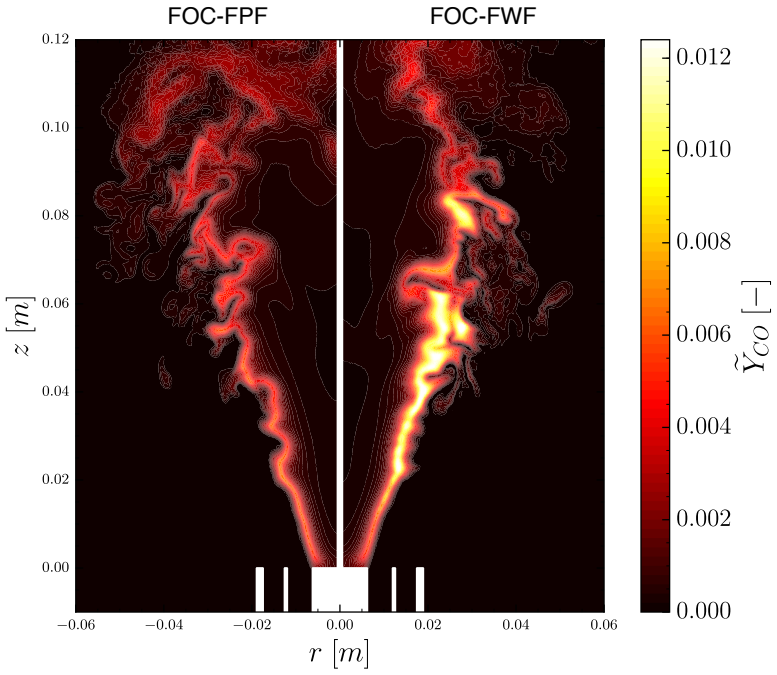

Figure 4.32: *2-D fields of instantaneous CO for FOC-FWF and FOC-FPF models in the SwB3 case. These fields are obtained in the plane $x = 0$ (also defined by $\theta \equiv 0$ [π]). On the left: instantaneous CO field for filtered laminar optimized model. On the right: instantaneous CO field for wrinkled optimized model.*

while model 2 largely over-predicts the CO mass fraction. This is due to the fact that with model 2, Ξ_Δ reaches its saturated value downstream (see Fig. 4.30). It is not consistent with the flame behavior observed experimentally and shows that the over-estimation of the wrinkling factor leads to an over-prediction of mean CO. For $z \geq 20$mm, the predicted wrinkling factor is larger than 1 (see Fig. 4.30 for mean profiles), and the wrinkled model improves the prediction of CO mass fractions with respect to the FOC-FPF model. SGS Wrinkling models 1 and 2 give similar results while model 3 predicts higher values, which are in better agreement with experimental CO peaks. This is emphasized in Fig. 4.33 (left) where $\{\widetilde{Y}_{CO}\}$ peak values are plotted as a function of the axial position z. Only the simulation with SGS wrinkling model 3 is able to predict an accurate value for the CO peak. The CO integral $\mathcal{I}_{CO}$ is shown on the right of Fig. 4.33. Unlike to SwB1 analysis, the study is directly performed on $\mathcal{I}_{CO}$ (instead of $\delta\mathcal{I}_{CO}$) as differential diffusion effects are weak. TFLES strongly over-predicts the CO integral while the FOC-FPF model under-predicts it. The introduction of the SGS wrinkling influence improves of the predictions, in particular when using SGS wrinkling model 2 and 3. The higher value observed in experimental data is partly attributed to the under-prediction of the radial flame expansion.

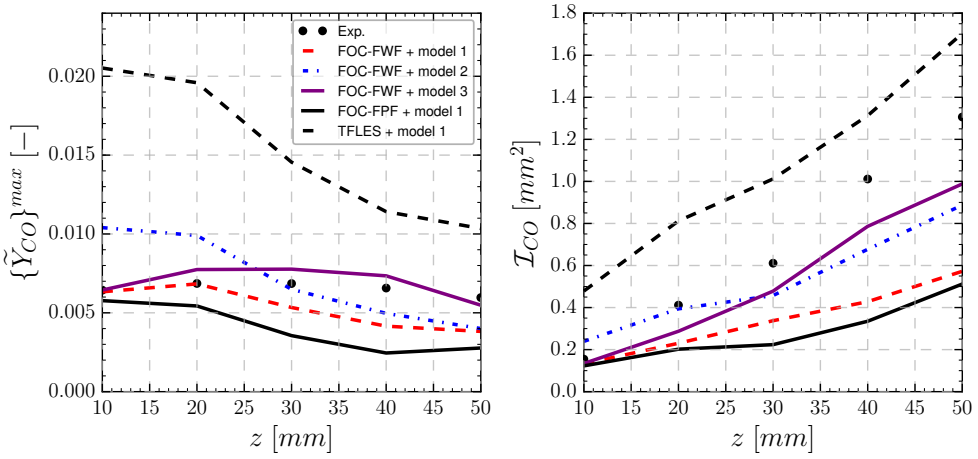

Figure 4.33: *Analysis of mean CO* $\{\widetilde{Y}_{CO}\}$ *peak and integral on planes* $z = cte$ *for the different combustion models considered for the simulation of the SwB3 case. On the left: CO peak* $\{\widetilde{Y}_{CO}^{max}\}$ *as a function of* z*. On the right: CO integral* $\mathcal{I}_{CO}$ *in planes* $z = cte$ *as a function of* z*.*

4.4.3 Concluding remarks on the highly swirled premixed Cambridge simulation

In this section, the Cambridge burner has been simulated in its premixed highly swirled operating conditions. The study is focused on the FOC-FWF model which is compared to a classical TFLES model as well as to the FOC-FPF model. TFLES severely over-predicts the CO mass fractions and the FOC-FPF model under-predicts them. A significant influence of the SGS wrinkling model is observed when using the FOC-FWF model. Artificially increasing the wrinkling factor by setting the model constant β to 0.9 leads to accurate predictions of CO peaks. Further investigations must however be performed to validate quantitatively the model on the SwB3 configuration.

4.5 Computational costs

An important criteria for assessing the suitability of a combustion model is the associated computational cost. Keeping costs at a reasonable level is indeed essential for applying a methodology on realistic cases. The flow through time (FTT) of the Cambridge burner is estimated as FTT $= L_r/U_i$ where $L_r \approx 0.1m$ is a characteristic height of the reaction zone and $U_i \approx 10m/s$ the bulk velocity of the inner tube (Mercier (2016)). Hence, 1 FTT = 10 ms.
The amount of CPU hours required for the simulation of 1 FTT for the different combustion models on the SwB1 and SwB3 cases is summarized in Tab. 4.5. The cost reported here are for simulations performed with Intel Xeon CPU E5-2670 v3 (2.30 GHz, Haswell) processors. The main conclusion is that com-

Table 4.5: *Computational cost of the Cambridge burner for the three tested combustion models (TFLES, FOC-FPF and FOC-FWF) and the two simulated reactive cases (SwB1 and SwB3).*

Combustion model	Case	1 FFT cost (CPU hours)	Normalized w.r.t TFLES
TFLES	SwB1	2 200 h	1
	SwB3	6 200 h	1
FOC-FPF model	SwB1	2 700 h	1.2
	SwB3	10 700 h	1.7
FOC-FWF model	SwB1	3 300 h	1.5
	SwB3	11 700 h	1.9

putational costs of the two optimized models is of the same order of magnitude than a simulation with TFLES. Increased costs for FOC-FPF and FOC-FWF models are attributed to additional table reading and interpolations in order to compute coefficients α^* and $\mathcal{A}^*$.

4.6 Conclusions

The work in this chapter focused on the validation of the LES combustion models proposed in chapter 3 on an academic burner. The retained configuration for challenging the models is the Cambridge SwB burner. It has been simulated in premixed non-swirled and premixed highly swirled operating conditions. The main conclusions are the following:

- TFLES modeling significantly over-predicts the mean CO mass fractions levels in any of the studied configuration. The explanation lies in the fact that thickening a flame leads to a multiplication of the overall CO mass. This is rigorously demonstrated in 1-D and is likely to have a strong impact in 3-D cases.

- The FOC-FPF model tends to under-predict mean CO mass fraction when confronted to experimental data. This is attributed to the effects of sub-grid scale wrinkling on the filtered profiles, which is not taken into account in this formulation.

- Adding the influence of SGS wrinkling on CO through the methodology developed in chapter 3 leads to more accurate results. Significant improvements are made when considering CO mass fractions integrated in the flame zone. Results are however influenced by the way the SGS wrinkling is computed and further studies have to be carried out to gain more insight on this dependency.

A summary of the abilities of TFLES, FOC-FPF and FOC-FWF models to correctly capture the overall CO mass in the LES of a fictive volume $\mathcal{V}$ is illustrated in Fig. 4.34. The reported masses are the ones expected from theoretical considerations and numerical results obtained in this chapter. The FOC-FWF model is the only model predicting at the same time the correct CO mass in situations where the wrinkling is fully resolved (top row of the table) and an increase of the mass when the flame in wrinkled at the subgrid scale (bottom row). Compensation errors might happen if the artificial increase of CO mass due to thickening balances the increase due to SGS wrinkling.

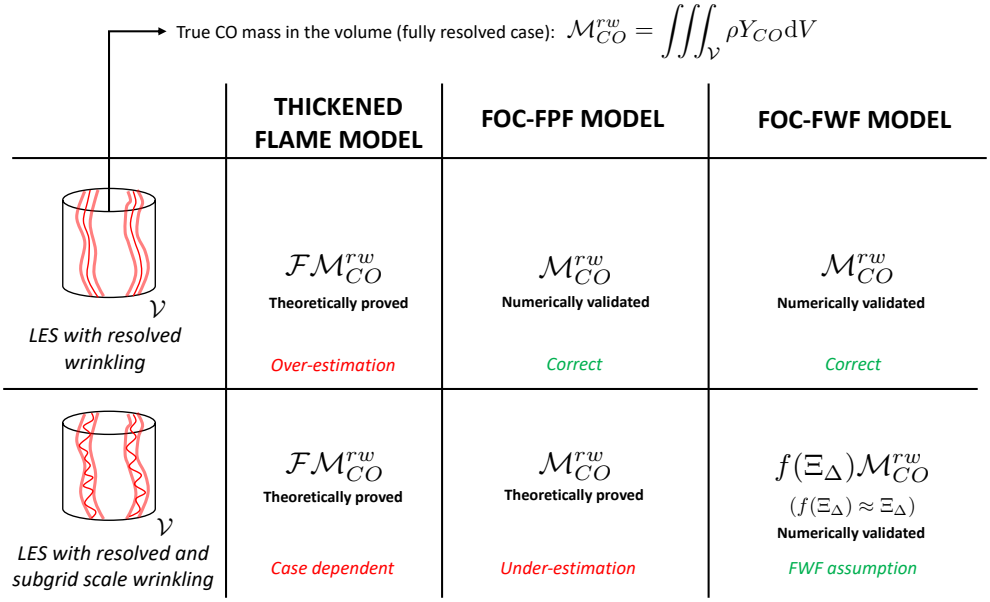

Figure 4.34: *Summary of the ability of TFLES, FOC-FPF and FOC-FWF models to conserve CO mass in the LES of a fictive volume $\mathcal{V}$. Values of the CO mass computed with each LES model are reported in the cells.*

Further work has to be undertaken to be able to apply the new model to more complex flames:

- The models presented in chapter 3 target premixed combustion regimes, and stratified regimes where sub-grid scale fluctuations of mixture fractions are neglected. Extension to partially premixed situations where sub-grid mixture fraction variance is important and to non-premixed regimes requires an additional modeling effort.

- In its current formulation, the FOC-FWF model requires the solving of a large number optimization problems. The next chapter proposes a solution to simplify the optimization procedure.

Chapter 5

FOC-FWF modeling with simplified optimization

Contents

The FOC-FWF model is built by optimizing model coefficients for a wide range of SGS wrinkling factors. This chapter presents a simplification of the optimization procedure. It is based on the derivation of analytic relationships for the model parameters, leading to a simplified optimization in the pre-processing step, where only two parameters are optimized for each equivalence ratio. The simplified model is first validated on FWF flamelets computation and then on the Cambridge SwB1 turbulent premixed burner.

5.1 Motivations

THE FOC-FWF modeling strategy, developed in chapter 3 for including sub-grid scale wrinkling effects on the flame chemical structure, leads to promising results on the Cambridge swirled burner in premixed operating conditions (see chapter 4). The methodology is based on the optimization of Arrhenius coefficients of a chemical mechanism by targeting Filtered Wrinkled Flamelets (FWF), parametrized by the wrinkling factor Ξ_Δ, the number of wrinkling patterns in a subfilter box n_Δ and the equivalence ratio ϕ. As optimization is done in a pre-processing step for a wide range of these parameters, it is computationally expensive.

The cost and complexity of the FOC-FWF model implementation trigger the need for a simpler alternative. The underlying motivation is the continuity observed in the evolution of the model coefficients ξ_i^T and ξ_i^{CO} $(i = 1, 2)$ with the sub-grid scale wrinkling factor Ξ_Δ. This feature is illustrated in Figs. 5.1 and 5.2, where the parameters for methane/air flames at an equivalence ratio $\phi = 0.75$ and filter size $\Delta = 4\delta_l^0$ and obtained from optimization are recalled. A model based on analytic relationships for computing model coefficients ξ_i^T and ξ_i^{CO} is investigated in this chapter.

Prerequisites for deriving the analytic model are first presented in Sec. 5.2. These include a model for computing the thickness of FWF flamelets and the definition of a flame sub-grid density. The simplified version of the FOC-FWF model based on analytic relationships for ξ_i^T and ξ_i^{CO} is then presented in Sec. 5.3 and is applied to the Cambridge burner in Sec. 5.4.

5.2 Prerequisites for building a simplified FOC-FWF model

5.2.1 Analytic model for the wrinkled thickness $\overline{\delta}_\Xi$

A model for the thickness $\overline{\delta}_\Xi$ of manufactured FWF flamelets is provided here. In this chapter, $\overline{\delta}_\Xi$ is defined as the length over which the FWF temperature profile $\widetilde{T}^\Xi$ grows from $T_0 + 0.01(T_{eq} - T_0)$ to $T_0 + 0.9(T_{eq} - T_0)$, where T_{eq} and

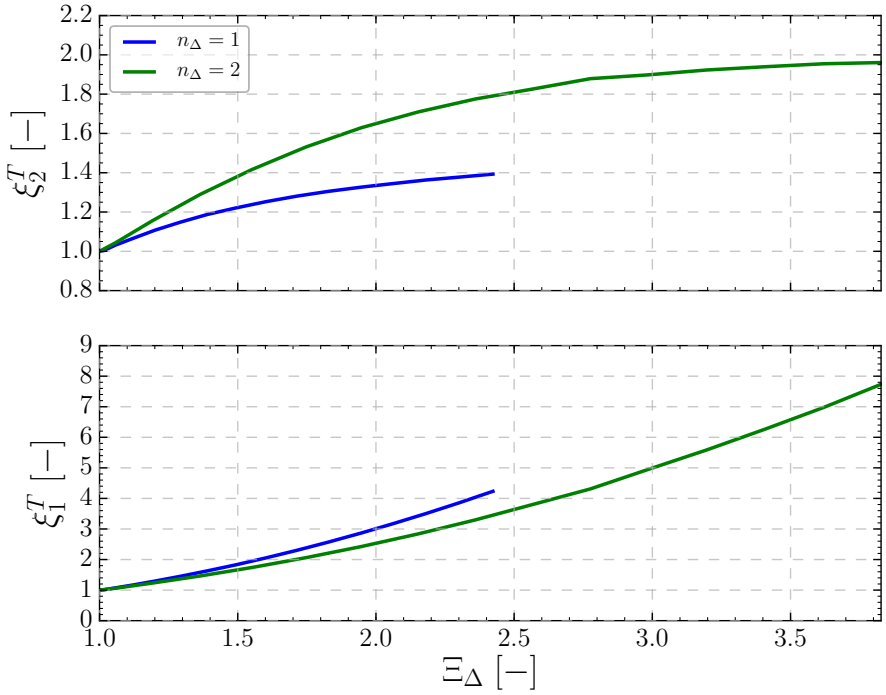

Figure 5.1: *Dimensionless factors* ξ_1^T *and* ξ_2^T *for* $\phi = 0.75$ *and* $\Delta = 4\delta_l^0$. *Legend:* — $n_\Delta = 1$, — $n_\Delta = 2$.

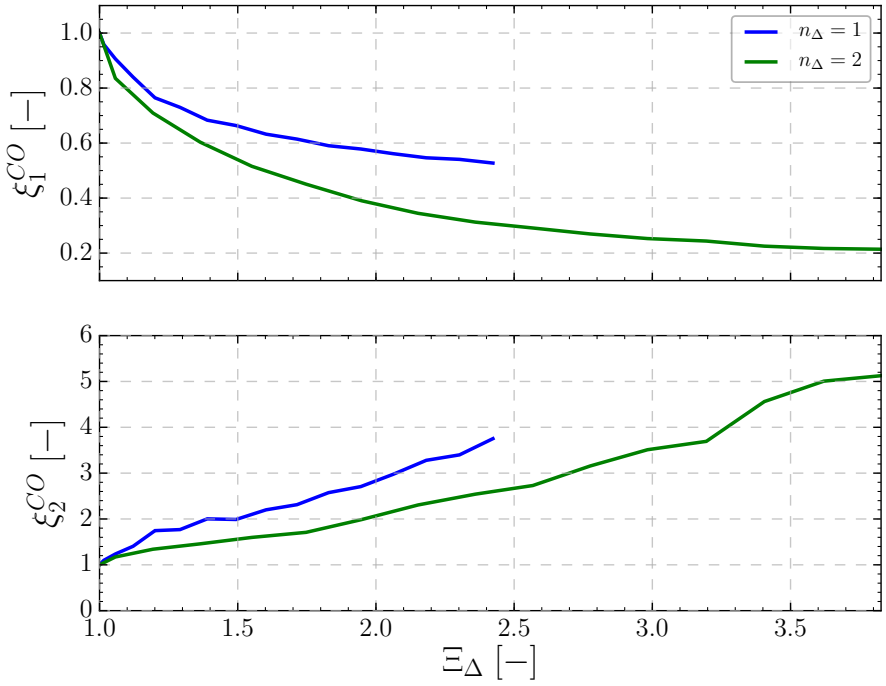

Figure 5.2: *Dimensionless factors* ξ_1^{CO} *and* ξ_2^{CO} *for* $\phi = 0.75$ *and* $\Delta = 4\delta_l^0$. *Legend:* — $n_\Delta = 1$, — $n_\Delta = 2$.

T_0 are the equilibrium and the fresh gas temperature, respectively.

Presuming the functional form of $\overline{\delta}_\Xi(\Xi_\Delta)$ The thickness evolution of a FWF flamelet is close to linear when the wrinkling factor Ξ_Δ is high. This is illustrated in Fig. 5.3 (solid lines) for $\Delta/\delta_l^0 = 2$, 4 and 8. The evolution of the thickness with the sub-grid scale wrinkling is thus assumed to follow a simple linear law. By taking into account the relationship $\overline{\delta}_\Xi(1) = \overline{\delta}_l$ in the limit of no sub-grid scale wrinkling, the following function is proposed:

$$\overline{\delta}_\Xi(\Xi_\Delta) = \alpha\,(\Xi_\Delta - 1) + \overline{\delta}_l \tag{5.1}$$

where α is the slope of the linear function.

Estimating the slope in Eq. (5.1) For the model to be closed, a value has to be specified for the slope α. Since Eq. (5.1) is linear, this coefficient can formally be defined as:

$$\alpha = \left(\frac{\partial\overline{\delta}_\Xi}{\partial\Xi_\Delta}\right) \tag{5.2}$$

This derivative cannot be evaluated directly and a simplified analysis is thus proposed. The coefficient α is computed in the asymptotic limit $\Xi_\Delta \to +\infty$. For a given value of n_Δ, $\Xi_\Delta \to +\infty$ leads to a large amplitude of the sine A compared to the filter Δ. The effect of the LES filter on the flame thickness is thus negligible compared to the thickness induced by the sine amplitude. Hence, $\overline{\delta}_\Xi \approx 2A$ is an acceptable approximation. This leads to:

$$\left(\frac{\partial\overline{\delta}_\Xi}{\partial\Xi_\Delta}\right) \approx 2\left(\frac{\partial A}{\partial\Xi_\Delta}\right) = 2\left(\frac{\partial\Xi_\Delta}{\partial A}\right)^{-1} \tag{5.3}$$

In the case of infinitely thin flame assumption, an analytic model for $\Xi_\Delta(A)$ is found (see Eq. (3.49)). It can be shown that $\Xi_\Delta(A)$ tends to a linear function when $A \to +\infty$ and hence its derivative tends to a constant value (see Appendix B for the mathematical demonstration). This translates to:

$$\left(\frac{\partial\overline{\delta}_\Xi}{\partial\Xi_\Delta}\right) = \frac{2}{\lim\limits_{A\to+\infty}\left(\frac{\partial\Xi_\Delta}{\partial A}\right)} \tag{5.4}$$

The limit $\lim_{A\to+\infty}(\partial\Xi_\Delta/\partial A)$ is computed as:

$$\lim_{A\to+\infty}\left(\frac{\partial\Xi_\Delta}{\partial A}\right)=\frac{4n_\Delta}{\Delta} \tag{5.5}$$

Details about the derivation can be found in Appendix B. The slope of the FWF flame thickness is hence $\alpha=\Delta/2n_\Delta$ and the model for the thickness becomes:

$$\overline{\delta}_\Xi(\Xi_\Delta)=\frac{\Delta}{2n_\Delta}(\Xi_\Delta-1)+\overline{\delta}_l \tag{5.6}$$

Thickness profiles computed using Eq. (5.6) are compared against numerical data in Fig. 5.3 for three filter sizes and several values of n_Δ. Discrepancies are observed for $\Delta/\delta_l^0=2$. This can be related to the fact that the analytic model for Ξ_Δ severely mispredicts the numerical wrinkling factor (see Fig. 3.14). The agreement between analytic and numerical functions is good for $\Delta/\delta_l^0=4$ and for $\Delta/\delta_l^0=8$ with $n_\Delta=1$. Differences are seen for higher values of n_Δ, which may also be due to the infinitely thin flame assumption and the use of the analytic model $\Xi_\Delta(A)$.

5.2.2 Flame sub-grid density definition

A feature of FWF flamelets encountered in chapter 3 is that for a given sub-grid scale wrinkling factor, the structure of the flame depends on n_Δ, the number of sine patterns in the sub-filter domain. As a reminder, it is illustrated in Fig. 5.4, where FWF temperature $\widetilde{T}^\Xi$ and FWF CO mass fraction $\widetilde{Y}_{CO}^\Xi$ are represented for several SGS wrinkling factors and $n_\Delta=1$ and 2. For a given value of Ξ_Δ, the flame thickness is smaller for $n_\Delta=2$ than for $n_\Delta=1$. The CO peak is also higher when $n_\Delta=2$.

In order to discriminate between situations where the sub-grid scale wrinkling factor is identical, a sub-grid flame density d_f (in m/m^2) is defined as the length of a flame included in a sub-filter box of width Δ and length $\overline{\delta}_\Xi$, divided by the area of the same region. Hence:

$$d_f(\Xi_\Delta)=\frac{\mathcal{L}}{\overline{\delta}_\Xi\times\Delta}=\frac{\Xi_\Delta}{\overline{\delta}_\Xi} \tag{5.7}$$

The flame density concept is illustrated in Fig. 5.5 where a low density flame is schematically compared to a high density flame with the same wrinkling factor. The density represents the length of the sinusoidal curve in the boxes $(\Delta,\overline{\delta}_{\Xi,i})$. This definition of the flame density leads to a finite value $d_f^{lam}=1/\overline{\delta}_l$ in the

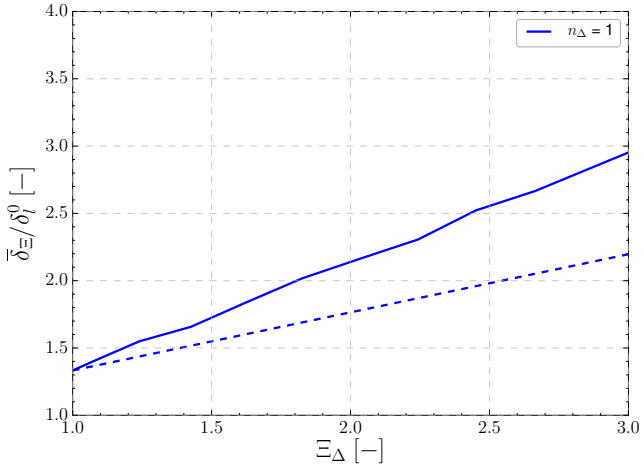

(a) $\Delta/\delta_l^0 = 2$

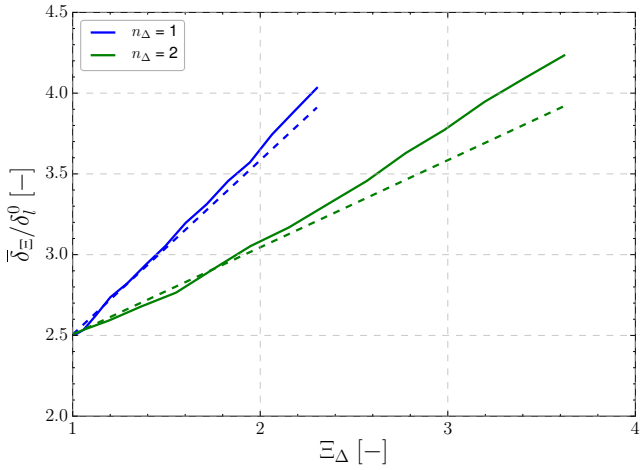

(b) $\Delta/\delta_l^0 = 4$

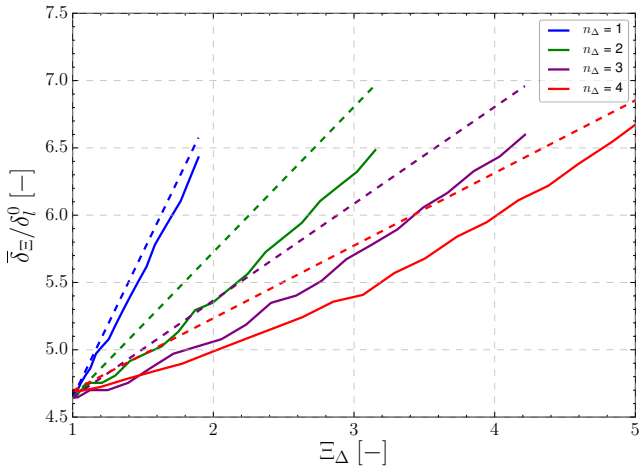

(c) $\Delta/\delta_l^0 = 8$

Figure 5.3: *Normalized thickness of FWF flamelets as a function of the SGS wrinkling factor Ξ_Δ. Numerical values computed using 2-D filtered manufactured flames (solid lines) are compared to thicknesses computed analytically using Eq. (5.6) (dashed lines).*

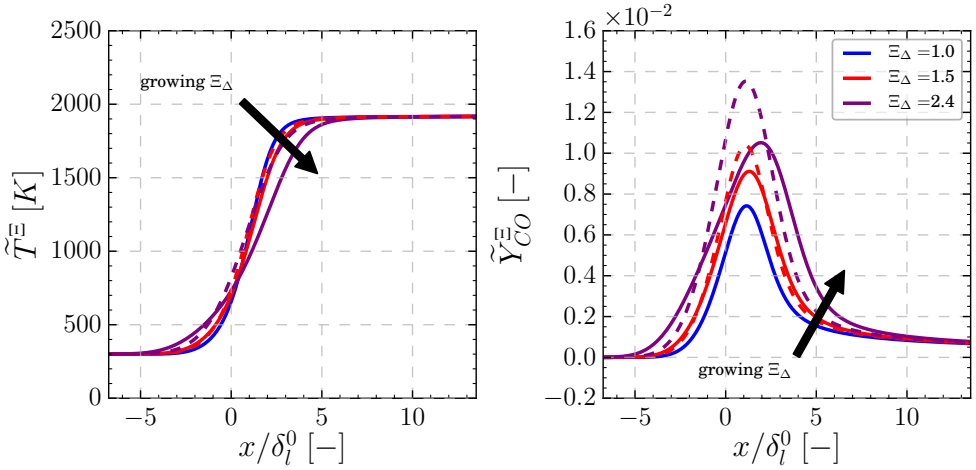

Figure 5.4: *Illustration of the flamelet library for different wrinkling factors for* $\phi = 0.75$, $\Delta = 2.5mm$ *and* $n_\Delta = 1$ *and* 2. *Profiles for* $n_\Delta = 1$ *are represented in solid lines while* $n_\Delta = 2$ *profiles are in dashed lines. On the left: filtered temperature. On the right: filtered CO mass fraction.*

laminar case ($\Xi_\Delta = 1$), where $\overline{\delta}_l$ is the thickness of the laminar filtered flame. For a given value of Ξ_Δ, $\overline{\delta}_\Xi$ decreases with n_Δ and the density thus increases. Using the approximation $\overline{\delta}_\Xi \approx 2A$ for large values of A and the model provided by Eq. (5.6), the flame sub-grid density is approximated as:

$$d_f(\Xi_\Delta) \approx \frac{2n_\Delta \Xi_\Delta}{\Delta\,(\Xi_\Delta - 1) + 2n_\Delta \overline{\delta}_l} \tag{5.8}$$

And a density normalized by its laminar value is consequently written:

$$\frac{d_f(\Xi_\Delta)}{d_f^{lam}} = \frac{2n_\Delta \overline{\delta}_l \Xi_\Delta}{\Delta\,(\Xi_\Delta - 1) + 2n_\Delta \overline{\delta}_l} \tag{5.9}$$

An illustration of the flame sub-grid density evolution with Ξ_Δ is provided in Fig. 5.6. The analytic flame density computed from Eq. (5.8) (dashed lines) is compared to the numerically computed density obtained from Eq. (5.7) (solid lines).

5.3 Simplified methodology for computing FOC-FWF model coefficients

A simplified version of the FOC-FWF modeling strategy is presented in this section. The model is constructed for virtual chemical mechanisms. The for-

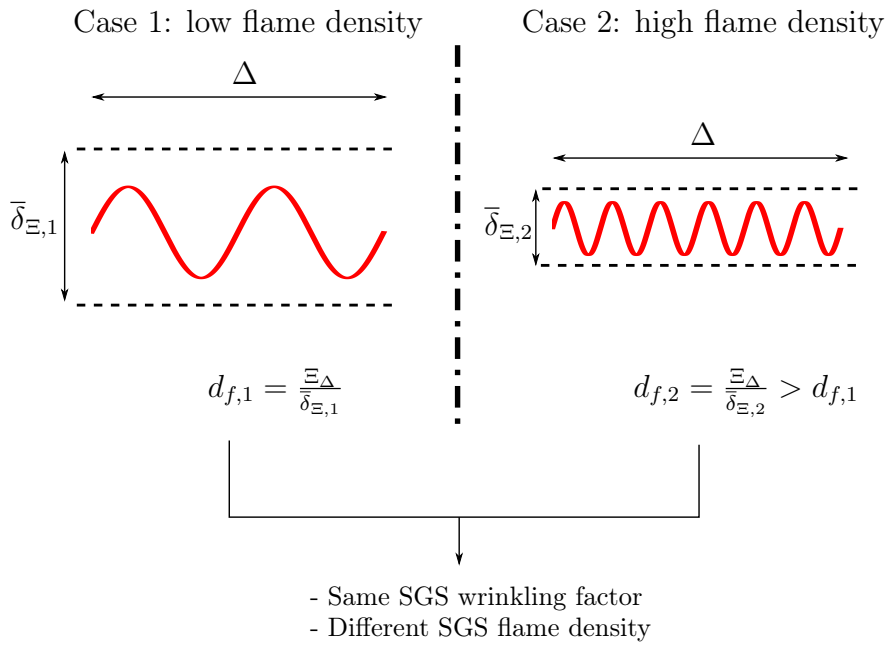

Figure 5.5: *Schemes representing two filtered wrinkled flames in sub-filter boxes with the same SGS wrinkling factor Ξ_Δ but with different flame subgrid densities d_f. On the left: low SGS density flame. On the right: high SGS density flame.*

malism and notations previously presented in chapter 3 are briefly recalled here, and analytic relationships for ξ_i^T and ξ_i^{CO} are then derived. The starting point of the study is the virtual chemical scheme reproducing Filtered Planar Flames (FPF), presented in Sec. 3.3 (FOC-FPF model). In FOC-FPF, the Arrhenius parameters of the main mechanism and CO sub-mechanism are written:

$$\begin{cases} \mathcal{A}_T^{*,\mathrm{FPF}} = \left(A_1^{*,\mathrm{FPF}}, E_{a,1}^{*,\mathrm{FPF}}, F_{F,1}^{*,\mathrm{FPF}}, F_{Ox,1}^{*,\mathrm{FPF}}, A_2^{*,\mathrm{FPF}}, E_{a,2}^{*,\mathrm{FPF}}, F_{I,2}^{*,\mathrm{FPF}}\right) & \text{(5.10a)} \\ \mathcal{A}_{CO}^{*,\mathrm{FPF}} = \left(A_4^{*,\mathrm{FPF}}, E_{a,4}^{*,\mathrm{FPF}}, F_{CO,2}^{*,\mathrm{FPF}}, F_{V1,2}^{*,\mathrm{FPF}}\right) & \text{(5.10b)} \end{cases}$$

Coefficients $\alpha_T^{*,\mathrm{FPF}}$ and $\alpha_{CO}^{*,\mathrm{FPF}}$ are the multiplicative factors for diffusive terms in respectively the main and CO mechanisms. The analysis is done here for a given equivalence ratio ϕ, which is therefore omitted in notations. Wrinkling effects on the flame structure are included through the functions ξ_1^T, ξ_2^T, ξ_1^{CO}

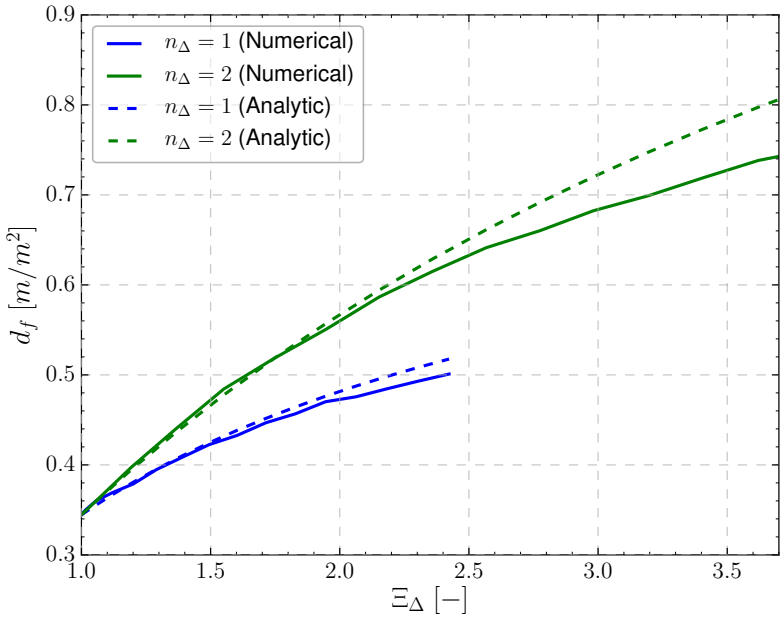

Figure 5.6: *Flame sub-grid density d_f of wrinkled flamelets as a function of the SGS wrinkling factor Ξ_Δ for $\Delta/\delta_l^0 = 4$. Numerical values computed using filtered 2-D manufactured flames (solid lines) are compared to densities computed analytically using Eq. (5.8) (dashed lines). Legend: — Numerical computation with $n_\Delta = 1$, - - - Analytic computation with $n_\Delta = 1$, — Numerical computation with $n_\Delta = 2$, - - - Analytic computation with $n_\Delta = 2$.*

and ξ_2^{CO}. These dimensionless coefficients are defined in chapter 3 as:

$$\begin{cases} \alpha_T^{*,\mathrm{FWF}}(\Xi_\Delta) = \xi_1^T(\Xi_\Delta)\,\alpha_T^{*,\mathrm{FPF}} & \text{(5.11a)} \\ A_1^{*,\mathrm{FWF}}(\Xi_\Delta) = \xi_2^T(\Xi_\Delta)\,A_1^{*,\mathrm{FPF}} & \text{(5.11b)} \\ \alpha_{CO}^{*,\mathrm{FWF}}(\Xi_\Delta) = \xi_1^{CO}(\Xi_\Delta)\,\alpha_{CO}^{*,\mathrm{FPF}} & \text{(5.11c)} \\ A_4^{*,\mathrm{FWF}}(\Xi_\Delta) = \xi_2^{CO}(\Xi_\Delta)\,A_4^{*,\mathrm{FPF}} & \text{(5.11d)} \end{cases}$$

where coefficients on the LHS of Eqs. (5.11a)-(5.11d) are the Arrhenius and diffusive correction parameters of FOC-FWF modeling approach.

The impact of SGS wrinkling on the filtered flame structure as observed in chapter 3 and 4 and illustrated in Fig. 5.4 is twofold:

- SGS wrinkling thickens the filtered flame front.
- The CO production is enhanced by SGS wrinkling. In particular, CO peak and mass increase with Ξ_Δ.

Table 5.1: *Summary of assumptions and models for the thickness of wrinkled flames* $\overline{\delta}_\Xi$ *and flame SGS density* d_f.

	Assumptions	**Model**
Wrinkled thickness	• Linear model for $\overline{\delta}_\Xi$ • $\overline{\delta}_\Xi = 2A$ for high sine amplitudes A	$\overline{\delta}_\Xi(\Xi_\Delta) = \frac{\Delta}{2n_\Delta}(\Xi_\Delta - 1) + \overline{\delta}_l$
Flame SGS density	• Thickness $\overline{\delta}_\Xi$ described by model Eq. (5.6)	$\frac{d_f(\Xi_\Delta)}{d_f^{lam}} = \frac{2n_\Delta \overline{\delta}_l \Xi_\Delta}{\Delta(\Xi_\Delta - 1) + 2n_\Delta \overline{\delta}_l}$

The objective is to find analytic models for the coefficients ξ_1^T, ξ_2^T, ξ_1^{CO} and ξ_2^{CO} defined in Eqs. (5.11a)-(5.11d). A model for ξ_1^T and ξ_2^T is derived in Sec. 5.3.2 from a flame thickness analysis. Analytic models for ξ_1^{CO} and ξ_2^{CO} are consequently designed by studying the local filtered CO production/consumption balance in Sec. 5.3.3.

5.3.1 Disctinction between semi and fully analytic formulations

The proposed modeling strategy requires in particular the knowledge of the flame thickness $\overline{\delta}_\Xi$. This function can be analytically modeled or computed numerically, as seen in Sec. 5.2. This distinction leads to the development of two strategies. In the first case (semi-analytic), the thickness is computed using the FWF database created in a pre-processing step and in the second case (fully analytic) the thickness is computed with an analytic model (Eq. (5.6)). This is summarized in Fig. 5.7.

5.3.2 Thickening effects of SGS wrinkling: modification of main mechanism

As illustrated in Fig. 5.4, SGS Wrinkling thickens the filtered flame front. The thickening due to SGS wrinkling is modeled by a broadening of the flame front.

Simplified analysis of flame speed and thickness Adapting the analysis made by Poinsot and Veynante (2005) to filtered flames, flame speed and filtered flame thickness are related to filtered diffusive term $\overline{D}_{th}$ and filtered reaction term $\overline{\dot{\Omega}}$ by the following relationships:

$$S_l^0 \propto \sqrt{\overline{D}_{th}\overline{\dot{\Omega}}} \quad ; \quad \overline{\delta}_l \propto \sqrt{\frac{\overline{D}_{th}}{\overline{\dot{\Omega}}}} \tag{5.12}$$

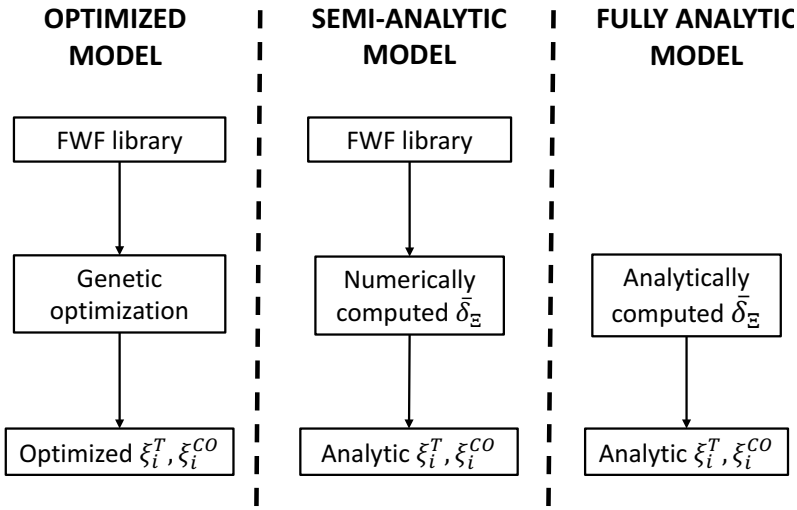

Figure 5.7: *Distinction between optimized, semi-analytic and fully analytic models.*

FWF flamelets have a turbulent propagation speed S_T and a thickness $\overline{\delta}_\Xi$. They are linked to the FWF diffusive term $\overline{D}_{th}^{\Xi}$ and FWF reaction term $\overline{\dot{\Omega}}^{\Xi}$ by:

$$S_T \propto \sqrt{\overline{D}_{th}^{\Xi}\overline{\dot{\Omega}}^{\Xi}} \quad ; \quad \overline{\delta}_\Xi \propto \sqrt{\frac{\overline{D}_{th}^{\Xi}}{\overline{\dot{\Omega}}^{\Xi}}} \tag{5.13}$$

As the turbulent propagation speed is $S_T = \Xi_\Delta S_l^0$, the following relationships are obtained:

$$\begin{cases} \overline{D}_{th}^{\Xi} = \Xi_\Delta \left(\dfrac{\overline{\delta}_\Xi}{\overline{\delta}_l}\right) \overline{D}_{th} & \text{(5.14a)} \\ \overline{\dot{\Omega}}^{\Xi} = \Xi_\Delta \left(\dfrac{\overline{\delta}_l}{\overline{\delta}_\Xi}\right) \overline{\dot{\Omega}} & \text{(5.14b)} \end{cases}$$

The impact of SGS wrinkling is hence modeled by a multiplication of the turbulent speed by Ξ_Δ and a thickening of the filtered flame front with a thickening factor $\mathcal{F}_\Xi = \overline{\delta}_\Xi / \overline{\delta}_l$.

Modification of wrinkled main mechanism parameters Wrinkling effects are included in the virtual main mechanism via the coefficients ξ_1^T and

ξ_2^T:

$$\begin{cases} \xi_1^T\left(\Xi_\Delta\right) = \Xi_\Delta\left(\dfrac{\overline{\delta}_\Xi}{\overline{\delta}_l}\right) & \text{(5.15a)} \\ \xi_2^T\left(\Xi_\Delta\right) = \Xi_\Delta\left(\dfrac{\overline{\delta}_l}{\overline{\delta}_\Xi}\right) & \text{(5.15b)} \end{cases}$$

to recover the correct thermal flame thickness and turbulent flame speed. The two coefficients are hence completely defined by Ξ_Δ and $\overline{\delta}_\Xi$ and no optimization is required.

5.3.3 SGS wrinkling effects on pollutants formation: modification of CO sub-scheme

It is shown in Sec. 4.3.2.3 that the inclusion of SGS wrinkling effects by a multiplication of diffusive and reactive terms with Ξ_Δ is not adapted to capture CO mass fractions in turbulent combustion. The use of chemical mechanisms optimized for recovering the structure of FWF flamelets leads to an improvement of predictions. A formulation involving analytic expressions for coefficients ξ_1^{CO} and ξ_2^{CO} is investigated here.

Filtered CO production in wrinkled flames As a reminder, the virtual CO sub-mechanism is defined as follows:

$$\alpha_F F + \alpha_{Ox} Ox \rightarrow CO \quad \text{(R3)}$$
$$CO \rightleftharpoons V_1 \quad \text{(R4)}$$

SGS wrinkling increases the peak and thickness of the filtered CO mass fraction $\widetilde{Y}_{CO}$. The mass of CO in the filtered flame front is thus increased. The idea is here to enhance the production of filtered CO in the flame front to model the added mass. The filtered CO reaction rate is split into production and consumption contributions:

$$\frac{\overline{\rho}\widetilde{\dot{\omega}}_{CO}^{l}}{W_{CO}} = \overline{w}^{prod,l} - \overline{w}^{cons,l} \quad \text{(5.16)}$$

where $\overline{w}^{prod,l}$ is the production rate of progress and $\overline{w}^{cons,l}$ the consumption rate of progress of filtered CO mass fraction. The superscript l refers to values obtained with the mechanism reproducing filtered laminar flames (FOC-FPF). By considering production and consumption of CO in reactions (R3) and (R4), these are can be assessed by:

$$\overline{w}^{prod,l} = \overline{w}_3^l + \overline{w}_4^{r,l} \tag{5.17}$$

$$\overline{w}^{cons,l} = \overline{w}_4^{f,l} \tag{5.18}$$

where $\overline{w}_3^l$ is the rate of progress of (R3), $\overline{w}_4^{f,l}$ the forward rate of progress of (R4) and $\overline{w}_4^{r,l}$ the reverse rate of progress of (R4). For a given thermo-chemical state $\mathbf{\Phi} = \left(\overline{\rho}, \widetilde{T}, \widetilde{Y}_k\right)$, the balance between production and consumption in the FOC-FWF model is formally expressed as a function of the FOC-FPF values by substituting Eqs. (5.11b) and (5.11d) in the expressions of the rates of progress:

$$\frac{\overline{w}^{prod,\Xi}(\mathbf{\Phi})}{\overline{w}^{cons,\Xi}(\mathbf{\Phi})} = \frac{\xi_2^T(\Xi_\Delta)\overline{w}_3^l(\mathbf{\Phi}) + \xi_2^{CO}(\Xi_\Delta)\overline{w}_4^{r,l}(\mathbf{\Phi})}{\xi_2^{CO}(\Xi_\Delta)\overline{w}_4^{f,l}(\mathbf{\Phi})} \tag{5.19}$$

where $\overline{w}^{prod,\Xi}$ and $\overline{w}^{cons,\Xi}$ are the rates of progress obtained with FOC-FWF. To further pursue the development, the assumption $\overline{w}_4^{r,l} \ll \overline{w}_3^l$ is made and validated in Fig. 5.8 for an equivalence ratio $\phi = 0.75$. A factor of approximately 65 is found between the peak values of $\overline{w}_3^l$ and $\overline{w}_4^{r,l}$.

By applying this assumption to Eq. (5.19), the following identity is found:

$$\frac{\overline{w}^{prod,\Xi}(\mathbf{\Phi})}{\overline{w}^{cons,\Xi}(\mathbf{\Phi})} = \left(\frac{\xi_2^T(\Xi_\Delta)}{\xi_2^{CO}(\Xi_\Delta)}\right)\left(\frac{\overline{w}^{prod,l}(\mathbf{\Phi})}{\overline{w}^{cons,l}(\mathbf{\Phi})}\right) \tag{5.20}$$

This formal expression shows that the SGS wrinkling influence on the filtered CO production/consumption balance can be controlled by choosing an appropriate $\mathcal{R} = \xi_2^T/\xi_2^{CO}$ ratio. The following conditions must be satisfied for the analysis to be valid:

- The chemistry is modeled using virtual chemical mechanisms.
- The influence of SGS wrinkling is integrated in the chemical mechanism by modifying the pre-exponential constants (see Eqs. (5.11b) and (5.11d)).
- The CO production due to the reverse contribution of reaction (R4) is small compared to the production of CO due to (R3).

Analytic models for ξ_1^{CO} and ξ_2^{CO} A model needs to be specified for $\mathcal{R} = \xi_2^T/\xi_2^{CO}$ in order to capture the filtered CO mass increase due to SGS wrinkling. This ratio is assumed to be dependent on the SGS wrinkling factor Ξ_Δ. Additionally, the influence of n_Δ is investigated through the use of the flame sub-grid density defined in Sec. 5.2. Two models are thus challenged:

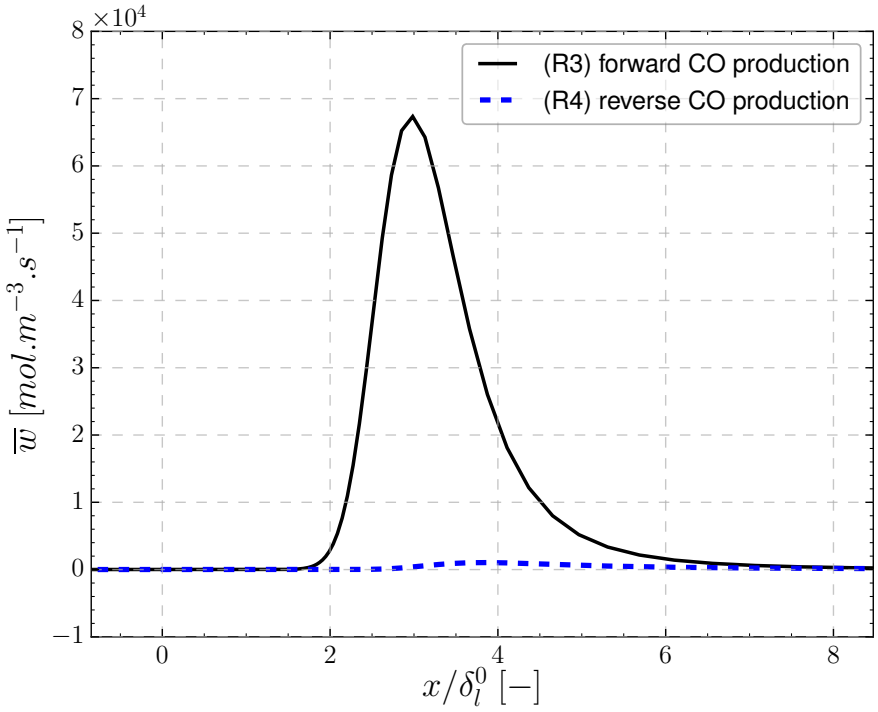

Figure 5.8: *Comparison between rates of progress of produced CO due to forward contribution of reaction (R3) and reverse contribution of reaction (R4). CO rates of progress are evaluated using virtual chemistry at* $\phi = 0.75$. *Legend: — Contribution* $\overline{w}_3^l$ *due to forward (R3) reaction. - - - Contribution* $\overline{w}_4^{f,l}$ *due to reverse (R4) reaction.*

- **CO correction model 1**: A first model is build by assuming that the ratio ξ_2^T/ξ_2^{CO} only varies with the wrinkling factor Ξ_Δ. The model needs to satisfy $(\xi_2^T/\xi_2^{CO})(\Xi_\Delta = 1) = 1$ and should be a growing function of the wrinkling factor, as the CO mass increases with Ξ_Δ. A power-law is retained:

$$\mathcal{R}\left(\Xi_\Delta\right) = \Xi_\Delta^\alpha \tag{5.21}$$

  where $\alpha > 0$ is a model parameter, which can obtained by an optimization.

- **CO correction model 2**: A second model is investigated by supposing that the ratio ξ_2^T/ξ_2^{CO} varies with the wrinkling factor and also with the flame sub-grid density. The model should be a growing function of Ξ_Δ and a growing function of d_f as the CO peak increases when the flame

is denser. The following power-law is proposed:

$$\mathcal{R}\left(\Xi_\Delta\right) = \Xi_\Delta^{\beta_1}\left(\frac{d_f(\Xi_\Delta)}{d_f^{lam}}\right)^{\beta_2} \tag{5.22}$$

where $\beta_1 > 0$ and $\beta_2 > 0$ are model parameters, which can be obtained by an optimization.

In order to keep a consistent CO thickness, the choice $\xi_1^{CO}(\Xi_\Delta) = \xi_1^T(\Xi_\Delta)$ is made. This implies that the thickening effect of wrinkling on CO is similar to its effect on the temperature. The analytic relationships for ξ_1^{CO} and ξ_2^{CO} are finally:

$$\begin{cases} \xi_1^{CO}\left(\Xi_\Delta\right) = \xi_1^T\left(\Xi_\Delta\right) & \text{(5.23a)} \\ \xi_2^{CO}\left(\Xi_\Delta\right) = \xi_2^T\left(\Xi_\Delta\right)/\mathcal{R}\left(\Xi_\Delta\right) & \text{(5.23b)} \end{cases}$$

Contrarily to the computation of ξ_1^T and ξ_2^T, model coefficients α (or β_1 and β_2), must be optimized to compute ξ_1^{CO} and ξ_2^{CO}. This optimization can be carried out by targeting FWF flamelets CO mass fractions and CO peaks. The optimization objective function in the CO prediction model 2 reads for instance:

$$\begin{aligned} \mathcal{F}^{CO}\left(\beta_1,\beta_2\right) = \sum_{(\Xi_\Delta,n_\Delta)} \Bigg[& \frac{\|\widetilde{Y}_{CO}\left(\beta_1,\beta_2\right) - \widetilde{Y}_{CO}^{ref}\left(\Xi_\Delta,n_\Delta\right)\|_2}{\|\widetilde{Y}_{CO}^{ref}\left(\Xi_\Delta,n_\Delta\right)\|_2} \\ & + \gamma_{CO}\frac{\left|\left[\widetilde{Y}_{CO}\right]^{max}\left(\beta_1,\beta_2\right) - \left[\widetilde{Y}_{CO}^{ref}\left(\Xi_\Delta,n_\Delta\right)\right]^{max}\right|}{\left[\widetilde{Y}_{CO}^{ref}\left(\Xi_\Delta,n_\Delta\right)\right]^{max}} \Bigg] \end{aligned} \tag{5.24}$$

where $\gamma_{CO} = 1$ and superscript *ref* refers to FWF reference flames. The computational effort is drastically reduced as, for a given equivalence ratio ϕ, only two (or one if the CO prediction model 1 is considered) parameters have to be optimized for the whole range of (Ξ_Δ, n_Δ) values.

5.3.4 Comparison between the fully optimized model and the simplified FOC-FWF models

The performance of the models derived for ξ_i^T and ξ_i^{CO} are assessed in two steps:

- The evolution of the analytic parameters with Ξ_Δ for $n_\Delta = 1$ and 2 are compared to the numerically computed values obtained in chapter 3. The differences between the semi-analytic and fully analytic models will

Table 5.2: *Summary of assumptions and models for the coefficients* ξ_i^T *and* ξ_i^{CO}.

	Assumptions	**Models**
Main mechanism coefficients	• Wrinkling thickens the flame	$\xi_1^T = \Xi_\Delta\left(\overline{\delta}_\Xi/\overline{\delta}_l\right)$ $\xi_2^T = \Xi_\Delta\left(\overline{\delta}_l/\overline{\delta}_\Xi\right)$
	• Virtual chemistry with a two-step CO sub-mechanism	
CO mechanism coefficients	• CO production by reverse (R4) smaller than production by (R3)	$\xi_1^{CO} = \xi_1^T$
	• Only pre-exponential constants are modified to account for SGS wrinkling effects	$\xi_2^{CO} = \xi_2^T/\mathcal{R}$

be emphasized.

- 1-D *a posteriori* simulations of FWF flamelets are performed using the analytic formulation of ξ_i^T and ξ_i^{CO} and compared to the flame profiles obtained using fully optimized coefficients.

The comparison is made for a filter size $\Delta = 4\delta_l^0$ and an equivalence ratio $\phi = 0.75$. The cases $n_\Delta = 1$ and $n_\Delta = 2$ are treated.

Comparison between analytic and optimized parameters The coefficients ξ_1^T and ξ_2^T computed with the semi and fully analytic models (Eqs. (5.15a) and (5.15b)) are compared in Fig. 5.9 to the parameters obtained from optimization. Optimized and analytic parameters are in close agreement. Minor discrepancies are observed at high SGS wrinkling factors in the case $n_\Delta = 2$. The departure from the optimized model is slightly more important for the fully analytic model. This suggests that modeling the effect of SGS wrinkling on the thermal structure of a filtered flame by a thickening factor is an accurate assumption.

The same comparison is carried out for CO sub-mechanism parameters using successively the first CO prediction model (Eq. (5.21)) and the second CO prediction model (Eq. (5.22)) for ξ_2^{CO}. For the first model, the model parameter $\alpha = 1$ is selected and for the second model, $\beta_1 = 0.5$ and $\beta_2 = 2$. Results using the first model are shown in Fig. 5.10 while the predictions obtained with the second model are illustrated in Fig. 5.11. In both cases, the analytic model predicts a decrease of the coefficient ξ_2^{CO} for any value of n_Δ. This in good qualitative agreement with the behavior of fully optimized coefficients. For the first model, predictions of the coefficients are however not accurate, especially in the case $n_\Delta = 2$. Results are improved when using the second model and the agreement with numerically computed coefficients is good. Moreover,

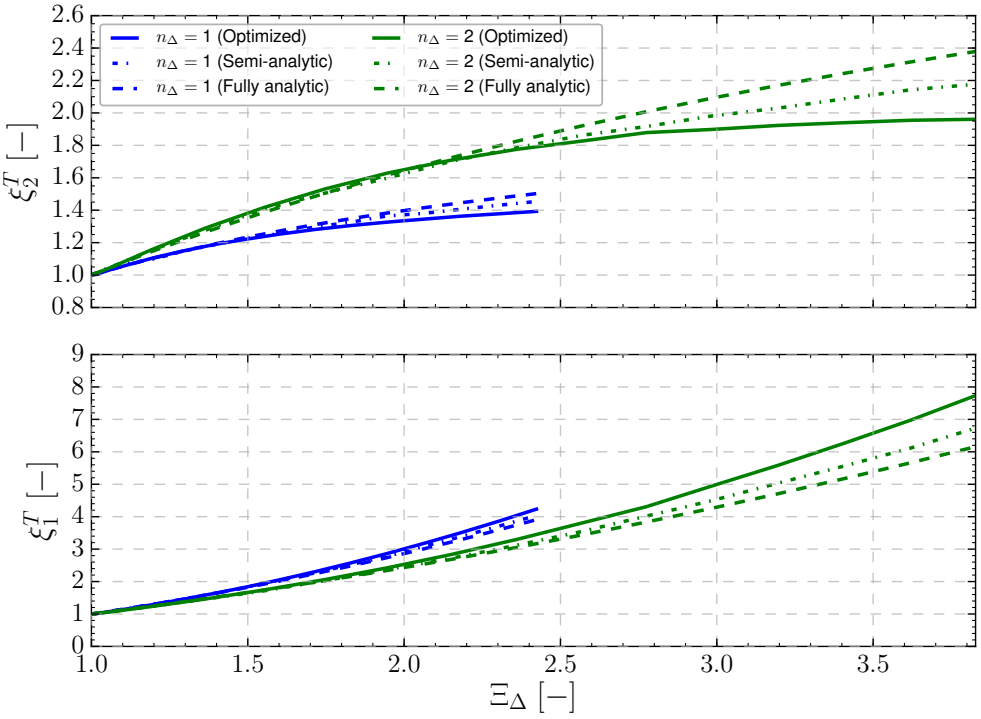

Figure 5.9: *Dimensionless factors* ξ_1^T *and* ξ_2^T *as a function of* Ξ_Δ *for* $\phi = 0.75$ *and* $\Delta = 4\delta_l^0$. *Values obtained with genetic optimization are shown in solid lines while analytically computed coefficients are in dashed lines. Legend:* — *Numerical computation with* $n_\Delta = 1$, - . - *Semi-analytic computation with* $n_\Delta = 1$, - - - *Fully analytic computation with* $n_\Delta = 1$, — *Numerical computation with* $n_\Delta = 2$, - . - *Semi-analytic computation with* $n_\Delta = 2$. - - - *Fully analytic computation with* $n_\Delta = 2$.

$\xi_2^{CO}(n_{\Delta=1}) < \xi_2^{CO}(n_{\Delta=2})$ when the first model is used, meaning that the influence of the flame density on the coefficients is not correctly recovered. This behavior is corrected when explicitly adding the flame density in the expression of ξ_2^{CO}. The difference between semi and fully analytic models is moreover negligible.

Simulation of 1-D FWF flamelets for different wrinkling factors FWF flamelets are then computed *a posteriori* with the analytic model for different values of sub-grid scale wrinkling and compared to simulation performed with optimized coefficients ξ_i^T and ξ_i^{CO}. The fully analytic model is selected with $\beta_1 = 0.5$ and $\beta_2 = 2$. Temperature profiles are shown in Fig. 5.12 for $n_\Delta = 1$ (top row of the figure) and $n_\Delta = 2$ (bottom row of the figure). A good agreement on the thermal flame structure is observed between analytic and optimized models.

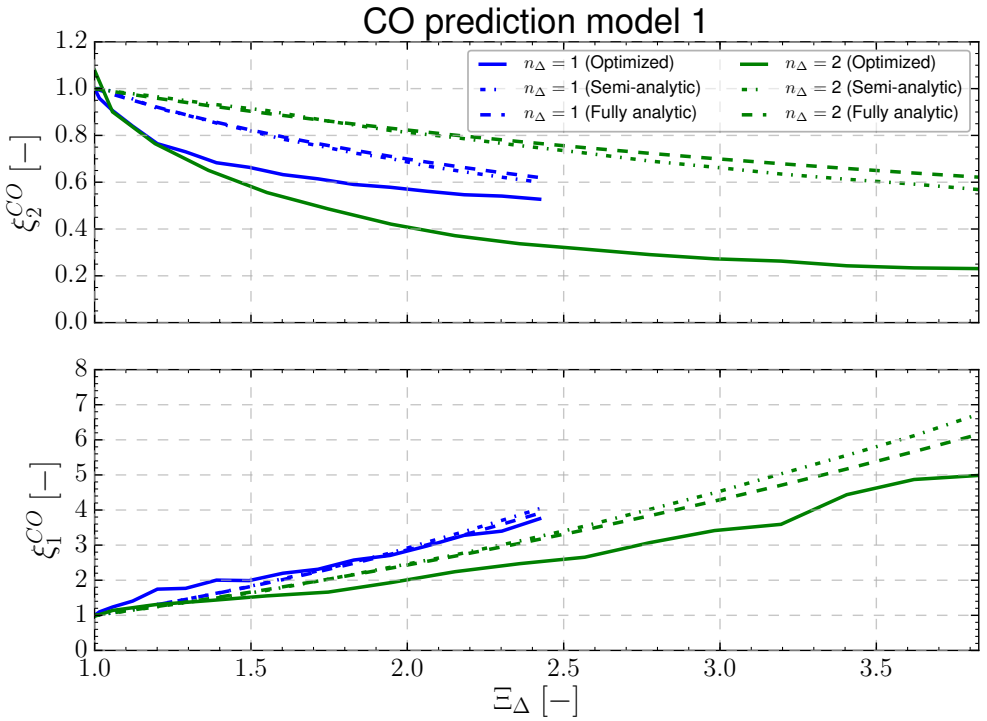

Figure 5.10: *Dimensionless factors ξ_1^{CO} and ξ_2^{CO} as a function of Ξ_Δ for $\phi = 0.75$ and $\Delta = 2.5mm$. Values obtained with genetic optimization are shown in solid lines while analytically computed coefficients with CO prediction model 1 (Eq. (5.21)) are in dashed lines. Legend: — Numerical computation with $n_\Delta = 1$, - . - Semi-analytic computation with $n_\Delta = 1$, - - - Fully analytic computation with $n_\Delta = 1$, — Numerical computation with $n_\Delta = 2$, - . - Semi-analytic computation with $n_\Delta = 2$. - - - Fully analytic computation with $n_\Delta = 2$.*

CO profiles are shown in Fig. 5.13. Analytic profiles using CO prediction models 1 and 2 are challenged against the profiles computed with optimized coefficients. For $n_\Delta = 1$, the CO mass fractions obtained with models 1 and 2 are in close agreement with the fully optimized model computations. A slight improvement is observed with analytic CO model 2, especially for $\Xi_\Delta = 1.5$. Regarding the case $n_\Delta = 2$, the CO peak is largely under-predicted by model 1, while the use of model 2 significantly improves results. This is in good agreement with the behavior observed when comparing analytic and optimized coefficients ξ_i^T and ξ_i^{CO}. As expected from the analysis of ξ_1^{CO}, which is over-predicted by analytic models, the flames computed with the analytic modeling strategy are slightly thicker than the reference flames.

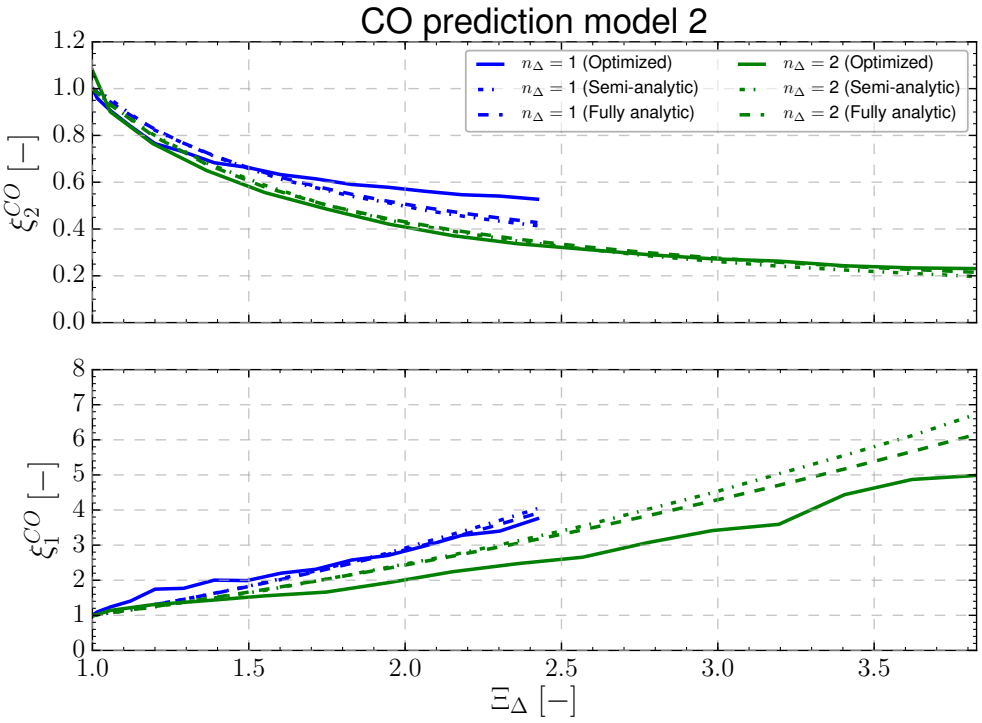

Figure 5.11: *Dimensionless factors ξ_1^{CO} and ξ_2^{CO} as a function of Ξ_Δ for $\phi = 0.75$ and $\Delta = 4\delta_l^0$. Values obtained with genetic optimization are shown in solid lines while analytically computed coefficients with CO prediction model 2 (Eq. (5.22)) are in dashed lines. Legend: — Numerical computation with $n_\Delta = 1$, - . - Semi-analytic computation with $n_\Delta = 1$, - - - Fully analytic computation with $n_\Delta = 1$, — Numerical computation with $n_\Delta = 2$, - . - Semi-analytic computation with $n_\Delta = 2$. - - - Fully analytic computation with $n_\Delta = 2$.*

5.4 Validation on the Cambridge burner

The simplified FOC-FWF model is tested on the Cambridge burner in its non-swirled premixed operating conditions SwB1. It is challenged against the results obtained with the FOC-FWF in chapter 4.

5.4.1 Modeling details

The Charlette wrinkling model with model parameter $\beta = 0.5$ is retained. The analytic model for ξ_i^T and ξ_i^{CO} is built using $\Delta = 4\delta_l^0$ and $n_\Delta = 2$. The second CO prediction model, including the influence of the sub-grid scale flame density, is selected.

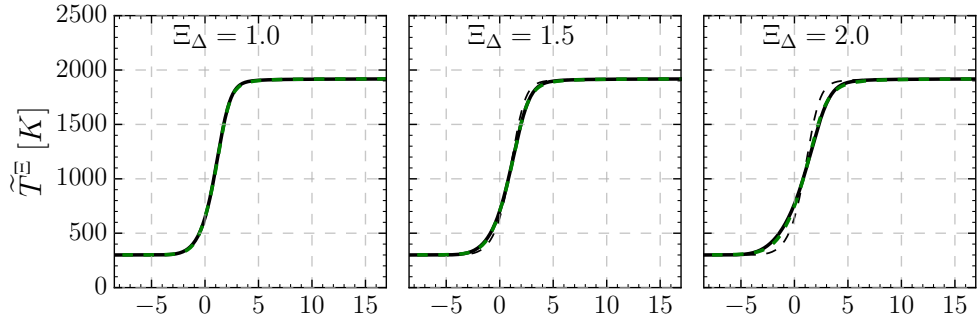

(a) $\Delta/\delta_l^0 = 4$, $n_\Delta = 1$

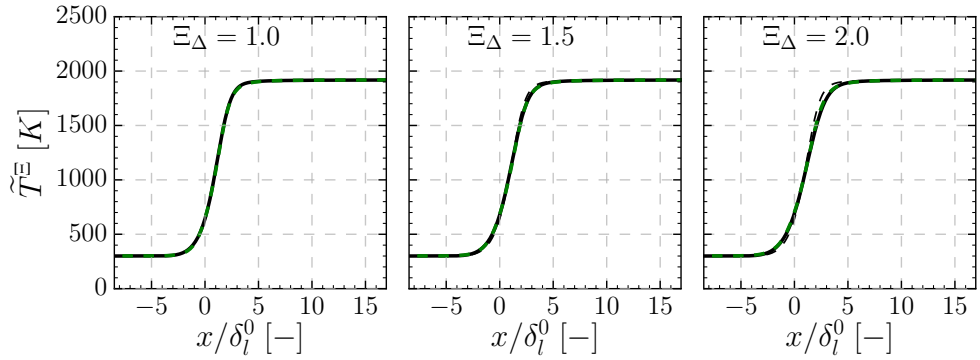

(b) $\Delta/\delta_l^0 = 4$, $n_\Delta = 2$

Figure 5.12: *Comparison between the temperatures of 1-D wrinkled flamelets computed with either optimized or analytic coefficients ξ_i^T. Legend: - - - Filtered (non-wrinkled) flame, — Optimized coefficients. - - - Analytic coefficients.*

5.4.2 Results

The results obtained with the simplified FOC-FWF model are shown and compared to the results obtained with the fully optimized FOC-FWF model. The performance of the models for the prediction of temperature and CO mass fractions fields are successively described.

Temperature and CO statistics Mean temperature and CO mass fraction fields are shown respectively in Fig. 5.14 and Fig. 5.15. An excellent agreement is obtained between simplified and fully optimized FOC-FWF models. This validates the analytic computation of the model parameters and illustrates the possibility to replace the time-consuming optimization of these parameters by simpler relationships involving fewer optimized variables.

CO formation Similarly to the work done in chapter 4, The emphasis is put on the CO predictions. Instantaneous $\widetilde{Y}_{CO}$ fields computed using simplified

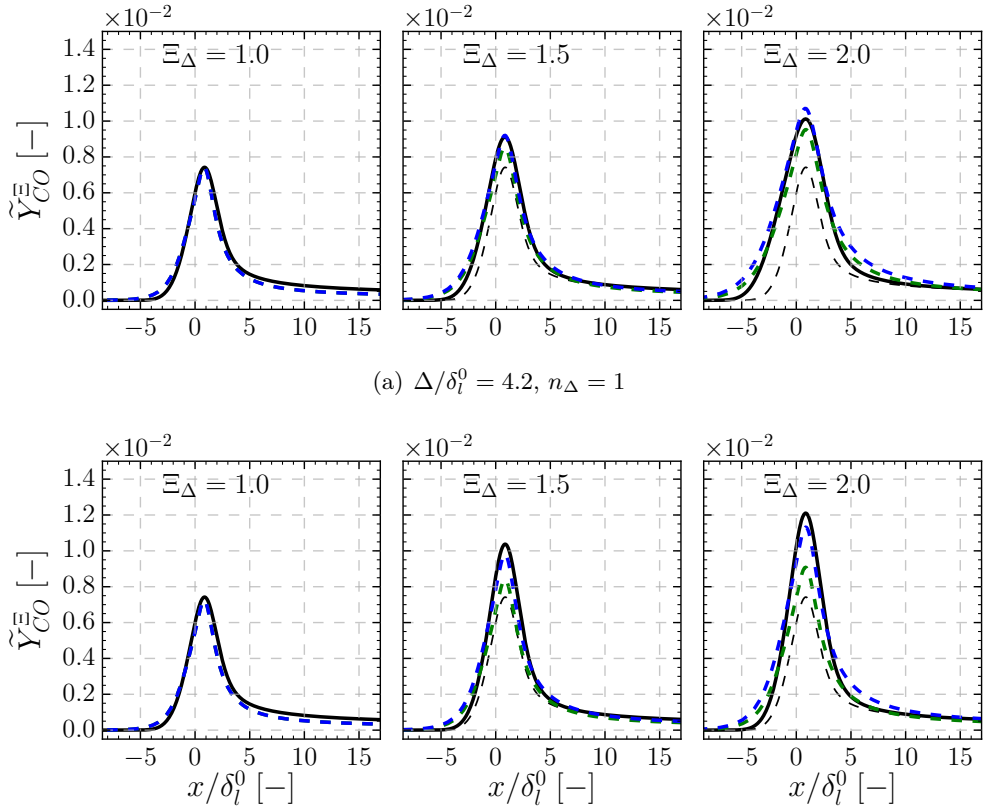

(a) $\Delta/\delta_l^0 = 4.2$, $n_\Delta = 1$

(b) $\Delta/\delta_l^0 = 4.2$, $n_\Delta = 2$

Figure 5.13: *Comparison between the CO mass fractions of 1-D wrinkled flamelets computed with either optimized or analytic coefficients ξ_i^{CO}. Legend: - - - Filtered (non-wrinkled) flame, — Optimized coefficients. - - - Analytic coefficients (CO prediction model 1). - - - Analytic coefficients (CO prediction model 2).*

and fully optimized FOC-FWF models is illustrated in Fig. 5.16(a). The fields obtained with both methods exhibit similar behaviors. In particular the maximal value of CO mass fraction reached is identical. Fig. 5.16(b) highlights the link between instantaneous CO mass fraction and the subgrid scale wrinkling factor Ξ_Δ. Finally, the CO integral $\mathcal{I}_{CO}$ (see chapter 4 for its definition and interpretation) is plotted as a function of axial position z in Fig. 5.17. An excellent agreement is observed between optimized and analytic models.

5.5 Conclusion

An analytic model for the coefficients ξ_i^T and ξ_i^{CO} is built to simplify the heavy process of optimizing the FOC-FWF model parameters in the (Ξ_Δ, n_Δ) space. Analytic relationships are derived by considering (i) the additional broadening

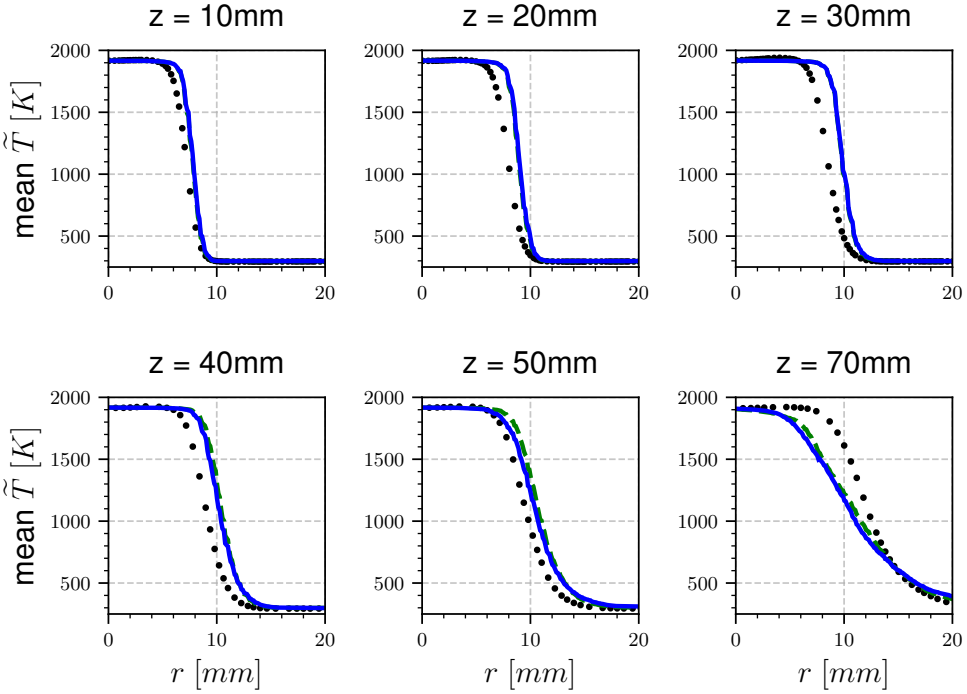

Figure 5.14: *Radial profiles of mean temperature for the reacting non-swirled case SwB1 at z=10, 20, 30, 40, 50 and 70mm from the burner nozzle. Legend: • • Experimental data. - - - Fully optimized FOC-FWF. — Simplified FOC-FWF.*

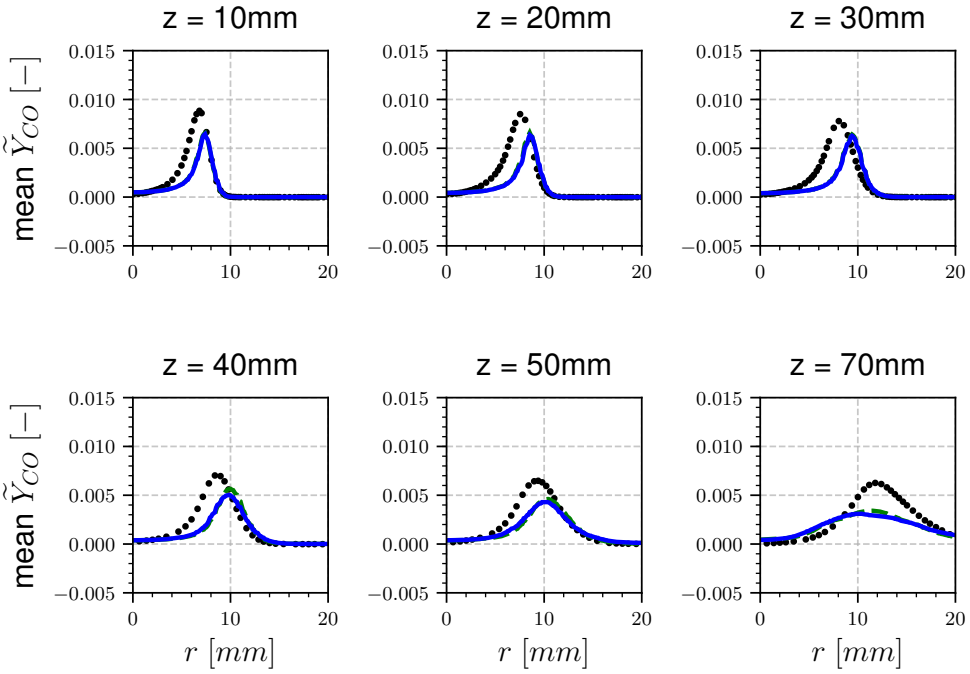

Figure 5.15: *Radial profiles of mean CO mass fraction for the reacting non-swirled case SwB1 at z=10, 20, 30, 40, 50 and 70mm from the burner nozzle. Legend: • • Experimental data. - - - Fully optimized FOC-FWF. — Simplified FOC-FWF.*

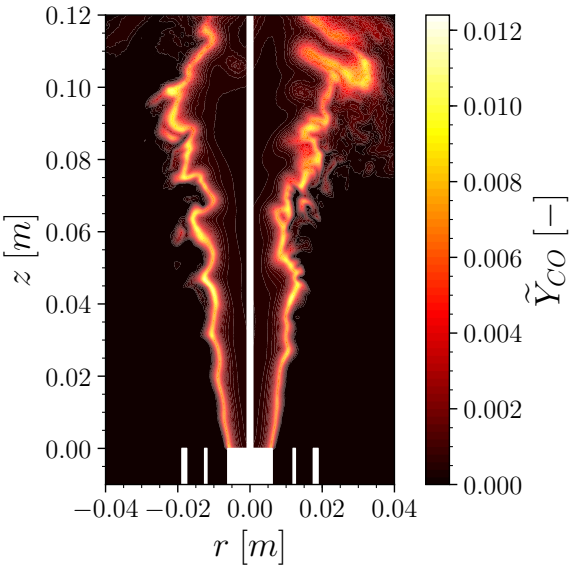

(a) Comparison between $\widetilde{Y}_{CO}$ fields obtained with wrinkled optimized (left) and analytic (right) models.

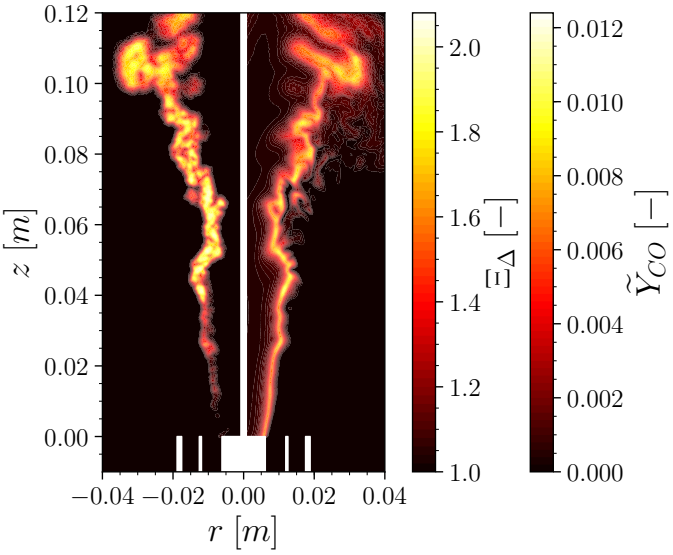

(b) Confrontation between Ξ_Δ field (left) and $\widetilde{Y}_{CO}$ field (right) obtained with the wrinkled analytic model.

Figure 5.16: *Analysis of the 2-D fields of CO mass fraction obtained with the wrinkled analytic model and comparison with wrinkled optimized model. These fields are obtained in the plane $x = 0$ (also defined by $\theta \equiv 0$ $[\pi]$).*

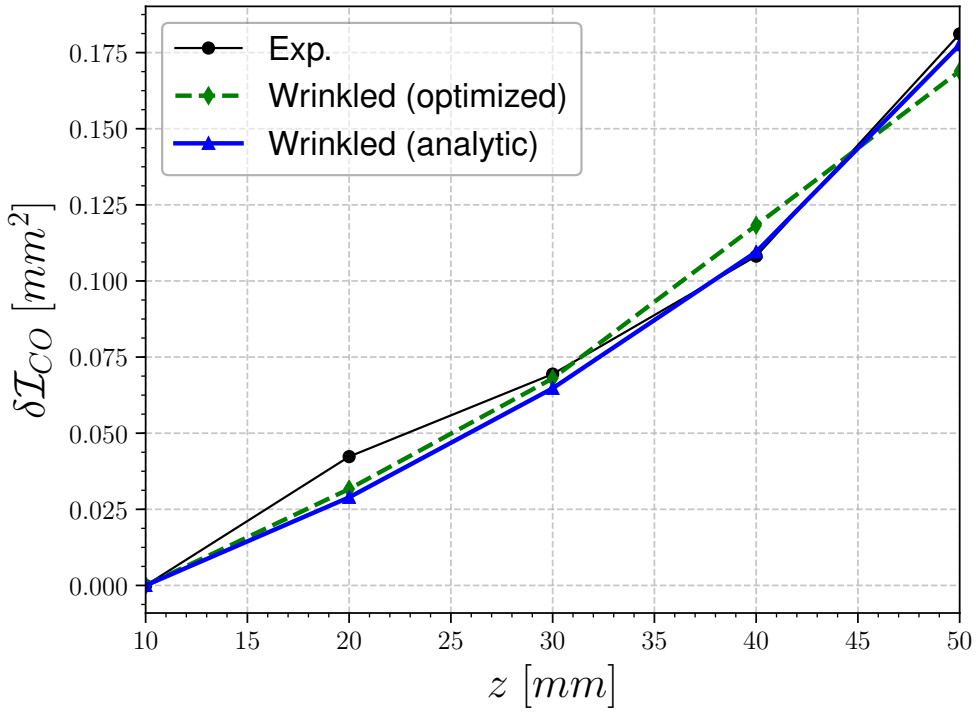

Figure 5.17: *Integral of CO mass fractions $\mathcal{I}_{CO}$ in planes (r, θ) as a function of the axial positions z. Legend:* ●—● *Experimental data.* ▲—▲ *Fully optimized FOC-FWF.* ♦- - -♦ *Simplified FOC-FWF.*

of the filtered flame due to SGS wrinkling; (ii) the increase of filtered CO mass in the flame front generated by flame wrinkling. An analytic formula for the thickness of FWF flamelets and the introduction of the notion of flame sub-grid density has enabled to construct a fully analytic formulation for the inclusion of the SGS wrinkling influence on the filtered flame structure.

A significant gain in terms of simplicity and cost is made with respect to the fully optimized version of the model, as only two parameters have to be optimized in the pre-processing step. The simplified FOC-FWF model has been successfully validated on the Cambridge SwB1 burner.

Conclusion

TURBULENT combustion modeling with complex chemistry improves the predictive capabilities of numerical simulations. Modeling strategies based on tabulated flames are powerful but limited to well identified combustion regimes. In particular, pollutants prediction and flame ignition/extinction phenomena are challenging to predict. Several turbulent combustion models have been designed to couple transported chemistry to LES but none of them is able to recover both the turbulent flame propagation speed and the pollutants formation, while being computationally affordable. This has triggered the need for new strategies and hence the motivation for the present thesis. Two novel modeling routes aimed at predicting filtered thermo-chemical variables have been investigated in this thesis. The first strategy aims to recover non-filtered thermo-chemical quantities from their LES filtered counterpart through a deconvolution algorithm. The second strategy, Filtered Optimized Chemistry (FOC), relies on the design in a pre-processing step of a chemical mechanism able to the structure of explicitly filtered flames. A first formulation, FOC-FPF, targets filtered laminar premixed flames, also called Filtered Planar Flames (FPF). As it lacks the modeling of the impact of sub-grid scale wrinkling on pollutants, an alternative solution, FOC-FWF, is based on the recovery of filtered wrinkled flamelets (FWF). The main conclusions regarding the two models are presented below, and perspectives for future work are detailed.

Advances in turbulent combustion modeling with transported chemistry

Deconvolution modeling applied to turbulent combustion

A recent idea for including complex chemistry effects in LES is to use the concept of deconvolution. Initially proposed by Stolz and Adams (1999) for closing the filtered Navier-Stokes equations in non-reacting LES, the modeling has been extended to scalars transport equations in the past years. Several models have been proposed and differ in the way the deconvolution is performed (Domingo and Vervisch (2014), Wang and Ihme (2016), Mathew (2002)). The models have been tested on 3-D configurations but no extensive studies on canonical flames have been published. In particular, the ability of models based on de-

convolution to predict the correct flame propagation speed has not been clearly established.

In this context, a detailed study of deconvolution modeling applied to the simulation of an unstrained 1-D laminar premixed flame has been carried out. Three models proposed in the literature and a new methodology based on sub-grid scale interpolation coupled to parametric functions have been challenged in *a priori* and *a posteriori* tests. The main conclusion is that it is necessary to include sub-grid scale information in the deconvolution step. It contributes to the stabilization of the ill-posed deconvolution problem by constraining the solutions and leads to more accurate predictions of the flame propagation and CO peaks. In particular, it has been shown that it is necessary to use a refined grid for deconvolved variables in order to represent the fine scales information. The three methods found in the literature do not predict the flame propagation accurately. Adding information through second-order sub-grid interpolation and parametric functions improves predictions as long as the filter size is not too large compared to the laminar flame thickness. However, as the methodology requires a fine grid to represent deconvolved data, it leads to significant computing costs.

This work led to the publication of a peer-reviewed article (Mehl et al. (2017)).

Filtered Optimized Chemistry modeling

To face the difficulties encountered when performing on-the-fly deconvolution, an alternative strategy has been explored. *A priori* studies have shown a significant advantage of the filtered flame formalism against the thickened flame formalism when it comes to chemical flame structure and pollutants prediction. Extending an approach proposed in the literature by Abou-Taouk et al. (2015), the Filtered Optimized Chemistry (FOC) modeling route consists in the generation, in a pre-processing step, of a mechanism able to reproduce explicitly filtered flames.

Contrarily to the work of Abou-Taouk et al. (2015) who focused on the recovery of filtered unstrained laminar premixed flames, the FOC model developed in this thesis considers the optimization on generic canonical flames. The model has been applied with a virtual chemical mechanism recently introduced in the literature (Cailler et al. (2018)). Moreover, a particular focus has been made on the model's accuracy in configurations where sub-grid scale wrinkling plays an important role. Two variants of the model have been studied:

- **FOC-FPF**: In the first case, optimization is performed on filtered planar flames (FPF). The wrinkling factor is computed using an algebraic model (Wang et al. (2011)) and wrinkling effects are included in trans-

port equations following a classical formulation which consists in multiplying the diffusive and reactive terms by this factor.

- **FOC-FWF**: A second variant features optimization on 1-D filtered wrinkled flamelets (FWF). These flamelets are computed from 2-D manufactured wrinkling patterns (Mercier et al. (2018)) and consequently filtered. The sub-grid scale wrinkling effect on the flame structure is here directly included in the chemical mechanism.

The FOC-FPF and FOC-FWF approaches have been successfully validated on 1-D flames and have been challenged on the premixed Cambridge burner for both non-swirled and highly swirled operating conditions (Sweeney et al. (2012a), Sweeney et al. (2012b)). The main result is that CO quantities are largely over-predicted by the thickened flame model (TFLES), while the FOC strategy leads to an improvement of the results. The FOC-FPF model performs well when the wrinkling is fully resolved at large scales but under-predicts the CO quantities in regions where sub-grid scale wrinkling is significant. Improvements are obtained in the latter situation with the FOC-FWF approach.

Simplification of the optimization procedure in the FOC-FWF model

Despite its ability to capture the impact of SGS wrinkling on intermediate pollutants formation, the FOC-FWF model involves the resolution of many optimization problems. An alternative based on analytic relationships for the optimized coefficients has thus been developed to simplify the model. It consists in building analytic formula for the mechanism coefficients. These relationships depend on the sub-grid scale wrinkling and are obtained by carrying out an analysis of the impact of SGS wrinkling on the flame structure. The optimization is finally reduced to two parameters for the whole range of SGS wrinkling factor values.

The newly developed model has been successfully tested on 1-D flames and on the Cambridge swirled premixed burner. In particular, the results are in good agreement with the results obtained using the fully optimized FOC-FWF model.

Perspectives for future work

The FOC-FWF strategy, developed in the present thesis for premixed combustion, needs improvements in order to be applied to more complex and realistic combustion systems. The perspectives for future work are the following:

- The modeling strategy described in chapter 3 targets premixed combustion. Further work has to be performed in order to extend the applica-

bility of the model to stratified and non-premixed combustion regimes. An important issue is to model the effects of sub-grid scale mixture fraction variations on both flame structure and propagation. Additionally, the definition of explicit filtering in non-premixed combustion is a challenge. Further work is also required for modeling the impact of sub-grid scale wrinkling on non-premixed CO profiles.

- In its current state, FOC-FWF is not able to predict heat losses to burner walls. Additional work on FOC-FWF consists in developing a strategy to take thermal losses into account, using the recent extension of virtual chemistry to non-adiabatic conditions (Maio et al. (2019)). Flame structure and propagation are also affected by differential diffusion effects. While the present formulation takes into account the effects of differential diffusion on flame propagation through the optimization on target flames computed with detailed transport, the impact on the flame structure is neglected and requires further developments.

- The generation of 2-D wrinkled manufactured flames require a flamelet regime assumption and thus constraints the applicability of the FOC-FWF model. Further work is needed to evaluate the ability of the FOC-FWF to perform well in thin and broken reaction zones regimes.

Appendix A

Deconvolution of simulated mean Favre-filtered data

Contents

A significant influence of the LES filter on time averaged LES data is observed in situations where the filter size is smaller or of the same order of magnitude than the turbulent mean flame brush. The effects are particularly important for averaged pollutants mass fractions. A methodology for deconvolving LES data based on Tikhonov regularization is presented in this appendix. The quality of the obtained results is shown to be dependent on the ratio between the filter size and the mean flame brush.

A.1 Motivations

The study carried out in chapter 4 shows that when turbulent mean flame brush δ_T is of the same order of magnitude than the LES filter size Δ, LES

profiles obtained from Favre averaging in space and time cannot be compared to experimental averages. The solution adopted in chapter 4 to validate the Filtered Optimized Chemistry (FOC) model is to explicitly filter experimental data using the LES filter. Results are improved but the methodology requires the knowledge of experimental data and is thus not predictive. An alternative is to use the concept of deconvolution explored in chapter 2. While deconvolution is not robust enough and too expensive to be used as a turbulent combustion closure strategy, it is a promising approach for LES data post-processing in the light of the following arguments:

- LES averaged thermo-chemical variables vary on length scales typically larger than the laminar flame thickness. The conditioning of the deconvolution problem is hence better than in the case of an instantaneous flame front.
- There are enough grid points to represent both filtered and non-filtered averages on the LES grid. No intermediate refined grid is needed to compute the deconvolved profiles. This contrasts with the resolution problem encountered in chapter 2.

The deconvolution method is presented in Sec. A.2 and an application on the Cambridge burner (Sweeney et al. (2012a)) is provided in Sec. A.3.

A.2 Presentation of the deconvolution method

The LES simulated means considered in this work are Favre-averaged in time and in space. The general methodology is presented in Sec. A.2.1 and deconvolution algorithms are described in detail in Sec. A.2.2.

A.2.1 General methodology

A thermo-chemical variable φ is considered and the LES simulated average of this variable is written $\{\widetilde{\varphi}\}$. By definition of Favre-filtering in time, the average is split as:

$$\{\widetilde{\varphi}\} = \frac{\langle\overline{\rho}\widetilde{\varphi}\rangle}{\langle\overline{\rho}\rangle} \tag{A.1}$$

where $\langle\overline{\rho}\rangle$ is the Reynolds averaged density. Reynolds averages in time and space commute and thus $\langle\overline{\rho}\widetilde{\varphi}\rangle = \overline{\langle\rho\varphi\rangle}$ and $\langle\overline{\rho}\rangle = \overline{\langle\rho\rangle}$. Finally the Favre average reads

$$\{\widetilde{\varphi}\} = \frac{\overline{\langle\rho\varphi\rangle}}{\overline{\langle\rho\rangle}} \tag{A.2}$$

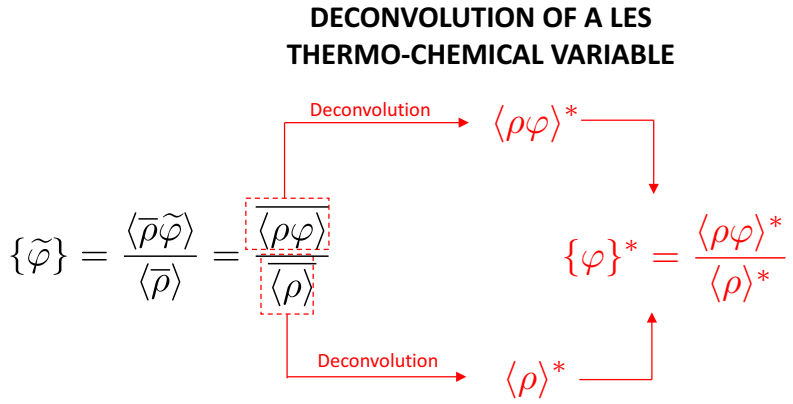

Figure A.1: *General methodology of LES averaged function deconvolution.*

The numerator and denominator of Eq. (A.2) can be deconvolved separately, and the final deconvolved Favre-averaged variable is:

$$\{\varphi\}^* = \frac{\langle\rho\varphi\rangle^*}{\langle\rho\rangle^*} \tag{A.3}$$

where superscript $*$ denotes deconvolved functions. The deconvolution methodology is summarized in Fig. A.1.

A.2.2 Deconvolution problems solving

A.2.3 Regularized deconvolution

Deconvolution of density and density weighted thermo-chemical variables are performed separately.

Density Although LES averages are smooth, they are corrupted by errors and deviate from the exact filtered solutions. A regularization strategy is necessary to invert the LES filter due to the high conditioning of the filtering operator. The selected strategy for carrying out the filter inversion is a generalization of the Tikhonov regularization method (Tikhonov (1963)). The underlying idea is to solve the deconvolution problem by using a least square criterion and limiting the size of the solution to diminish the effects of both errors and noise. In this context, the Reynolds averaged density is inverted by solving the following minimization problem:

$$\min_{\langle\rho^*\rangle} \underbrace{\|G * \langle\rho\rangle^* - \langle\overline{\rho}\rangle\|_2^2}_{\text{Fit to LES data}} + \alpha_{reg}^2 \underbrace{\|L\left(\langle\rho\rangle^* - \langle\rho\rangle_0\right)\|_2^2}_{\text{Size of solution}} \tag{A.4}$$

where L is a linear regularization operator, α_{reg} a regularization coefficient and $\langle\rho\rangle_0$ an *a priori* solution of the problem. If no *a priori* solution is known, $\langle\rho\rangle_0$ is set to zero. L is an operator aimed at quantifying the size of the solution. The standard choice is the identity matrix $L = \mathbb{1}$. The regularization cancels effects of noise by minimizing the norm of the solution. The quality of the solution is nevertheless affected as high frequencies are damped. The trade-off between the fit to LES data and the size of solution is controlled by α_{reg}. Finding the optimal α_{reg} is a difficult task and a few elements for choosing a value are given in Sec. A.2.4.

Thermo-chemical variable A similar strategy is used to deconvolve $\langle\overline{\rho}\widetilde{\varphi}\rangle$:

$$\min_{\langle\rho\varphi\rangle^* \ s.t \ \{\varphi\}_{min}\leq\{\varphi\}^*\leq\{\varphi\}_{max}} \underbrace{\|G * \langle\rho\varphi\rangle^* - \langle\overline{\rho}\widetilde{\varphi}\rangle\|_2^2}_{\text{Fit to LES data}} + \alpha_{reg}^2 \underbrace{\|L\left(\langle\rho\varphi\rangle^* - \langle\rho\varphi\rangle_0\right)\|_2^2}_{\text{Size of solution}} \tag{A.5}$$

where $\langle\rho\varphi\rangle_0$ is an *a priori* solution, and $\{\varphi\}_{min}$, $\{\varphi\}_{max}$ are bounds added to the problem in order to enforce additional physical information in the inversion. Mass fractions are for instance bound to stay in the range $[0, 1]$.

A.2.4 Regularization parameter

The main issue when using a Tikhonov regularization strategy is the choice of the regularization parameter α_{reg}, which controls the trade-off between fit to LES data and size of the solution. A non-zero value is necessary to reduce the effects of errors and noise on the deconvolved functions. If the function to retrieve after inversion of $\{\widetilde{\varphi}\}$ is written $\{\varphi\}^{exact}$, the optimal parameter is formally defined as:

$$\alpha_{reg}^{opt} = \min_{\alpha_{reg}} \|\{\varphi\}^*_{\alpha_{reg}} - \{\varphi\}^{exact}\|_2^2 \tag{A.6}$$

where $\{\varphi\}^*_{\alpha_{reg}}$ is the solution obtained after regularized deconvolution with parameter α_{reg}. As the function to retrieve is not known, the optimal parameter cannot be computed from Eq. (A.6) directly and alternative techniques have to be developed.

A commonly used strategy is the L-curve method proposed by Hansen and O'Leary (1993). The idea is to graphically study the trade-off between the deconvolution residual and the size of the regularized solution. The original method proposed by Hansen and O'Leary (1993) is here applied by considering the deconvolution as the global operation leading to the estimation of $\{\varphi\}^*_{\alpha_{reg}}$ from $\{\widetilde{\varphi}\}$. The deconvolution residual is $\|\widetilde{G} * \{\varphi\}^*_{\alpha_{reg}} - \{\widetilde{\varphi}\}\|_2$ and the size

of the regularized deconvolved profile is $\|L\left(\{\varphi\}^*_{\alpha_{reg}} - \{\varphi\}_0\right)\|_2$, where $\{\varphi\}_0 = \langle\rho\varphi\rangle_0/\langle\rho\rangle_0$. In a log-log plot, the residual error as a function of the solution size often leads to a "L" shaped curve. A method for choosing the regularization parameter is to select the parameter at the edge of the curve, as it leads to a solution with a low norm and a low residual.

A.3 Application to the non-swirled premixed Cambridge SwB burner

The deconvolution of simulated data will be applied to the non-swirled premixed Cambridge burner (SwB1) studied in chapter 4 and 5. Details on the considered LES simulation are given in Sec. A.3.1, followed by modeling choices for the deconvolution algorithms in Sec. A.3.2. Results on the burner profiles are finally provided and analyzed in Sec. A.3.3.

A.3.1 Details of the simulation

The simulation of the Cambridge non-swirled SwB1 burner is here carried out with the FOC-FWF model in order to take the effects of SGS wrinkling on the flame chemical structure into account. The filter size is set to $\Delta = 4\delta_l^0$ and the LES grid size in the flame front is $\Delta_x = 0.5\text{mm} \approx \delta_l^0$. The wrinkling factor Ξ_Δ is computed with a Charlette model and $\beta = 0.5$.

A.3.2 Deconvolution modeling

As the burner is axi-symmetric and the opening angle of the flame is small, 1-D deconvolution operations are performed in the radial direction. The deconvolution is applied to the filtered CO mass fraction $\widetilde{Y}_{CO}$. No *a priori* solutions of the deconvolution problem is known and thus $\langle\rho\rangle_0 = 0$ and $\langle\rho Y_{CO}\rangle_0 = 0$. The regularization operator in chosen in its standard form $L = \mathbb{1}$.

A.3.3 Deconvolution results

The unregularized deconvolved solutions, obtained for $\alpha_{reg} = 0$, are shown in Fig. A.2 for axial positions $z = 10$, 20 and 50mm. For $z = 10$ and 20mm, the mean flame brush is of the same order of magnitude than Δ and large oscillations are observed in the deconvolved profiles. This is due to the amplification of errors and noise in $\{\widetilde{\varphi}\}$. The regularization of the deconvolution post-processing operation is thus mandatory. When the flame brush is higher, at $z = 50$mm, these oscillations are diminished because high frequencies are not present in the LES profile. At this location however, the deconvolution is not useful since the LES filtering effect is weak.

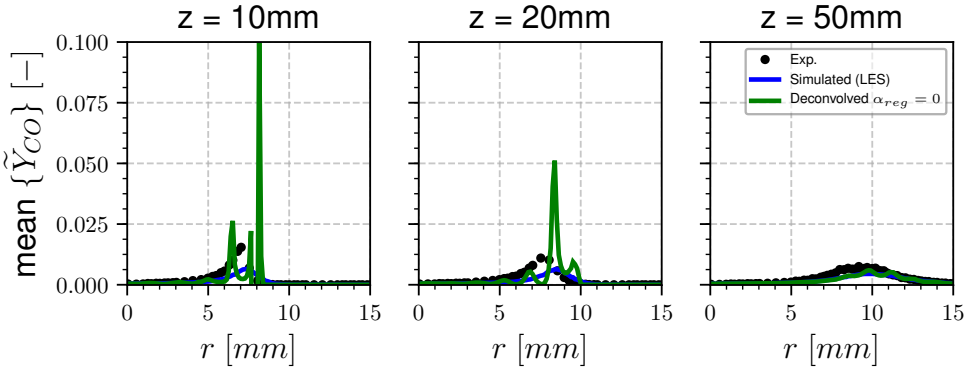

Figure A.2: *Unregularized deconvolution of simulated mean CO mass fraction profiles for the non-swirled premixed Cambridge burner. Legend:* • • *Non-filtered experimental data.* — *LES average* $\{\widetilde{Y}_{CO}\}$. — *Deconvolved average* $\{Y_{CO}\}^*$.

The behavior of the regularized deconvolution is studied for $z = 10$, 20 and 30mm in Fig. A.3. At these locations, the LES filter is of the same order of magnitude than the mean flame brush and has thus a significant effect on mean profiles (refer to chapter 4 for details). On the plots at the left in Fig. A.3, the deconvolution is illustrated for several values of α_{reg} and the L-shaped trade-off curve proposed in Sec. A.2.4 is shown on their right.
For $z = 10$mm, the trade-off curve does not have a distinguishable edge. After an initial vertical line due to a decrease of the noise influence on the solution, the norm of the regularized solution is linearly decreasing when the deconvolution residual increases. This leads to a high sensitivity of the deconvolved profile to α_{reg}. While the solution for $\alpha_{reg} = 0.2$ is satisfying, it is difficult at this location to identify an optimal regularization parameter without previous knowledge of the experimental data.
For $z = 20$ and 30mm, the L shape of the trade-off curve is pronounced and an edge can be distinguished. The initial vertical drop of the norm is followed by a horizontal plateau, before shrinking. Choosing a regularization parameter on this plateau has a low impact on the regularized solution (see profiles on the left in Fig. A.3), and the edge value leads to an accurate prediction of the non-filtered experimental CO peak.

A.4 Conclusion

In this appendix, a regularized deconvolution method has been proposed in order to retrieve non-filtered Favre averaged thermo-chemical quantities from their LES filtered counterparts. The method consists in a generalized Tikhonov approach parametrized by a regularization coefficient α_{reg}. This parameter can be set by studying the trade-off between the size of the regularized deconvolution solution as a function of the norm of the deconvolution residual. The

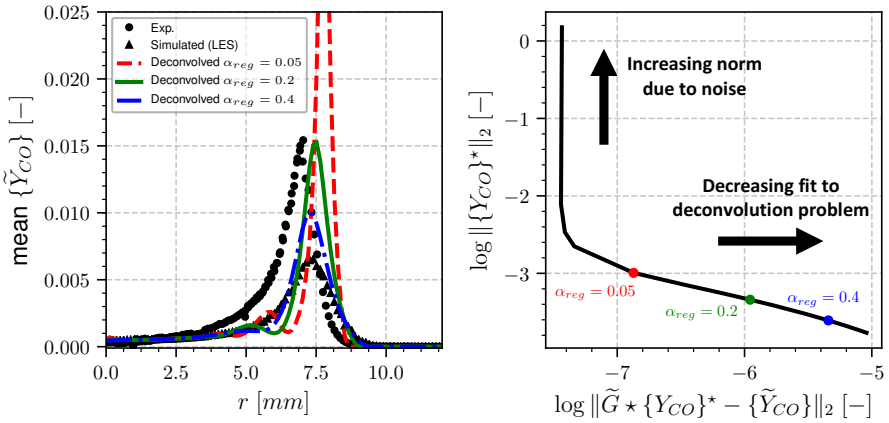

(a) Axial location $z = 10$mm

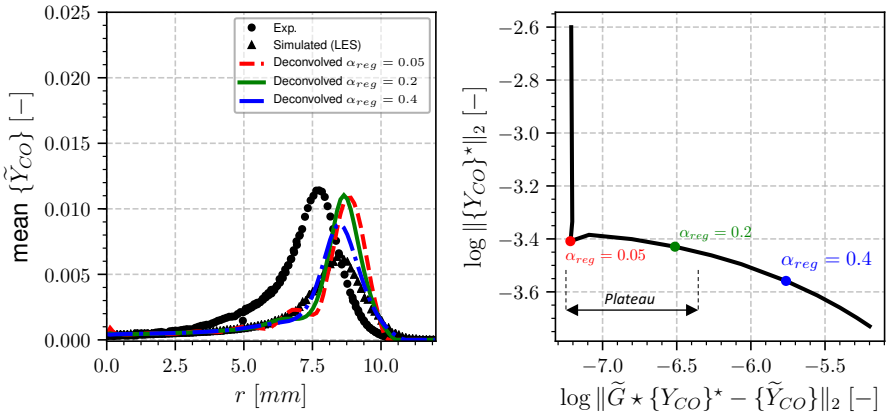

(b) Axial location $z = 20$mm

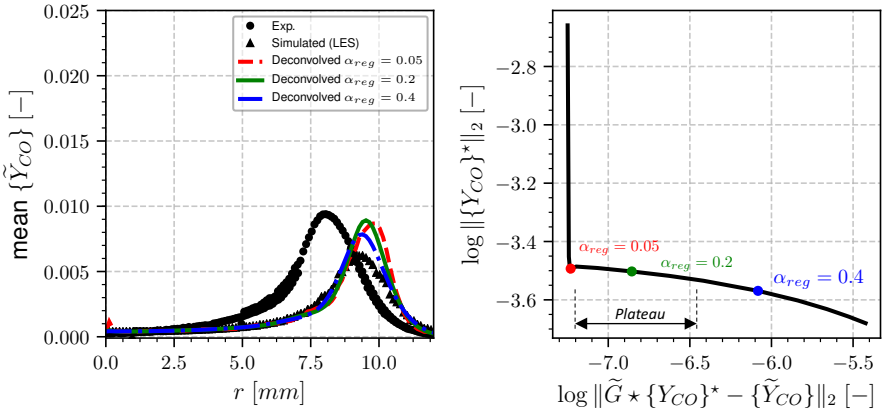

(c) Axial location $z = 30$mm

Figure A.3: *Analysis of regularized deconvolution at different location of the Cambridge burner and for different values of α_{reg}. On the left: Deconvolved profiles compared against experimental data. On the right: Illustration of the trade-off between regularized part $\|\{Y_{CO}\}^*\|_2$ and least-square part $\|\widetilde{G} * \{Y_{CO}\}^* - \{\widetilde{Y}_{CO}\}\|_2$ of the deconvolution solving.*

deconvolution has been applied to LES data obtained from the simulation of the non-swirled premixed Cambridge burner using the FOC-FWF model. While the identification of an optimal regularization parameter is difficult in the near burner region, good results have been further downstream. In particular, a significant improvement of the CO peak prediction is obtained. The work is however preliminary and further investigations have to be carried out. In particular, the proposed methodology has to be extended to 3-D cases in order to deal with burners where the geometry is more complex.

Appendix B

Analytic expression of the thickness of FWF flames

Contents

This appendix details the derivation of the model presented in chapter 5 for computing the thickness of a FWF flamelet. The model is linear and its slope is determined by differentiating the wrinkling factor as a function of the wrinkling pattern amplitude.

B.1 FWF flame thickness

The objective of this appendix is to explicit the derivation of the analytic model for wrinkled flame thickness proposed in Sec. 5.2.1 (refer to this section for more details about the context of the study). The thickness $\overline{\delta}_\Xi$ of a filtered wrinkled flame is assumed to follow a linear evolution with Ξ_Δ:

$$\overline{\delta}_\Xi(\Xi_\Delta) = \alpha\,(\Xi_\Delta - 1) + \overline{\delta}_l \tag{B.1}$$

where the slope α of the function is to be determined. Using simple arguments, the slope is expressed as:

$$\alpha = \left(\frac{\partial \overline{\delta}_\Xi}{\partial \Xi_\Delta}\right) = \frac{2}{\lim\limits_{A\to+\infty}\left(\frac{\partial \Xi_\Delta}{\partial A}\right)} \tag{B.2}$$

The limit $\lim\limits_{A\to+\infty}(\partial\Xi_\Delta/\partial A)$ has thus to be found. An analytic expression for

the dependence of Ξ_Δ on the sine amplitude A under infinitely thin flame assumption is used. It is defined in Eq. (3.49) and recalled here:

$$\Xi_\Delta(A, n_\Delta) = \frac{2}{\pi}\sqrt{1 + \frac{4\pi^2 A^2 n_\Delta^2}{\Delta^2}}\, E\left(\frac{1}{\sqrt{1 + \frac{\Delta^2}{4\pi^2 A^2 n_\Delta^2}}}\right) \tag{B.3}$$

where E is the complete elliptic integral of the second kind. The proof that $\lim_{A\to+\infty} (\partial\Xi_\Delta/\partial A)$ is finite is done in the next section and its value is provided.

B.2 Derivation of the slope α

Expression of the derivative For simplifying notations, a variable x is defined as:

$$x = \frac{4\pi^2 A^2 n_\Delta^2}{\Delta^2} \tag{B.4}$$

And hence the analytic wrinkling factor can be written as:

$$\Xi_\Delta(x) = \frac{2}{\pi}\sqrt{1+x}\, E\left(\frac{1}{\sqrt{1 + \frac{1}{x}}}\right) \tag{B.5}$$

And the derivative can be computed using a chain rule:

$$\frac{\partial \Xi_\Delta}{\partial A} = \underbrace{\left(\frac{\partial x}{\partial A}\right)}_{\text{(I)}} \underbrace{\left(\frac{d\Xi_\Delta}{dx}\right)}_{\text{(II)}} \tag{B.6}$$

The first term evaluation is straightforward:

$$\text{(I)} = \frac{8\pi^2 n_\Delta^2 A}{\Delta^2} \tag{B.7}$$

The second term is computed by splitting the product and using the fact that $(E(u))' = (E(u) - K(u))/u$ where K is the complete elliptic integral of the

first kind. Thus:

$$(\mathrm{II}) = \frac{1}{\pi\sqrt{1+x}} E\left(\frac{1}{\sqrt{1+\frac{1}{x}}}\right) + \frac{1}{\pi x\sqrt{1+x}}\left[E\left(\frac{1}{\sqrt{1+\frac{1}{x}}}\right) - K\left(\frac{1}{\sqrt{1+\frac{1}{x}}}\right)\right] \tag{B.8}$$

After substitution, the partial derivative finally reads:

$$\frac{\partial \Xi_\Delta}{\partial A} = \underbrace{\frac{8\pi n_\Delta^2 A}{\Delta^2\sqrt{1+\frac{4\pi^2A^2n_\Delta^2}{\Delta^2}}} E\left(\frac{1}{\sqrt{1+\frac{\Delta^2}{4\pi^2A^2n_\Delta^2}}}\right)}_{(1)} + \underbrace{\frac{2}{\pi A\sqrt{1+\frac{4\pi^2A^2n_\Delta^2}{\Delta^2}}}\left[E\left(\frac{1}{\sqrt{1+\frac{\Delta^2}{4\pi^2A^2n_\Delta^2}}}\right) - K\left(\frac{1}{\sqrt{1+\frac{\Delta^2}{4\pi^2A^2n_\Delta^2}}}\right)\right]}_{(2)} \tag{B.9}$$

Evaluation of the limit The limit $\lim_{A\to+\infty}(\partial\Xi_\Delta/\partial A)$ is found by performing $A \to +\infty$ in Eq. (B.9). Using E(1)=1 and $\lim_{u\to+\infty}\sqrt{u}/\sqrt{1+u} = 1$, the limit of the first term in the RHS of Eq. (B.9) is finite and is equal to:

$$\lim_{A\to+\infty}(1) = \frac{4n_\Delta}{\Delta} \tag{B.10}$$

The second term is shown to tend towards zero:

$$\lim_{A\to+\infty}(2) = 0 \tag{B.11}$$

This can be obtained by using asymptotic expressions for elliptic integrals E and K. Finally this proves that the limit is finite and its value it $4n_\Delta/\Delta$. The slope of the thickness linear function is thus:

$$\alpha = \frac{\Delta}{2n_\Delta} \tag{B.12}$$

Appendix C

Implementation of the LES Gaussian filter

Contents

This appendix illustrates the implementation of Gaussian filtering by a diffusion operator. Gaussian convolutive kernels can indeed be linked to linear heat diffusion problems. This equivalence enables the filtering of functions on arbitrary grids at a reasonable cost.

C.1 Thermal analogy for Gaussian filtering

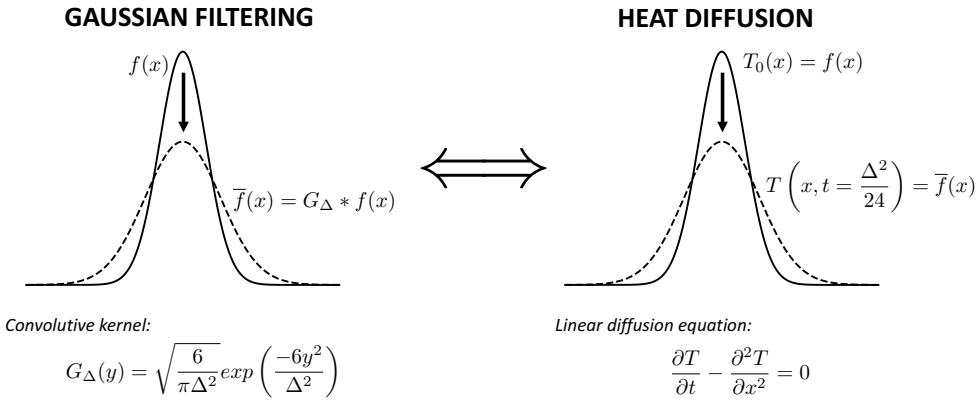

Figure C.1: *Analogy between Gaussian filtering and unbounded heat diffusion.*

The explicit filtering operations in this thesis are performed with a Gaussian filter kernel defined as $G_\Delta(\mathbf{x}) = \sqrt{6/\pi\Delta^2} exp\left(6\mathbf{x}^2/\Delta^2\right)$. It is widely used in

reactive and non-reactive LES and is the only filter satisfying linearity, spatial invariance, isotropy and scale invariance (Layton and Rebholz (2012)). Several implementations of the Gaussian filter exist, and the most convenient way is probably to use Fourier transforms. This approach is however limited to uniform grids and an alternative is thus proposed. The filtering of a function f is illustrated. The diffusion equation on an unbounded domain for a temperature T is considered:

$$\frac{\partial T}{\partial t} = \nabla^2 T \tag{C.1}$$

with an initial field $T_0(\mathbf{x}) = f(\mathbf{x})$. It can be shown that filtering f with a Gaussian kernel of size Δ is equivalent to diffusing T up to a time $t_\Delta = \Delta^2/24$ and defining:

$$\overline{f}(\mathbf{x}) = T\left(\mathbf{x}, t = t_\Delta\right) \tag{C.2}$$

This result implies that a diffusion operator can be used to filter a function. In particular, function can easily be filtered on an unstructured grid by using the spatial derivatives scheme of the LES solver. The Gaussian filtering / Heat diffusion equivalence is illustrated in Fig. C.1 in one dimension.

C.2 Practical implementation

The stability of numerical methods for solving linear diffusion equations is well mastered. Time integration of Eq. (C.1) can for instance be performed in a stable way by using a first order Euler implicit scheme. By writing k the time integration index, the equation is discretized as:

$$\frac{T_{k+1} - T_k}{dt} = \nabla^2 T_{k+1} \tag{C.3}$$

where dt is the time increment. The method is stable regardless the value of dt. The accuracy however increases with the number of iterations. In the thesis, the solving is done using a number N_{ite} of iterations, typically set to 20 in one dimension. In this case, $dt = \Delta^2/24N_{ite}$.

References

Abou-Taouk, A., B. Farcy, P. Domingo, L. Vervisch, S. Sadasivuni, and L.-E. Eriksson (2015). Optimized Reduced Chemistry and Molecular Transport for Large Eddy Simulation of Partially Premixed Combustion in a Gas Turbine. *Combust. Sci. Technol. 188*(1), 21–39. *(p. 16, 39, 41, 42, 84, 85, 93, 192)*

Ansari, N., P. A. Strakey, G. M. Goldin, and P. Givi (2015). Filtered density function simulation of a realistic swirled combustor. *Proc. Combust. Inst. 35*(2), 1433–1442. *(p. 23)*

Arrhenius, S. (1967). On The reaction velocity of the inversion of cane sugar by acids. In *Sel. Readings Chem. Kinet.*, pp. 31–35. *(p. 8)*

Auzillon, P. (2012). *Modélisation de la structure et de la dynamique des flammes pour la simulation aux grandes échelles.* Ph. D. thesis. *(p. 102)*

Auzillon, P., B. Fiorina, R. Vicquelin, N. Darabiha, O. Gicquel, and D. Veynante (2011). Modeling chemical flame structure and combustion dynamics in les. *Proc. Combust. Inst. 33*(1), 1331–1338. *(p. 11, 36, 37, 38, 39, 102, 139)*

Auzillon, P., O. Gicquel, N. Darabiha, D. Veynante, and B. Fiorina (2012). A Filtered Tabulated Chemistry model for LES of stratified flames. *Combust. Flame 159*(8), 2704–2717. *(p. 10, 11)*

Ayache, S. and E. Mastorakos (2012). Conditional Moment Closure/Large Eddy Simulation of the Delft-III natural gas non-premixed jet flame. In *Flow, Turbul. Combust.*, Volume 88, pp. 207–231. *(p. 27)*

Barlow, R. S., M. J. Dunn, M. S. Sweeney, and S. Hochgreb (2012). Effects of preferential transport in turbulent bluff-body-stabilized lean premixed CH 4/air flames. *Combust. Flame 159*(8), 2563–2575. *(p. 146, 147, 148)*

Bibrzycki, J. and T. Poinsot (2010). Reduced chemical kinetic mechanisms for methane combustion in O 2 / N 2 and O 2 / CO 2 atmosphere. *Work. note ECCOMET WN/CFD/10/17, CERFACS*. *(p. 51)*

Bilger, R. W. (1993). Conditional Moment Closure for Turbulent Reacting Flow. *Phys. Fluids a-Fluid Dyn. 5*(2), 436–444. *(p. 25)*

Bilger, R. W., S. H. Stårner, and R. J. Kee (1990). On reduced mechanisms for methane for air combustion in nonpremixed flames. *Combust. Flame 80*(2), 135–149. *(p. 13)*

Borghesi, G., E. Mastorakos, and R. S. Cant (2013). Complex chemistry

DNS of n-heptane spray autoignition at high pressure and intermediate temperature conditions. *Combust. Flame 160*(7), 1254–1275. *(p. 12)*

Brauner, T., W. P. Jones, and A. J. Marquis (2016). LES of the Cambridge Stratified Swirl Burner using a Sub-grid pdf Approach. *Flow, Turbul. Combust. 96*(4), 965–985. *(p. 23, 24, 125)*

Bray, K., M. Champion, and P. A. Libby (2010). Systematically reduced rate mechanisms and presumed PDF models for premixed turbulent combustion. *Combust. Flame 157*(3), 455–464. *(p. 19, 20)*

Bray, K. N. C., M. Champion, P. A. Libby, and N. Swaminathan (2006). Finite rate chemistry and presumed PDF models for premixed turbulent combustion. *Combust. Flame 146*(4), 665–673. *(p. 20)*

Bray, K. N. C. and J. B. Moss (1977). A unified statistical model of the premixed turbulent flame. *Acta Astronaut. 4*, 291–319. *(p. 104)*

Butler, T. and P. O'Rourke (1977). A numerical method for two dimensional unsteady reacting flows. *Symp. Combust. 16*(1), 1503–1515. *(p. 15, 34)*

Byrd, R. H., P. Lu, J. Nocedal, and C. Zhu (1995). A Limited Memory Algorithm for Bound Constrained Optimization. *SIAM J. Sci. Comput. 16*(5), 1190–1208. *(p. 57)*

Cailler, M., N. Darabiha, and B. Fiorina (2018). Virtual chemistry for pollutant emissions prediction. *submitted*. *(p. 89, 90, 91, 192)*

Cailler, M., N. Darabiha, D. Veynante, and B. Fiorina (2016). Building-up virtual optimized mechanism for flame modeling. *Proc. Combust. Inst.*, –. *(p. 89, 90)*

Cailler, M., R. Mercier, V. Moureau, N. Darabiha, and B. Fiorina (2017). Prediction of CO emissions in LES of turbulent stratified combustion using virtual chemistry. In *55th AIAA Aerosp. Sci. Meet. (p. 37, 88, 89, 91)*

Calhoon, W. and S. Menon (1996). Subgrid modeling for reacting large eddy simulations. In *34th Aerosp. Sci. Meet. Exhib.*, Number January, pp. 96–516. *(p. 31)*

Cao, S. and T. Echekki (2008). A low-dimensional stochastic closure model for combustion large-eddy simulation. *J. Turbul. 9*(2), 1–35. *(p. 31, 32, 33)*

Charlette, F., C. Meneveau, and D. Veynante (2002a). A power-law flame wrinkling model for LES of premixed turbulent combustion Part I: non-dynamic formulation and initial tests. *Combust. Flame 131*(1), 159–180. *(p. 35, 36, 85, 103, 120)*

Charlette, F., C. Meneveau, and D. Veynante (2002b, oct). A power-law flame wrinkling model for LES of premixed turbulent combustion Part II: dynamic formulation. *Combust. Flame 131*(1-2), 181–197. *(p. 36, 103)*

Cleary, M. J. and A. Y. Klimenko (2009). A generalised multiple mapping conditioning approach for turbulent combustion. *Flow, Turbul. Combust. 82*(4), 477–491. *(p. 28, 29, 30, 31)*

Cleary, M. J. and A. Y. Klimenko (2011a). A detailed quantitative analysis of sparse-Lagrangian filtered density function simulations in constant and variable density reacting jet flows. *Phys. Fluids 23*(11). *(p. 28, 29, 30)*

Cleary, M. J. and A. Y. Klimenko (2011b). Multiple Mapping Conditioning: A New Modelling Framework for Turbulent Combustion. In *Turbul. Combust. Model.*, Chapter 7, pp. 143–173. *(p. 28)*

Colin, O., F. Ducros, D. Veynante, and T. Poinsot (2000). A thickened flame model for large eddy simulations of turbulent premixed combustion. *Phys. Fluids 12*(7), 1843–1863. *(p. 15, 34, 35, 36, 37, 85, 94, 101, 103, 143)*

Colucci, P. J., F. A. Jaberi, P. Givi, and S. B. Pope (1998). Filtered density function for large eddy simulation of turbulent reacting flows. *Phys. Fluids 10*(2), 499–515. *(p. 18)*

Cook, A. W. and W. H. Cabot (2004). A high-wavenumber viscosity for high-resolution numerical methods. *J. Comput. Phys. 195*(2), 594–601. *(p. 127)*

Cook, A. W. and J. J. Riley (1994). A subgrid model for equilibrium chemistry in turbulent flows. *Phys. Fluids 6*(8), 2868–2870. *(p. 20)*

Coussement, A., T. Schmitt, and B. Fiorina (2015). Filtered Tabulated Chemistry for non-premixed flames. *Proc. Combust. Inst. 35*(2), 1183–1190. *(p. 10, 13)*

Darabiha, N. (1992). Transient behaviour of laminar counterflow hydrogen-air diffusion flames with complex chemistry. *Combust. Sci. Technol. 86*(1-6), 163–181. *(p. 95)*

Devaud, C. B., I. Stankovic, and B. Merci (2013). Deterministic Multiple Mapping Conditioning (MMC) applied to a turbulent flame in Large Eddy Simulation (LES). *Proc. Combust. Inst. 34*(1), 1213–1221. *(p. 28)*

Doan, N. A. K., N. Swaminathan, and Y. Minamoto (2018). DNS of MILD combustion with mixture fraction variations. *Combust. Flame 189*, 173–189. *(p. 12)*

Dodoulas, I. A. and S. Navarro-Martinez (2013). Large eddy simulation of premixed turbulent flames using the probability density function approach. *Flow, Turbul. Combust. 90*(3), 645–678. *(p. 23)*

Domaradzki, J. A. and K. C. Loh (1999). The subgrid-scale estimation model in the physical space representation. *Phys. Fluids 11*(8), 2330–2342. *(p. 52)*

Domaradzki, J. A., K. C. Loh, and P. P. Yee (2002). Large eddy simulations using the subgrid-scale estimation model and truncated Navier-stokes dynamics. *Theor. Comput. Fluid Dyn. 15*(6), 421–450. *(p. 52)*

Domingo, P. and L. Vervisch (2014). Large Eddy Simulation of premixed turbulent combustion using approximate deconvolution and explicit flame filtering. *(p. 39, 41, 49, 52, 56, 57, 191)*

Dong, G., Y. Chen, L. Li, Z. Wu, and R. Dibble (2017). A skeletal gasoline flame ionization mechanism for combustion timing prediction on HCCI engines. *Proc. Combust. Inst. 36*(3), 3669–3676. *(p. 12)*

Donini, A., R. Bastiaans, J. van Oijen, and L. de Goey (2015, jan). Differential diffusion effects inclusion with flamelet generated manifold for the modeling of stratified premixed cooled flames. *Proc. Combust. Inst. 35*(1), 831–837. *(p. 4)*

Duwig, C. and L. Fuchs (2008). Large Eddy Simulation of a H2/N2 Lifted Flame in a Vitiated Co-Flow. *Combust. Sci. Technol. 180*(3), 453–480. *(p. 24, 51)*

Duwig, C., K. Nogenmyr, C. Chan, and M. J. Dunn (2011). Large Eddy Simulations of a piloted lean premix jet flame using finite-rate chemistry. *Combust. Theory Model. 15*(4), 537–568. *(p. 24, 25, 51)*

Echekki, T., A. R. Kerstein, and J. C. Sutherland (2011). The One-Dimensional-Turbulence Model. In T. Echekki and E. Mastorakos (Eds.), *Turbul. Combust. Model.*, Chapter 11, pp. pp 249–276. Springer Netherlands. *(p. 31)*

Elliott, L., D. Ingham, A. Kyne, N. Mera, M. Pourkashanian, and C. Wilson (2005). Reaction mechanism reduction and optimization using genetic algorithms. *Ind. Eng. Chem. Res. 44*(4). *(p. 12)*

Esclapez, L., P. C. Ma, E. Mayhew, R. Xu, S. Stouffer, T. Lee, H. Wang, and M. Ihme (2017a, jul). Fuel effects on lean blow-out in a realistic gas turbine combustor. *Combust. Flame 181*, 82–99. *(p. 3)*

Esclapez, L., P. C. Ma, E. Mayhew, R. Xu, S. Stouffer, T. Lee, H. Wang, and M. Ihme (2017b). Fuel effects on lean blow-out in a realistic gas turbine combustor. *Combust. Flame 181*, 82–99. *(p. 11)*

Euler, M., R. Zhou, S. Hochgreb, and A. Dreizler (2014). Temperature measurements of the bluff body surface of a swirl burner using phosphor thermometry. *Combust. Flame 161*(11), 2842–2848. *(p. 124, 130)*

Farrace, D., K. Chung, S. S. Pandurangi, Y. M. Wright, K. Boulouchos, and N. Swaminathan (2017). Unstructured LES-CMC modelling of turbulent premixed bluff body flames close to blow-off. In *Proc. Combust. Inst.*, Volume 36, pp. 1977–1985. *(p. 27)*

Felden, A., E. Riber, and B. Cuenot (2018). Impact of direct integration of Analytically Reduced Chemistry in LES of a sooting swirled non-premixed combustor. *Combust. Flame 191*, 270–286. *(p. 12, 36)*

Fernandez-Tarrazo, E., A. L. Sanchez, A. Linan, and F. A. Williams (2006). A simple one-step chemistry model for partially premixed hydrocarbon combustion. *Combust. Flame 147*(1-2), 32–38. *(p. 13)*

Fiorina, B., O. Gicquel, L. Vervisch, S. Carpentier, N. Darabiha, A. Lipatnikov, F. Dinkelacker, and J. H. Chen (2005). Premixed turbulent combustion modeling using tabulated detailed chemistry and PDF. *Proc. Combust. Inst. 30 I*, 867–874. *(p. 11, 19)*

Fiorina, B., O. Gicquel, and D. Veynante (2009). Turbulent flame simulation taking advantage of tabulated chemistry self-similar properties. *Proc. Combust. Inst. 32 II*, 1687–1694. *(p. 58)*

Fiorina, B., R. Mercier, G. Kuenne, A. Ketelheun, A. Avdić, J. Janicka,

D. Geyer, A. Dreizler, E. Alenius, C. Duwig, P. Trisjono, K. Kleinheinz, S. Kang, H. Pitsch, F. Proch, F. Cavallo Marincola, and A. Kempf (2015). Challenging modeling strategies for LES of non-adiabatic turbulent stratified combustion. *Combust. Flame 162*(11), 4264–4282. *(p. 25)*

Fiorina, B., D. Veynante, and S. Candel (2014). Modeling Combustion Chemistry in Large Eddy Simulation of Turbulent Flames. *Flow, Turbul. Combust.*, 3–42. *(p. 11, 16, 38, 49)*

Fiorina, B., R. Vicquelin, P. Auzillon, N. Darabiha, O. Gicquel, and D. Veynante (2010). A filtered tabulated chemistry model for LES of premixed combustion. *Combust. Flame 157*(3), 465–475. *(p. 10, 13, 16, 17, 37, 38, 39, 49)*

Franzelli, B., B. Fiorina, and N. Darabiha (2013). A tabulated chemistry method for spray combustion. *Proc. Combust. Inst. 34*(1), 1659–1666. *(p. 11)*

Franzelli, B., E. Riber, and B. Cuenot (2013, jan). Impact of the chemical description on a Large Eddy Simulation of a lean partially premixed swirled flame. *Comptes Rendus M?canique 341*(1-2), 247–256. *(p. 36)*

Franzelli, B., E. Riber, L. Y. M. Gicquel, and T. Poinsot (2012). Large Eddy Simulation of combustion instabilities in a lean partially premixed swirled flame. *Combust. Flame 159*(2), 621–637. *(p. 5, 36, 37)*

Franzelli, B., E. Riber, M. Sanjosé, and T. Poinsot (2010). A two-step chemical scheme for kerosene-air premixed flames. *Combust. Flame 157*(7), 1364–1373. *(p. 13)*

Fureby, C. (2007). Comparison of Flamelet and Finite Rate Chemistry LES for Premixed Turbulent Combustion. In *45th AIAA Aerosp. Sci. Meet. Exhib. (p. 25)*

Galindo, S., F. Salehi, M. J. Cleary, and A. R. Masri (2017). MMC-LES simulations of turbulent piloted flames with varying levels of inlet inhomogeneity. In *Proc. Combust. Inst.*, Volume 36, pp. 1759–1766. *(p. 30)*

Gao, F. and E. O'Brien (1993). A large-eddy simulation scheme for turbulent reacting flows. *Phys. Fluids A Fluid Dyn. 5*(6), 1282. *(p. 20)*

Garmory, A. and E. Mastorakos (2011). Capturing localised extinction in Sandia Flame F with LES CMC. *Proc. Combust. Inst. 33*(1), 1673–1680. *(p. 27)*

Garmory, A. and E. Mastorakos (2013, feb). Sensitivity analysis of LES CMC predictions of piloted jet flames. *Int. J. Heat Fluid Flow 39*, 53–63. *(p. 27)*

Ge, Y., M. J. Cleary, and A. Y. Klimenko (2011). Sparse Lagrangian FDF simulations of Sandia Flame E with density coupling. *Proc. Combust. Inst. 33*(1), 1401–1409. *(p. 30)*

Gicquel, O., N. Darabiha, and D. Thévenin (2000). Laminar premixed hydrogen/air counterflow flame simulations using flame prolongation of ILDM with differential diffusion. *Proc. Combust. Inst. 28*(2), 1901–1908. *(p. 10, 11)*

Giusti, A. and E. Mastorakos (2017). Detailed chemistry LES/CMC simu-

lation of a swirling ethanol spray flame approaching blow-off. In *Proc. Combust. Inst.*, Volume 36, pp. 2625–2632. *(p. 4, 12, 14, 27)*

Givi, P. (1989). Model-free simulations of turbulent reactive flows. *(p. 18)*

Givi, P. (2006). Filtered density function for subgrid scale modeling of turbulent combustion. In *Aiaa J.*, Volume 44, pp. 16–23. *(p. 5, 18)*

Goldin, G. M. (2005). Evaluation of LES Subgrid Reaction Models in a Lifted Flame. *43rd AIAA Aerosp. Sci. Meet. Exhib.* (January), 1–13. *(p. 24)*

Goussis, D. A. and U. Maas (2011). Model Reduction for Combustion Chemistry. In *Turbul. Combust. Model.*, Volume 95, pp. 193–220. *(p. 12)*

Grinstein, F. F. and K. Kailasanath (1995). Three-dimensional numerical simulations of unsteady reactive square jets. *(p. 24, 25)*

Hansen, P. C. and D. P. O'Leary (1993). The Use of the L-Curve in the Regularization of Discrete Ill-Posed Problems. *SIAM J. Sci. Comput. 14*(6), 1487–1503. *(p. 198)*

Harris, S., L. Elliott, D. B. Ingham, M. Pourkashanian, and C. W. Wilson (2000). The optimisation of reaction rate parameters for chemical kinetic modelling of combustion using genetic algorithms. *Comput. Methods Appl. Mech. Eng. 190*(8-10), 1065–1090. *(p. 89)*

Haworth, D. C. (2010). Progress in probability density function methods for turbulent reacting flows. *(p. 18, 19, 20, 21, 22, 23, 24)*

Hernández Pérez, F. E., N. Mukhadiyev, X. Xu, A. Sow, B. J. Lee, R. Sankaran, and H. G. Im (2018, mar). Direct numerical simulations of reacting flows with detailed chemistry using many core/GPU acceleration. *Comput. Fluids*. *(p. 4)*

Hilbert, R., F. Tap, H. El-Rabii, and D. Thévenin (2004). Impact of detailed chemistry and transport models on turbulent combustion simulations. *Prog. Energy Combust. Sci. 30*(1), 61–117. *(p. 9, 11, 12)*

Hodzic, E., M. Jangi, R. Szasz, and X. Bai (2017). Large eddy simulation of bluff body flames close to blow-off using an Eulerian stochastic field method. *Combust. Flame 181*, 1–15. *(p. 23)*

Irannejad, A., A. Banaeizadeh, and F. Jaberi (2015). Large eddy simulation of turbulent spray combustion. *Combust. Flame 162*(2), 431–450. *(p. 12, 14, 23)*

Jaberi, F. A., P. J. Colucci, S. James, P. Givi, and S. B. Pope (1999). Filtered mass density function for large-eddy simulation of turbulent reacting flows. *J. Fluid Mech. 401*, S0022112099006643. *(p. 18)*

James, S., J. Zhu, and M. Anand (2006). LES/FDF of turbulent flames using complex chemical kinetics. In *AIAA Pap. No. 2006-4746*. *(p. 24)*

Jaouen, N., L. Vervisch, and P. Domingo (2017). Auto-thermal reforming (ATR) of natural gas: An automated derivation of optimised reduced chemical schemes. *Proc. Combust. Inst. 36*(3), 3321–3330. *(p. 12)*

Jaouen, N., L. Vervisch, P. Domingo, and G. Ribert (2017). Automatic reduction and optimisation of chemistry for turbulent combustion modelling: Impact of the canonical problem. *Combust. Flame 175*, 60–79. *(p. 12)*

Jaravel, T. (2016). *Prediction of pollutants in gas turbines using large eddy simulation*. Ph. D. thesis. *(p. 3, 16, 35, 37)*

Jaravel, T., E. Riber, B. Cuenot, and G. Bulat (2017). Large Eddy Simulation of an industrial gas turbine combustor using reduced chemistry with accurate pollutant prediction. *Proc. Combust. Inst. 36*(3), 3817–3825. *(p. 5, 12, 14, 15, 36, 37, 38)*

Jaravel, T., E. Riber, B. Cuenot, and P. Pepiot (2018). Prediction of flame structure and pollutant formation of Sandia flame D using Large Eddy Simulation with direct integration of chemical kinetics. *Combust. Flame 188*, 180–198. *(p. 3, 12, 36)*

Jones, W. and V. Prasad (2010, sep). Large Eddy Simulation of the Sandia Flame Series (D to F) using the Eulerian stochastic field method. *Combust. Flame 157*(9), 1621–1636. *(p. 23)*

Jones, W. P., A. J. Marquis, and V. N. Prasad (2012). LES of a turbulent premixed swirl burner using the Eulerian stochastic field method. *Combust. Flame 159*(10), 3079–3095. *(p. 23)*

Kaipio, J. and E. Somersalo (2005). *Statistical and Computational Inverse Problems*. Springer-Verlag New York. *(p. 59)*

Kamal, M. M., R. Zhou, S. Balusamy, and S. Hochgreb (2015). Favre- and Reynolds-averaged velocity measurements: Interpreting PIV and LDA measurements in combustion. *Proc. Combust. Inst. 35*(3), 3803–3811. *(p. 131)*

Kerstein, A. R. (1989). Linear-eddy modeling of turbulent transport. II: Application to shear layer mixing. *Combust. Flame 75*(3-4), 397–413. *(p. 31)*

Kerstein, A. R. (1999). One-dimensional turbulence: model formulation and application to homogeneous turbulence, shear flows, and buoyant stratified flows. *J. Fluid Mech. 392*, S0022112099005376. *(p. 31, 33)*

Kim, S. H. and K. Y. Huh (2004). Second-order conditional moment closure modeling of turbulent piloted Jet diffusion flames. *Combust. Flame 138*(4), 336–352. *(p. 26)*

Klimenko, A. Y. (1990). Multicomponent diffusion of various admixtures in turbulent flow. *Fluid Dyn. 25*(3), 327–334. *(p. 25)*

Klimenko, A. Y. and S. B. Pope (2003). The modeling of turbulent reactive flows based on multiple mapping conditioning. *Phys. Fluids 15*(7), 1907–1925. *(p. 28)*

Kolmogorov, A. N. (1942). Equations of turbulent motion of an incompressible flow. *Physics (College. Park. Md). 6*(1 &2), 56–58. *(p. 36)*

Kronenburg, A. (2004). Double conditioning of reactive scalar transport equations in turbulent nonpremixed flames. *Phys. Fluids 16*(7), 2640–2648. *(p. 26)*

Kronenburg, A. and E. Mastorakos (2011). The conditional moment closure model. *Fluid Mech. its Appl. 95*, 91–117. *(p. 26)*

Kuenne, G., A. Avdić, and J. Janicka (2017). Assessment of subgrid in-

terpolation for the source term evaluation within premixed combustion simulations. *Combust. Flame 178*, 225–256. *(p. 15, 57)*

Kuenne, G., A. Ketelheun, and J. Janicka (2011). LES modeling of premixed combustion using a thickened flame approach coupled with FGM tabulated chemistry. *Combust. Flame 158*(9), 1750–1767. *(p. 16, 35, 36)*

Kuenne, G., F. Seffrin, F. Fuest, T. Stahler, A. Ketelheun, D. Geyer, J. Janicka, and A. Dreizler (2012, aug). Experimental and numerical analysis of a lean premixed stratified burner using 1D Raman/Rayleigh scattering and large eddy simulation. *Combust. Flame 159*(8), 2669–2689. *(p. 35)*

Labahn, J. W., C. B. Devaud, T. A. Sipkens, and K. J. Daun (2014). Inverse analysis and regularisation in conditional source-term estimation modelling. *Combust. Theory Model. 18*(3), 474–499. *(p. 57, 59)*

Layton, W. and L. G. Rebholz (2012). *Approximate Deconvolution Models of Turbulence*. Springer-Verlag Berlin Heidelberg. *(p. 40, 208)*

Lecocq, G., S. Richard, O. Colin, and L. Vervisch (2010). Gradient and counter-gradient modeling in premixed flames: Theoretical study and application to the les of a lean premixed turbulent swirl-burner. *Combust. Sci. Technol. 182*(7), 465–479. *(p. 17)*

Legier, J. P., T. Poinsot, and D. Veynante (2000). Dynamically thickened flame LES model for premixed and non-premixed turbulent combustion. *Proc. Summer Program, Cent. Turbul. Res.*, 157–168. *(p. 35, 137)*

Lignell, D. O., J. H. Chen, and H. A. Schmutz (2011). Effects of Damköhler number on flame extinction and reignition in turbulent non-premixed flames using DNS. *Combust. Flame 158*(5), 949–963. *(p. 13)*

Linse, D., A. Kleemann, and C. Hasse (2014). Probability density function approach coupled with detailed chemical kinetics for the prediction of knock in turbocharged direct injection spark ignition engines. *Combust. Flame 161*(4), 997–1014. *(p. 19)*

Lu, T., Y. Ju, and C. K. Law (2001). Complex CSP for chemistry reduction and analysis. *Combust. Flame 126*(1-2), 1445–1455. *(p. 12)*

Lu, T. and C. K. Law (2005). A directed relation graph method for mechanism reduction. *Proc. Combust. Inst. 30*(1), 1333–1341. *(p. 12)*

Lu, T. and C. K. Law (2008). A criterion based on computational singular perturbation for the identification of quasi steady state species: A reduced mechanism for methane oxidation with NO chemistry. *Combust. Flame 154*(4), 761–774. *(p. 12)*

Lu, T. and C. K. Law (2009). Toward accommodating realistic fuel chemistry in large-scale computations. *(p. 11, 12, 13)*

Maas, U. and S. B. Pope (1992). Simplifying chemical kinetics: Intrinsic low-dimensional manifolds in composition space. *Combust. Flame 88*(3-4), 239–264. *(p. 10)*

Maio, G., M. Cailler, R. Mercier, and B. Fiorina (2019). Virtual chemistry for temperature and CO prediction in LES of non-adiabatic turbulent flames. *Submitted*. *(p. 194)*

Massias, A., D. Diamantis, E. Mastorakos, and D. A. Goussis (1999). An algorithm for the construction of global reduced mechanisms with CSP data. *Combust. Flame 117*(4), 685–708. *(p. 12)*

Mathew, J. (2002). Large eddy simulation of a premixed flame with approximate deconvolution modeling. *(p. 40, 52, 191)*

McMurthy, P. A., S. Menon, and A. R. Kerstein (1992). A linear eddy subgrid model for turbulent reacting flows: Application to hydrogen-AIR combustion. *Symp. Combust. 24*(1), 271–278. *(p. 31)*

Meares, S. and A. R. Masri (2014). A modified piloted burner for stabilizing turbulent flames of inhomogeneous mixtures. *Combust. Flame 161*(2), 484–495. *(p. 30)*

Mehl, C., B. Fiorina, and J. Idier (2017). Evaluation of deconvolution modelling applied to numerical combustion. *Combust. Theory Model.*. *(p. 192)*

Mellado, J. P., S. Sarkar, and C. Pantano (2003). Reconstruction subgrid models for nonpremixed combustion. *Phys. Fluids 15*(11), 3280. *(p. 40, 48, 55)*

Menon, S. and A. R. Kerstein (2011). The linear-Eddy model. *Fluid Mech. its Appl. 95*, 221–247. *(p. 31)*

Mercier, R. (2016). *Turbulent combustion modeling for Large Eddy Simulation of non-adiabatic stratified flames*. Ph. D. thesis, Ecole Centrale Paris. *(p. 4, 125, 135, 161)*

Mercier, R., C. Mehl, B. Fiorina, and V. Moureau (2018). Filtered Wrinkled Flamelets model for Large-Eddy Simulation of turbulent premixed combustion. *submitted*. *(p. 85, 86, 93, 94, 104, 111, 125, 156, 193)*

Mercier, R., T. Schmitt, D. Veynante, and B. Fiorina (2015). The influence of combustion SGS submodels on the resolved flame propagation. Application to the LES of the Cambridge stratified flames. *Proc. Combust. Inst. 35*(2), 1259–1267. *(p. 85, 125, 130, 152, 156)*

Moureau, V., P. Domingo, and L. Vervisch (2011a). Design of a massively parallel CFD code for complex geometries. *Comptes Rendus Mécanique 339*(2-3), 141–148. *(p. 37, 102, 127)*

Moureau, V., P. Domingo, and L. Vervisch (2011b). From Large-Eddy Simulation to Direct Numerical Simulation of a lean premixed swirl flame: Filtered laminar flame-PDF modeling. *Combust. Flame 158*(7), 1340–1357. *(p. 39)*

Mukhopadhyay, S. and J. Abraham (2012, sep). Influence of heat release and turbulence on scalar dissipation rate in autoigniting n-heptane/air mixtures. *Combust. Flame 159*(9), 2883–2895. *(p. 4)*

Mustata, R., L. Valino, C. Jimenez, W. Jones, and S. Bondi (2006, apr). A probability density function Eulerian Monte Carlo field method for large eddy simulations: Application to a turbulent piloted methane/air diffusion flame (Sandia D). *Combust. Flame 145*(1-2), 88–104. *(p. 23)*

Nambully, S., P. Domingo, V. Moureau, and L. Vervisch (2014a). A filtered-

laminar-flame PDF sub-grid-scale closure for LES of premixed turbulent flames: II. Application to a stratified bluff-body burner. *Combust. Flame 161*(7), 1775–1791. *(p. 125)*

Nambully, S., P. Domingo, V. Moureau, and L. Vervisch (2014b). A filtered-laminar-flame PDF sub-grid scale closure for LES of premixed turbulent flames. Part I: Formalism and application to a bluff-body burner with differential diffusion. *Combust. Flame 161*(7), 1756–1774. *(p. 16, 39, 125, 134, 139)*

Navarro-Martinez, S. and A. Kronenburg (2007, jan). LES-CMC simulations of a turbulent bluff-body flame. *Proc. Combust. Inst. 31*(2), 1721–1728. *(p. 27)*

Navarro-Martinez, S. and A. Kronenburg (2009). LES-CMC simulations of a lifted methane flame. *Proc. Combust. Inst. 32*(1), 1509–1516. *(p. 27, 28)*

Navarro-Martinez, S., A. Kronenburg, and F. Di Mare (2005). Conditional moment closure for large eddy simulations. *Flow, Turbul. Combust. 75*(1-4), 245–274. *(p. 25, 26, 27)*

Nicoud, F., H. B. Toda, O. Cabrit, S. Bose, and J. Lee (2011). Using singular values to build a subgrid-scale model for large eddy simulations. *Phys. Fluids 23*(8). *(p. 130)*

Nilsson, P. and X. Bai (2002, jan). Effects of flame stretch and wrinkling on co formation in turbulent premixed combustion. *Proc. Combust. Inst. 29*(2), 1873–1879. *(p. 85, 104)*

Nocedal, J. and S. J. Wright (1999). *Numerical Optimization*, Volume 43. *(p. 59)*

Oijen, J. V. and L. D. Goey (2000). Modelling of Premixed Laminar Flames using Flamelet-Generated Manifolds. *Combust. Sci. Technol. 161*(May 2016), 113–137. *(p. 11)*

O'Rourke, P. J. and F. V. Bracco (1979). Two scaling transformations for the numerical computation of multidimensional unsteady laminar flames. *J. Comput. Phys. 33*(2), 185–203. *(p. 15, 34)*

Pantano, C. and S. Sarkar (2001). A subgrid model for nonlinear functions of a scalar. *Phys. Fluids 13*(12), 3803–3819. *(p. 40)*

Park, J. and T. Echekki (2012). LES-ODT study of turbulent premixed interacting flames. *Combust. Flame 159*(2), 609–620. *(p. 31, 32, 33)*

Pepiot-Desjardins, P. and H. Pitsch (2008). An efficient error-propagation-based reduction method for large chemical kinetic mechanisms. *Combust. Flame 154*(1-2), 67–81. *(p. 12)*

Perona, P. and J. Malik (1990). Scale-space and edge detection using anisotropic diffusion. *IEEE Trans. Pattern Anal. Mach. Intell. 12*(7), 629–639. *(p. 107)*

Peters, N. (1988). Laminar flamelet concepts in turbulent combustion. *Symp. Combust. 21*(1), 1231–1250. *(p. 14)*

Peters, N. (1991). *Reducing mechanisms. (p. 13)*

Philip, M., M. Boileau, R. Vicquelin, E. Riber, T. Schmitt, B. Cuenot, D. Durox, and S. Candel (2015). Large Eddy Simulations of the ignition sequence of an annular multiple-injector combustor. *Proc. Combust. Inst. 35*(3), 3159–3166. *(p. 3, 4, 37)*

Poinsot, T. and D. Veynante (2005). *Theoretical and Numerical Combustion*. *(p. 4, 14, 15, 17, 34, 52, 87, 94, 174)*

Polifke, W., W. Geng, and K. Döbbeling (1998). Optimization of rate coefficients for simplified reaction mechanisms with genetic algorithms. *Combust. Flame 113*(1-2), 119–135. *(p. 89)*

Pope, S. B. (1981). A Monte Carlo Method for the PDF Equations of Turbulent Reactive Flow. *Combust. Sci. Technol. 25*(5-6), 159–174. *(p. 22)*

Pope, S. B. (1985). PDF methods for turbulent reactive flows. *(p. 21)*

Pope, S. B. (1991a). Computations of turbulent combustion: Progress and challenges. *Symp. Combust. 23*(1), 591–612. *(p. 18)*

Pope, S. B. (1991b). Mapping closures for turbulent mixing and reaction. *Theor. Comput. Fluid Dyn. 2*(5-6), 255–270. *(p. 28)*

Proch, F., P. Domingo, L. Vervisch, and A. M. Kempf (2017). Flame resolved simulation of a turbulent premixed bluff-body burner experiment. Part I: Analysis of the reaction zone dynamics with tabulated chemistry. *Combust. Flame 180*, 321–339. *(p. 125, 134, 146)*

Proch, F. and A. M. Kempf (2014). Numerical analysis of the Cambridge stratified flame series using artificial thickened flame LES with tabulated premixed flame chemistry. *Combust. Flame 161*(10), 2627–2646. *(p. 125, 134)*

Raman, V. and H. Pitsch (2007, jan). A consistent LES/filtered-density function formulation for the simulation of turbulent flames with detailed chemistry. *Proc. Combust. Inst. 31*(2), 1711–1719. *(p. 5, 23)*

Ribert, G., O. Gicquel, N. Darabiha, and D. Veynante (2006). Tabulation of complex chemistry based on self-similar behavior of laminar premixed flames. *Combust. Flame 146*(4), 649–664. *(p. 58)*

Salehi, F., M. Cleary, A. Masri, Y. Ge, and A. Klimenko (2017). Sparse-Lagrangian MMC simulations of an n-dodecane jet at engine-relevant conditions. *Proc. Combust. Inst. 36*(3), 3577–3585. *(p. 4, 30)*

Schmidt, R. C., A. R. Kerstein, and R. McDermott (2010). ODTLES: A multi-scale model for 3D turbulent flow based on one-dimensional turbulence modeling. *Comput. Methods Appl. Mech. Eng. 199*(13-16), 865–880. *(p. 31)*

Schulz, O., T. Jaravel, T. Poinsot, B. Cuenot, and N. Noiray (2017). A criterion to distinguish autoignition and propagation applied to a lifted methane-air jet flame. In *Proc. Combust. Inst.*, Volume 36, pp. 1637–1644. *(p. 36)*

See, Y. C. and M. Ihme (2015). Large eddy simulation of a partially-premixed gas turbine model combustor. *Proc. Combust. Inst. 35*(2), 1225–1234. *(p. 11)*

Sheikhi, M. R. H., T. G. Drozda, P. Givi, and S. B. Pope (2003). Velocity-scalar filtered density function for large eddy simulation of turbulent flows. *Phys. Fluids 15*(8), 2321–2337. *(p. 18)*

Sheikhi, M. R. H., P. Givi, and S. B. Pope (2007). Velocity-scalar filtered mass density function for large eddy simulation of turbulent reacting flows. *Phys. Fluids 19*(9). *(p. 18)*

Smith, T. and S. Menon (1998). Subgrid combustion modeling for premixed turbulent reacting flows. In *36th AIAA Aerosp. Sci. Meet. Exhib. (p. 31)*

Stolz, S. and N. A. Adams (1999). An approximate deconvolution procedure for large-eddy simulation. *Phys. Fluids 11*(7), 1699–1701. *(p. 40, 41, 48, 55, 56, 191)*

Stolz, S., N. A. Adams, and L. Kleiser (2001a). An approximate deconvolution model for large-eddy simulation with application to incompressible wall-bounded flows. *Phys. Fluids 13*(4), 997–1015. *(p. 40)*

Stolz, S., N. A. Adams, and L. Kleiser (2001b). The approximate deconvolution model for large-eddy simulation of compressible flows and its application to shock-turbulent-boundary-layer interaction. *Phys. Fluids 13*(10), 2985–3001. *(p. 40)*

Sundaram, B., A. Y. Klimenko, M. J. Cleary, and Y. Ge (2016). A direct approach to generalised multiple mapping conditioning for selected turbulent diffusion flame cases. *Combust. Theory Model. 20*(4), 735–764. *(p. 30)*

Sweeney, M. S., S. Hochgreb, M. J. Dunn, and R. S. Barlow (2012a). The structure of turbulent stratified and premixed methane/air flames I: Non-swirling flows. *Combust. Flame 159*(9), 2896–2911. *(p. 85, 124, 135, 193, 196)*

Sweeney, M. S., S. Hochgreb, M. J. Dunn, and R. S. Barlow (2012b). The structure of turbulent stratified and premixed methane/air flames II: Swirling flows. *Combust. Flame 159*(9), 2912–2929. *(p. 85, 124, 127, 131, 151, 158, 193)*

Tang, Q., W. Zhao, M. Bockelie, and R. O. Fox (2007). Multi-environment probability density function method for modelling turbulent combustion using realistic chemical kinetics. *Combust. Theory Model. 11*(6), 889–907. *(p. 23)*

Tikhonov, A. N. (1963). Solution of incorrectly formulated problems and the regularization method. *Sov. Math. Dokl. 4*(4), 1035–1038. *(p. 57, 197)*

Tikhonov, A. N. and V. Y. Arsenin (1978). Solutions of Ill-Posed Problems. *Math. Comput. 32*, 1320–1322. *(p. 57)*

Turanyi, T. (1990). Reduction of large reaction mechanisms. *New J. Chem. 14*(11), 795–803. *(p. 12)*

Valino, L. (1998). Field Monte Carlo formulation for calculating the probability density function of a single scalar in a turbulent flow. *Flow, Turbul. Combust. 60*(2), 157–172. *(p. 22)*

Vermorel, O., P. Quillatre, and T. Poinsot (2017). LES of explosions in vent-

ing chamber: A test case for premixed turbulent combustion models. *Combust. Flame 183*, 207–223. *(p. 4, 37, 85)*

Vervisch, L., P. Domingo, G. Lodato, and D. Veynante (2010). Scalar energy fluctuations in Large-Eddy Simulation of turbulent flames: Statistical budgets and mesh quality criterion. *Combust. Flame 157*(4), 778–789. *(p. 132)*

Veynante, D., B. Fiorina, P. Domingo, and L. Vervisch (2008). Using self-similar properties of turbulent premixed flames to downsize chemical tables in high-performance numerical simulations. *Combust. Theory Model. 12*(6), 1055–1088. *(p. 58)*

Veynante, D. and R. Knikker (2006). Comparison between LES results and experimental data in reacting flows. *J. Turbul. 7*(August 2015), N35. *(p. 131, 132)*

Veynante, D. and A. Trouvé (1997). Gradient and counter-gradient scalar transport in turbulent premixed flames. *J. Fluid Mech. 332*(1997), 263–293. *(p. 17)*

Villermaux, J. and L. Falk (1994). A generalized mixing model for initial contacting of reactive fluids. *Chem. Eng. Sci. 49*(24), 5127–5140. *(p. 21)*

Vo, S., O. T. Stein, A. Kronenburg, and M. J. Cleary (2017). Assessment of mixing time scales for a sparse particle method. *Combust. Flame 179*, 280–299. *(p. 29)*

Volpiani, P. S., T. Schmitt, and D. Veynante (2017). Large eddy simulation of a turbulent swirling premixed flame coupling the TFLES model with a dynamic wrinkling formulation. *Combust. Flame 180*, 124–135. *(p. 4, 5, 13, 15, 36)*

Vreman, A. W., R. J. M. Bastiaans, and B. J. Geurts (2009). A similarity subgrid model for premixed turbulent combustion. *Flow, Turbul. Combust. 82*(2), 233–248. *(p. 40)*

Wang, G., M. Boileau, and D. Veynante (2011). Implementation of a dynamic thickened flame model for large eddy simulations of turbulent premixed combustion. *Combust. Flame 158*(11), 2199–2213. *(p. 13, 36, 135, 192)*

Wang, H. and M. Frenklach (1991). Detailed reduction of reaction mechanisms for flame modeling. *Combust. Flame 87*(3-4), 365–370. *(p. 12)*

Wang, P. and X. S. Bai (2005). Large eddy simulation of turbulent premixed flames using level-set G-equation. *Proc. Combust. Inst. 30*(1), 583–590. *(p. 37)*

Wang, Q. and M. Ihme (2016). Regularized deconvolution method for turbulent combustion modeling. *Combust. Flame*. *(p. 41, 49, 52, 57, 73, 191)*

Westbrook, C. K. and F. L. Dryer (1981). Simplified reaction mechanisms for the xxidation of hydrocarbon fuels in flames. *Combust. Sci. Technol. 27*, 31–43. *(p. 13)*

Whitehouse, L. E., A. S. Tomlin, and M. J. Pilling (2004). Systematic reduction of complex tropospheric chemical mechanisms, Part I: sensitivity

and time-scale analyses. *Atmos. Chem. Phys. 4*(7), 2025–2056. *(p. 12)*

Xin, Y., C. Yoo, J. Chen, and C. Law (2015, jan). A DNS study of self accelerating cylindrical hydrogen air flames with detailed chemistry. *Proc. Combust. Inst. 35*(1), 753–760. *(p. 4)*

Yaldizli, M., K. Mehravaran, and F. A. Jaberi (2010). Large-eddy simulations of turbulent methane jet flames with filtered mass density function. *Int. J. Heat Mass Transf. 53*(11-12), 2551–2562. *(p. 5, 23, 31)*

Yoo, C. S., Z. Luo, T. Lu, H. Kim, and J. H. Chen (2013). A DNS study of ignition characteristics of a lean iso-octane/air mixture under HCCI and SACI conditions. *Proc. Combust. Inst. 34*(2), 2985–2993. *(p. 12)*

Zhang, H. and E. Mastorakos (2016). Prediction of Global Extinction Conditions and Dynamics in Swirling Non-premixed Flames Using LES/CMC Modelling. *Flow, Turbul. Combust. 96*(4), 863–889. *(p. 14, 27)*

Zhang, H. and E. Mastorakos (2017). Modelling local extinction in Sydney swirling non-premixed flames with LES/CMC. In *Proc. Combust. Inst.*, Volume 36, pp. 1669–1676. *(p. 27)*

Zhou, R., S. Balusamy, M. S. Sweeney, R. S. Barlow, and S. Hochgreb (2013). Flow field measurements of a series of turbulent premixed and stratified methane/air flames. *Combust. Flame 160*(10), 2017–2028. *(p. 124, 126, 127, 128, 144)*

Zhu, C., R. H. Byrd, P. Lu, and J. Nocedal (1997). Algorithm 778: L-BFGS-B: Fortran subroutines for large-scale bound-constrained optimization. *ACM Trans. Math. Softw. 23*(4), 550–560. *(p. 57)*

université PARIS-SACLAY | ÉCOLE DOCTORALE Sciences mécaniques et énergétiques, matériaux et géosciences (SMEMAG)

Titre : Simulation aux Grandes Echelles et chimie complexe pour la modélisation de la structure chimique des flammes turbulentes

Mots clés : Simulation aux Grandes Echelles, Combustion turbulente, Prédiction des polluants, Plissement de sous-maille, Structure chimique des flammes, Déconvolution

Résumé : La Simulation aux Grandes Echelles (SGE) est appliquée à des brûleurs industriels pour prédire de nombreux phénomènes physiques complexes, tel que l'allumage ou la formation de polluants. La prise en compte de réactions chimiques détaillées est alors indispensable pour obtenir des résultats précis. L'amélioration des moyens de calculs permet de réaliser des simulations de brûleurs avec une chimie de plus en plus détaillée. La principale problématique est le couplage entre les réactions chimiques et l'écoulement turbulent. Bien que la dynamique de flamme soit souvent bien reproduite avec les modèles actuels, la prédiction de phénomènes complexes comme la formation de polluants reste une tâche difficile. En particulier, des études ont montré que l'influence du plissement de sous-maille sur la structure chimique des flammes n'était pas prise en compte de manière précise. Deux modèles basés sur le filtrage explicite des fronts de flammes sont étudiés dans cette thèse afin d'améliorer la prédiction de polluants en combustion turbulente prémélangée : (i) le premier modèle met en jeu une méthode de déconvolution des variables filtrées ; (ii) le second modèle implique l'optimisation de la chimie pour obtenir des flammes turbulentes filtrées. L'objectif de la thèse est d'obtenir une prédiction précise des polluants à coût de calcul réduit.

Title : Large Eddy Simulations and complex chemistry for modeling the chemical structure of turbulent flames

Keywords : Large Eddy Simulation, Turbulent combustion, Pollutants prediction, Subgrid scale wrinkling, Flame chemical structure, Deconvolution

Abstract : Large Eddy Simulation (LES) is applied to industrial burners to predict a wide range of complex physical phenomena, such as flame ignition and pollutants formation. The prediction accuracy is tightly linked to the ability to describe in detail the chemical reactions and thus the flame chemical structure. With the improvement of computational clusters, the simulation of industrial burners with detailed chemistry becomes possible. A major issue is then to couple detailed chemical mechanisms to turbulent flows. While the flame dynamics is often correctly simulated with state-of-the-art models, the prediction of complex phenomena such as pollutants formation remains a difficult task. Several investigations show that, in many models, the impact of flame subgrid scale wrinkling on the chemical flame structure is not accurately taken into account. Two models based on explicit flame front filtering are explored in this thesis to improve pollutants formation in turbulent premixed combustion: (i) a model based on deconvolution of filtered scalars; (ii) a model involving the optimization of chemistry to reproduce filtered turbulent flames. The objective of the work is to achieve high accuracy in pollutants formation prediction at low computational costs.

Université Paris-Saclay
Espace Technologique / Immeuble Discovery
Route de l'Orme aux Merisiers RD 128 / 91190 Saint-Aubin, France